Multiscale Process Modeling of Residual Deformation and Defect Formation for Laser Powder Bed Fusion Additive Manufacturing

by

Qian Chen

B.S., Xi'an Jiaotong University, 2013

M.S., Xi'an Jiaotong University, 2016

Submitted to the Graduate Faculty of the

Swanson School of Engineering in partial fulfillment

of the requirements for the degree of

Doctor of Philosophy

University of Pittsburgh

2021

UNIVERSITY OF PITTSBURGH

SWANSON SCHOOL OF ENGINEERING

This dissertation was presented

by

Qian Chen

It was defended on

October 29, 2021

and approved by

Xiayun Zhao, Ph.D., Assistant Professor, Department of Mechanical Engineering and Materials Science

Qihan Liu, Ph.D., Assistant Professor, Department of Mechanical Engineering and Materials Science

Kevin P. Chen., Ph.D., Paul E. Lego Chair Professor, Department of Electrical and Computer Engineering

Dissertation Director: Albert C. To, Ph.D., William Kepler Whiteford Professor, Department of Mechanical Engineering and Materials Science

Multiscale Process Modeling of Residual Deformation and Defect Formation for Laser Powder Bed Fusion Additive Manufacturing

Qian Chen, PhD

University of Pittsburgh, 2021

Laser powder bed fusion (L-PBF) additive manufacturing (AM) is capable of producing complex parts near net shape with good mechanical properties. However, undesired residual stress and distortion that lead to build failure and defects such as porosity are preventing broader applications of L-PBF. To realize the full potential of L-PBF, a multiscale modeling methodology is developed to predict residual deformation, melt pool, and porosity formation.

To predict the residual deformation and stress in L-PBF at part-scale, a multiscale process modeling framework based on inherent strain method is proposed. Inherent strain vectors are extracted from detailed multi-layer process simulation with high fidelity at micro-scale. Uniform but anisotropic strains are then applied to L-PBF part in a layer-by-layer fashion in a quasi-static equilibrium finite element analysis (FEA) to predict residual distortion and stress. Besides residual distortion and stress prediction at part scale, multiphysics modeling at powder scale is performed to study the melt pool variation and defect formation induced by process parameters, preheating temperature and spattering particles. Melt pool dynamics and porosity formation mechanisms associated with these factors are revealed through simulation and experiments.

Based on the proposed part-scale residual stress and distortion model, path planning method is developed to tailor the laser scanning path for a given geometry to prevent large residual deformation and building failures. Gradient based path planning for continuous and island scanning strategy is formulated and full sensitivity analysis for the formulated compliance- and

stress-minimization problem is performed. The feasibility and effectiveness of this proposed path planning method is demonstrated experimentally using the AconityONE L-PBF system.

In addition, a data-driven framework utilizing machine learning is developed to predict the thermal history at part-scale for L-PBF. In this work, a sequential machine learning model including convolutional neural network (CNN) and recurrent neural network (RNN), long short-term memory unit, is proposed for real-time thermal history prediction. A 100x prediction speed improvement is achieved compared to the finite element analysis which makes the prediction faster than real fabrication process and real-time temperature profile available.

Table of Contents

List of Tables

List of Figures

Preface

At this moment when I finally reach the destination of my PhD study, there are lots of memories streaming through my mind. I could still remember the first time I met Prof. Albert To in his office and the conversation we had about the future, the moment the experiments and programs worked and my papers got accepted. Recalling the 5 years' life at University of Pittsburgh, I realize that I have gained a lot from this research adventure and would like to thank many people.

First and foremost, I would like to thank Prof. Albert To for the guidance, motivation and mentorship in the past few years. I appreciate the freedom I was granted to explore the research topics I was interested in and all the support offered that kept me on the right track. I benefited and learnt a lot from his kind personality, good communication skills, professional knowledge and strong passion for research and the unknown world.

I would like to express my sincere gratitude to my committee members, Prof. Xiayun Zhao, Prof. Qihan Liu and Prof. Kevin P. Chen for serving on my committee. I am grateful for their insightful and professional feedbacks on my dissertation which definitely have improved it.

I am also grateful to all the colleagues in our group. I learnt a lot from them and enjoy working together. Thanks to Lin Cheng, Xuan Liang, Jikai Liu, Wen Dong, Jian Liu, Florian Dugast, Shawn Hinnebusch, Praveen Vulimiri, Basil Paudel, Xavier Jimenez, Seth Strayer, Hai Tran, Santanu Paul and among others, for all the generous support and advice.

Last but most important, thanks to my wife, my parents, my sister and brother in law for putting up with me and give me your unconditional support! Without their love, I would not have been able to pursue this journey.

1.0 Introduction

The primary goal of this work is to develop simulation methods at part-scale and meso-scale to predict the distortion of as-built AM part due to residual stress and study the melt pool variation and porosity formation mechanism during laser scanning process. Manufacturing process optimization is conducted to prevent building failures based on the proposed part-scale model. The main focus of the multiscale modeling and optimization objective lies within the fields of solid mechanics and heat transfer. The motivation, background and research objective will be provided in this chapter.

1.1 Laser Powder Bed Fusion

Powder bed fusion (PBF) is one of 7 additive manufacturing (AM) process categories classified by ASTM F42 standard [1]. Most current metal additive manufacturing systems are of the powder bed fusion type. Powder bed fusion process, including direct metal laser melting (DMLM), selective laser melting (SLM), and electron beam melting (EBM), is an emerging and fast evolving technique and draw unprecedented attention from both academia and industry due to its capability to manufacture functional parts with complex geometry and intricate internal structures in a layer-by-layer fashion. Compared to traditional subtractive manufacturing techniques, which suffer from geometric limitations, L-PBF AM enables extensive design freedom, an appealing advantage for both the industrial and research settings. Additionally, fine grains and dislocations generated from the rapid heating and cooling process enable engineers to

obtain localized and optimized mechanical properties that are not possible in wrought or cast counterparts. Figure 1.1 schematically illustrate the laser powder bed fusion process: the spreader (*a.k.a.* recoater blade) spreads a thin powder layer from reservoir to the build plate, and the laser beam melts the powders and welds them with previously deposited according to the sliced CAD model with predefined scanning path. Then the build platform moves downwards by a distance equal to the layer thickness, and this process repeats itself each layer until the part is built completely.

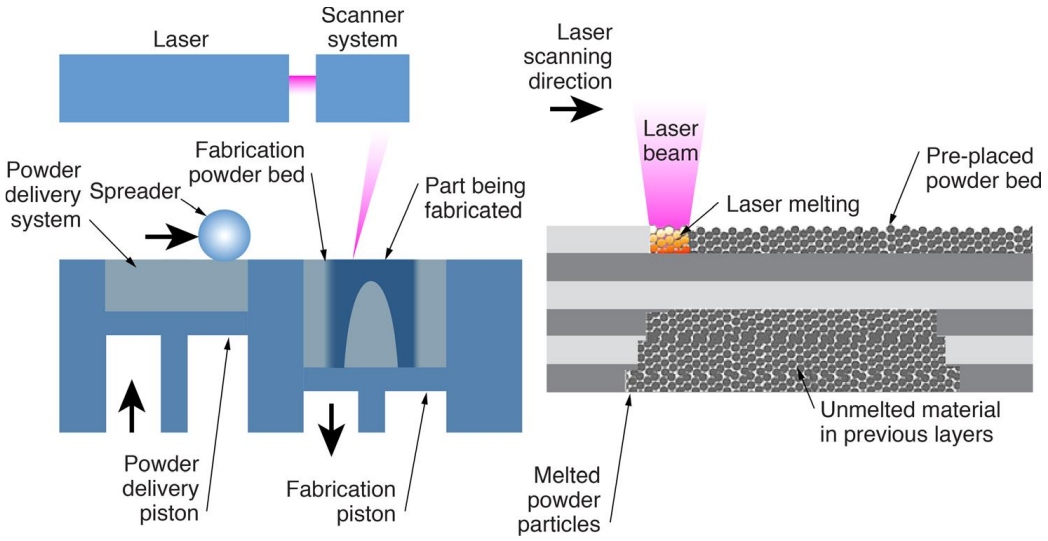

Figure 1.1: Schematic Overview of Metal Laser Powder Bed Fusion Process [2]

Commercial powder bed fusion systems, such as EOS M290 (EOS), RenAM 500 (Renishaw), Arcam AB and Concept Laser (acquired by GE) as shown in Figure 1.2, have been extensively employed in industry such as turbine blade, combustion chamber nozzles in aerospace, light-weight biomedical implants and conformal cooling channels with thin wall for injection molding. In October 2018, GE Aviation announced its 30,000th 3D-printed fuel nozzle tip for the LEAP engine shown in Figure 1.3(a), which achieves 25% weight and 95% inventory reduction while 5x durable improvement compared to its counterparts by conventional manufacturing. Powder bed fusion additive manufacturing has the advantages including accelerate design

innovation, reduce supply chain cost, simplify systems, increase product performance and return on investment over conventional manufacturing process.

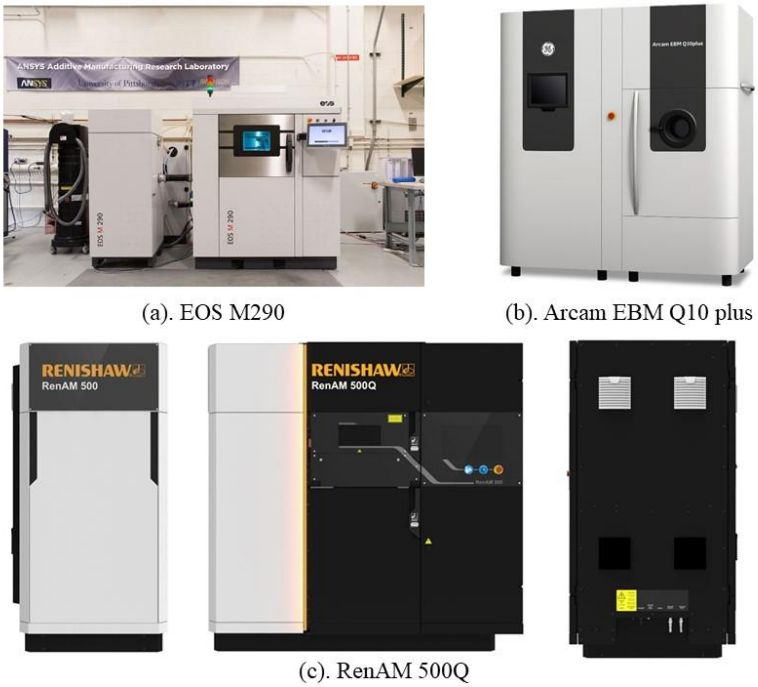

(a). EOS M290 (b). Arcam EBM Q10 plus

(c). RenAM 500Q

Figure 1.2: Commercial Powder Bed Fusion Systems

(a) (b)

Figure 1.3: Commercial Metal Components Fabricated by Powder Bed Fusion Additive Manufacturing: (a) GE Fuel Nozzle; (b) Stryker Hip Biomedical Implant.

1.2 Multiscale Modeling

Numerical modeling for powder bed fusion process has proven to be a powerful tool to: (1). help understand the mechanism including residual stress and deformation due to rapid heating and cooling, and melt pool morphology variation and defect formation associated with processing parameter and particle motion; (2). guide design and ensure manufacturability; (3). optimize manufacturing process and lower the expense. A variety of computation models for powder bed fusion process have been developed with different purposes, assumptions and underlying physics. According to Yan et al. [3], existing computation models are categorized into three main types:

1. Continuum-based thermal models that simplify the powder bed as a continuum material, and only incorporate heat transfer but no fluid flow [4-10].Most of this type of models are developed by finite element software such as ANSYS, ABAQUS and COMSOL. Due to neglecting the expensive CFD and particle behaviors, the simulation cost is less expensive and scale is extended to part-scale by commercial software such as Autodesk Netfabb [11-13], 3DSim (acquired by ANSYS) [14, 15] and MSC Simufact [16].

2. High-fidelity computational fluid dynamics (CFD) models that resolve the thermal-fluid flow behaviors of individual powder particles [2, 17-24]. Simulation cost for this type of simulation is extremely high, and can be up to thousands of central processing unit (CPU) hours although the simulation domain is usually limited to a minimal number of scan tracks or layers. This type simulation is mainly used to study the melt pool dynamics and defect formation mechanism.

3. Semi-analytical thermal-conduction models that only consider thermal conduction in a homogeneous continuum, such as the Rosenthal solution [25] based on semi-infinite plate assumption. Those models can estimate the steady-state temperature field [26] and predict lack-

of-fusion porosity [27], and can be integrated with finite element method for part-scale thermal profile prediction [28, 29].

1.2.1 Continuum-based Thermal Simulation

Fast and accurate simulation of residual stress/distortion in AM-processed parts is a promising method for ensuring manufacturability and improving component quality. Considering the limited computational speed, early simulation efforts for powder bed fusion mainly focus on models on the order of millimeter or even smaller scale such as single track. Dai and Shaw [4, 5] developed a 3D finite element model to investigate the effect of fabrication sequences, laser scanning patterns, and laser scanning rates on residual stresses and distortion. Similarly, Cheng et al. [30] explored residual stress and deformation subject to different scanning strategies in selective laser melting, where eight different scanning strategies were simulated. Fu and Guo [7] used a micro-scale SLM model with surface moving Gaussian heat flux to study the temperature gradient mechanism within the molten pool. Prabhakar et al. [8] proposed a layer-by-layer finite element based modeling approach to study residual stress and deformation of the electron beam melting process. Hussein et al. [31] implemented a non-linear transient thermo-mechanical analysis to study the temperature and stress field of a single layer consists of multi-tracks. In this way, part-scale distortion and residual stress prediction requires thermo-mechanical analysis with millions of time steps. With very small laser spot size and thin layer thickness, simulation of powder bed AM process requires prohibitively large number of elements and high computation cost. Various techniques have been proposed to make AM process simulation model more efficient lately. For instance, layer scaling, which simultaneously models a number of layers grouped together, is a common method used by the majority of simulation work to reduce element number and

computation cost [32-36]. Others have attempted uniform thermal load [33], stress [34], or temperature field [35] from detailed micro-scale analysis and pass the results to macro-scale analysis with scaled up layers for distortion and stress prediction. Simulation results of these methods show good agreement with experimental measurements. Several faster and more robust commercial simulation tools have also been developed for industrial applications, such as AutoDesk Netfabb, 3DSim (now part of ANSYS), MSC Simufact, GE GeonX, and Amphyon Works. Dynamic adaptive mesh refinement and coarsening algorithm has been developed by Pan Computing Cube (now part of Netfabb) [11-13] and 3DSim [14, 15] to reduce computation expense in performing part-scale simulation.

1.2.2 High-fidelity Multiphysics Simulation

Different from previous works that treat the powder bed as a homogenous continuum body, recent simulations have seen a paradigm shift towards incorporating the discrete and randomly distributed nature of the powder bed. Namely, a variety of studies have been conducted to study melt pool dynamics and corresponding defect mechanism such as spattering and pore formation, in powder bed fusion process numerically. Lee et al. [37] developed a 3D mesoscale simulation framework for L-PBF of IN718, which accounts for the effect of powder packing, surface tension, and evaporation. Yan et al. [22] conducted both single-track and multi-track simulations to study the underlying physics of single-track defects in the electron beam melting process, including balling effects and track non-uniformity. Shrestha et al. [23] developed a 3D multiphysics model using Flow-3D to study keyhole behavior and related pore formation mechanism in L-PBF process. Besides the commercial software Flow-3D using the finite volume method, a multiphysics simulation code developed by Lawrence Livermore National Laboratory (LLNL) using the finite

element method (ALE3D) has been employed to simulate the melt pool formation and associated physics in L-PBF. Specifically, Khairallah et al. [17] considered a powder bed with experimentally measured particle size distribution in the simulation for 316L stainless steel. The significance of simulating the partial contacts between particles to consider the reduction in effective thermal conductivity of powder was emphasized. Matthews et al. [18] revealed the dynamics of the denudation process in L-PBF, which were observed by high-speed imaging. The high-fidelity simulation revealed the dominant role of powder particle entrainment by surrounding gas flow on powder particle denudation near a melt track. Metal vapor flowing outward and directly from the laser spot competes with entrainment of powder particle that is driven by vapor jet when the ambient pressure is low. In contrast to conventional simulations with volumetric energy deposition, laser ray-tracing energy deposition was used, which enables partial particle melting and accounts for the multiple reflections of laser rays in the depression region [17, 18, 20].

1.2.3 Data-driven Modeling

Data-driven approaches that utilizing machine learning models and existing data from experiments and simulation have been widely employed in design for additive manufacturing, process and production. Scime and Beuth [38] leveraged a convolutional neural network (CNN) to autonomously detect and classify building defects and anomalies in L-PBF such as part damage, debris, recoater hopping and streaking. They also applied support vector machine (SVM) to in-process monitoring to classify the melt pool morphologies [39]. Xie et al. [40] developed a mechanistic data-driven framework to predict location-dependent mechanical properties based on process-induced thermal histories and achieved good predictions using a small amount of experimental data with noise. Interested readers are referred to Ref. [41] for a comprehensive

review on the state-of-the-art of machine learning application in additive manufacturing. The feasibility of using data-driven approach based on machine learning techniques to predict thermal histories in additive manufacturing has been explored as well. Li et al. [42] developed a surrogate model using functional Gaussian process based on finite element analysis and employed a Bayesian calibration method to enable layer-to-layer thermal prediction for fused deposition modeling (FDM) process. A data-driven thermal history prediction model based on recurrent neural network is proposed for DED process for real-time process control and optimization [43, 44].

1.3 Path Planning for Laser Powder Bed Fusion

Residual stress is inherent in these AM processes due to sharp thermal gradient and rapid cooling rate, which may lead to severe part distortion, cracking, and delamination from the build plate. This type of thermal stress-induced failure will cause a build to stop abruptly and thus will increase manufacturing time and cost. To address this issue, the effect of scanning strategy on residual stress has been extensively investigated. Scanning strategy can be divided into two parts, namely the scanning parameters (heat source power and velocity, hatching space and layer thickness) and scanning path. Studies on scanning parameters in SLM have been performed to improve fabrication quality of parts with horizontal structures [45] and downfacing structures [46]. Kruth et al. [47] found that shorter scan vector could decrease residual stress in their experiment with Ti-6Al-4V selective laser melting (SLM). Studies on scanning path were mainly focused on the so-called island-type scanning pattern, a patent hold by Concept laser, which divides each layer into islands forming a checkboard pattern and these islands are raster scanned with shorter scan

tracks. It has been reported that island scanning strategy can effectively decrease residual stress and cracks in EBM. Island scanning strategy has been employed by commercial metal additive manufacturing systems such as Renishaw AM500, Arcam Q20 and Aconity One used in this study. Different scanning orientations and island sizes have been explored to examine the influence on thermal residual stress [5, 6, 12, 47-50]. Kruth et al [51] conducted experiments to study the effect of island scanning strategy with rotation on residual stress in Ti-6Al-4V SLM. It has been confirmed island scanning strategy could reduce residual stress and the maximum reduction is achieved when rotating the island 45° inclined to the X-axis. It has also been reported that changing island size does not give any further contributions. Lu et al [48]studied the microstructure, mechanical properties and residual stress of Inconel 718 parts manufactured by SLM with different island size. It has been reported that enlarging island size leads to higher density while the smallest island size leads to the lowest residual stress which may result from stress release due to cracks. Cheng et al [6] compared the residual deformation and stress of different scanning strategies and confirmed the effect of island scanning strategy on residual deformation and stress reduction. Thijs et al [52] studied the influence of varying laser path, unidirectional and bidirectional, and rotating scanning direction layer-wise on microstructure and texture of parts fabricated by Concept Laser M1.

Besides optimizing the island scanning pattern, we will also explore free-form continuous scanning path optimization on residual stress mitigation for metal parts. The continuous scanning strategy is a scanning pattern with high efficiency widely used for different metal AM processes, including PBF, wire-feed additive manufacturing [53] and DED process [54]. Ding et al [55, 56] proposed a continuous path planning method based on medial axis transformation algorithm to produce void- and gap-free part in wire + arc additive manufacturing (WAAM). To the best of the

authors' knowledge, optimizing continuous scanning path for residual stress reduction has not been studied yet. The main obstacles include complexity of the optimization problem and computational expense of full-scale AM process simulation.

Even though continuous scanning path optimization for metal additive manufacturing has never been tackled, there are extensive numerical studies on optimal path planning on fiber reinforcement design or polymer AM, wherein material properties are greatly affected by build path orientation. Ponche [57] proposed a global design for AM (DfAM) framework to consecutively design the build direction, structural shape, and deposition paths. Hoglund [58] performed compliance minimization topology optimization with fiber angles as additional design variables for fiber-reinforced polymer printing. A limitation of this method is that fiber angles are treated as discrete variables without considering the overall printing path smoothness and continuity. To address this issue, filters [59-61] are introduced to project the discrete angle variables for smoothness improvement. Other than that, a level set-based continuous fiber path optimization method was proposed by Brampton et al [62]. Fiber paths were defined by iso-value level set contours, so that continuity is always guaranteed. Beyond that, smoothness of the paths can be addressed by adding curvature constraints, and signed distance property of the level set field makes it trivial to derive a ready-to-print deposition path. However, there are also limitations of this method that the solution is heavily dependent on the initial guess and convergence is reported to be slow. Another level set-based continuous path optimization method was developed by Liu et al [63], wherein the structural topology was concurrently optimized rather than fixing the structural geometry. With that method, deposition path planning is performed by offsetting the structural boundary, and hence it cannot handle deposition path optimization for fixed geometry.

In addition to fiber deposition and polymer printing, the level set method has been applied to contour-offset path generation for traditional machining [64, 65] as well.

1.4 Research Objective

The aim of this research work is to develop process simulation models at different scale for powder bed fusion process to study the mechanisms for residual stress and distortion, building failures and defect formation. The developed models are calibrated by various experiment measurements including thermal histories, deformation data by laser faro arm and *ex-situ* melt pool cross-sections. Moreover, the laser scanning path and island scan pattern is optimized based on the insights obtained from part-scale simulation. The research objectives including future research plans are summarized as follows:

Part-scale residual deformation and stress prediction. An inherent strain based multiscale process simulation model is developed for fast part-scale distortion and residual stress prediction. Int this work, detailed process simulation of the DMLM process is first validated by far-field temperature history measurement of single-layer deposition. Line heat source model is employed in single-layer scale model to reach the spatial scale of experiment. Once the detailed process model is validated, a micro-scale RVE model using Goldak's point heat source model is employed to extract the inherent strains based on the modified inherent strain theory. For part-scale model, the extracted inherent strains are applied as thermal expansion coefficients (CTEs) with a unit temperature rise. Several physical layers are merged as one and activated layer-by-layer in mechanical analysis. Simulation of AM parts with moderately complex geometries can be completed within an hour. Distortion from simulation has been validated by direct experimental

measurement. Residual stress is computed by the displacement field and the stress profile obtained matches well with previous studies in the literature.

Multiphysics modeling at meso-scale. The role of preheating temperature on melt pool variation is confirmed firstly by experiments and then studied via simulation. Melt tracks in conduction, transition, and keyhole regime were deposited on substrate heated up to 100 – 500 °C by heating module in the experiments. *Ex-situ* cross-sectional measurements were performed to study the variation of melt pool morphology with preheating temperature. Multiphysics models were developed and calibrated by *ex-situ* cross-sectional measurements to reveal the underlying mechanism of melt pool morphology variation in conduction, transition, and keyhole regimes.

Path planning for residual stress and deformation reduction. A continuous laser scanning path and an island scan pattern optimization method are proposed for laser powder bed fusion process based on the inherent strain method, respectively. In the continuous scanning path optimization framework, the individual level contours are employed as scanning paths of which the continuity and equal hatching space are ensured, and the relevant thermal loading is calculated from scanning orientation dependent inherent strain vectors. The numerical examples exhibit the effectiveness of this proposed optimization method in mitigating stress concentration and compliance minimization, while the constant hatching space among scanning lines are always guaranteed owing to the signed distance feature of the level set function. This scanning path optimization method exhibits the scalability to much taller and complex structures consisting of multiple layers and features such as overhang, and the ability to extend to concurrent design that takes both topology optimization and laser scanning path planning into account. For the island scan pattern optimization, part deformation is obtained from a multi-step static equilibrium analysis including layer-by-layer activation and cutting off at last step. Since post removal after

building is considered in both finite element and sensitivity analysis, deformation of the as-built part after cutting off the building platform is minimized directly in the gradient-based optimization. Two numerical examples are investigated to examine the performance of proposed method. The optimized scan patterns for the block and connecting rod, are written into .cli files for the build by Aconity One. The fabricated parts are cut off by electric discharge machine for stress relief. The effectiveness of the proposed island scan pattern optimization method is demonstrated by comparing the upward bending of part under initial and optimized scan pattern,

Data-driven and real-time thermal prediction tool at part-scale. A scalable and elastic thermal prediction model based on recurrent neural network (RNN) is developed for real-time quality-assurance systems. This model can fully exploit the data emanate from simulation and experimental measurements including in-situ monitoring heatmap. In this work, part-scale simulation data is employed to train the proposed RNN model for proof of concept. The model has a few advantages over the convectional method based on finite element or volume simulation: (1) Prediction speed is immensely improved (100x) while computation cost is lowered; (2) Prediction scale is flexible since the prediction for each node is separated and independent, i.e., predicting thermal history for one point of interest can be easily extended to the prediction for the entire part; (3) As a supervised-learning framework, prediction accuracy depends on the data quality and can be improved with training data that has higher resolution.

2.0 Residual Deformation and Stress Prediction at Part-scale

In this chapter, the modified inherent strain method developed for L-PBF and its application on part-scale residual stress and distortion will be introduced. A meso-scale thermomechanical model is developed to extract the anisotropic inherent strain vector which will be applied in a layer-by-layer way on as-built AM part in pure mechanical analysis to predict residual stress and distortion. Single layer deposition and part-scale building experiments will be conducted to calibrate and validate this proposed method.

2.1 Model Calibration with Line Heat Source Model

Considering the unaffordable time and computational cost of a detailed simulation, a multiscale process modeling approach is proposed to integrate accurate micro-scale modeling with part-scale distortion prediction. The procedure of the multiscale process model developed in this study is shown in Figure 2.1 and summarized below:

- A representative volume element (RVE) detailed process model is employed to extract inherent strains based on the modified inherent strain model.
- Residual distortion and stress at the part scale is performed using the inherent strains extracted in the layer-wise inherent strain method.

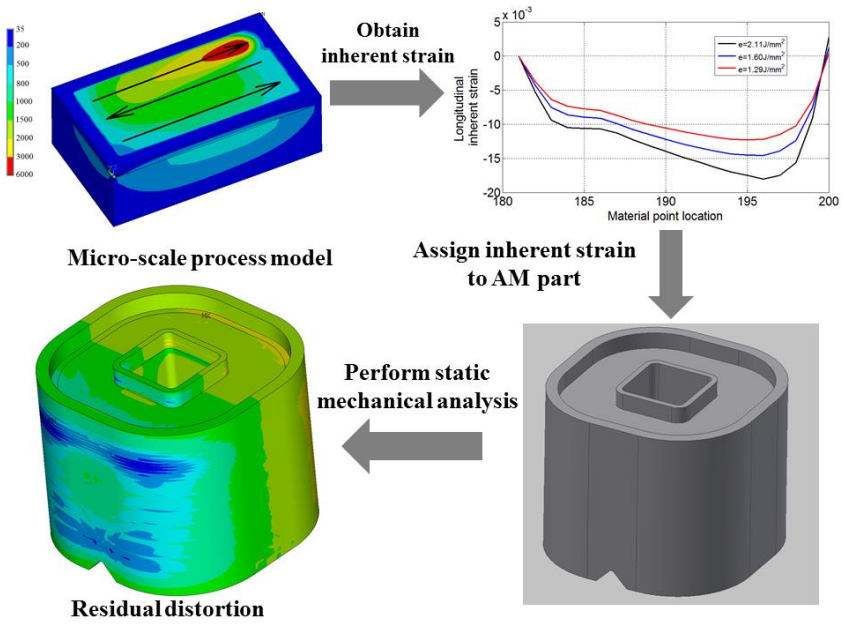

Figure 2.1: Proposed Multiscale Process Simulation Framework

2.2 Multiscale Modeling Approach

2.2.1 Governing Equations

The governing equation for thermal analysis in the detailed process simulation is the heat conduction equation:

$$\rho c_p \frac{dT}{dt} = \frac{\partial}{\partial x}\left(k\frac{\partial T}{\partial x}\right) + \frac{\partial}{\partial y}\left(k\frac{\partial T}{\partial y}\right) + \frac{\partial}{\partial z}\left(k\frac{\partial T}{\partial z}\right) + Q \tag{2.1}$$

where ρ is the material density, T is the temperature, c_p is the temperature dependent heat capacity, t is time, k is the temperature dependent thermal conductivity of material, and Q is the volumetric heat input term.

Temperature dependent thermal properties of bulk Inconel 718 can be found in [66]. For metallic powder, various thermal conductivity models have been developed to account for the

porosity effect [67-69]. Powder thermal conductivity from these simple models is much larger than real value, since thermal conductivity is mainly dictated by the surrounding gas embedded within the voids. The model above which accounts for the surrounding gas effect has been developed [70] and utilized in thermal analysis:

$$k_{eff} = \frac{\rho_R k_s}{1+\phi k_s/k_g} \tag{2.2}$$

where k_{eff} is the effective thermal conductivity of the powder bed, k_s and k_g are the temperature dependent thermal conductivities of the solid material and surrounding gaseous environment, respectively; ρ_R is the initial relative density of the powder; and the empirical coefficient $\phi = 0.02 \times 10^{2(0.7-\rho_R)}$.

Initial condition and boundary conditions of the governing equation are shown in Eqs. (2.3) – (2.6), respectively:

$$T(x,y,z,t_0) = T_0, (x,y,z) \in \Omega \tag{2.3}$$

$$T = \bar{T}, (x,y,z) \in \partial\Omega_D \tag{2.4}$$

$$-k\nabla T \cdot \boldsymbol{n} = h(T - T_0), (x,y,z) \in \partial\Omega_R \tag{2.5}$$

where T_0 is the initial temperature. Since there is powder preheating, the initial temperature equals to 80 °C in detailed process modeling. Equations (2.4)-(2.5) define the Dirchlet boundary $\partial\Omega_D$ and Robin or convection boundary $\partial\Omega_R$, respectively, and $\partial\Omega = \partial\Omega_D \cup \partial\Omega_R$.

The heat loss due to radiation is given as:

$$-k\nabla T \cdot \boldsymbol{n} = \sigma\zeta(T^4 - T_0^4) \tag{2.6}$$

where σ is the Stephan-Boltzmann constant and ζ is the emssivity.

A quasi-static mechanical analysis is conducted in sequential thermal load steps using the temperature history obtained to solve the mechanical response. The governing equation for the mechanical analysis is the stress equilibrium equation written as:

$$\nabla \cdot \boldsymbol{\sigma} + \rho \boldsymbol{b} = 0 \tag{2.7}$$

where $\boldsymbol{\sigma}$ is the stress tensor and $\boldsymbol{b}$ is the body force per unit volume and the boundary condition is defined as:

$$\boldsymbol{U} = \bar{\boldsymbol{U}}, (x, y, z) \in \partial \Gamma_u \tag{2.8}$$

$$\boldsymbol{\sigma} \cdot \boldsymbol{n} = \bar{\boldsymbol{t}}, (x, y, z)\ ) \in \partial \Gamma_t \tag{2.9}$$

where the displacement vector $\boldsymbol{U}$ on boundary $\partial \Gamma_u$ is specified as $\bar{\boldsymbol{U}}$ and the surface vector on boundary $\partial \Gamma_t$ is defined as $\bar{\boldsymbol{t}}$. In mechanical analysis, the material constitutive model is assumed to be elastic and perfect plastic with J2-von Mises plasticity law:

$$\boldsymbol{\sigma} = \boldsymbol{C} : \boldsymbol{\varepsilon_{elastic}} \tag{2.10}$$

$$\boldsymbol{\varepsilon_{total}} = \boldsymbol{\varepsilon_{elastic}} + \boldsymbol{\varepsilon_{plastic}} + \boldsymbol{\varepsilon_{thermal}} \tag{2.11}$$

$$\boldsymbol{\varepsilon_{thermal}} = \boldsymbol{\alpha} \cdot \Delta T \tag{2.12}$$

$$f^{yield} = \sqrt{\frac{3}{2}\sigma_{ij}\sigma_{ij} - \frac{1}{2}\sigma_{kk}\sigma_{kk}} - \sigma_Y \tag{2.13}$$

where $\boldsymbol{C}$ is the fourth order stiffness tensor and $\varepsilon_{elastic}$ is the elastic strain tensor. The stress tensor can be expressed as the double-dot product of the stiffness tensor and elastic strain tensor. Total strain ε_{total} is the sum of elastic strain $\varepsilon_{elastic}$, plastic strain $\varepsilon_{plastic}$ and thermal strain $\varepsilon_{thermal}$, α is the temperature dependent coefficient of thermal expansion (CTE) and ΔT denotes the change in temperature. When $f^{yield} = 0$, yielding occurs and the generates plastic strains. Temperature dependent mechanical properties of Inconel 718 in mechanical analysis can be found in Refs [71, 72].

2.2.2 Single Layer Process Model

In order to calibrate the thermal finite element model, process simulation for a 40×10×0.04 mm^3 layer of Inconel 718 is performed, and the thermal histories obtained for the far field points located on the bottom surface of the substrate are compared with experimental measurements. The reasons for the far field temperature comparison are that: 1) It is impractical to measure the near field temperature within a melt pool with contact measurement and in general, the temperature value is out of range of a thermocouple. 2) The temperature history of a far field point (i.e., far away from the heat affect zone) mainly depends on the total energy input and boundary conditions instead of localized and concentrated laser energy input. Therefore, through comparison between simulated and experimentally measured thermal histories, the parameters in the numerical models, including laser power and velocity of EOS M290 DMLM, absorption efficiency, penetration depth, and heat convection coefficients, can be calibrated. The one layer of rectangle of Inconel 718 is deposited on a 101.6×101.6×3.18 mm^3 substrate using the EOS M290 DMLM with the default core-skin scanning strategy. The substrate is mounted by screws onto four short columns deposited onto the build platform *a priori* as shown in Figure 2.2(a). Three Omega SA1XL-K-72 thermocouples, with a sample rate of 100 Hz, are attached at the bottom side of the mounted substrate. Their relative locations with the deposition layer are geometrically shown in Figure 2.2(b), where measurement point 1 is located underneath the center of the deposition layer, and points 2 and 3 are located 10 mm outside the two edges of the deposition layer, respectively.

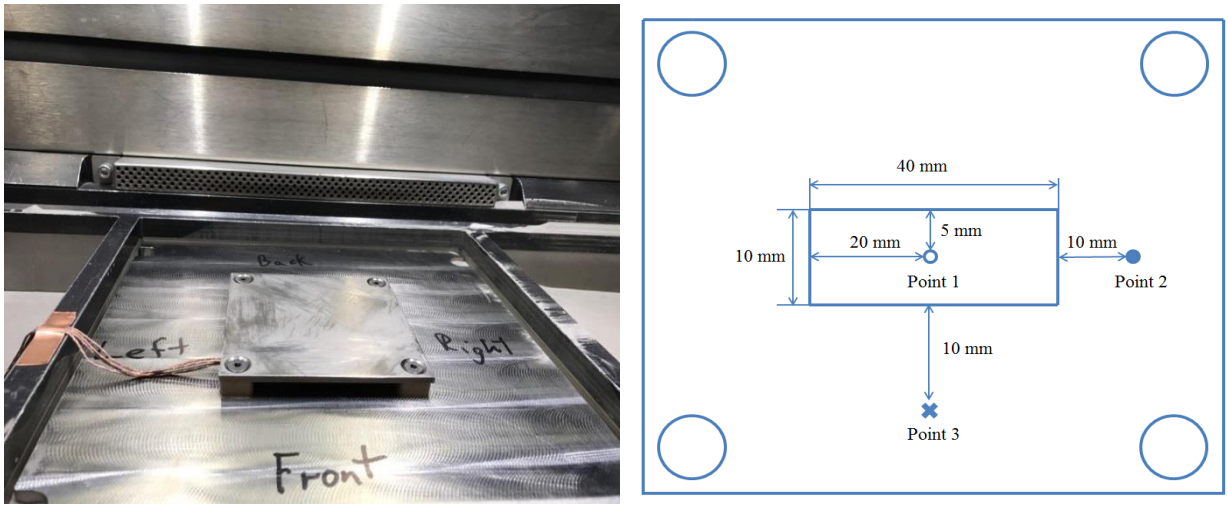

(a) (b)

Figure 2.2: (a) Experimental Setup for In-situ Thermocouple Measurement in the EOS M290 Build Chamber; (b) Themocouple Locations on the Bottom Side of the Substrate.

This one-layer deposition on the order of centimeter could generate temperature change high enough to be measured. However, the number of total time steps needed is estimated to be 77,760 for this thermal analysis with Goldak's double ellipsoid heat source model [73] defined in Eq. (2.14), which is a point heat source model extensively employed in welding and AM process simulation. Using this point heat source model, it would have taken three months to complete the simulation using commercial finite element software.

$$Q = \frac{6\sqrt{3}P\eta}{abc\pi\sqrt{\pi}} exp\left(-3\frac{(x_0+v_s t-x)^2}{a^2} - 3\frac{(y_0-y)^2}{b^2} - 3\frac{(z_0-z)^2}{c^2}\right) \quad (2.14)$$

where P is the laser power; v_s is the laser speed; η is the laser beam absorption efficiency; a and b represent the length and width of the ellipsoid and c is the penetration depth. In this study, the laser power and velocity under default core-skin scanning pattern is shown in Table 1. The absorption efficiency η is set to 0.40 [12, 74], while a and b are set to 50 μm, which equals to the

laser beam spot size. Based on the melt pool depth measurement, the laser optical penetration depth for Inconel 718 powder under default parameters is taken as 125 μm.

Table 2.1: Default Process Parameters Employed in EOS M290 DMLM to Process Inconel 718 [12]

	Core-Skin
Laser Power/W	285
Velocity/mm·s^{-1}	1000
Hatching Space/mm	0.11
Stripe Width/mm	10.0
Stripe Overlap/mm	0.8

Hence to reduce the computational cost, a line heat source model [75], which instantaneously apply the heat over one scan line by integration, is employed in the process simulation for experimental validation. The line heat source model is expressed as:

$$\bar{Q} = \frac{3P\eta}{\pi b c v_s \Delta t} exp\left(-3\frac{y^2}{b^2} - 3\frac{z^2}{c^2}\right)\left\{erf\left[\frac{\sqrt{3}(x_{end}-x)}{a}\right] - erf\left[\frac{\sqrt{3}(x_{start}-x)}{a}\right]\right\} \quad (2.15)$$

The finite element model for single layer deposition with line heat source is shown in Figure 2.3. The finite element size within the deposition region has a fine resolution of 5 μm and is gradually coarsened away from this region to the substrate. In the thermal analysis, the deposition layer is assigned the material properties of Inconel 718 powder initially in the simulation, and when a hatch line is being deposited, the material property of nearby elements is changed to bulk metal during the simulation. To some extent, the boundary condition depends on the real building process and experimental setup. The build chamber of the EOS DMLM system is purged with argon gas that serves as protective and cooling media. Forced convection is applied to the deposition layer and surrounding powder layer and the convection coefficient is set to 55W/(m^2·°C) [76, 77]. The space under the substrate is blocked with powder and a natural convection coefficient $h = 5$ W/(m^2·°C) is applied to the bottom surface of the substrate. Heat loss caused by radiation is also introduced and surface emissivity is set to 0.3. The ambient temperature

inside the chamber, measured by the temperature monitoring sensor, is ~25 °C during the entire building process. For the single layer deposition, pre-heating is turned off, and thus the initial temperature is set to 25 °C. Nodal temperature histories at three thermocouple measurement points on bottom surface of the substrate (see Figure. 2.2(b)) will be compared with experimental measurement in order to validate the model.

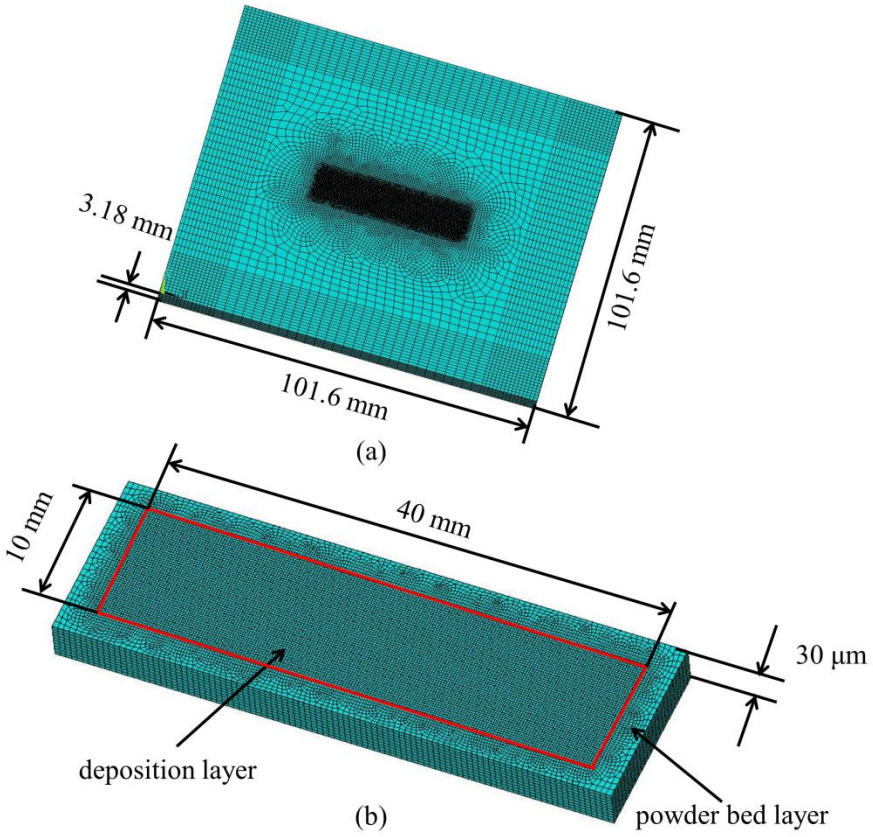

Figure 2.3: (a) Finite Element Model for Single Layer Thermal Analysis; (b) Deposition Layer.

In the DMLM process, the core-skin scanning strategy is designed to build the majority of core part, while the up-skin strategy is designed to build the surface layer. Although different scanning pattern and laser parameters for the surface layer may lead to different temperature and residual stress profile locally, this effect is negligible in the part-scale distortion and stress since the up-skin strategy is used in less than 0.1% of the entire part. Experiment and simulation details for the core-skin scanning strategy are presented in Figure 2.4. The hatch line applied in each time

step can be observed from the contour. Steep temperature gradient can be observed in front of the moving heat source [31, 78] as shown in Figure 2.4(c). Employing the line heat source model reduces this simulation to 450 time steps, and the numerical far-field temperature history matches well with experiment measurement in trend and magnitude, which serves to validate the thermal process model. A critical point to mention here is that the peak temperature in this simulation is lower than the material melting point, since the heat energy is averaged over a larger time and space in the line heat source model. In the real laser scanning process, extremely high cooling rate within the melt pool [31] makes the melted material cools down very rapidly, and this single layer simulation using the line heat source model fails to capture the physical peak temperature. Thermo-mechanical analysis using Goldak's point heat source model is critical for predicting thermal stress and strain accurately, and will be presented in Section 2.3.3. Even so, the line heat source model can still effectively validate the thermal process model based on the far-field temperature history.

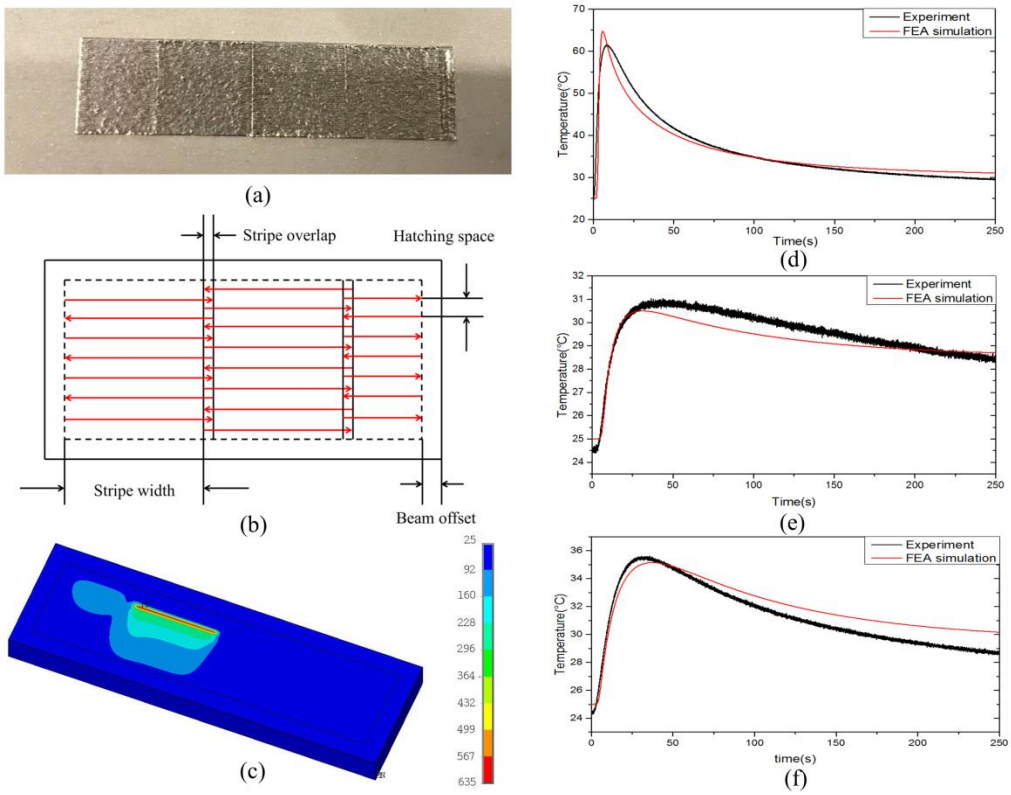

Figure 2.4: Core-skin layer: (a) Surface Morphology; (b) Scanning Strategy; (c) Transient Temperature Distribution and Temperature History at (d) Point 1; (e) Point 2 and (f) Point 3

2.2.3 Micro-scale Representative Volume Model and Inherent Strain Method

Having validated the detailed process model, a micro-scale RVE detailed process model is developed next to simulate residual deformation and stress and extract the inherent strains for part-scale deformation simulation using the inherent strain method. Instead of the line heat source model used in experimental validation (see previous section), Goldak's double ellipsoid point heat source model is employed in this RVE simulation of a 3-layer, 600×300×120 μm^3 model shown in Figure 2.5. It should be noted that the building platform is preheated using the default parameters for Inconel 718. Therefore, the initial temperature of the building platform is set as 80 °C here. Hatch lines of adjacent layers are rotated by 67° in the DMLM process. When the deposition of

each layer is done, a 10-second cooling process is introduced into the analysis to simulate the process of recoater blade moving back and forth to spread powder for the next building layer. In transient thermal analysis, elements of the RVE model are activated layer-by-layer, and the material properties of the elements near the moving heat source is changed from powder to bulk Inconel 718. In the detailed process simulation, temperature history obtained from transient thermal analysis is applied as thermal load to the elasto-plastic mechanical analysis. All deposition layer elements are deactivated initially in the simulation, and elements nearby the laser beam are activated as bulk Inconel 718 in each time step. Mechanical behavior is assumed to be perfect plastic in mechanical analysis.

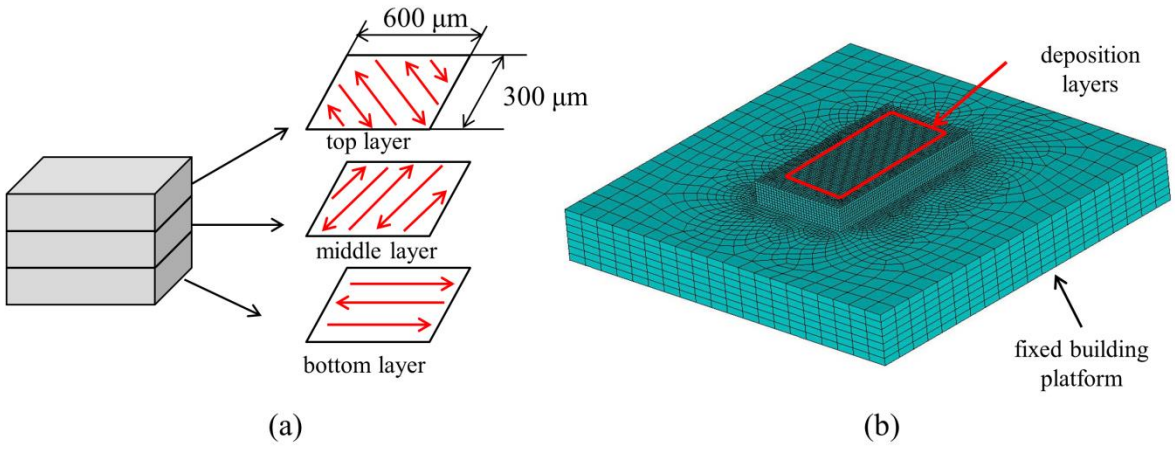

Figure 2.5: (a) Scanning Orientation of Each Layer; (b) Finite Element Model for Micro-scale Representative Volume

Figure 2.5 shows the temperature and strain evolution histories of the central node on the bottom layer. In Figure 2.5 (a), three temperature peaks are observed with very rapid cooling afterwards which occurs within a few tenths of a second. The first temperature peak is caused by the deposition itself, and the following two peaks are due to subsequent layer depositions. Previously deposited layer is re-melted by the subsequent layer deposition, which fused them together and partly relieves the accumulated residual stress and strains as well. Temperature

gradient mechanism is a generally accepted theory to explain the strain evolution in powder bed AM process as shown Figure 2.5 (b) and Figure 2.5 (c), highly localized heat input results in steep temperature gradient in the immediate vicinity of the melt pool which in turn induces non-uniform thermal expansion. Thermal expansion is constrained by the surrounding solidified metal part and thus generates compressive strain and stress. Since both the yield strength and elastic modulus decrease significantly at high temperature, this heating process accumulates compressive plastic strains easily. When further cooled, thermal contraction is inhibited by the surrounding depositions, and the material would develop tensile strain and stress. Thermal expansion and contraction cycle repeat because of the subsequent layer deposition and relieves the accumulated plastic and elastic strains. This phenomenon is called the annealing effect.

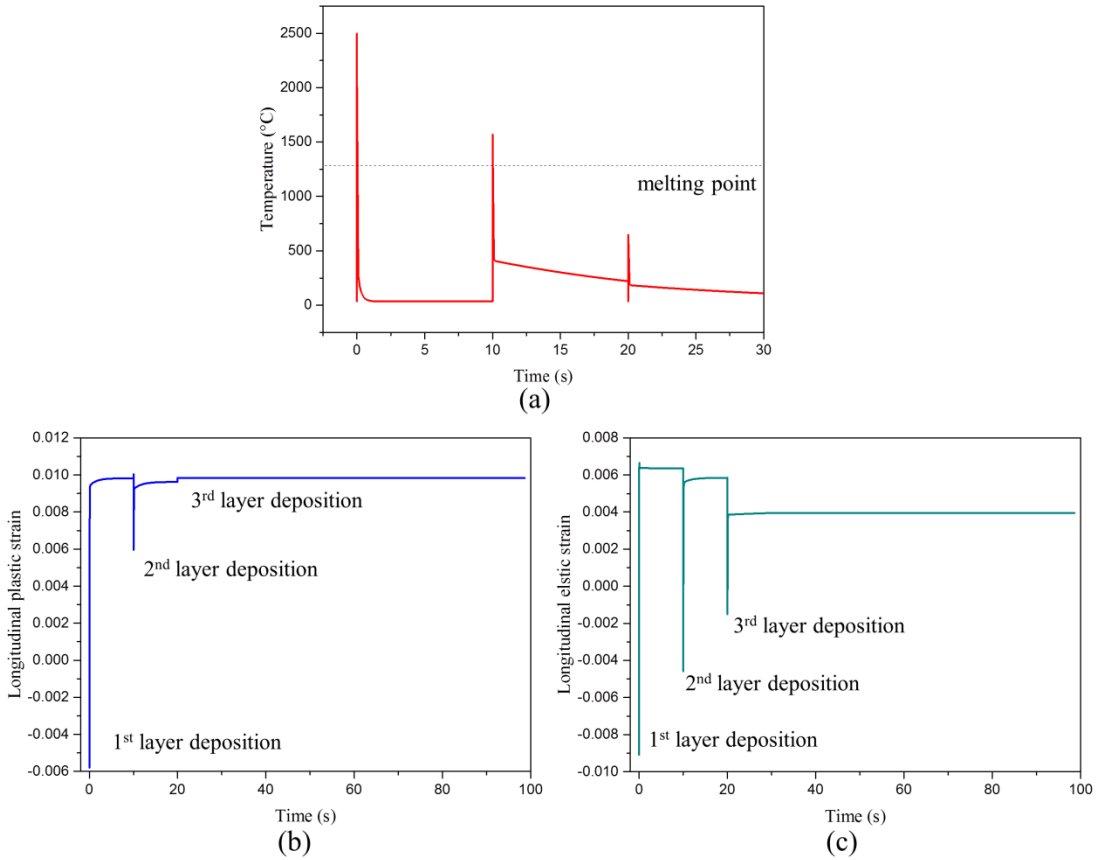

Figure 2.6: Bottom Layer (a) Thermal History; (b) Plastic Strain and (c) Elastic Strain Evolution History

As an effective method to simulate residual distortion and stress prediction, the inherent strain method has drawn increasing attention from both industry and academia. The original inherent strain theory assumes that elastic strain is relaxed since the welded parts are not fixed when cooling to the ambient temperature, and hence the plastic strain generated in welding process is directly applied as initial strain in the method. However, the physical process of powder bed fusion is quite different from the welding problem. New mechanical boundaries keep emerging with the melting and solidification, and elastic strain cannot be totally released when the part cools to ambient temperature as shown in Figure. 2.6(c). Therefore, the modified inherent strain model [79, 80] is formulated to extract the anisotropic inherent strain values for distortion and stress prediction of AM part. The modified inherent strain is defined as the difference between the total

mechanical strain at the intermediate state and the elastic strain at the steady state and can be expressed as:

$$\varepsilon^{\mathrm{In}} = \varepsilon_{t_1}^{\mathrm{Plastic}} + \varepsilon_{t_1}^{\mathrm{Elastic}} - \varepsilon_{t_2}^{\mathrm{Elastic}} \tag{2.16}$$

where t_1 is the intermediate state when the heat source just passes by and the compressive mechanical strain reaches the peak magnitude, and t_2 is the steady state when the deposited part cools down to the ambient temperature.

The reason why these two specific mechanical states are chosen is associated with the strain evolution within the melt pool due to melting and solidification. It can be deduced that there are two major contributions to the inherent strain. The first contribution is the compressive plastic strain induced by super-heating and cooling process, similar to conventional welding prediction; while the second one is the increment between compressive and tensile elastic strain after the slower cooling process. More details regarding the modified inherent strain theory can be found in Refs. [79, 80]. As shown in Figure. 2.7, the anisotropic inherent strains of the bottom layer along the horizontal building path are extracted from the RVE model simulation result. Inherent strains along the *X*, *Y* and *Z* directions are almost constant in the middle region, and the exterior value changes nearly along a linear curve from zero to a stable value. With default process parameters, the steady-state inherent strain values in the middle scan line of the bottom layer, (-0.015, -0.015, 0.02) will be utilized in part-scale prediction for distortion and residual stress.

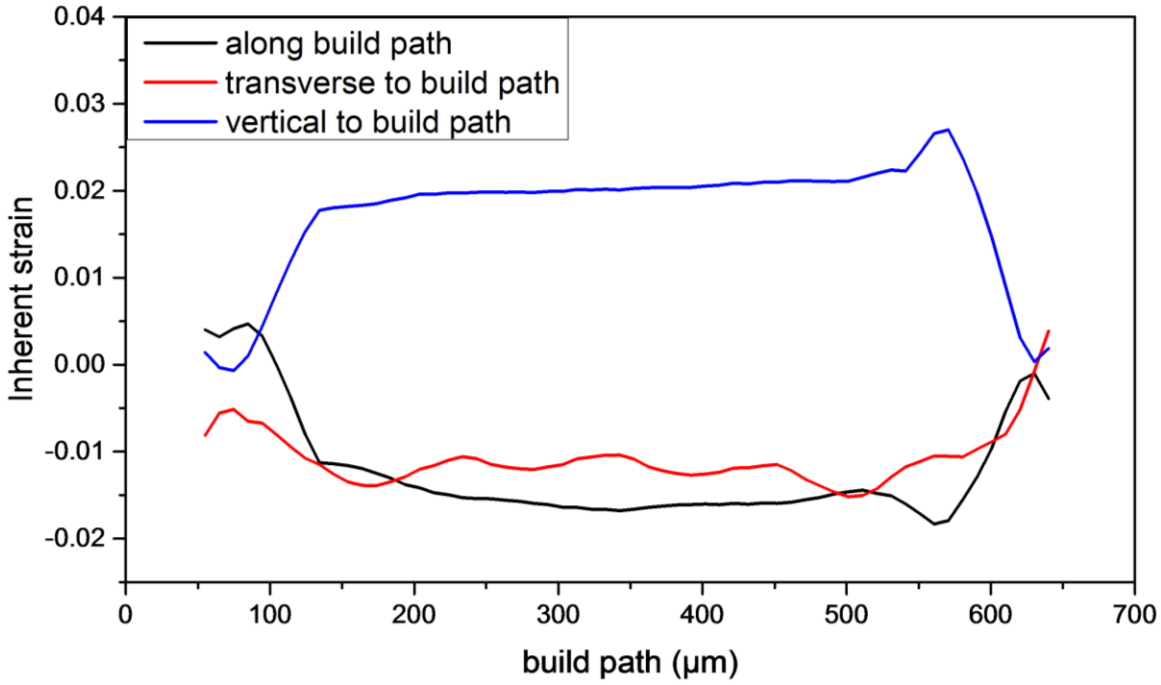

Figure 2.7: Bottom Layer Inherent Strain under Default Process Parameters along Horizontal Scanning Path

2.2.4 Part-scale Model

In this section, part-scale distortion and residual stress simulation based on the inherent strain method is performed on a double cantilever beam structure and a canonical part built, respectively, by the EOS DMLM process in Inconel 718. Both of these models have been used as benchmarks for part-scale process simulation. In the inherent strain method, the inherent strains extracted from the micro-scale RVE model are loaded into the model as constant thermal expansion coefficients in three normal directions. Ten real physical layers are grouped together to form one numerical layer and activated in layer-by-layer fashion along the build direction as shown in Figure 2.8 for the double cantilever beam structure. Once the grouped layer is activated, a uniform unit temperature rise is applied to the newly activated elements to introduce the inherent

strains and a quasi-static equilibrium analysis at room temperature is performed. This simulation process repeats itself for the deposition of each layer.

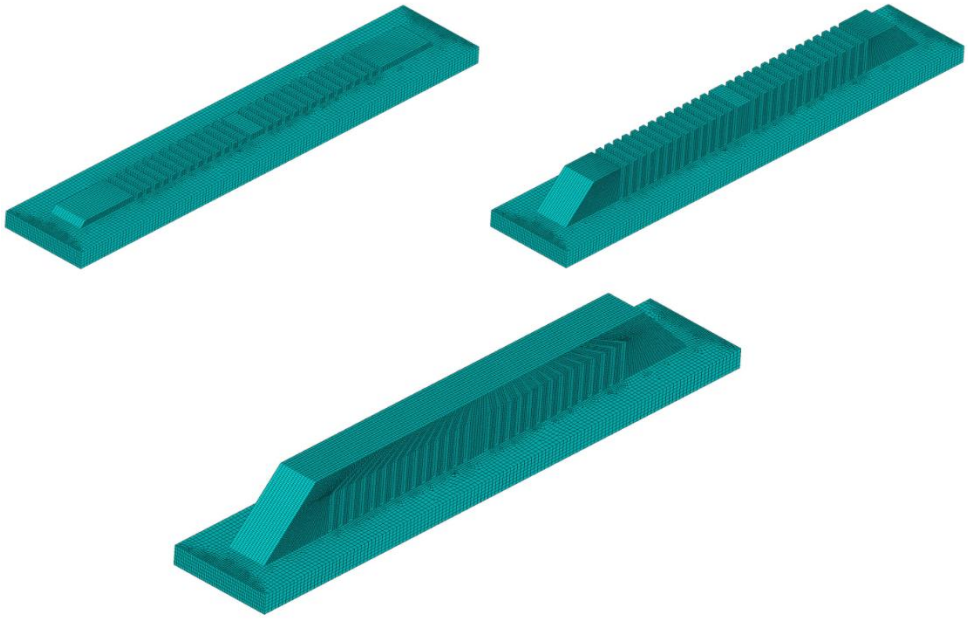

Figure 2.8: Snapshots of the Element Activation Process

The predicted distortion is validated by experimental measurements. A 127 × 12.7× 18.5 mm^3 double cantilever beam with teeth-style support structure is built under the default processing mode and is shown in Figure 2.9(a). The bridge span in the supports is 2 mm which is less than the critical bridge span of EOS-processed Inconel of 4 mm. When the build is finished, the support structure is cut off from the left end and then from the right end to create a cantilever beam on each side as shown in Figure 2.9 (b). The stress relaxation due to the cutting leads the beams to bend upward, but it is interesting to observe that the beam that is created first has larger residual displacement. Deformation distribution after stress relaxation is measured by a 3D laser scanning device called Laser ScanArm V3 (Faro Technologies, Lake Mary, FL). Further comparison of the scanned geometry with the design goemetry is made using the Geomagic Control software. In the simulation, two additional quasi-static steps are introduced to simulate the left-then-right column support cutting off procedure. Support removal has been implemented by changing material

properties. The mesh used for double cantilever beam distortion prediction consists of 153,614 HEX-elements and 187,054 nodes. Total simulation time is less than 0.5 hour.

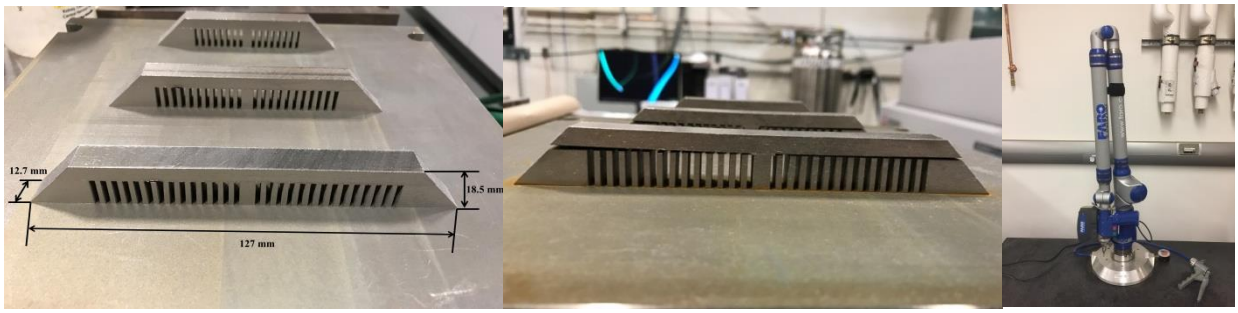

Figure 2.9: Double Cantilever Beam Structure Built by the EOS M290 DMLM Process (a) Before and (b) After Cutting off; (c) Faro Laser ScanArm V3 for Distortion Measurement

The second model is an $81.6 \times 81.6 \times 64.5$ mm^3 square canonical part built using the default parameters for Inconel 718 as shown in Figure. 2.10. Four additional spheres are built as reference points to align the AM build with the original CAD file and are not being modeled in the simulation model, as shown in Figure. 2.11. In contrast to the double cantilever beam structure mainly composed of solid blocks, the geometry of this canonical part is much more complex, particularly its internal structure. The internal and outer contours of the lower canonical part are composed of thin walls of respective thickness of 1.0 mm and 2.9 mm. The internal thin walls gradually thicken along the build direction and finally merge with the outer contour near the top of the part. The height of this transition section is ~51 mm. For the sake of having flat upper surface for each newly activated layer, HEX-element is employed for mesh generation as well. The mesh for canonical part simulation consists of 369,570 elements and 444,626 nodes.

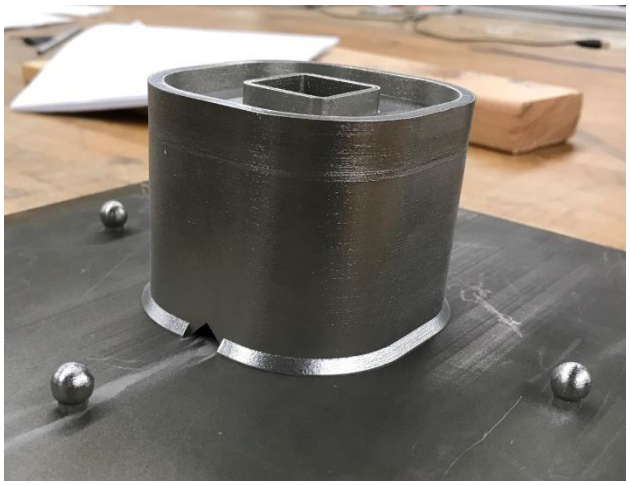

Figure 2.10: Square Canonical Structure Built by the EOS M290 DMLM Process

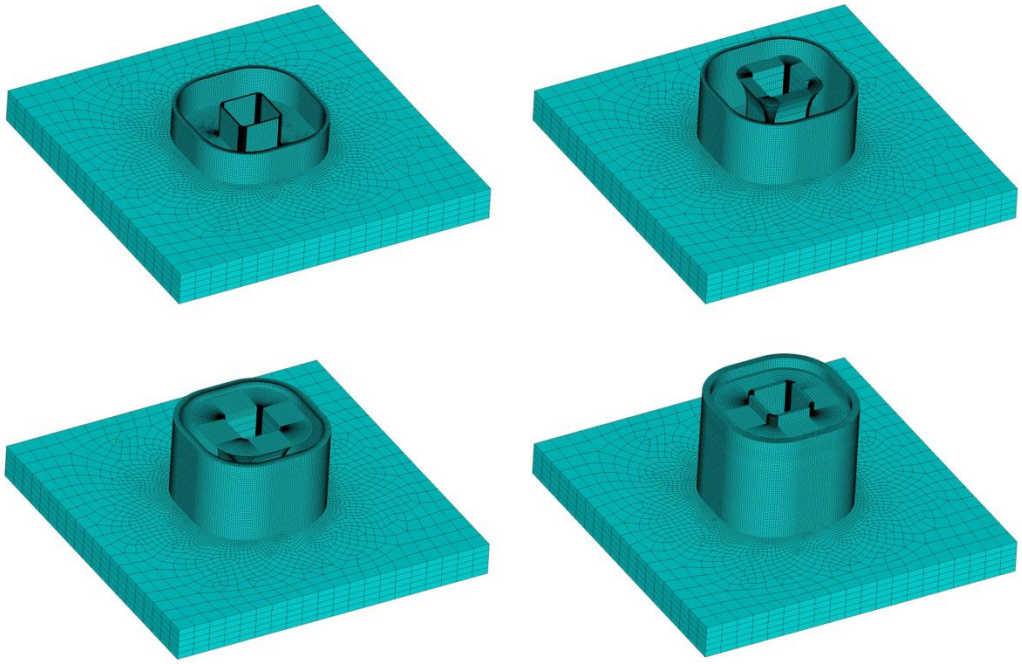

Figure 2.11: Finite Element Mesh for the Square Canonical and Snapshots of Element Activation Process

2.3 Results and Discussion

2.3.1 Distortion Prediction

For the first double cantilever beam, the distortion profile computed from the proposed inherent strain method is compared with that obtained from a commercial AM simulation software, Simufact Additive 3.1, and from experimental measurement. The total distortion before support removal between the proposed inherent strain method and Simufact Additive 3.1 is shown in Figure 2.12. The distortion profile and magnitude before cutting off the supports as obtained from the proposed inherent strain method and Simufact Additive 3.1 simulation is similar. The total displacement on the top surface is very small because both the right and left side beams are still fixed on the support columns. Large deflection is observed along the connections between the beam and support columns from both inherent strain method and Simufact simulation. However, it should be noted that different to the symmetrical distortion profile obtained by the proposed inherent strain method simulation, Simufact Additive 3.1 gives an unsymmetrical distortion profile before support removal. This is because the applied inherent strain vector is rotated in the Simufact simulation [16] rather than averaging the strain components along x and y direction in the proposed method.

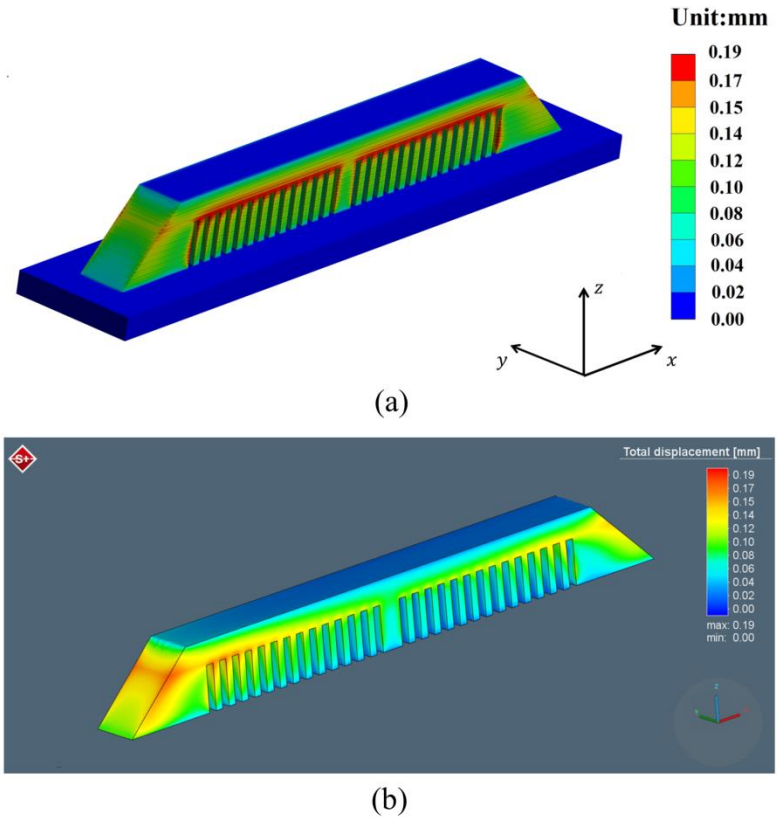

Figure 2.12: Simulated Distortion Field for the Double Cantilever Beam before Cutting off the Supports: (a) Inherent Strain Method; (b) Simufact Additive 3.1

Next, the distortion profiles after cutting of the supports obtained from simulation and experiment are compared in Figure. 2.13. The simulation result and experimental measurement have very similar distortion profile and magnitude. Since all the support columns of the double cantilever beam are part of the as-built geometry rather than the added support structures, it is not possible to simulate the removal of these support columns in Simufact Additive 3.1 yet. Both simulation and experimental measurement show an asymmetric bending profile due to the stress relaxation sequence. The maximum displacement at the leftmost end is 0.93 mm in simulation and 0.84 mm from experimental measurement. At the rightmost end, the largest distortion value is 0.45 mm in simulation and 0.42 mm from measurement. The simulation results are in good agreement with the measured distortion values. Given the order of reduction by the inherent strain method,

it only over-predicts the maximum distortion by less than 11%. Asymmetric bending curves along the center line of the top surface are shown in Figure. 2.13(c). The bending curve from measurement is not as smooth as the simulation curve due to the possible influence of surface roughness of as-fabricated surface, which is not considered in the simulation.

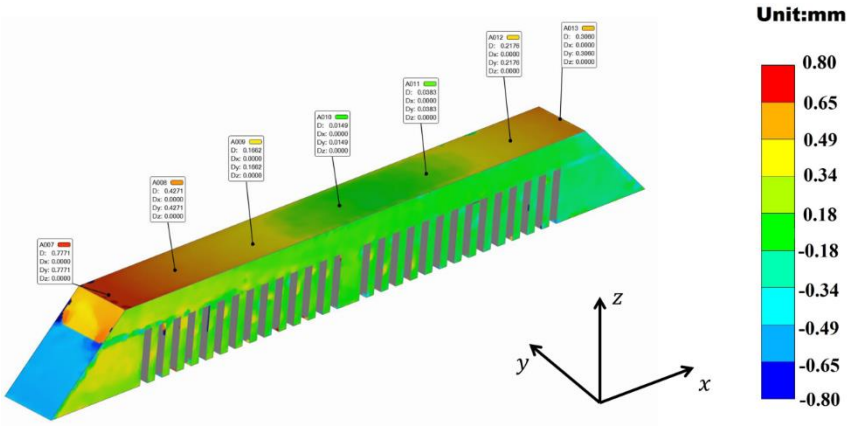

(a)

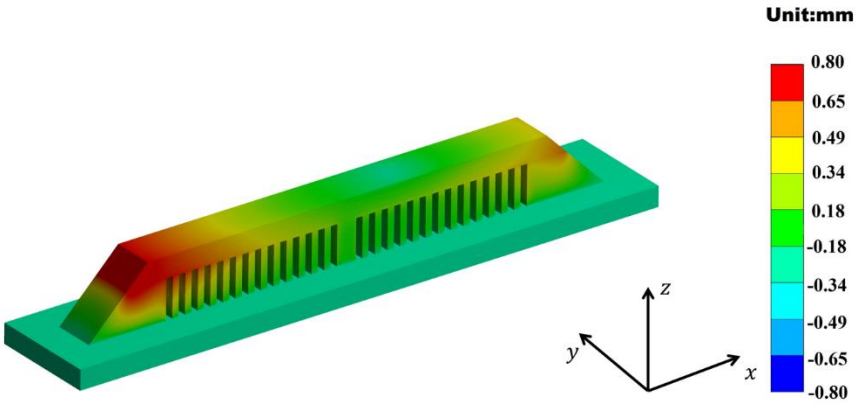

(b)

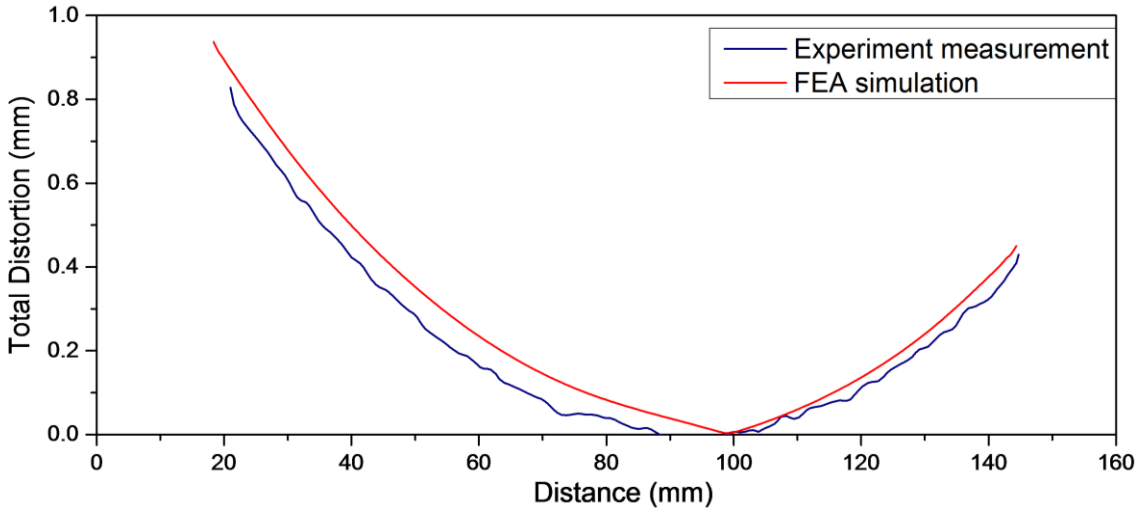

(c)

Figure 2.13: Distortion Field for the Double Cantilever Beam after Cutting off the Supports: (a) Experimental Measurement; (b) Inherent Strain Simulation; (c) Distortion along the Center Line of the Top Surface

Distortion prediction results of the canonical part are summarized in Figure. 2.14. The comparison between the predicted distortion by the proposed inherent strain method and Simufact Additive 3.1 and experiment measurement along the sample path is shown in Figure. 2.14 (b). The overall distortion trend for the outer surface is shrinking because of the contraction in cooling process. There are two peaks along the sample path which are successfully captured by the prediction. The position of the first contraction peak near top of the part suggests that the part undergoes necking where the outer wall merges with the inner wall (Figure. 2.14). On the other hand, the second peak near the bottom is due to contraction of the plate that causes lower portion of the thin wall to shrink more. The predicted distortion by both the proposed inherent strain method and Simufact Additve 3.1 simulation of the top part matches well with the measurement data in both trend and magnitude. As for the distortion peak near the bottom, there is some discrepancy in magnitude. The predicted maximum distortion by the proposed method simulation

near the substrate is -0.21 mm while the measured maximum distortion is -0.14 mm. The over-prediction of the contraction near the bottom of the canonical part may be due to the assumption of identical temperature history. In our part-scale simulation, the same inherent strains are applied in every numerical layer, which implicitly assumes that the temperature history of every deposited layer is identical. However, the heat conduction for the solid block and thin wall is apparently different, and thus, the residual strain accumulated during the build process cannot be the same. Apparently, the absolute values of the inherent strains applied on the lower part composed of thin walls are likely to be somewhat larger than the real values. How to extend the proposed part-scale method to incorporate temperature history without compromising computational efficiency too much will be an important topic for future investigation.

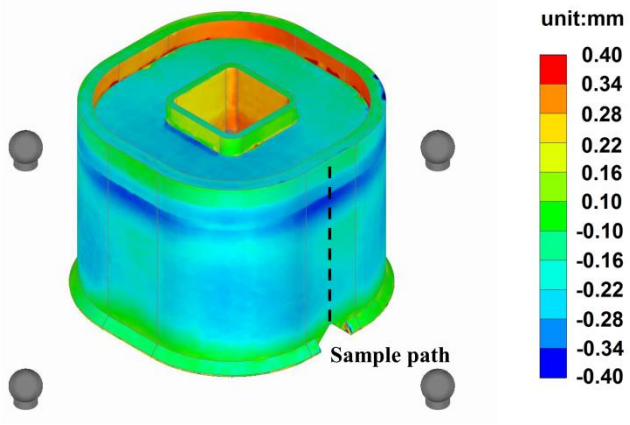

(a)

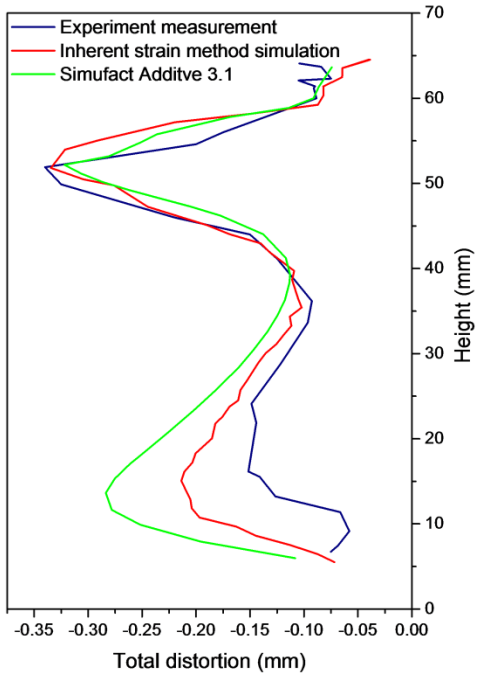

(b)

Figure 2.14: Distortion Field for the Canonical Part: (a) Experimental Measurement; (b) Distortion Profile along the Dashed Line

2.3.2 Residual Stress Prediction

In this section, residual stress computed using the modified inherent strain method is presented, and detailed explanation for both the stress magnitude and distribution is given as well. In addition, the residual stress computed is compared and analyzed with the results in published literature.

The residual stress distribution computed for the as-built double cantilever beam structure can be found in Figure 2.15. The longitudinal normal stress profile (along x direction) consists of a thin layer of large tensile stress near the top and base of the as-built part, while compressive stress occurs in the center of the part, where similar trend can be found in previous experimental

studies [81, 82]. The tensile stress within the top deposited layer is caused by the contraction of the molten material after cooling. In contrast, a thin layer of large transverse stress (along y direction) is located along the side surface as shown in Figure 2.15(b). Both longitudinal and transverse stresses are tensile near the surfaces and compressive internally and reach values of 1400 MPa and 1600 MPa, respectively, which exceed the yield strength of Inconel 718. For layers underneath the top layer, tensile stress is reduced and gradually changes into compressive stress because of the annealing effect by subsequent deposition layers. In the simulation, negative inherent strain components along x and y directions are applied in a layer-by-layer fashion. Shrinkage of the newly activated layer is prohibited by the lower deposited layers and thus generates tensile stress in the new layer and partially relieves tensile stress of the previous deposited layers. This stress profile characteristics are also reported in Ref. [12]. Residual stress along the build direction, also called through-thickness stress, is the main driving force for delamination. Similarly, it is mainly compressive in the center of the part and tensile near the exterior surfaces as shown in Figure 2.15(c). Interior walls of the part are found to be compressive below the top surface. Similar trend has been noticed in both numerical study by Hodge et al [83] and Li et al [35], as well as in neutron diffraction measurement by Wu [84]. Relatively high through-thickness stress (up to 840 MPa) is located at the substrate-part surface and is lower than the yield strength of Inconel 718 at room temperature indicating that delamination will not occur as shown in Figure 2.9.

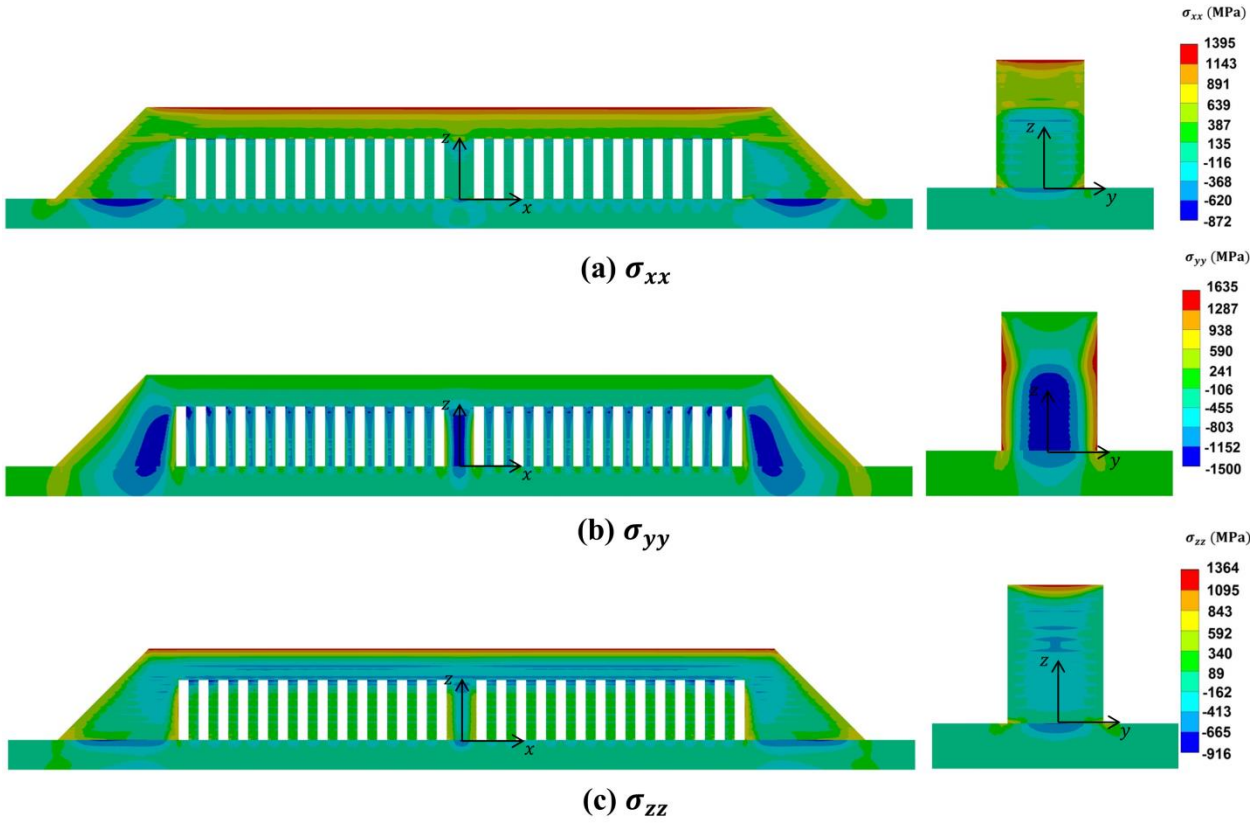

Figure 2.15: Residual Stress Distribution of the Double Cantilever Beam before Support Removal

After removing the supports, the normal residual stresses in all directions are relieved significantly except for the center support in Figure 2.16. Tensile stress near the surface area is partially relieved and even transition to compressive due to re-equilibration and plastic deformation. For the center support connected with the build plate, stress is still very high and the transition of tensile stress on the surface to compressive inside the support is obvious. This is caused by the tensile residual stress on the left and right cantilever beams. By comparing the stress distribution on the center support cross section before and after support removal, transition of tensile stress to compressive stress inside the center support can be easily observed because of the plastic deformation occurring during the building process. Similar trend can be found in Ref. [85] as well.

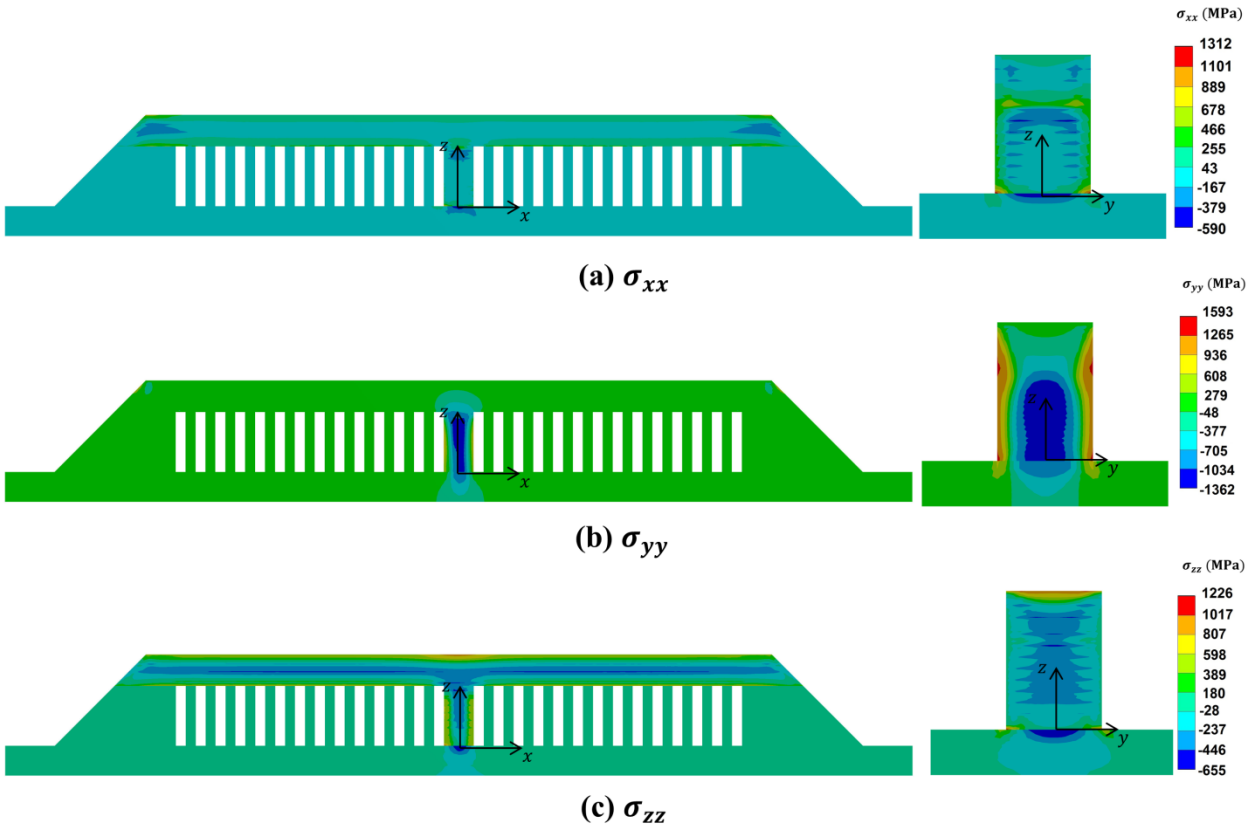

Figure 2.16: Residual Stress Distribution of the Double Cantilever Beam after Support Removal

2.4 Conclusions

An inherent strain based multiscale process simulation model is developed for fast part-scale distortion and residual stress prediction. Combining the inherent strain method with DMLM process modeling, distortion and residual stress prediction of double cantilever beam and canonical part can be completed within 0.5 hour and 3 hours in ANSYS 17.2. Accuracy of the proposed method is validated by various experiments. Conclusion can be summarized as follows:

- Detailed process simulation of the DMLM process is first validated by far-field temperature history measurement of single-layer deposition. Line heat source model is employed in single-layer scale model to reach the spatial scale of experiment. Process parameters, thermal boundary conditions and element methods are verified;
- Once the detailed process model is validated, a micro-scale RVE model using Goldak's point heat source model is employed to extract the inherent strains based on the modified inherent strain theory.
- For part-scale model, the extracted inherent strains are applied as thermal expansion coefficients (CTEs) with a unit temperature rise. Several physical layers are merged as one and activated layer-by-layer in mechanical analysis. Simulation of AM parts with moderately complex geometries can be completed within an hour. Distortion from simulation has been validated by direct experimental measurement. Residual stress is computed by the displacement field and the stress profile obtained matches well with previous studies in the literature.

3.0 Multiphysics Modeling at Mesoscale

In this chapter, melt pool dynamics and porosity formation associated with spattering particles in L-PBF is studied by multiphysics models including heat transfer, multiphase flow, particle contact. The effect of preheating temperature on melt pool variation and porosity formation due to spattering particles are revealed by simulation results and confirmed by experiments in this work.

3.1 Experimental Details

In this experiment, a heating module as shown in Figure 3.1, consisting of a large building platform made of carbon steel, two heaters inside the EOS M290 building chamber and a Smart Series® SSM-15-12 temperature control module outside the chamber, was used to control the preheating temperature. One Omega SA1XL-K-72 thermocouple was attached to the top surface of small substrate to monitor the preheating temperature in real time. The small IN718 substrate on the dimension of 101.6×101.6×3.18 mm^3, which was first sandblasted before the deposition experiment, was gradually heated from 100 °C to 500 °C with an increment of 100 by the heating module. At each heating temperature, 1cm-long single tracks were deposited under the power of 200 W, 250 W, 285 W and 300 W, and scan speed of 0.5 m/s, 0.75 m/s, 1 m/s and 1.5 m/s. Sixteen single tracks were deposited at one preheating temperature and eighty single tracks totally were obtained for *ex-situ* cross section measurements. All the single tracks were prepared by the EOS M290 DMLM system that uses a 400W Ytterbium fiber laser with a wavelength of 1060-1100 nm

and focus diameter of 100 μm. The focal length is 410 mm. For each preheating temperature, the spacing between neighboring tracks was 1 mm and 16 single tracks were deposited successively which take 0.02 s. The influence of residual heating by neighboring tracks is negligible by the large spacing and rapid succession. All the as-built specimens were cross-sectioned in the middle by electrical discharge machine along the plane perpendicular to the laser scanning direction. The samples were mounted and polished by Auto Polisher, then etched in a solution of 10 g Cu_2SO_4, 50 ml Hydrochloric acid, and 50 ml water, and optically measured by ZEISS SmartZoom5.

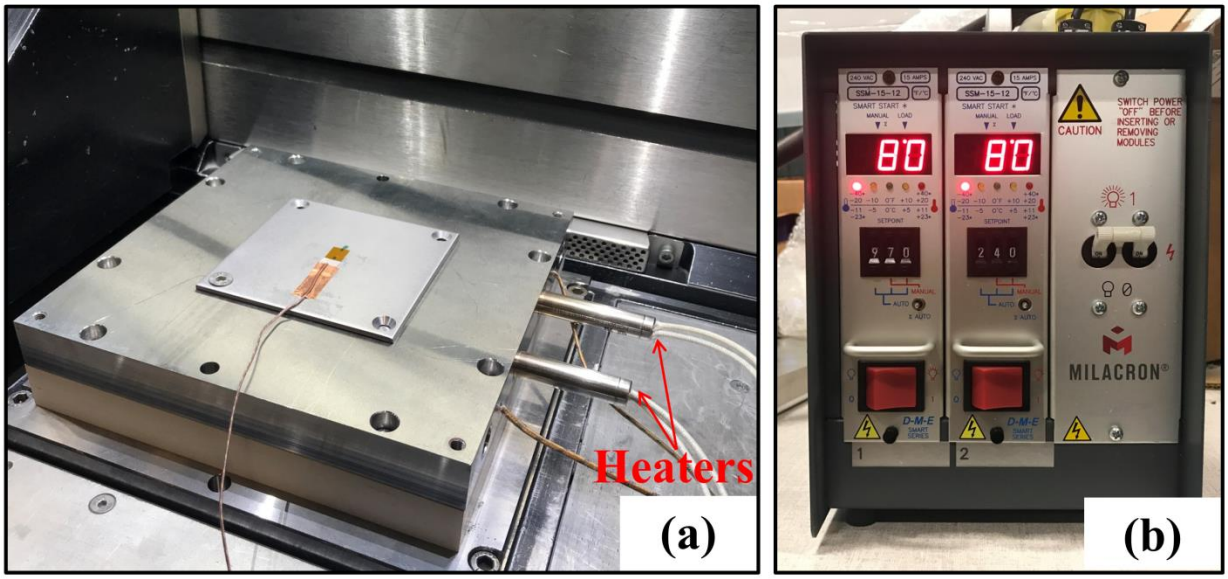

Figure 3.1: Heating Module Experiment Setup: (a) Substrate with Heater; (b) Control Panel with Temperature Indicators

3.2 Numerical Model

In order to gain more insights into the physical mechanisms besides *ex-situ* cross section measurement, a multiphysics model was developed based on Flow-3D v12.0, a commercial computational fluid dynamics (CFD) software, to simulate the complex melt pool dynamics at the

mesoscale. The molten metal flow is taken as Newtonian and incompressible in the simulation. Mass continuity, momentum and energy conservations in Eqs. (3.1) – (3.3) are solved:

$$\nabla \cdot \vec{v} = 0 \tag{3.1}$$

$$\frac{\partial \vec{v}}{\partial t} + (\vec{v} \cdot \nabla)\vec{v} = -\frac{1}{\rho}\nabla \vec{P} + \mu \nabla^2 \vec{v} + \vec{g}[1 - \alpha(T - T_m)] \tag{3.2}$$

$$\frac{\partial h}{\partial t} + (\vec{v} \cdot \nabla)h = \frac{1}{\rho}(\nabla \cdot k \nabla T) \tag{3.3}$$

where $\vec{v}$ is the velocity vector, $\vec{P}$ is the pressure, μ is the viscosity, $\vec{g}$ is the gravity vector, α is the thermal expansion coefficient, ρ is the density, h is the specific enthalpy and k is the thermal conductivity.

The location of melt pool free surface is tracked by the Volume of Fluid (VOF) method, in which the volume fraction of fluid occupying each mesh in the computation domain is defined by the fluid fraction F:

$$\frac{\partial F}{\partial t} + \nabla \cdot (F\vec{v}) = 0 \tag{3.4}$$

where $0 \leq F \leq 1$. For a reasonable and precise description of the L-PBF process, the physical model is customized based on the process conditions and accounts for buoyant flow, Marangoni convection, vapor recoil pressure and heat radiation in the simulation. The thermal properties of the IN718 alloy and the coefficients used in the simulation can be found in Ref. [86]. Notably, ray-tracing energy deposition model which improves over volumetric energy deposition and enables partial melting is used and coupled with the Fresnel energy absorption model that governs the portion of energy absorbed from the reflected laser rays [87], since multiple reflection effect of laser beam plays an essential role on the formation of melt pool.

3.3 Effect of Preheating Temperature

3.3.1 Melt Pool Morphology

Ex-situ cross section measurements for melt pool at different preheating temperature are reported in this section. The entire measurement data of eighty tracks and the corresponding process mapping are provided in Appendix. Multiphysics models for single track depositions in conduction regime (P = 250 W and V = 1.5 m/s), transition regime (P = 285 W and V = 1.0 m/s) and keyhole regime (P = 250 W and V = 0.5 m/s) were developed and validated by the *ex-situ* measurements. The definition of melt pool in each regime was adopted partially from Ref. [88]: (1) melt pool with W/D ratio over 1.5 is called as conduction regime; (2) melt pool with R/D ratio between 1.0 and 1.5 is referred to as transition regime; (3) melt pool with W/D ratio less than 1.0 is defined as keyhole regime. Also, in the following, the length of single track (l) in the simulation is 2.5 mm in the conduction and transition regimes and 1 mm in the keyhole regime. Melt pool cross sections in simulations were measured at five locations along the scanning direction x, where x/l varies from 0.3 to 0.7 with an increment of 0.1. Melt pool dimensions in the middle plane (x/l is 0.5) were taken as data points to compare with experimental measurement results for model calibration/validation, while the remaining points are used to generate the error bar (in Figure 3.3, Figure 3.5 and Figure 3.7). It is worth noting that the data points shown in Figure 3.3, 3.5 and 3.7 are the melt pool dimensions in the middle cross-section along the track (at $x/l = 0.5$), rather than the *mean* value. Because of the backward flow from laser hot spot, the melt track is not flat and melt pool dimensions vary significantly along the scanning direction. This variation can be observed via the error bar.

3.3.1.1 Conduction Regime

Figure 3.2 shows the cross-sectional melt pool areas, in the conduction regime with lower laser power and higher scan speed, under different preheating temperatures ranging from 100 °C to 500 °C. All the melt pool cross-sectional measurements in conduction regime were taken at 1000x magnification. The melt pool boundary between melt region and substrate, as indicated by the red dashed line in Figure 3.2 at the preheating temperature of 100 °C, can be clearly detected in the *ex-situ* measurements. Measured melt pool depth and width are indicated by the white lines in Figure 3.1 and the depth is measured by from the substrate to the bottom region and the top bead is neglected. In the conduction regime, the melt pool tends to have a semicircular shape and a W/D (width to depth ratio) equal to approximately 2. From Figure 3.2 it can be observed that under the same laser power and scan speed, the melt pool depth increases significantly with preheating temperature. Under the power of 250 W and speed of 1.5 m/s, the melt pool is increased by 48.96% (from 59.74 µm at the preheating temperature of 100 °C to 88.99 µm at 500 °C). Under the power of 285 W and speed of 1.5 m/s, the melt pool is increased by 29.93% (from 73.57 µm at the preheating temperature of 100 °C to 95.59 µm at 500 °C).

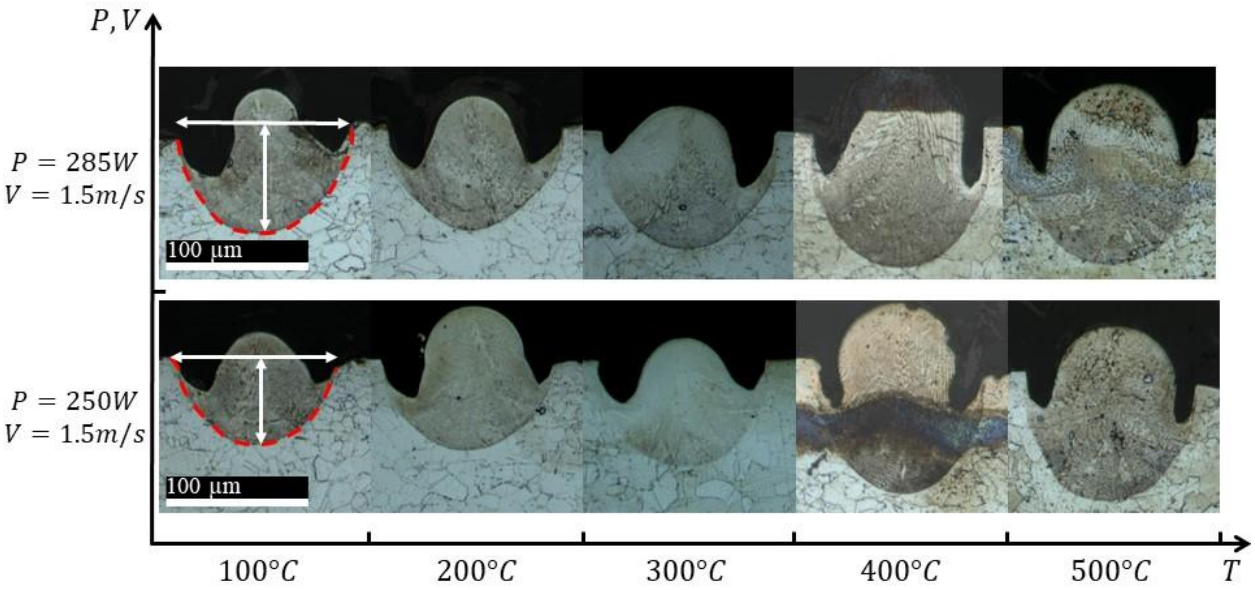

Figure 3.2: Melt Pool Morphology Variation with Preheating Temperature in Conduction Regime

Quantitatively, the melt pool dimensions (width and depth) and the W/D ratio under the power of 250 W and scan speed of 1.5 m/s are presented in Figure 3.3. With higher preheating temperature, the melt pool dimensions increase, forming a wider and deeper depression zone. As for the melt pool shape, the W/D ratio exhibits an overall decreasing trend, which indicates that the melt pool shape is no longer semicircular and transitions to the keyhole regime, becoming deeper under higher preheating temperature. For the single track with a laser power of 250 W and a scan speed of 1.5 m/s, the melt pool W/D ratio is 2.1 when the preheating temperature is 100 °C, and 2.0 when the preheating temperature is 200 °C, both of which exhibit a typical shape in the conduction regime (see Figure 3.2). When increasing the preheating temperature, although both width and depth increase, the W/D ratio decreases monotonically. With a preheating temperature of 500 °C, the W/D ratio is 1.5 which exhibits the feature of melt pool in transition regime. This indicates that with constant processing parameters, the melt pool shows the trend towards keyhole regime with increasing preheating temperature. The melt pool cross section comparisons between ex-situ measurement and simulation are presented in Figure 3.3 (d)-(f).

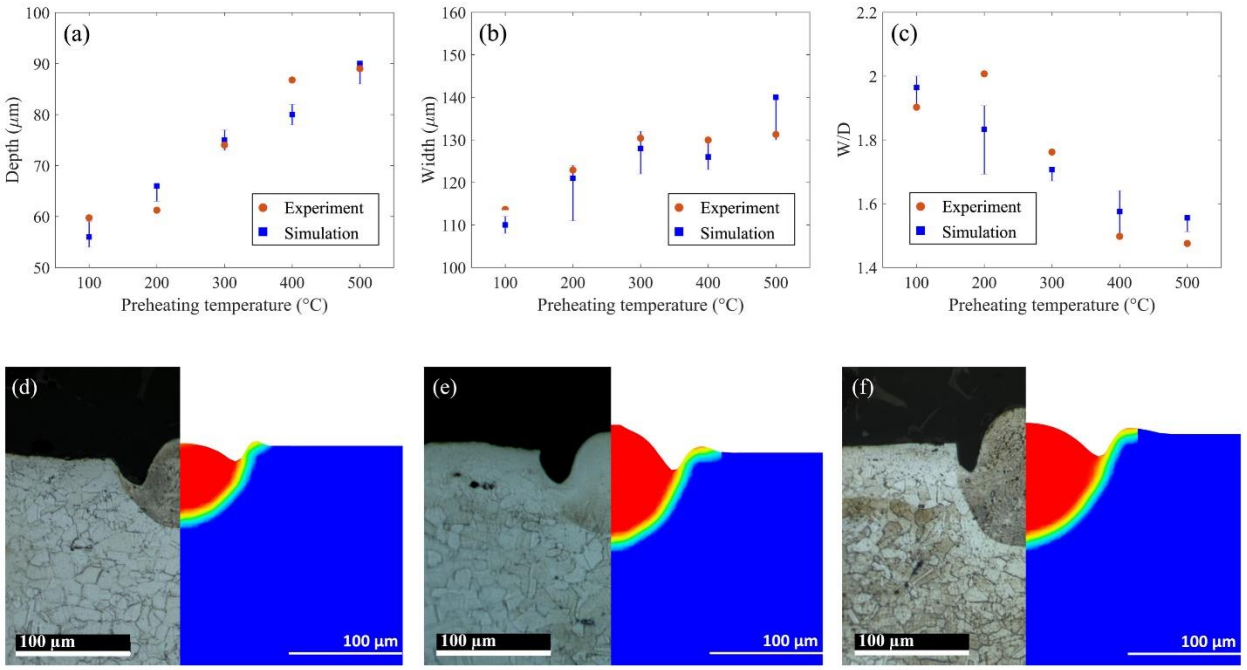

Figure 3.3: Melt Pool Dimensions versus Preheating Temperature in Conduction Regime (P = 250 W and V = 1.5 m/s): (a) Depth; (b) Width; (c) Aspect Ratio and Comparison of Melt Pool between Experiment and Simulation at the Preheating Temperature of (d) 100 °C; (e) 300 °C; and (f) 500 °C.

3.3.1.2 Transition Regime

When increasing the laser power or decreasing the scan speed, laser energy intensity increases, and the melt pool mode gradually transitions from the conduction mode to the keyhole regime. However, the transition from conduction to keyhole mode is not sharp, and there is a transitional regime between them [89]. The melt pool morphology variation with preheating temperature in this transitional regime is presented in Figure 3.4. All the melt pool cross-sections in transition regime were taken at 1000x magnification. By increasing the preheating temperature, the melt pool becomes wider and deeper, while the melt pool shape does not change significantly and the decreasing value of W/D ratio is not as large as the value in the conduction regime. Under the power of 285 W and speed of 1.0 m/s, the melt pool is increased by 31.09% (from 118.14 μm

at the preheating temperature of 100 °C to 154.87 µm at 500 °C). Under the power of 250 W and speed of 0.75 m/s, the melt pool is increased by 34.01% (from 131.42 µm at the preheating temperature of 100 °C to 176.11 µm at 500 °C).

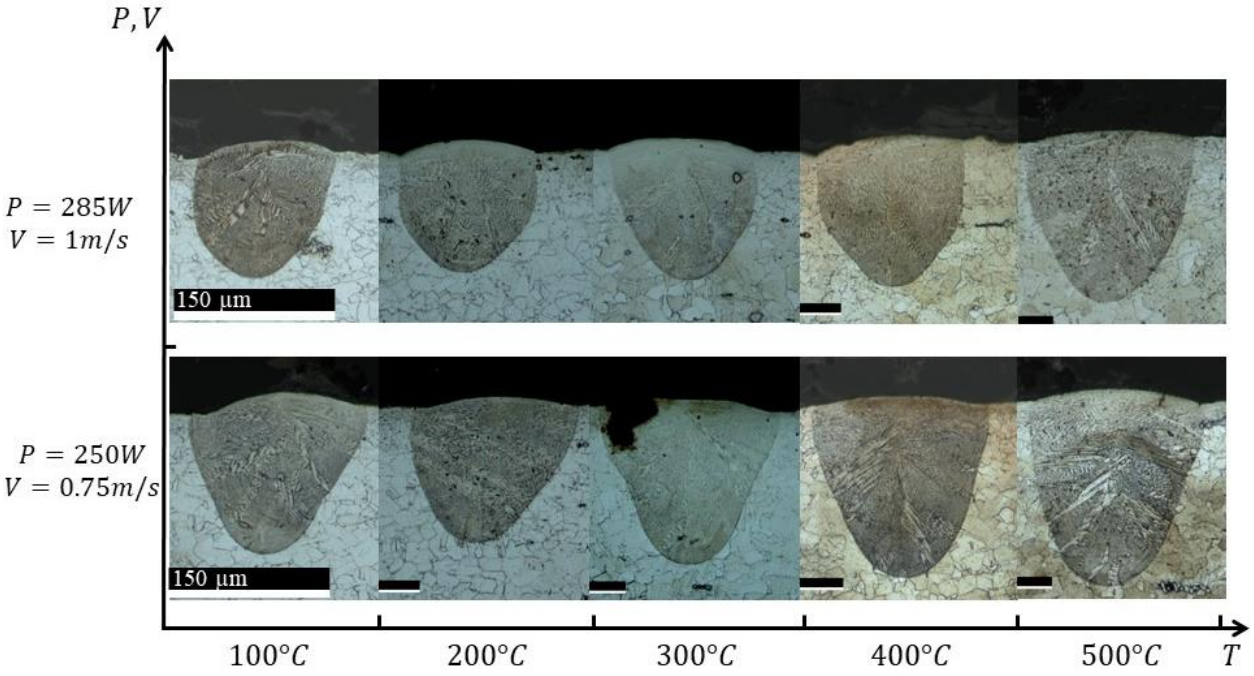

Figure 3.4: Melt Pool Morphology Variation with Preheating Temperature in Transition Regime

Melt pool dimensions and W/D ratios under the power of 285 W and scan speed of 1.0 m/s (EOS M290 default process parameters for Inconel 718) are presented in Figure 3.5(a)-(c). The melt pool depth exhibits an increasing tendency since the higher preheating temperature is favorable to the laser drilling effect, which leads to deeper melt pool. As for the melt pool width, similar increasing trend is observed. Melt pool comparisons between experiment and simulation at the preheating temperature of 100, 300 and 500 °C are presented in Figure 3.5 (d)-(f).

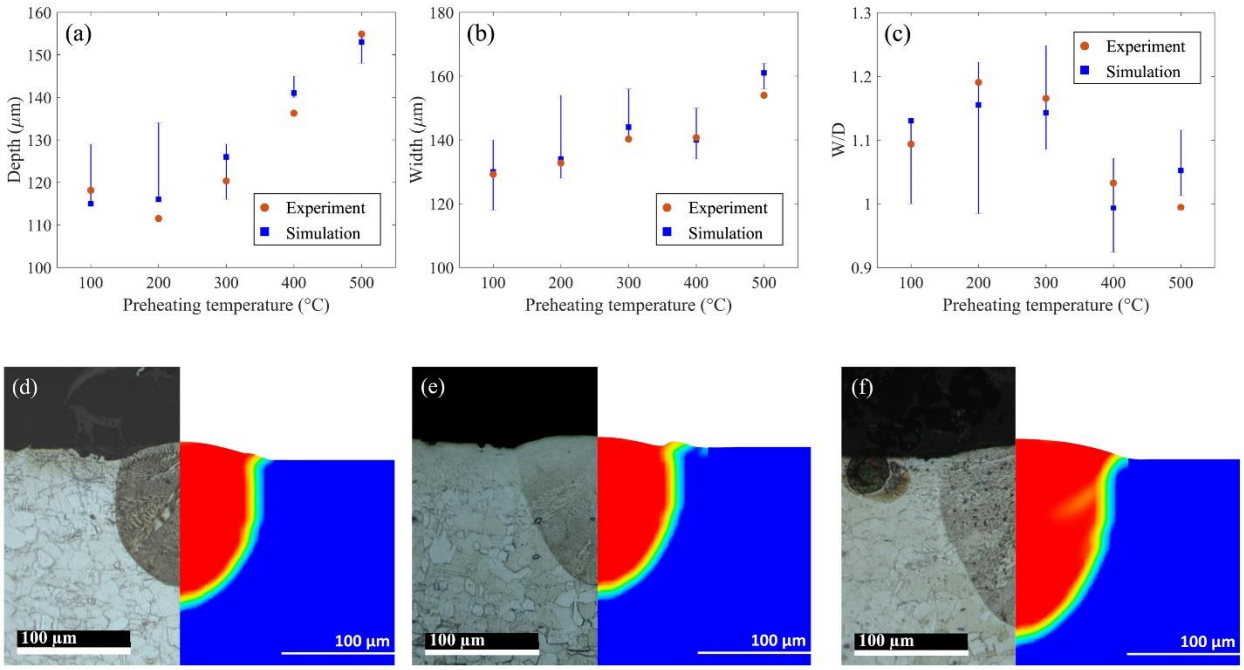

Figure 3.5: Melt Pool Dimensions versus Preheating Temperature in Transition Regime (P = 285 W and V = 1.0 m/s): (a) Depth; (b) Width; (c) Aspect Ratio and Comparison of Melt Pool between Experiment and Simulation at the Preheating Temperature of (d) 100 °C; (e) 300 °C; and (f) 500 °C.

3.3.1.3 Keyhole Regime

With a combination of high laser power and low scan speed, the melt pool displays the characteristics of the keyhole regime, which is known to lead to excessive porosity. The melt pool morphology variation with preheating temperature in the keyhole regime is shown in Figure 3.6. For all melt pools in the keyhole regime, cross sections were taken at 500x magnification. The trends indicate that under constant processing parameters, preheating temperature could remarkably increase the keyhole penetration depth. Under the power of 350 W and speed of 0.5 m/s, the melt pool is increased by 33.25% (from 343.36 μm at the preheating temperature of 100 °C to 457.52 μm at 500 °C). Under the power of 250 W and speed of 0.5 m/s, the melt pool is

increased by 23.64% (from 243.36 µm at the preheating temperature of 100 °C to 300.89 µm at 500 °C).

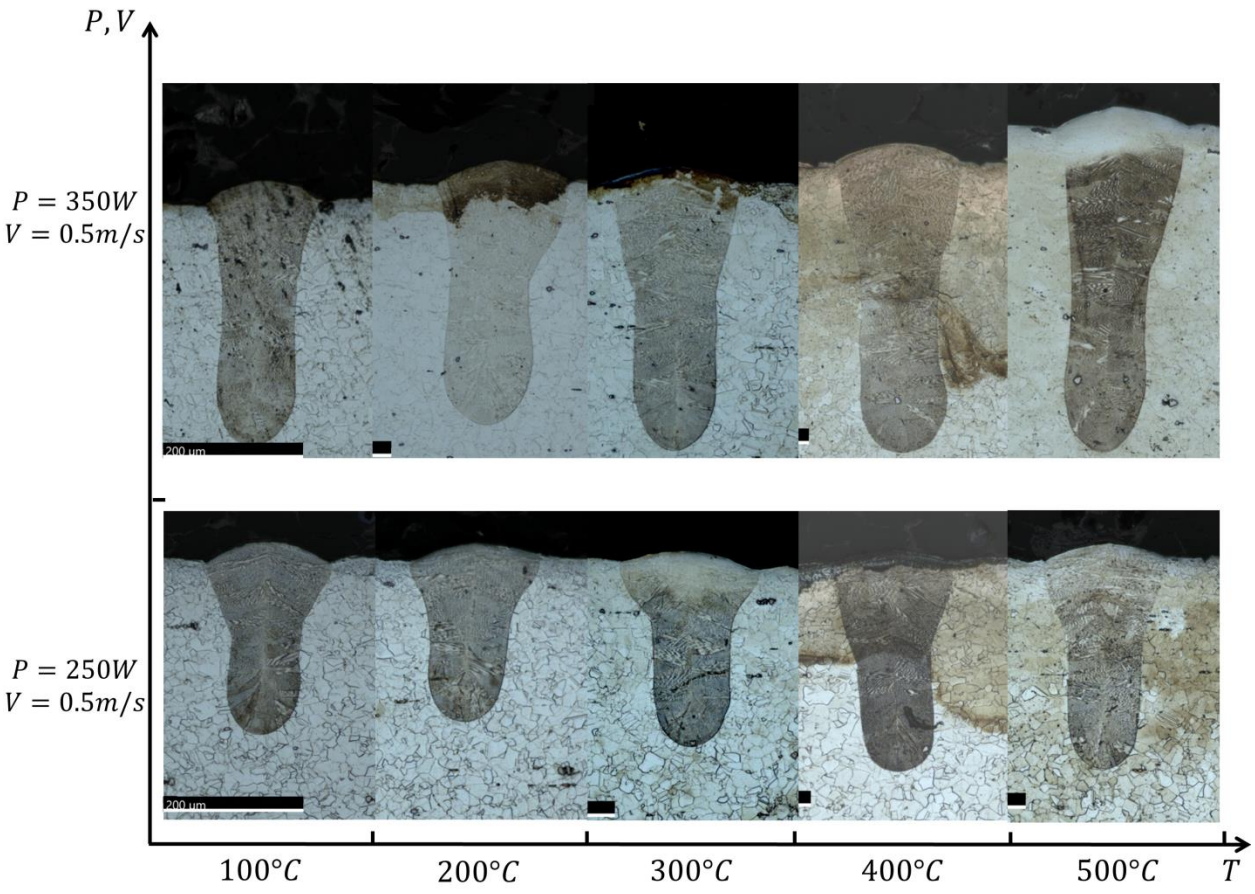

Figure 3.6: Melt Pool Morphology Variation with Preheating Temperature in Keyhole Regime

Figure 3.7 shows the melt pool dimensions and W/D ratios under the scan speed of 0.5 m/s, and laser power of 250 W. The melt pool depth exhibits a monotonically increasing trend with preheating temperature while the melt pool width initially increases and then drops down. A decreasing trend for the W/D ratio at higher preheating temperatures is observed, indicating that the laser drilling effect becomes dominant at higher preheating temperatures.

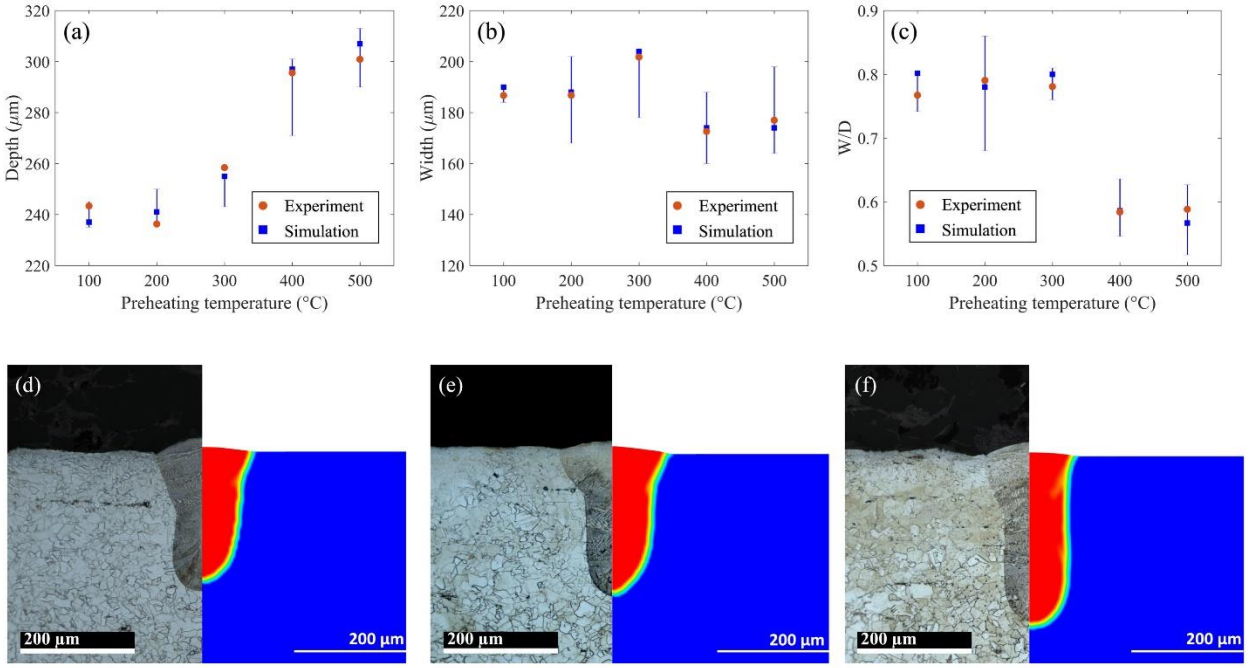

Figure 3.7: Melt Pool Dimensions versus Preheating Temperature in K Regime (P = 285 W and V = 1.0 m/s): (a) Depth; (b) Width; (c) Aspect Ratio and Comparison of Melt Pool between Experiment and Simulation at the Preheating Temperature of (d) 100 °C; (e) 300 °C; and (f) 500 °C.

3.3.2 Discussions

3.3.2.1 Temperature Dependent Thermal Properties

The variation of melt pool dimension with respect to preheating temperature can be attributed to factors including temperature dependent thermal properties, the enhancement of vapor depression and absorption. The following expression in Eq. (3.5) of melt pool width [26, 27] derived from Rosenthal solution [25] is employed to identify the contribution of temperature dependent material properties to melt pool morphology variation in heat conduction, since Rosenthal solution is derived from heat conduction equation and neglects convection, evaporation and Marangoni effect:

$$w = \sqrt{\frac{8}{\pi e} \cdot \frac{P\eta}{\rho C_p V (T_m - T_0)}} \tag{3.5}$$

where P is the laser power, η is the absorptivity, ρ is the density, C_p is the heat capacity, V is the scan speed, T_m is the melting point, and T_0 is the preheating temperature. Rosenthal solution is derived based on the assumption of temperature independent material properties and the thermal properties employed at different preheating temperature to compute melt pool width are listed in Table 3.1. Since it is valid in the conduction regime, the shape of melt pool derived from Rosenthal solution is semi-circular and the melt pool depth $d = w/2$.

Table 3.1: Temperature Dependent Material Properties of Inconel 718 Provided by Flow-3D

Temperature (°C)	Density (g/cm3)	Capacity (J/Kg/°C)	*k* (W/m·°C)
100	8.16	455	10.8
200	8.118	479	12.9
300	8.079	497	15.2
400	8.04	515	17.4
500	8.001	527	18.7

The analytical and experimental melt pool width and depth under the power of 250 W and scan speed of 1.5 m/s are presented in Table 3.2. It can be found that at preheating temperature of 100 °C and 200 °C, melt pool dimension obtained from Eq. (3.5) has a good agreement with experimental measurements. The melt pool obtained from *ex-situ* measurement has an aspect ratio of 1.90 at 100 °C and 2.01 at 200 °C, which has a semi-circular shape and exhibits the typical characteristic of conduction regime. At the preheating temperature of 300 – 500 °C, melt pool width value by analytical solution is still close to experimental value while the depth value is underestimated by analytical solution. Since melt pool width at different preheating temperature can be accurately predicted by the Rosenthal solution which is derived from heat conduction equation, it can be concluded that for melt pool in conduction regime, melt pool width depends on heat conduction and temperature dependent thermal properties leads to melt pool width variation

at different preheating temperature. For melt pool depth, it is determined by heat conduction at low preheating temperature, and when the preheating temperature is sufficiently high, vapor depression penetrates the semi-circular area and forms a deeper melt pool. The enhancement of preheating temperature on recoil pressure and vapor depression will be discussed in Section 3.3.2.2.

Table 3.2: Melt Pool Dimension in Conduction Regime Comparison between Analytical Solution and Experiment Measurement ($P = 250\ W, V = 1.5\ m/s$ and $\eta = 0.4$)

Temperature (°C)	Width			Depth			W/D ratio
	Analytical solution (μm)	Experiment (μm)	Error (%)	Analytical solution (μm)	Experiment (μm)	Error (%)	Experiment
100	118.40	113.66	4.17	59.20	59.74	-0.90	1.90
200	120.84	122.91	-1.68	60.42	61.24	-1.34	2.01
300	124.72	130.40	-4.36	62.36	74.01	-15.74	1.76
400	129.46	129.96	-0.38	64.73	86.78	-25.41	1.50
500	136.06	131.28	3.64	68.03	88.99	-23.55	1.48

The comparison of analytical and experimental melt pool dimension in the transition regime under the EOS M290 default process parameters of IN718 (P = 285 W and V = 1.0 m/s) is presented in Table 3.3. Similar to melt pool in conduction regime, under the default process parameters, melt pool width can be accurately predicted by analytical solution. However, the error of melt pool depth is extremely large compared to experimental measurements. This is because vapor depression become dominant on melt pool depth under the default process parameters. The important role of temperature dependent thermal parameters on melt pool width in conduction and transition regime is identified through comparison with analytical solution.

Table 3.3: Melt Pool Dimension in Transition Regime Comparison between Analytical Solution and Experiment Measurement ($P = 285\ W, V = 1.0\ m/s$ and $\eta = 0.3$)

Temperature (°C)	Width (μm)			Depth (μm)			W/D ratio
	Analytical solution (μm)	Experiment (μm)	Error (%)	Analytical solution (μm)	Experiment (μm)	Error (%)	Experiment
100	134.08	129.20	3.78	67.04	118.14	-43.25	1.09
200	136.84	132.74	3.09	68.42	111.5	-38.64	1.19
300	141.24	140.26	0.70	70.62	120.35	-41.32	1.17
400	146.61	140.71	4.19	73.305	136.28	-46.21	1.03
500	154.09	153.98	0.07	77.045	154.87	-50.25	0.99

3.3.2.2 Recoil Pressure

The role of recoil pressure and vapor depression on melt pool dimension at different preheating temperature is analyzed in this section. The recoil pressure can be obtained by Eq. (3.6):

$$P_s = A \cdot exp\left\{B\left(1 - \frac{T_v}{T}\right)\right\} \tag{3.6}$$

where the coefficient $A = \beta P_0$, $\beta \in [0.54, 0.56]$ and P_0 is ambient atmosphere pressure; the second coefficient B can be obtained by $B = {\Delta H_v}/{RT_v}$, ΔH_v is the latent heat of evaporation, R is the universal gas constant and T_v is the saturation temperature; T is the flow temperature obtained by solving Eq.(3.1-3.4).

Ultrahigh-speed x-ray imaging has demonstrated the presence of vapor depression under almost all conditions relevant to L-PBF, [90] and vapor depression is observed as well in all the simulations in this work, even for melt pool in conduction regime with the lowest preheating temperature (100 °C). For melt pool in conduction regime, as discussed in Section 3.3.2.1, both melt pool width and depth are determined by heat conduction at lower preheating temperature. Even though recoil pressure exists and pushes the molten material downward, the vapor depression does not penetrate the semi-circular heat conduction area as indicated by the black dashed line in

Figure 3.8(a). Recoil pressure and vapor depression become stronger at higher preheating temperature and ultimately the vapor depression penetrates the area affected by heat conduction as shown in Figure 3.8 (b). The enhancement of recoil pressure and vapor depression is experimentally and numerically demonstrated which makes the aspect ratio of melt pool in experiments small as shown in Table 3.2 (1.76 at 300 °C, 1.50 at 400 °C, and 1.48 at 500 °C).

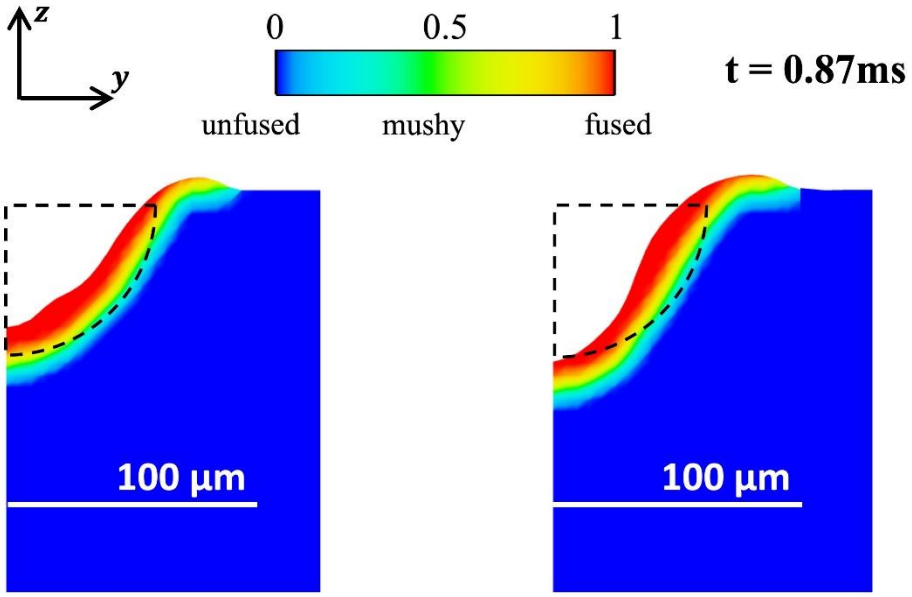

(a). Preheating temperature: 200 °C **(b).** Preheating temperature: 300 °C

Figure 3.8: Vapor Depression in the Formation of Melt Pool in Conduction Regime (P = 250W and V = 1.5 m/s) at Various Preheating Temperatures

Melt pool volume and evaporation mass per length at different preheating temperature are summarized in Figure 3.9. Preheating temperature significantly increases the melt pool volume in conduction, transition and keyhole regime as shown in Figure 3.9 (a-c). As shown in Figure 3.9 (d), evaporation mass does not vary too much in conduction regime which supports the conclusion in Section 3.3.2.1 that melt pool morphology variation in conduction regime is mainly attributed to heat conduction enhancement due to temperature-dependent material properties. In transition and keyhole regime, evaporation mass tends to increase along with preheating temperature.

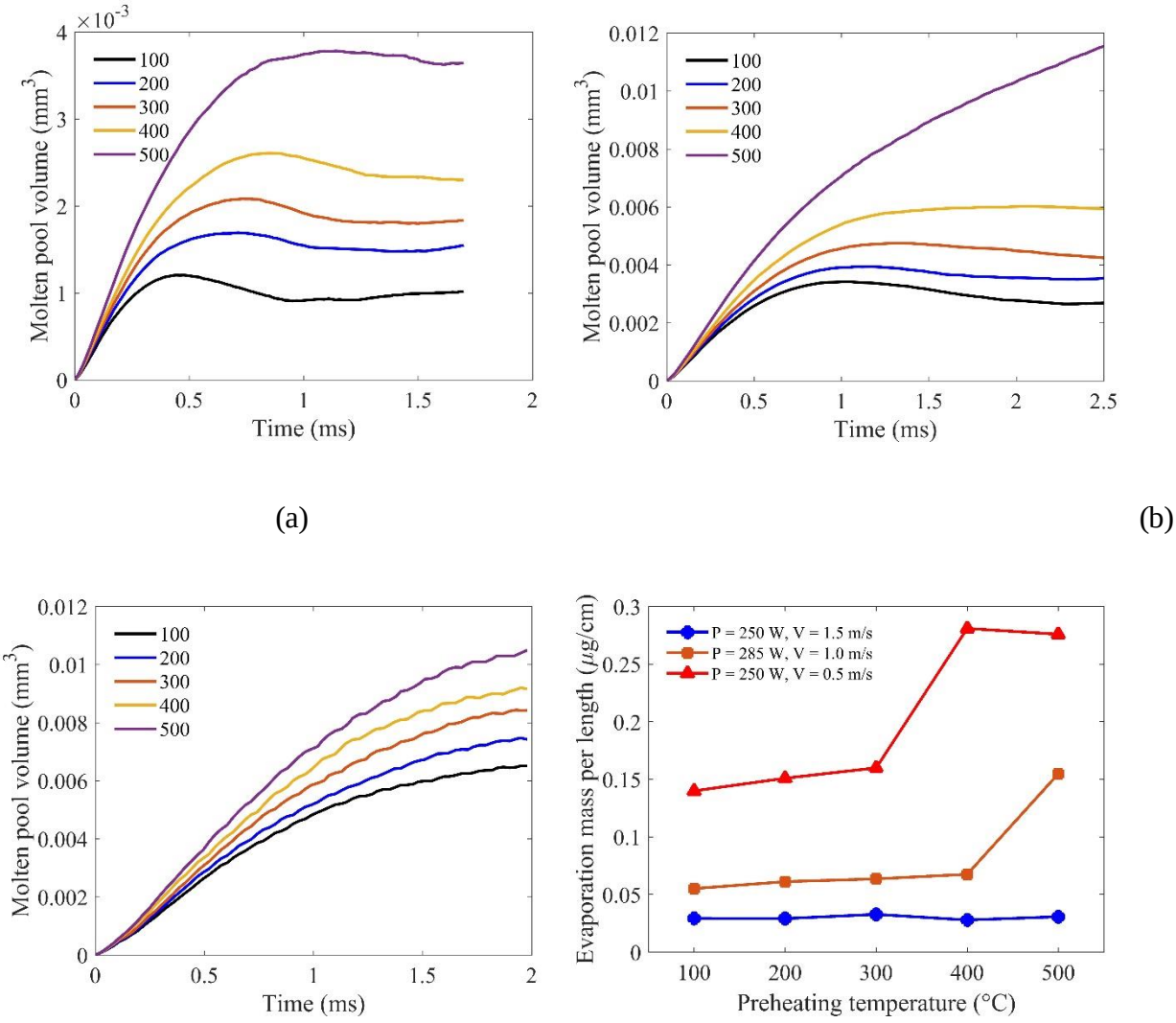

Figure 3.9: Molten Pool Volume in (a) Conduction Regime (P = 250W and V = 1.5 m/s): (b) Transition Regime (P = 285W and V = 1.0 m/s); (c) Keyhole Regime (P = 250W and V = 0.5 m/s); (d) Evaporation Mass at Different Preheating Temperature

Figure 3.10 shows a time series of melt track cross sections with the power of 250 W and scan speed of 0.5 m/s, at the preheating temperature of 100 °C. At 1.90 – 2.03 ms, keyhole cavity caused by recoil pressure and the strong fluctuation of depression depth is observed. This strong fluctuation of depression depth is attributed to the interplay between multiple reflections of laser

ray and laser absorption intensity [91]. The inclination angle of keyhole front wall (as seen in Fig. 29 at 1.90 ms) is relatively stable from 1.90 – 2.03 ms, while the rear wall shape varies significantly because the vapor flow from the front wall collides with the rear wall at different locations on various velocity as indicated by the black arrows in Figure 3.10 [92]. The moving laser is turned off at 2 ms and depression zone is cooling down rapidly accompanying with rapid decrease of recoil pressure. The keyhole is then closed under surface tension pressure, convection-induced pressure and hydrostatic pressure [17, 23] (see Figure 3.10 at 2.03 ms). Figure 3.11 shows the simulation results of the same single track at the preheating temperature of 500 °C. A much deeper depression zone than the case at 100 °C is found. At 1.98 ms, the keyhole reaches the deepest depth of 302.97 μm while for the case at 100 °C, the depth of the deepest keyhole is only 209.43 μm (see Figure 3.10 at 1.93 ms). This deeper depression zone at higher preheating temperature increases the chance of trapping gas bubble when keyhole collapses and therefore, gives rise to pores forming at the bottom region of melt track (see Figure 3.10 at 1.90, 1.98, 2.01 and 2.03 ms). These pores have a diameter around 50-70 μm and some of the pores are pierced by the vapor flow subsequently (see Figure 3.10 at 1.90-1.93 ms), while some are kept (see Figure 3.10 at 2.03 ms). Moreover, at 1.93 ms, the rear wall shape distorts significantly and forms a bottleneck at the middle which indicates vapor flow collision at 500 °C preheating temperature becomes stronger than that at 100 °C. Therefore, the enhancement of preheating temperature on recoil pressure is confirmed by simulation. Higher preheating temperature leads to stronger evaporation and recoil pressure, particularly for keyhole regime, which forms a deeper melt pool and further increases the energy absorption due to laser ray reflections. For melt pool in keyhole regime, higher preheating temperature also increases the chance of pore formation.

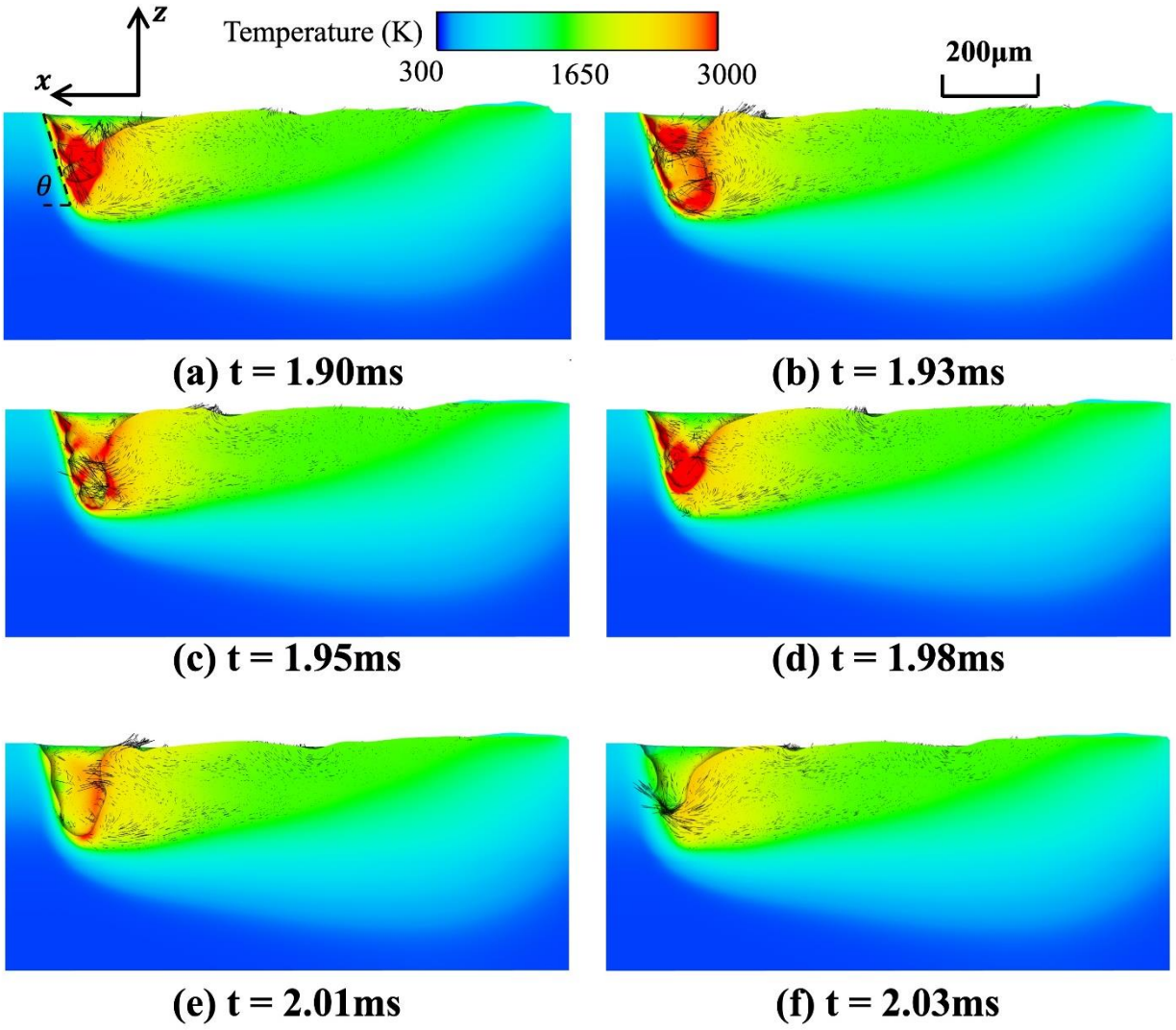

Figure 3.10: Snapshots of Temperature Profile for Single Track in Keyhole Regime (P = 250W and V = 0.5m/s) at the Preheating Temperature of 100 °C

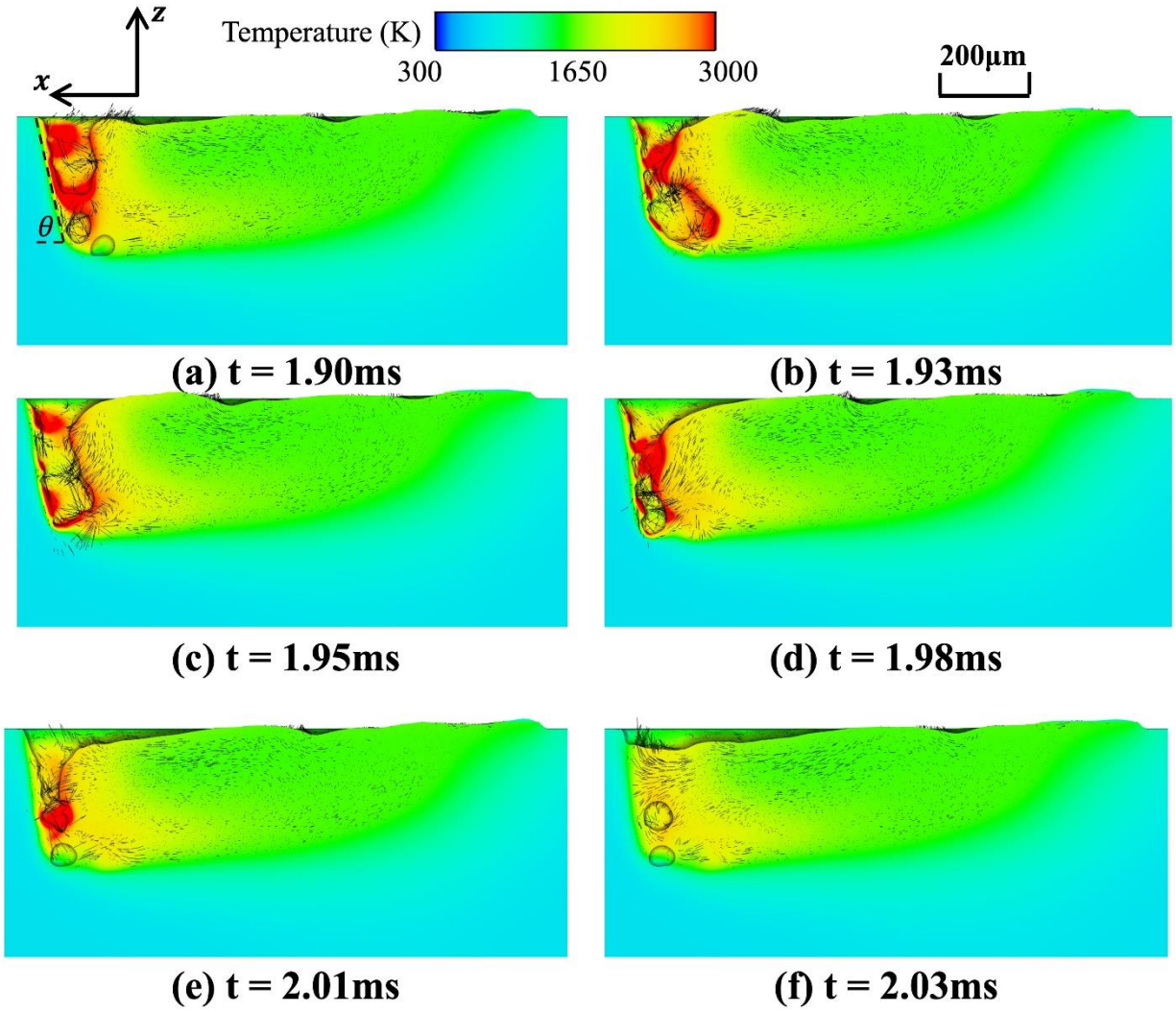

Figure 3.11: Snapshots of Temperature Profile for Single Track in Keyhole Regime (P = 250W and V = 0.5m/s) at the Preheating Temperature of 500 °C

The laser drill rate at different preheating temperature is estimated by the front wall angle of keyhole in accordance with the simplified model proposed by Fabbro et al [93] which determines the tangent of keyhole front wall angle as the ratio of laser drill rate and scan speed as follows:

$$tan(\theta) = \frac{V_d}{V} \tag{3.7}$$

where θ is the front wall angle of keyhole as depicted in Figure 3.12(a), V_d is the laser drill rate, and V is the laser scan speed. Therefore, laser drill rate can be obtained as $V_d = V \cdot tan(\theta)$ and

with constant scan speed, laser drill rate is proportional to $tan(\theta)$. The front wall angles and tangents in simulations at different preheating temperatures are summarized in in Figure 3.12 (c) and (d), respectively. It is found that the inclined angle of keyhole front wall increases along with preheating temperature and the tangent value which is proportional to laser drill rate in the estimation indicates that the laser drill rate at the preheating temperature of 500 °C (3.88 m/s) is 2.18 times larger than at 100 °C (1.78 m/s).

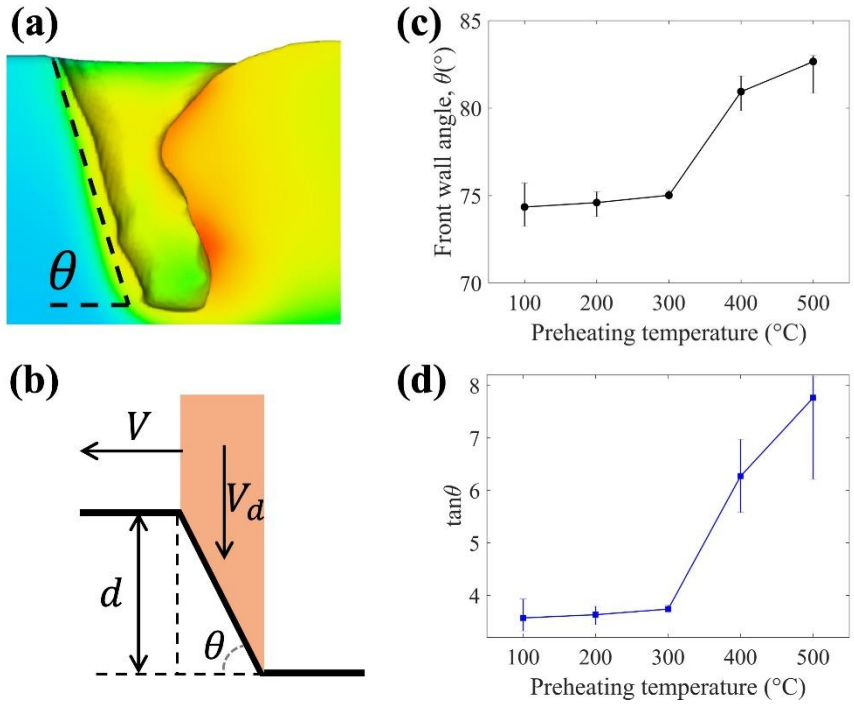

Figure 3.12: (a) Front Wall Angle of Keyhole in Simulation; (b) Schematic of Front Wall Angle, Depth and Scan Speed, Modified from Fabbro et al [93]; (c) Keyhole Front Wall Angle, θ; (d) $tan(\theta)$ along with Preheating Temperature (P = 250 W and V = 0.5 m/s).

3.3.2.3 Melt Track Length

Since melt pool length measurement is inaccessible in *ex-situ* experiment, melt pool length variation along with preheating temperature in simulation is studied in this section. Figure 3.13 presents the simulation results of melt pool length variation at different preheating temperatures at

t = 1.00 ms and 1.70 ms, respectively. At 1.00 ms, the length of melt track formed at 100 °C is 946 μm while the track is elongated to 1,551 μm at 200 °C as shown in Figure 3.13(a). Even though the melt track length does not change much at the preheating temperature from 200 to 500 °C, necking is about to happen at the tail end of melt track under 200 °C as indicated in Figure 3.13(b), where the melt track becomes narrow near the tail region and is about to divide into two parts. At the tail end of melt track, the backward flow becomes slow and starts to break up at 200 °C because the Marangoni effect becomes too weak to bring molten flow from the laser hot spot to the tail. Then surface tension tends to minimize surface energy by forming a bead [17]. At 1.70 ms, the melt pool is completely developed and the melt track length increases along with preheating temperature as shown in Figure 3.13(c)-(d). It is observed in Figure 3.13(d) that high preheating temperature increases the bead length at the tail end of track.

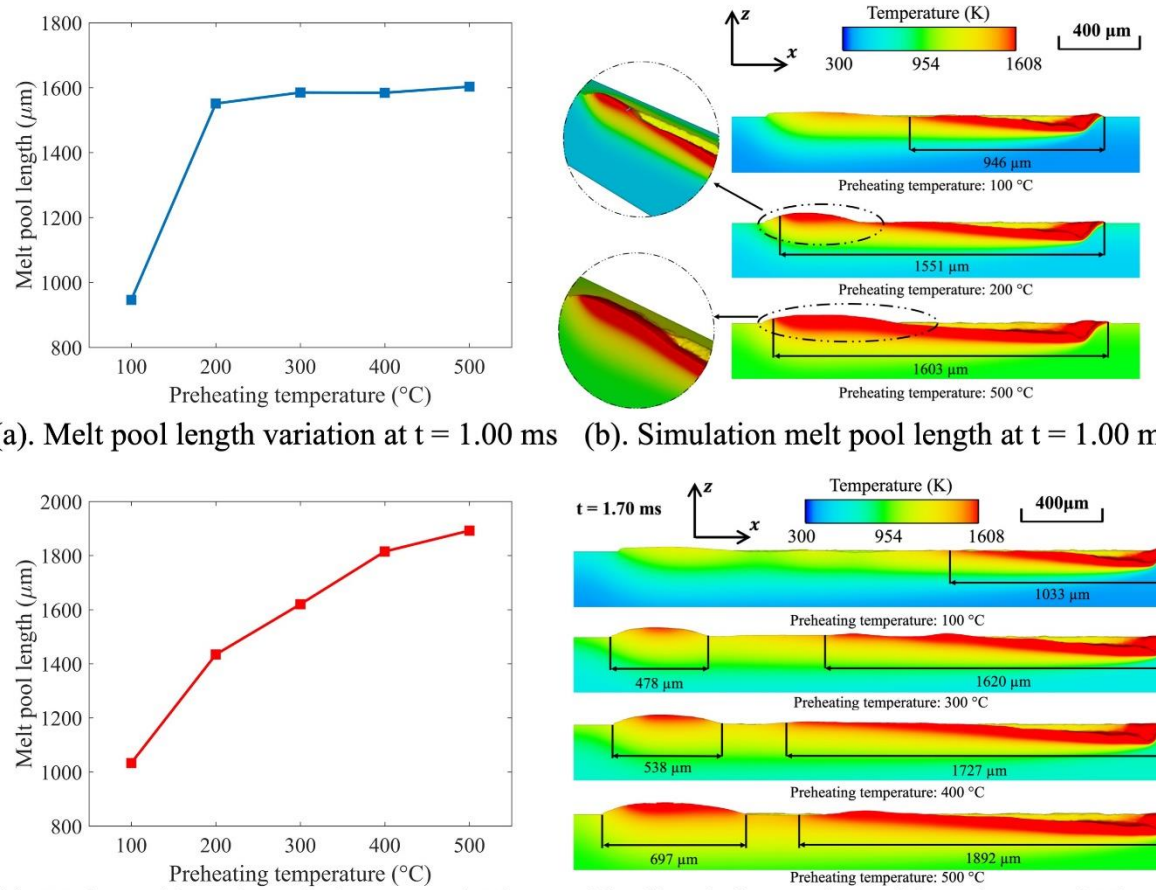

(a). Melt pool length variation at t = 1.00 ms (b). Simulation melt pool length at t = 1.00 ms

(c). Melt pool length variation at t = 1.70 ms (d). Simulation melt pool length at t = 1.70 ms

Figure 3.13: Simulation Result of Melt Pool Length Variation along with Preheating Temperature in Conduction Regime (P = 250 W and V = 1.5 m/s)

Figure 3.14(a) presents the global melt flow velocity in the center x-z plane at 1.0 ms when the preheating temperature is 100 °C and 500 °C, respectively. Figure 3.14(b) presents the melt flow velocity near the depression. It can be observed that the backward melt flow originating from the laser hot spot has higher velocity and flow rate at 500 °C than at 100 °C. High preheating temperature increases the melt flow volume, and therefore, leads to higher flow rate. The dominant driving forces of liquid flow are the Marangoni force, the surface tension due to temperature gradient which drives the melt flow from the hot laser spot, namely the depression zone, towards the tail end, and the recoil pressure due to vaporization that drives the melt flow outward normal to the vaporization surface. As indicated in Figure 3.9 that high preheating temperature improves

the evaporation mass and increases the recoil pressure inside the depression zone, which leads to higher velocity of the backward melt flow leaving the depression. The backward melt flow serves to cool down the laser hot spot and elongate the melt track length. At the tail end, the melt flow becomes slow and forms one or a few vortexes. The melt flow pattern in simulation is similar to the pattern obtained by in-situ synchrotron x-ray imaging [94] with uniformly dispersed micro-tracers as shown in Figure 3.14(c).

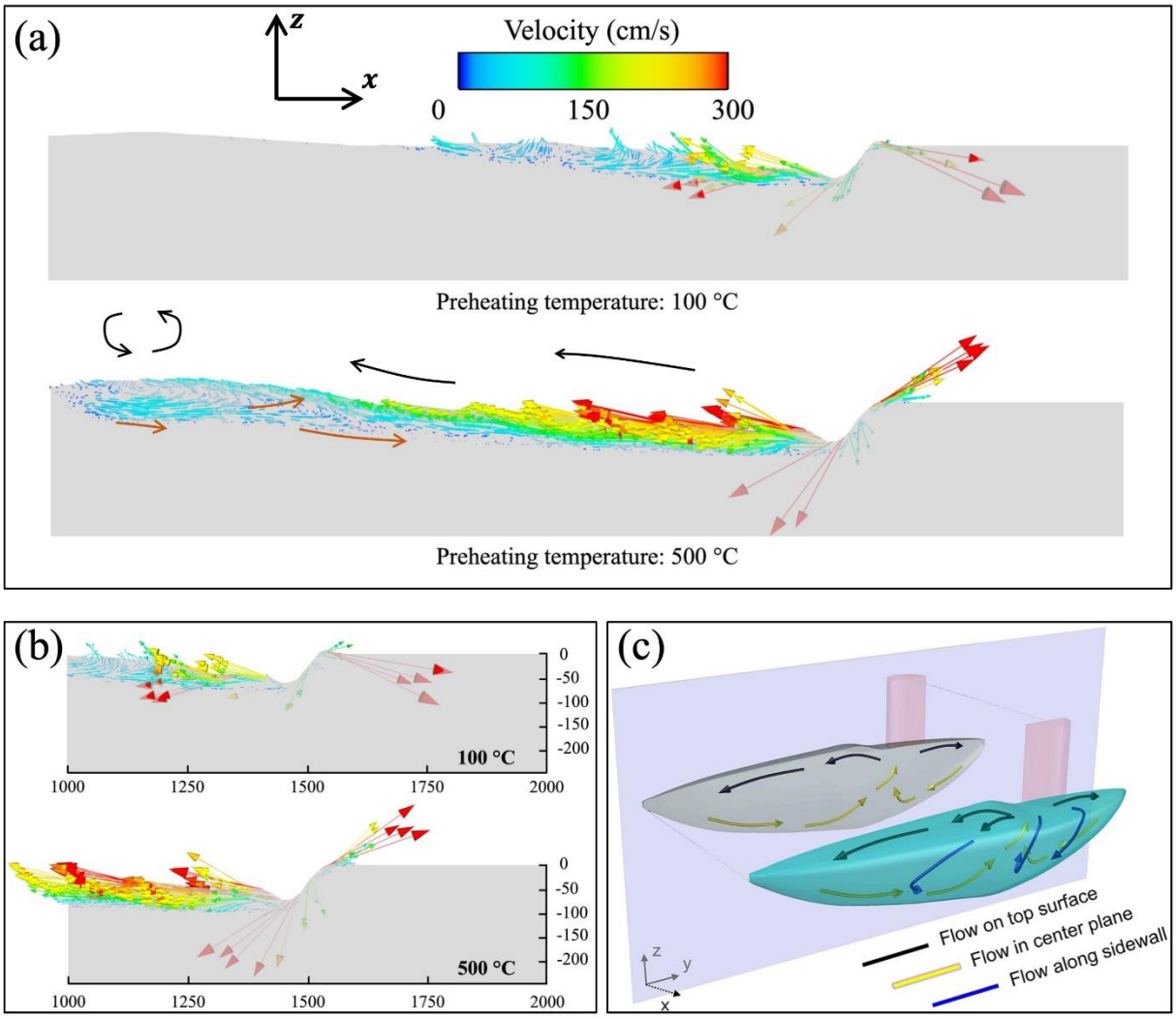

Figure 3.14: (a) Global Melt Flow Velocity Profile at 1.00 ms, (b) Melt Flow Velocity near the Depression Zone at 1.00 ms; (c) Schematic Melt Flow Pattern [94]

3.4 Defect Formation Mechanism Induced by Spattering Particles

Powder particle spattering induced by the metal vapor jetting and vortex flow near the melt pool significantly influences the porosity of final product. In this work, a high-fidelity multiphyiscs model is developed at powder-scale that unidirectional couples the powder spattering and laser welding simulation to study the spattering and porosity formation mechanism in laser powder bed fusion process. Vapor pressure from single-track laser welding simulation is applied as a moving boundary condition in a discrete element model to simulate the particle spattering. Then, coupling simulation between the mass particles and laser welding is performed to study the interaction between melt pool and spattering particles. Two porosity formation mechanisms are observed in experiments and simulation. The first one is the spattering particles falling into melt pool directly and leaving an un-melted or partially melted pores to the final product. The second mechanism is the particles near the melt track are dragged to the melt pool bead and partially melted due to heat conduction. This partially melted particles can be reserved as well in the as-built part.

3.4.1 Powder Laser Welding Model Calibration

To calibrate the simulation setup including absorptivity, evaporation model and boundary conditions, the melt pool cross sections from simulation for single-track deposition on powder bed with a layer thickness of 80 μm and triple-track deposition in S-pattern on bare plate are compared to experimental ex-situ measurements.

The comparison of melt pool cross section for single-track deposition between simulation and experiment is presented in Figure 3.15. In the experiment, we spread a layer of powder with a layer thickness of 80 μm. It can be found that melt pool bead height is around 80 μm in both

simulation and experiment. The melt pool width in simulation is 8.28% larger than experiment, while the melt pool width is 8.37% smaller than experiment. The difference of melt pool dimensions between simulation and experiment is attributed to the variation of powder bed layer thickness. In ex-situ cross section, two sphere particles are attached to the melt pool bead on the right and left side, respectively. This is caused by the particle entrapment due to molten flow during the laser scanning process.

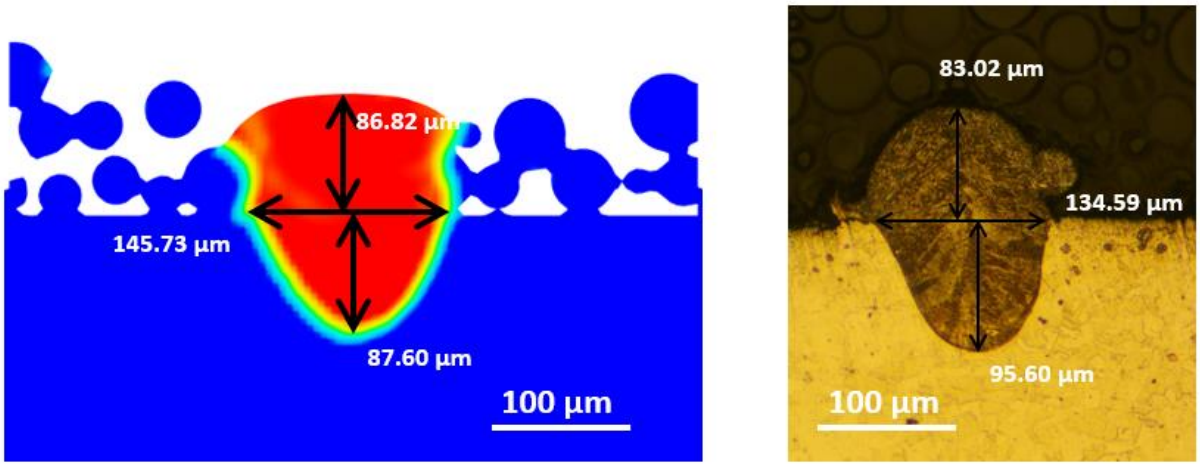

Figure 3.15: Melt Pool Cross Section Comparison Between Simulation and Experiment for Single Track

Calibration for the triple-track deposition simulation is performed as well. The comparison of melt pool cross section between simulation and experiment is presented in Fig. 3.16. It can be found that the melt pool depth increases from the first track to the third track (from left to right) in both simulation and *ex-situ* measurement, which is attributed to the residual heat. The absorptivity value is set to 0.28 and the simulation is performed for a bare plate without powder particles. In the experiment, one layer of powder with a layer thickness of 40 µm was spread. However, the purging took half an hour and most the particles are blown away. It can be found that the melt pool depths have a good agreement with experimental measurements. The top region of the melt pools in simulation is similar to the experiment measurement as well.

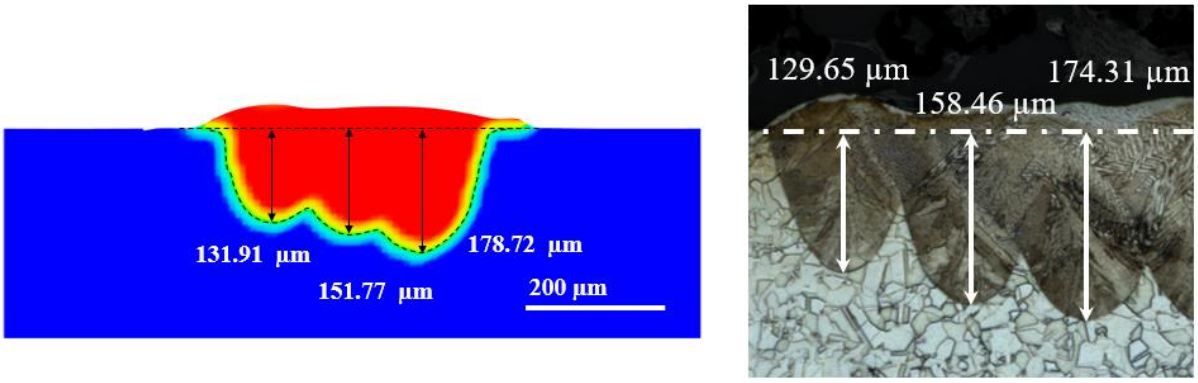

Figure 3.16: Melt Pool Cross Section Comparison Between Simulation and Experiment for Triple Tracks

3.4.2 Spattering Model by Discrete Element Method

The spattering simulation model is developed by Flow-3D discrete element method (DEM) module to study the particle motion driven by vapor flow caused by laser welding. The unidirectional DEM coupling model, as shown in Figure 3.17 is briefly discussed as follows:

- A moving jet hole with a radius of 80 µm is in the middle of the substrate underneath the powder bed generated by powder settling and spreading simulation.
- The moving speed of the jet hole equals to the laser scan speed of 1 m/s.
- The boundary condition for the moving jet hole is velocity boundary condition and the vertical speed is set as 150 m/s corresponding to the vapor coming out the depression zone.

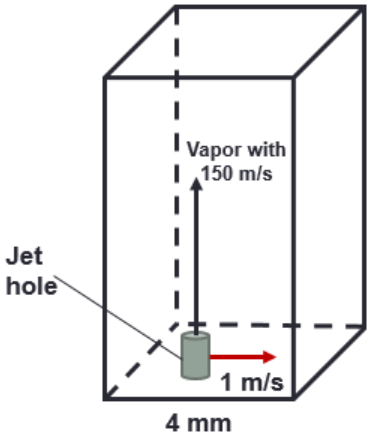

Figure 3.17: Schematic of Spattering Model Developed by Discrete Element Method

Simulation results of the spattering simulation is shown in Figure 3.18. The powder bed generated by powder settling and spreading before spattering simulation has a mean layer thickness of 80 μm and a packing density of 53%. The powder particles after the jet hole moving along the center line of the powder bed with a scan speed of 1.0 m/s and flow speed of 150 m/s become scattered. From the top view of the powder bed after spattering simulation, it can be found that the denudation zone as indicated by the black dashed lines are refilled with particles after the jet hole passes while the neighboring area is also influenced by the passing jet hole and becomes sparse. There are particles falling back to the denudation zone with a transverse (along y direction) or vertical (along z direction) speed which indicates a potential pore formation mechanism due to these particles.

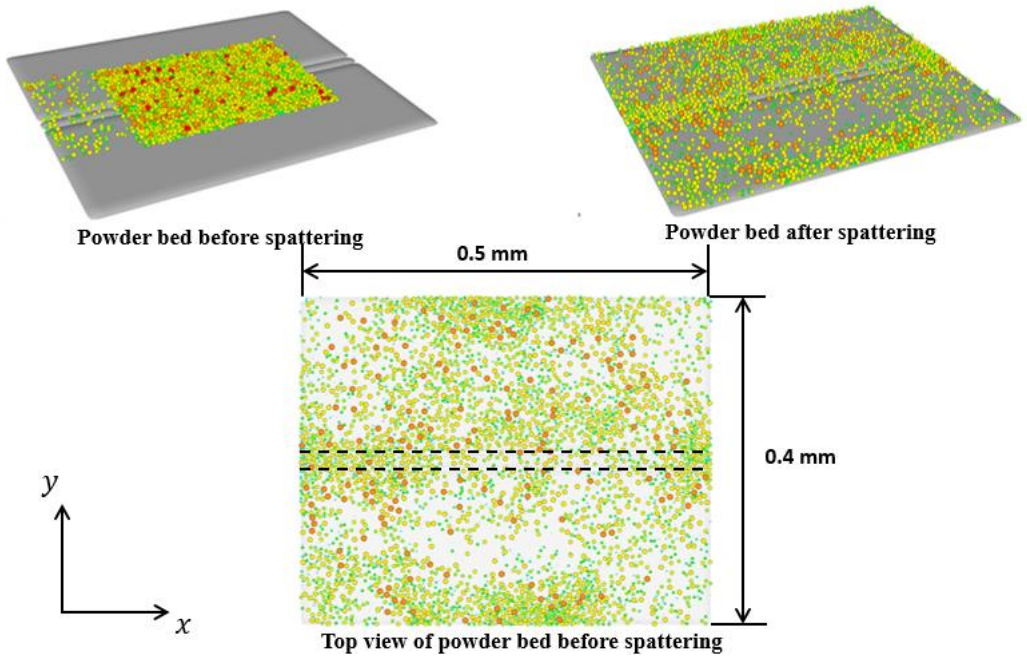

Figure 3.18: Simulation Results of Powder Bed Morphology by Spattering Model

3.4.3 Laser Welding Model Coupled with Spattering Particles

A coupling simulation model is developed that unidirectionally couples the laser welding and spattering particles as discussed in Section 3.4.2 to study the interaction between spattering particles and laser welding track and reveal the pore formation mechanism associated with the entrainment of mass particles into unsolidified melt pool. Three particle sources are added into the single-track laser welding simulation. The mass particle velocity coming out of each particle source is shown in Figure 3.19. The computation domain includes three particle sources, substrate and powder bed obtained from powder settling and spreading simulation. The laser power is 285 W and scan speed is 1.0 m/s.

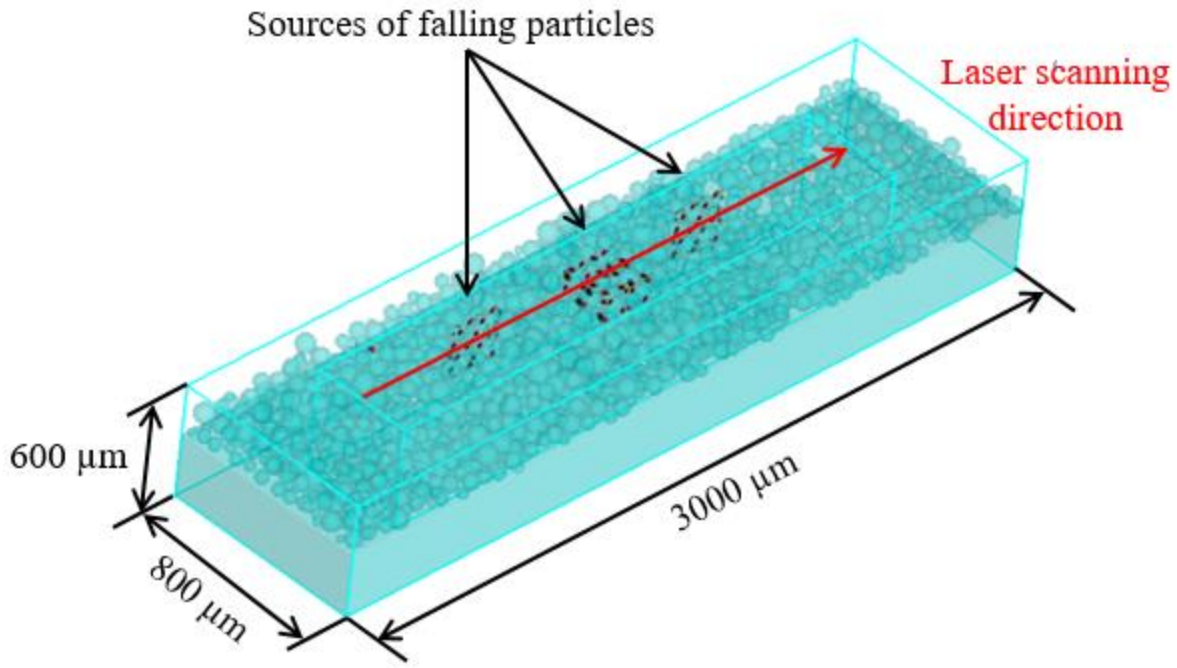

Figure 3.19: Simulation Model Coupling Laser Welding and Mass Particles

3.4.4 Results and Discussion

Figure 3.20 shows the snapshots of the simulation coupling laser welding and falling mass particles. At 0.61 ms, the first falling particle as indicated by the white arrow is right above the melt track the temperature of which is 80 °C. At 0.63 – 0.67 ms, this particle enters into the depression zone caused by vapor evaporation pressure. This particle is then melted by the molten flow and cannot be tracked at 0.68 ms. At 0.67 ms, there is another particle falling on the powder bed near the laser melt track as indicated by the black arrow. At 0.68 ms, this particle contacts with a few particles on the powder bed. Due to the heat conduction between falling particle and power bed, the particle temperature rises to around 300 °C at 0.71 ms.

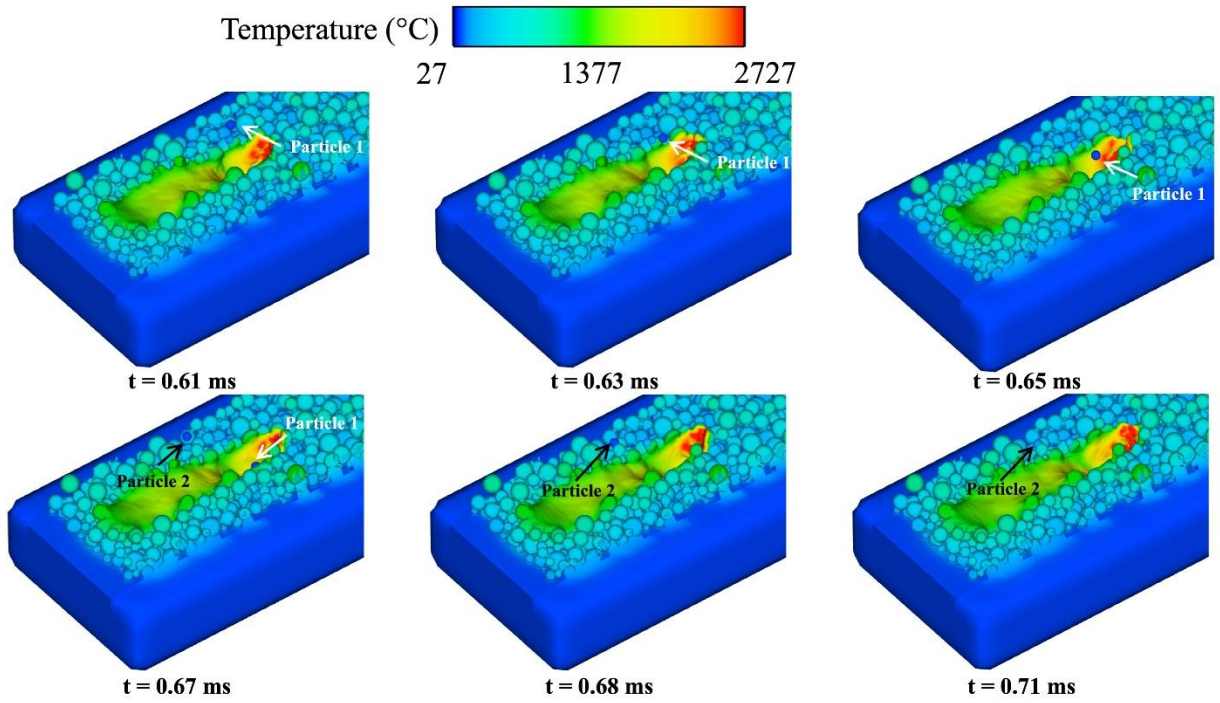

Figure 3.20: Snapshots of Coupling Simulation Results

The cross section where falling mass articles are attached to melt region is shown in Figure 3.21. Mass particles fall on the powder bed near the melt track and are heated up. In the real building process, these falling particles will change the local powder bed morphology and large particles can also lead to lack of fusion in the neighboring track or subsequent layers. Melt pool with partially melted particles attached to the top bead is observed in the *ex-situ* melt pool cross section as shown in Figure 3.22. These particles attached to the melt pool bead are not completely melted and increase the porosity of as-built part. Moreover, these particles also serve as origin of pores in the subsequent layers.

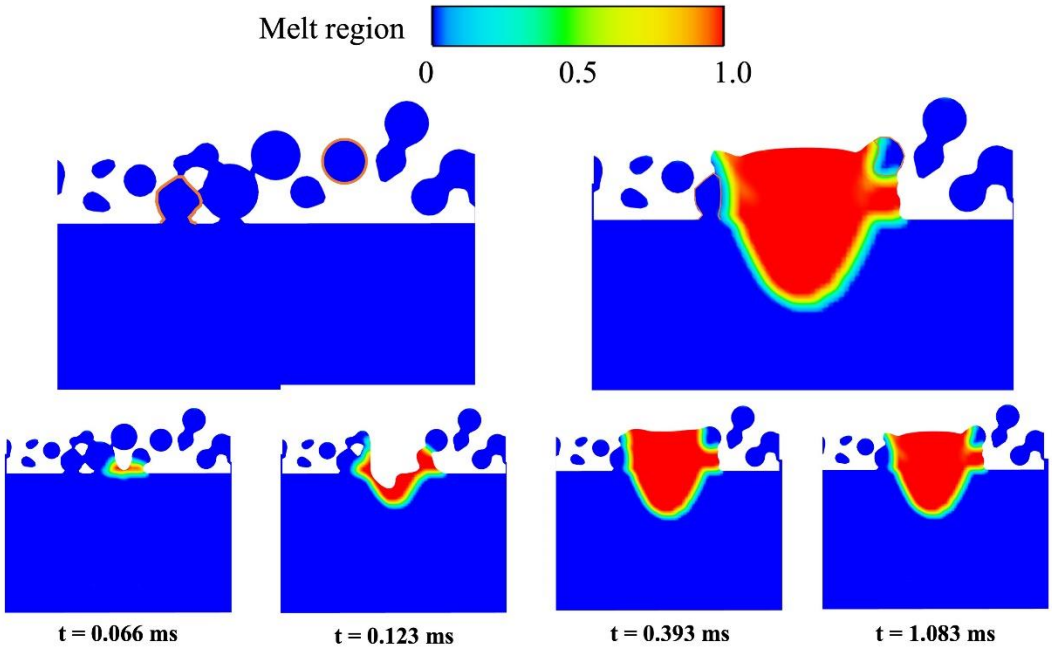

Figure 3.21: Evolution of Melt Pool Attached with Partially Melted Particles

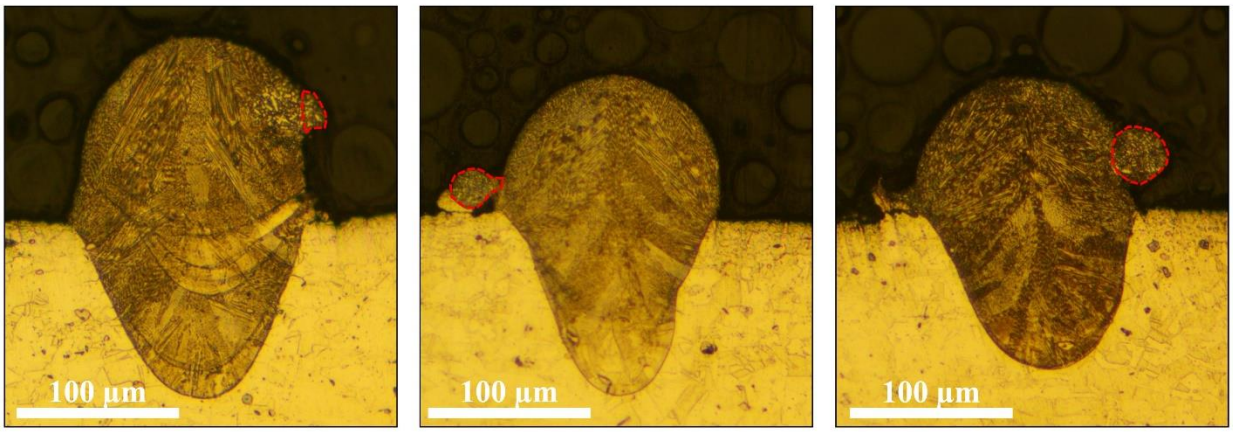

Figure 3.22: Ex-situ Melt Pool Cross Section with Particles Attached to Melt Pool Bead

Another porosity formation mechanism observed from the simulation is the spattering particle entrainment into melt pool region. In *ex-situ* cross section measurements, we noticed pores inside the melt pool even in conduction regime as shown in Figure 3.23. From the coupling

simulation results, we also observed spattering particle falling into the melt pool. Some particles are melted by the hot molten flow. However, under the scenario that molten flow temperature is not high and the falling spattering particle size is too large, this falling particle cannot be fully melted which finally form a pore inside the melt pool region shown in Figure 3.24.

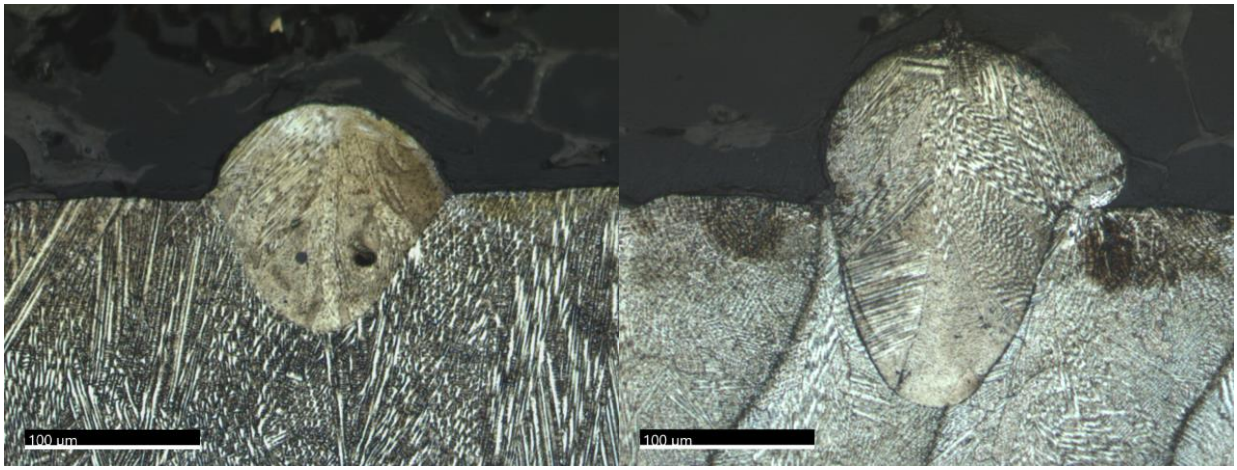

Figure 3.23: Ex-situ Cross Section Measurements of Melt Pool with Pores: (a) Conduction Regime; (b) Transition Regime

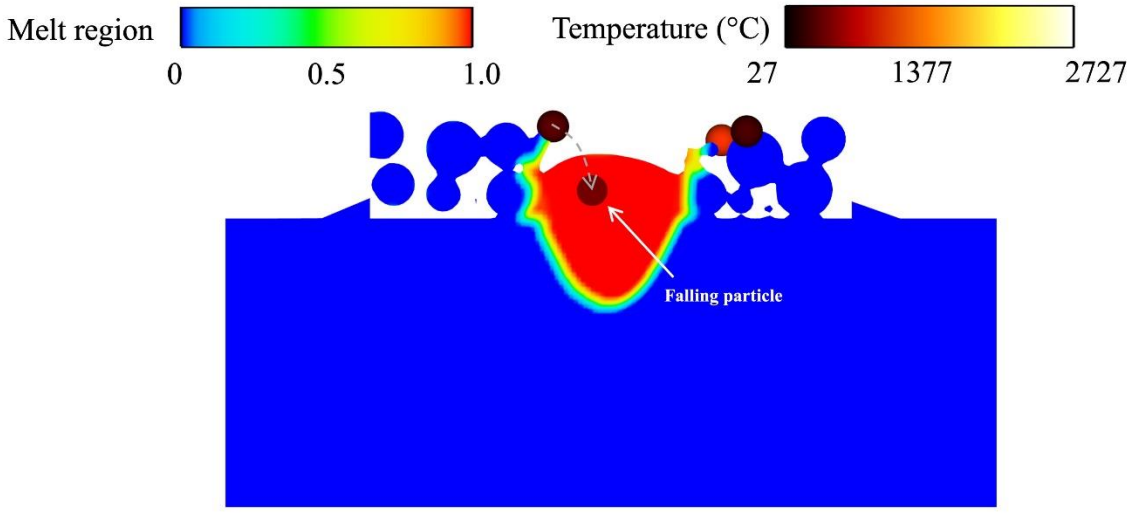

Figure 3.24: Cross Section of Melt Pool with Falling Particles

By far, two porosity formation mechanisms are revealed through multiphysics modeling: one is the spattering particles falling down on the powder bed near laser scan track get attached to the melt pool bead but remain partially melted; the other one is the spattering particles fall into the melt pool and cannot be completely melted by the molten flow. The first type of pores due to spattering particle attachment to melt pool bead can be eliminated by neighboring tracks with a proper hatch spacing or the laser scanning of subsequent layers. As for the second type of pores, if the pore locates on top of the melt pool or near the boundary, it could be eliminated due to re-melting. However, if the pore is at the bottom, it cannot be eliminated and is left inside the as-built part. Figure 3.25 gives a schematic of melt pool overlap between neighboring tracks and consecutive layers. The hatch spacing between neighboring tracks is 110 μm while melt pools on the top are shifted by 55 μm. The maximum bead height is half of the layer thickness and once the first layer scanning is done, a new powder layer is formed. It can be found that pores due to

attachment and falling particles in the re-melted region can be eliminated while pores at the bottom cannot be removed.

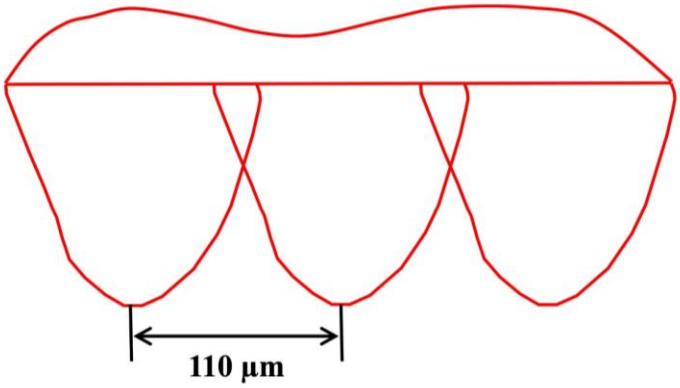

(a)

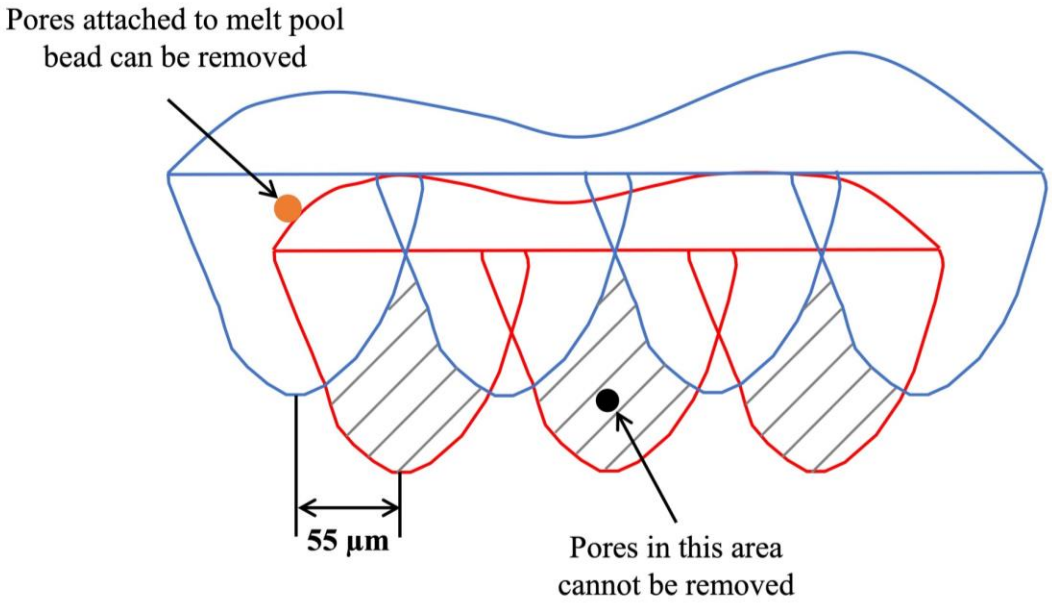

(b)

Figure 3.25: Schematic of the Melt Pool Cross Section Overlap Between Neighboring Tracks and Layers above: (a) between Neighboring Tracks; (b) between Layers

4.0 Path Planning Design

In this chapter, laser scanning path optimization method is proposed to tailor the scanning orientation for continuous scanning path and island scanning strategy. Formulations of the optimizations and full sensitivity analysis will be presented, respectively. The feasibility and effectiveness of the proposed method for island scanning pattern is demonstrated by experiments conducted on AconityONE L-PBF machine.

4.1 Continuous Scanning Path Design

4.1.1 Modified Inherent Strain Method

Although the mechanism of residual stress and distortion in laser powder AM process has been extensively studied through numerical simulations in micro-scale [4, 5, 7, 8], there is still a large gap between these finite element models and part scale AM part prediction. For example, a full-scale thermomechanical simulation for a large EBM part consisting of 107 layers takes 15 hours to complete by running the Pan Computing software [11], which is one of the fastest commercial software packages with well-developed numerical techniques. Because of the high computational expense, full-scale simulation for metal AM part residual distortion and stress prediction is impractical, particularly for gradient-based iterative optimization.

To address this issue, the inherent strain method is adopted as an alternative solution. The inherent strain method was originally introduced by Ueda to simulate conventional welding

decades ago [95]. The basic theory of this method is that residual distortion and stress are the result of incompatible internal strains, such as plastic, elastic and phase transformation strains. After the welding is completed, elastic strain is fully relaxed and thus the inherent strain equals the plastic strain generated in the welding process [96-99].

Unlike welding problems that only have single or a few welds, a metal part produced by AM utilizing a high energy source consists of thousands of layers and also thousands of scan lines in each layer. Boundary conditions in the process simulation dynamically evolve in a thermomechanical analysis. Hence, elastic strains due to thermal expansion mismatch cannot be fully released as in welding problems. Considering this new phenomenon in AM, Liang et al [79, 80] proposed a modified inherent strain model to predict residual stress and distortion at the part scale. The proposed model allows for extraction of accurate inherent strains directly from results of high-fidelity microscale detailed process simulation by solving the transient thermomechanical problem. As shown in these previous works, the inherent strains are anisotropic with respect to the scanning direction due to the non-uniform heat transfer caused by the moving heat source. In general, the inherent strain along the scan direction is compressive with the largest amplitude among the three normal strain components. The inherent strain transverse to the scan direction is also compressive but with a smaller amplitude, while that in the build direction is tensile due to the Poisson effect. This scanning orientation dependency in the inherent strains is the reason why changing the scanning path in the AM process has a significant effect on the residual stress and strain distribution.

After the scanning orientation-dependent inherent strains are computed from the elastic and plastic strain histories obtained, they are being treated as thermal strains on the AM part in a series of layer-by-layer static equilibrium analysis. To carry out the inherent strain-based analysis

in commercial finite element software, the scanning orientation-dependent thermal strains are inputted as the thermal expansion coefficients, and a unit temperature rise is applied to carry out the analysis. Due to its high efficiency, inherent strain based AM process simulation has drawn increasing attention from academia [16, 100, 101] and industry. Most of the commercial AM process simulation packages, such as Simufact (MSC), Amphyon, Pan Computing (AutoDesk) and 3DSim (ANSYS), have adopted the inherent strain method in their software. Unfortunately, as these software packages are proprietary, the detailed theory and algorithm employed in the software packages are not available to the general public.

In this work, scanning orientation-dependent inherent strain vector based on Ref. [102] is employed to approximate the thermal loading introduced in the metal AM process. In every iteration step, the nodal load vector of an element is given as:

$$\mathbf{f_e^{th}} = \int_{\Omega_e} \mathbf{B_e^T} \cdot \mathbf{C_e} \cdot \boldsymbol{\varepsilon}^{\mathbf{in}}(\theta_e)\Delta T \mathrm{d}\Omega \tag{4.1}$$

where $\mathbf{f_e^{th}}$ is the nodal vector of element e, $\mathbf{B_e^T}$ is the strain-displacement matrix, $\mathbf{C_e}$ is the element elasticity matrix, $\boldsymbol{\varepsilon}^{\mathbf{in}}(\theta_e)$ is the inherent strain vector as a function of the element scanning orientation θ_e, which can be obtained from the level set function. By rotating the local inherent strain vector, the inherent strains in the global coordinate system corresponding to different scanning angle can be computed.

4.1.2 Problem Formulation

The level set method is a mathematical framework developed by Osher and Sethian for implicit moving interface analysis and tracking [103]. This implicit representation can easily find if a point is inside or outside the boundary profile, and is a powerful tool for any physics-driven

boundary evolution problem. Wang et al [104] and Allaire et al [105] developed the structural topology optimization method with level set method, which has the advantages of clear-cut interface representation and accessible high-order boundary information. As a mainstream topology optimization method, level set method has further successful applications for complex design problems, such as multi-material design [106-109], manufacturing cost [110] and feature insertion [111, 112].

Here, we focus on evolving the continuous scanning paths with level set method subject to a pre-defined part geometry, and hence, the problem formulation is similar to that for topology optimization. Beyond scanning path optimization, concurrent design that optimizes structure and scanning path simultaneously will be explored. Therefore, we will have the design domain (D) and material domain (Ω) definitions in the problem formulation for consistency, even though the part geometry would not change when only optimizing scanning path. The level set function is defined by Eq. (4.2) to interpolate the design domain. A positive level set value indicates solid domain, negative value represents void, and zero-value contour represents a boundary:

$$\begin{cases} \Phi(\mathbf{X}) > 0, & \mathbf{X} \in \Omega/\partial\Omega \\ \Phi(\mathbf{X}) = 0, & \mathbf{X} \in \partial\Omega \\ \Phi(\mathbf{X}) < 0, & \mathbf{X} \in D/\Omega \end{cases} \tag{4.2}$$

Then, the part will be sliced into N layers, each of which is coupled with one level set function for scanning path and another for the well-defined geometry:

$$\mathbf{\Phi}^{\mathbf{scan}} = [\phi^{scan,1} \quad \phi^{scan,2} \quad \cdots \quad \phi^{scan,n}] \tag{4.3}$$

$$\mathbf{\Phi}^{\mathbf{geo}} = [\phi^{geo,1} \quad \phi^{geo,2} \quad \cdots \quad \phi^{geo,n}] \tag{4.4}$$

Then, scanning path profile update will be identical to that in level set topology optimization. Updating velocities are derived from sensitivity analysis and the scanning paths are updated by solving the Hamilton-Jacobi equation through the standard up-wind scheme:

$$\phi_t + V_N|\nabla\phi| = 0 \tag{4.5}$$

where V_N is the boundary velocity along the normal direction.

Beyond continuity, another advantage of using level set method for scanning path optimization is that $\phi^{scan,k}$ is a signed distance function ($|\nabla\phi| = 1$), so that scanning paths can be trivially obtained by extracting iso-value level set contours. A constant interval value will be employed between any pair of adjacent level set contours, and this value would just be set equal to the hatch spacing for the laser scanning paths. Therefore, reinitialization is incorporated in each iteration step to keep the signed distance property. The reinitialization is performed through fast marching method proposed by Sethian [113, 114], as shown below:

$$\phi_t + S(\phi)\cdot(\nabla\phi - 1) = 0 \tag{4.6}$$

where $S(\phi)$ is a sign function taken as 1 when $\phi > 0$, -1 when $\phi < 0$, and 0 on the boundary. In the fast marching method, it is formulated as:

$$S(\phi) = \frac{\phi}{\sqrt{\phi^2 + |\nabla\phi|^2\Delta x}} \tag{4.7}$$

Compliance Minimization: In this sub-section, thermomechanical loading induced by laser melting will be modified through laser scanning path optimization for stiffness improvement, i.e. reducing compliance and residual deformation by optimizing the scanning paths. The problem is formulated as below:

$$min.\ \ J = \sum_{k=1}^{N}\left[\int_{D_k}\mathbf{D_k}\mathbf{e}(\mathbf{u_k})\mathbf{e}(\mathbf{u_k})H(\phi^{geo,k})d\Omega\right] \tag{4.8}$$

$$s.t.\ a(\mathbf{u},\mathbf{v},\mathbf{\Phi^{geo}}) = l(\mathbf{v},\mathbf{\Phi^{geo}}),\quad \forall\mathbf{v}\in\mathbf{U_{ad}}$$

$$where.\ a(\mathbf{u},\mathbf{v},\mathbf{\Phi^{geo}}) = \sum_{k=1}^{N}\int_{D_k}\mathbf{D_k}\mathbf{e}(\mathbf{u_k})\mathbf{e}(\mathbf{v_k})H(\phi^{geo,k})d\Omega$$

$$l(\mathbf{v},\mathbf{\Phi^{geo}}) = \sum_{k=1}^{N}\int_{D_k}\mathbf{D_k}\mathbf{e}\left(\mathbf{u^{in}}\left(\boldsymbol{\theta}^{\mathbf{k}}\right)\right)\mathbf{e}(\mathbf{v_k})\,H(\phi^{geo,k})d\Omega$$

where $\mathbf{u_k}$ and $\mathbf{v_k}$ are the deformation vector and test vector of the k^{th} building layer, $\boldsymbol{\theta}^{\mathbf{k}}$ is the scanning orientation vector of k^{th} building layer and $\mathbf{e}\left(\mathbf{u}^{\mathbf{in}}\left(\boldsymbol{\theta}^{\mathbf{k}}\right)\right)$ is the deposition orientation-dependent inherent strain vector. In this formulation, each printing layer is defined by a single level set function, and we assume N layers in total are involved. Next, the geometry is defined by Φ^{geo} and the Heaviside function is used to project the material domain. Here, Φ^{geo} is involved in this problem formulation for potential extension to concurrent design problems (simultaneous design of scanning path and part geometry). Note that, each level set function can represent a group of consecutive deposition layers in order to reduce computational expense, but the tradeoff is that the inter-layer scanning effect on inherent strain between deposition layers within the group is not taken into account.

To solve this optimization problem, the Lagrangian of the objective function is defined as:

$$L = J + a(\mathbf{u}, \mathbf{w}, \boldsymbol{\Phi}^{\mathbf{geo}}) - l(\mathbf{w}, \boldsymbol{\Phi}^{\mathbf{geo}}) \tag{4.9}$$

where $\mathbf{w}$ is the Lagrangian multiplier of the state equation, also known as adjoint variable. Compliance minimization can be categorized as self-adjoint problem which satisfies that $\mathbf{w_k} = -2\mathbf{u_k}$.

Then, the derivative of the Langrangian is:

$$L' = 2\sum_{k=1}^{N}\int_{D_k}\mathbf{D_k}\mathbf{e}\left(\mathbf{u}^{\mathbf{in}}\left(\boldsymbol{\theta}^{\mathbf{k}}\right)\right)'\mathbf{e}(\mathbf{u_k})\,H(\phi^{geo,k})\,d\Omega \tag{4.10}$$

The derivative term of the inherent strain, $\mathbf{e}\left(\mathbf{u}^{\mathbf{in}}\left(\boldsymbol{\theta}^{\mathbf{k}}\right)\right)'$ could be rewritten as:

$$\mathbf{e}\left(\mathbf{u}^{\mathbf{in}}\left(\boldsymbol{\theta}^{\mathbf{k}}\right)\right)' = \frac{\partial\boldsymbol{\varepsilon}^{\mathbf{in,k}}}{\partial\boldsymbol{\theta}^{\mathbf{k}}}\frac{\partial\boldsymbol{\theta}^{\mathbf{k}}}{\partial\phi^{scan,k}}\frac{\partial\phi^{scan,k}}{\partial t} \tag{4.11}$$

The expression for θ^k is defined as:

$$\boldsymbol{\theta}^{\mathbf{k}} = \frac{\pi}{2} + \arctan\left(\frac{\partial\phi^{scan,k}/\partial \mathrm{y}}{\partial\phi^{scan,k}/\partial \mathrm{y}}\right) \tag{4.12}$$

Specifically, for node(i,j,k), the scanning orientation, $\theta_{i,j}^{k}$ is derived using the central difference scheme:

$$\theta_{i,j}^{k} = \frac{\pi}{2} + \arctan\left(\frac{\phi_{i,j+1}^{scan,k} - \phi_{i,j-1}^{scan,k}}{\phi_{i+1,j}^{scan,k} - \phi_{i-1,j}^{scan,k}}\right) \tag{4.13}$$

Therefore, derivative of the inherent strains is expressed as:

$$\begin{aligned}\mathbf{e}\left(\mathbf{u}_{\mathbf{i,j}}^{\mathbf{in}}(\boldsymbol{\theta}^{\mathbf{k}})\right)' = {} & \frac{\partial \boldsymbol{\varepsilon}_{\mathbf{i,j}}^{\mathbf{in,k}}}{\partial \theta_{i,j}^{k}} \frac{\partial \theta_{i,j}^{k}}{\partial \phi_{i-1,j}^{scan,k}} \frac{\partial \phi_{i-1,j}^{scan,k}}{\partial t} + \frac{\partial \boldsymbol{\varepsilon}_{\mathbf{i,j}}^{\mathbf{in,k}}}{\partial \theta_{i,j}^{k}} \frac{\partial \theta_{i,j}^{k}}{\partial \phi_{i+1,j}^{scan,k}} \frac{\partial \phi_{i+1,j}^{scan,k}}{\partial t} \\ & + \frac{\partial \boldsymbol{\varepsilon}_{\mathbf{i,j}}^{\mathbf{in,k}}}{\partial \theta_{i,j}^{k}} \frac{\partial \theta_{i,j}^{k}}{\partial \phi_{i,j-1}^{scan,k}} \frac{\partial \phi_{i,j-1}^{scan,k}}{\partial t} + \frac{\partial \boldsymbol{\varepsilon}_{\mathbf{i,j}}^{\mathbf{in,k}}}{\partial \theta_{i,j}^{k}} \frac{\partial \theta_{i,j}^{k}}{\partial \phi_{i,j+1}^{scan,k}} \frac{\partial \phi_{i,j+1}^{scan,k}}{\partial t}\end{aligned} \tag{4.14}$$

Collecting all the terms containing $\frac{\partial \phi_{i,j}^{scan,k}}{\partial t}$, the scanning path level set function updated velocity at node (i,j,k) can be derived:

$$\begin{aligned}V_{N\,i,j}^{scan,k} = 2\Bigg\{ & \mathbf{D_k}\mathbf{e}\left(\mathbf{u}_{\mathbf{i-1,j}}^{\mathbf{k}}\right) \frac{\partial \boldsymbol{\varepsilon}_{\mathbf{i-1,j}}^{\mathbf{in,k}}}{\partial \theta_{i-1,j}^{k}} \frac{\partial \theta_{i-1,j}^{k}}{\partial \phi_{i,j}^{scan,k}} H\left(\phi_{i-1,j}^{scan,k}\right) \\ & + \mathbf{D_k}\mathbf{e}\left(\mathbf{u}_{\mathbf{i+1,j}}^{\mathbf{k}}\right) \frac{\partial \boldsymbol{\varepsilon}_{\mathbf{i+1,j}}^{\mathbf{in,k}}}{\partial \theta_{i+1,j}^{k}} \frac{\partial \theta_{i+1,j}^{k}}{\partial \phi_{i,j}^{scan,k}} H\left(\phi_{i+1,j}^{scan,k}\right) \\ & + \mathbf{D_k}\mathbf{e}\left(\mathbf{u}_{\mathbf{i,j-1}}^{\mathbf{k}}\right) \frac{\partial \boldsymbol{\varepsilon}_{\mathbf{i,j-1}}^{\mathbf{in,k}}}{\partial \theta_{i,j-1}^{k}} \frac{\partial \theta_{i,j-1}^{k}}{\partial \phi_{i,j}^{scan,k}} H\left(\phi_{i,j-1}^{scan,k}\right) \\ & + \mathbf{D_k}\mathbf{e}\left(\mathbf{u}_{\mathbf{i,j+1}}^{\mathbf{k}}\right) \frac{\partial \boldsymbol{\varepsilon}_{\mathbf{i,j+1}}^{\mathbf{in,k}}}{\partial \theta_{i,j+1}^{k}} \frac{\partial \theta_{i,j+1}^{k}}{\partial \phi_{i,j}^{scan,k}} H\left(\phi_{i,j+1}^{scan,k}\right)\Bigg\}\end{aligned} \tag{4.15}$$

Stress Minimization: The potential of laser deposition path optimization in minimizing residual stress is explored as well. Stress concentration can be mitigated and consequently prevent cracking and delamination during AM processing. To achieve this, the maximum von Mises stress

within the AM part should be decreased by optimizing the scanning path. However, the simple maximum function is not smooth and differentiable and cannot be applied directly to gradient-based optimization. The p-norm function [115, 116], an alternative formulation for maximum stress approximation in stress-based topology optimization, is adopted in this framework as:

$$\sigma_{PN} = \left(\sum_{e=1}^{N} \sigma_e^P\right)^{\frac{1}{P}} \tag{4.16}$$

where σ_{PN} is the p-norm stress, σ_e is the element stress, N is the total element number, and P is the stress norm parameter. When $P \to \infty, \sigma_{PN} \to \max(\sigma_e)$ without smoothness; when $P \to 1$, σ_{PN} is the average stress of the design domain. It is noted that for stress minimization problem of interest in this work, the stress norm parameter P is not as critical as in stress constrained problems, since it is sufficient for the p-norm stress to capture the trend of the global maximum stress rather than having an accurate approximation [115]. In this work, the value of the stress norm parameter P is taken as 8 in the stress minimization problem.

Stress at the element centroid is selected as the average element stress σ_e in computing the element von Mises stress. The residual stress minimization problem is formulated as:

$$min.\, \sigma_{PN} = \left[\sum_{k=1}^{n} \int_{D_k} \sigma_{von}^P \, H(\phi^{geo,k}) d\Omega\right]^{\frac{1}{P}} \tag{4.17}$$

$$s.t.\, a(\mathbf{u}, \mathbf{v}, \mathbf{\Phi}^{\mathbf{geo}}) = l(\mathbf{v}, \mathbf{\Phi}^{\mathbf{geo}}), \quad \forall \mathbf{v} \in \mathbf{U_{ad}}$$

The derivative of the above Lagrangian is shown below:

$$L' = -\sum_{k=1}^{n} \int_{D_k} \mathbf{D_k e}\left(\mathbf{u^{in}}(\theta^k)'\right) \mathbf{e}(\mathbf{w_k}) H(\phi^{geo,k}) d\Omega \tag{4.18}$$

where the adjoint variable $\mathbf{w_k}$ can be obtained by solving the following adjoint equation:

$$\sum_{k=1}^{n}\int_{D_k}\mathbf{D_k}\mathbf{e}(\mathbf{u_k'})\mathbf{e}(\mathbf{w_k})\,H(\phi^{geo,k})d\Omega+\left[\sum_{k=1}^{n}\int_{D_k}\sigma_{von}^{P}\,H(\phi^{geo,k})d\Omega\right]^{\frac{1}{P}-1}$$

$$\cdot\left[\sum_{k=1}^{n}\int_{D_k}\sigma_{von}^{P-1}\cdot\sigma_{von}'\,H(\phi^{geo,k})d\Omega\right]=0$$

(4.19)

Expanding all the inherent strain derivative terms $\mathbf{e}(\mathbf{u^{in}}(\theta^k)')$ in the Lagrangian**,** and collecting all the terms containing $\frac{\partial\phi_{i,j}^{scan,k}}{\partial t}$, the sensitivity at node(i,j,k), namely the level set function updated velocity along the normal direction can be derived:

$$V_{N}{}_{i,j}^{scan,k}=\left\{\mathbf{e}\left(\mathbf{w_{k,i-1,j}}\right)'\ \mathbf{D_k}\frac{\partial\boldsymbol{\varepsilon}_{\mathbf{i-1,j}}^{\mathbf{in,k}}}{\partial\theta_{i-1,j}^{k}}\cdot\frac{\partial\theta_{i-1,j}^{k}}{\partial\phi_{i,j}^{scan,k}}\cdot\frac{\partial\phi_{i,j}^{scan,k}}{\partial t}+\mathbf{e}\left(\mathbf{w_{k,i+1,j}}\right)'\ \mathbf{D_k}\frac{\partial\boldsymbol{\varepsilon}_{\mathbf{i+1,j}}^{\mathbf{in,k}}}{\partial\theta_{i+1,j}^{k}}\cdot\frac{\partial\theta_{i+1,j}^{k}}{\partial\phi_{i,j}^{scan,k}}\right.$$

$$\cdot\frac{\partial\phi_{i,j}^{scan,k}}{\partial t}+\mathbf{e}\left(\mathbf{w_{k,i,j-1}}\right)'\ \mathbf{D_k}\frac{\partial\boldsymbol{\varepsilon}_{\mathbf{i,j-1}}^{\mathbf{in,k}}}{\partial\theta_{i,j-1}^{k}}\cdot\frac{\partial\theta_{i,j-1}^{k}}{\partial\phi_{i,j}^{scan,k}}\cdot\frac{\partial\phi_{i,j}^{scan,k}}{\partial t}$$

$$\left.+\mathbf{e}\left(\mathbf{w_{k,i,j+1}}\right)'\ \mathbf{D_k}\frac{\partial\boldsymbol{\varepsilon}_{\mathbf{i,j+1}}^{\mathbf{in,k}}}{\partial\theta_{i,j+1}^{k}}\cdot\frac{\partial\theta_{i,j+1}^{k}}{\partial\phi_{i,j}^{scan,k}}\cdot\frac{\partial\phi_{i,j}^{scan,k}}{\partial t}\right\}$$

(4.20)

4.1.3 Adaptive Level Set Adjustment (ALSA)

Signed distance function is a fundamental feature of the level set method. It ensures the easiness and effectiveness of the numerical contour evolution. Importantly for this research, continuous scanning paths with consistent gaps (i.e. hatching space) can be trivially derived by extracting the iso-level set contours. Therefore, reinitialization, which adjusts the level set function based on the interface $(\phi=0)$, is implemented in each iteration step to enforce the updated level

set function to be a signed-distance field. However, one issue occurs due to reintialization and should be carefully addressed to ensure the proper convergence. Specifically, the velocity field, as derived in Eq. (4.15) and (4.16), is defined inside the entire material domain, and the whole level set field can be accordingly updated by solving the Hamilton-Jacobi equation. At this point, the Lagrangian is strictly decreasing with appropriate step size. However, reinitialization has to be performed following the design update to ensure a signed distance field, so that level set values in areas away from the interface will be altered. The impact of these changes is hard to evaluate and it is possible that the Lagrangian will increase. Conventionally in topology optimization, it is common to neglect the impact of these changes, and many cases of successful convergence have been witnessed, especially for compliance minimization problems [62, 63]. This is because, in topology optimization, the zero-value level set contour is the boundary between solid and void and its movement also changes the material layout. However, for the scanning path optimization, the zero level set contour does not represent the structure boundary; instead, it only represents one of the scanning lines and only the relevant scanning orientation affects the stress and deformation. The shrinkage of zero level set contour and decreasing perimeter is undesirable since the zero level set contour is the only effective updating scanning line while all the other scanning lines follow the shape of the zero level set contour because of the reinitialization. Therefore, maintaining as longer zero level set contour as possible motivates the development of the adaptive level set adjustment (ALSA) strategy. Similarly, over-expansion of the zero level set contour is also undesirable since all zero level set contour moves towards outside of the design domain, which may finally leave no zero contour inside the design domain for effective design update. Specifically in ALSA, what we are adjusting is only the level set values of the contours while not the shape of the contours. Therefore, the finite difference method-based local scanning direction

calculation would not be affected, so that the inherent strain-based finite element analysis result would be identical before and after adaptive change of the level set field.

In this work, a numerical strategy called the "adaptive level set adjustment" (ALSA) is proposed to reduce the potential negative impact, instead of just neglecting it. Using this technique, good convergence for complex continuous path optimization problems have been realized for both compliance- and stress-minimization problems. The basic idea of the ALSA strategy is to keep as much zero level set contour as possible inside the design domain during the entire optimization process, because the zero level set contour would not be affected by reinitialization. In fact, in some of the runs, we have observed that the zero level set contour keeps shrinking, which finally occupies a very small portion of the design domain and leads the optimization problem fails to converge in this situation. To remedy this issue, the ALSA adjusts the zero level set contour iteratively with Eq. (4.21):

$$\phi^{scan,k} = \begin{cases} \phi^{scan,k} - \alpha \cdot \phi_{max}^{scan,k}, & S_+ > S_- \\ \phi^{scan,k} - \alpha \cdot \phi_{min}^{scan,k}, & S_+ < S_- \end{cases} \tag{4.21}$$

where $\phi_{max}^{scan,k}$ is the maximum level set nodal value in layer k, $\phi_{min}^{scan,k}$ is the minimum nodal value, S_+ is the area of positive level set field, S_- is the area of negative level set field, and α $(0 < \alpha < 1)$ is the coefficient for level set function adjustment.

The physical meaning of ALSA is that the level set function is iteratively adjusted to equalize the positive-signed area and the negative-signed area, which in most cases could function to give a longer zero level set contour while not perturbing the scanning path field. While with ALSA, the zero level set interface will be dynamically adjusted to prevent this type of over-shrinking situation. Figure 1 illustrates an example to show the effectiveness of applying the ALSA strategy. As shown in Fig. 34(a), the initial scanning path is designed to have as longer zero level set contour as possible, so that to ensure effective and efficient design update. As discussed before,

only the boundary update is effective, thus only the sensitivities near the zero level set contour are calculated and shown in this case. After 20 iterations, Fig. 34(b) still holds a large area of zero level set interface by employing the ALSA strategy. In contrast, as shown in Fig. 34(c), the level set field moves outward and the zero-value interface keeps shrinking to very small closed contours without ALSA. Then, the design update effect of the later is quite questionable.

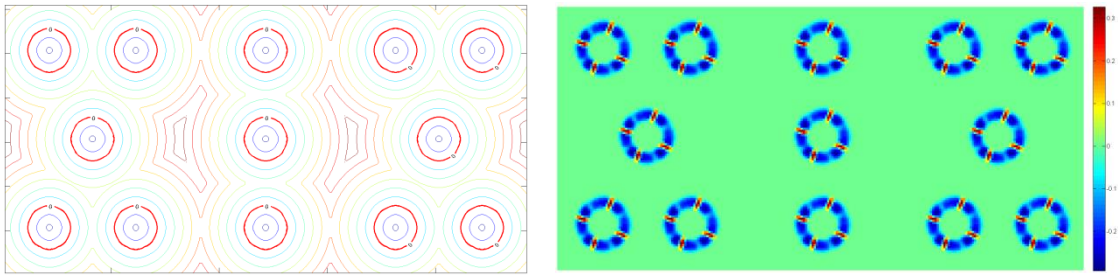

(a)

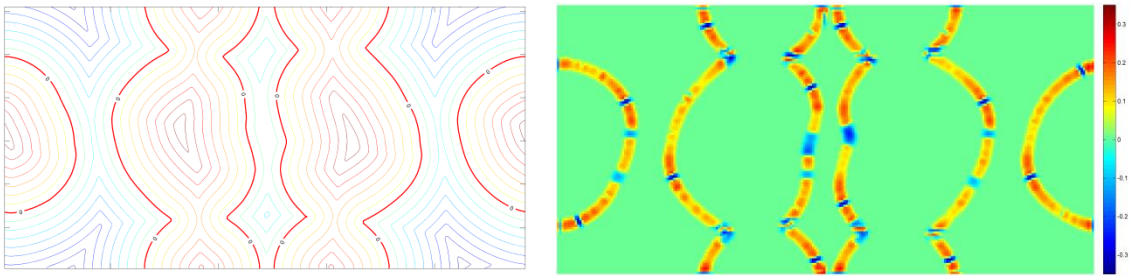

(b)

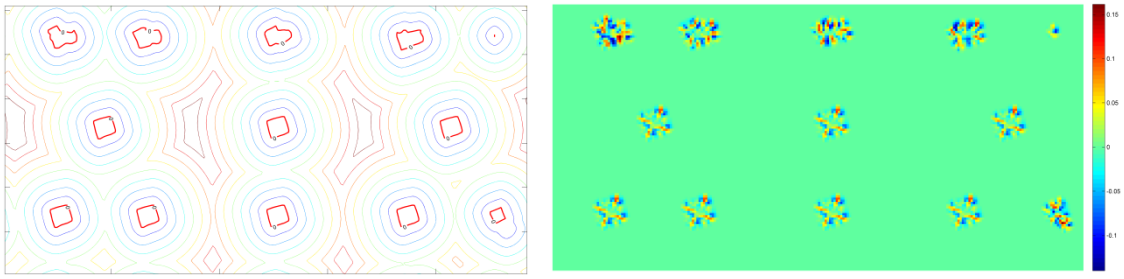

(c)

Figure 4.1: Sensitivity distribution: (a) Initial scanning path setup; (b) with ALSA; (c) without ALSA .

4.1.4 Numerical Examples: Compliance Minimization

In this section, the proposed algorithm will be demonstrated using a few numerical examples to prove its effectiveness. In all of the following numerical examples, we assume the material has a Young's modulus of 2,100 and Poisson's ratio of 0.3. All the design domains are discretized by 1×1×1 eight-node hexahedron mesh with 24 DoFs.

Case 1: The first case is compliance minimization of an L-bracket structure. The dimension and finite element mesh of the L-bracket is shown in Figure. 4.2(a). There are a total of four bundled printing layers, and the bottom nodes are fixed on the build plate. The scanning orientation-dependent inherent strain vector of [-0.0145, -0.0065, 0.012] is applied as the loading. The initial scanning path setup before optimization is shown in Figure. 4.2 (b), where the thermal loading induced compliance is 1,147.

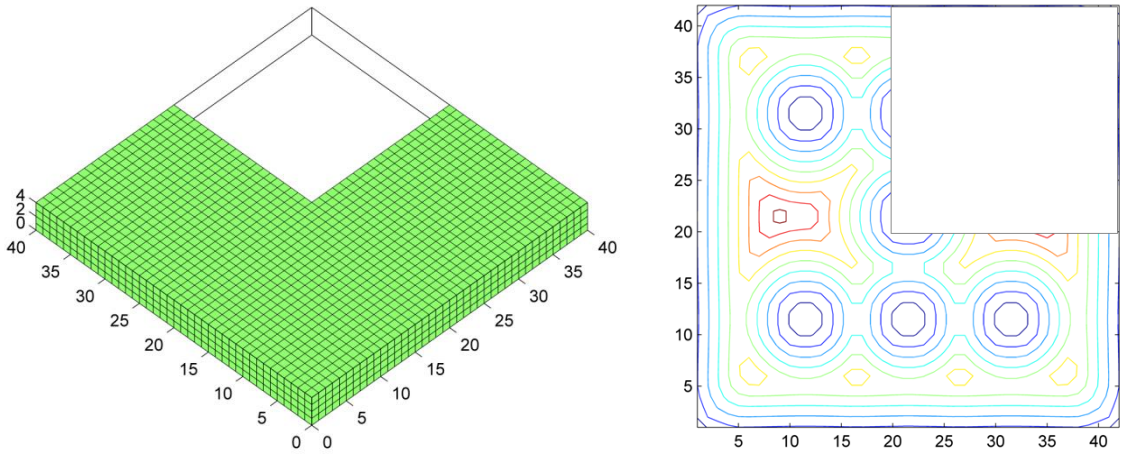

(a) (b)

Figure 4.2: Initial setup of the L-bracket optimization (Compliance 1,147): (a) Finite Element Model of the L-bracket; (b) Initial Scanning Path of Each Layer.

The optimized scanning path of each layer is presented in Figure. 4.3. Compared with the previous optimized scanning path by either experiment or simulation, this scanning path is irregular and counter-intuitive. The convergence history is shown in Figure. 4.4. The structural compliance is reduced by 15.4% (from 1,147 to 970) after optimization.

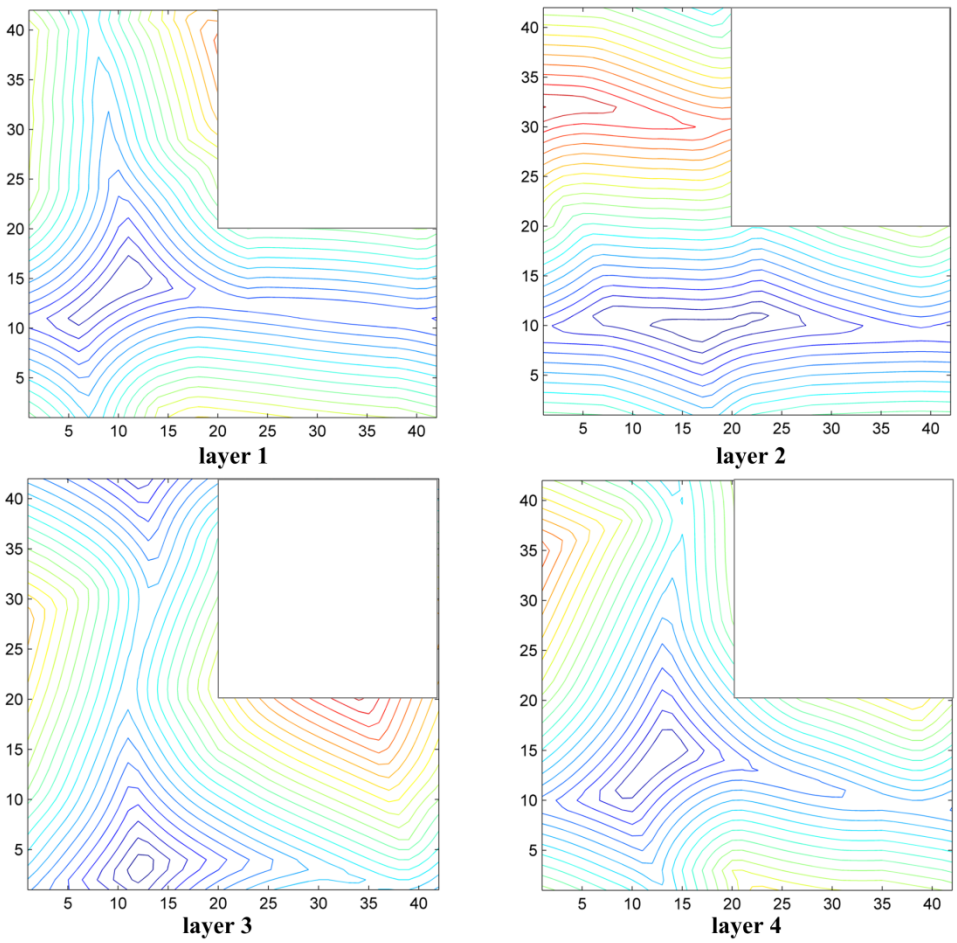

Figure 4.3: Layer-wise Deposition Optimization Results for L-bracket

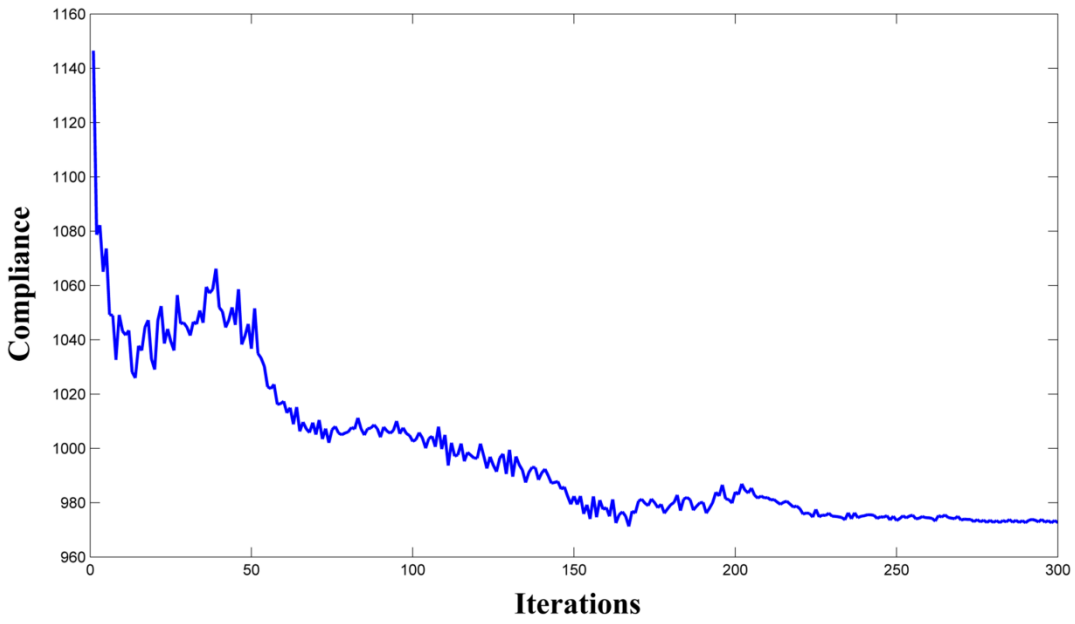

Figure 4.4: Convergence History of the L-bracket Compliance Minimization Case

Case 2: The third compliance minimization case is on a bearing bracket consisting of 35 layers as shown in Figure. 4.5(a). The same inherent strain vector and the same type of initial scanning path is utilized as shown in Figure. 4.5(b).

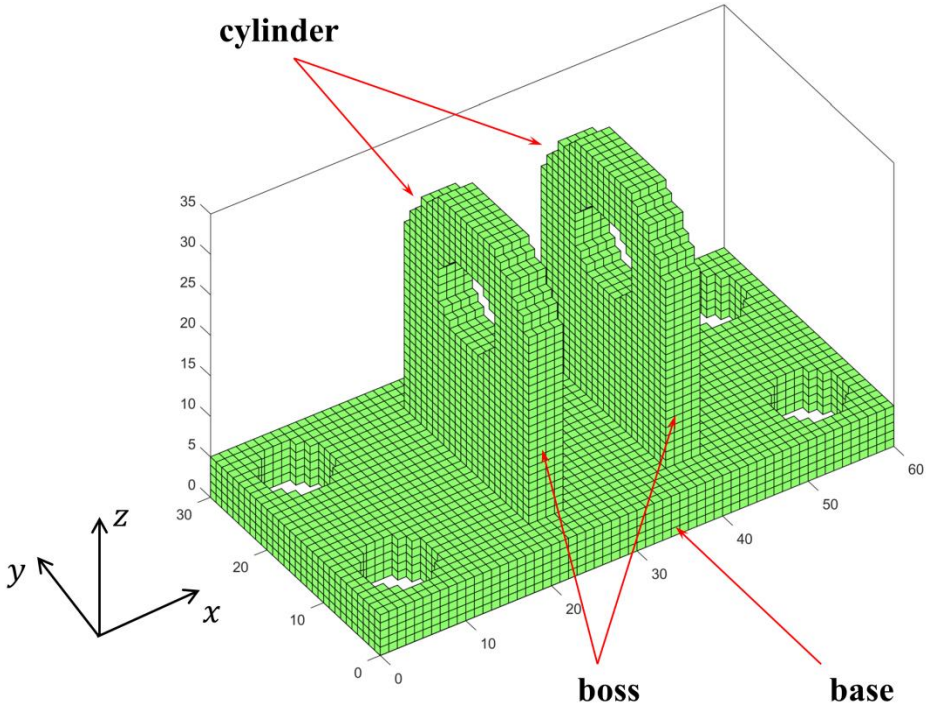

(a) Finite element model of the bearing bracket

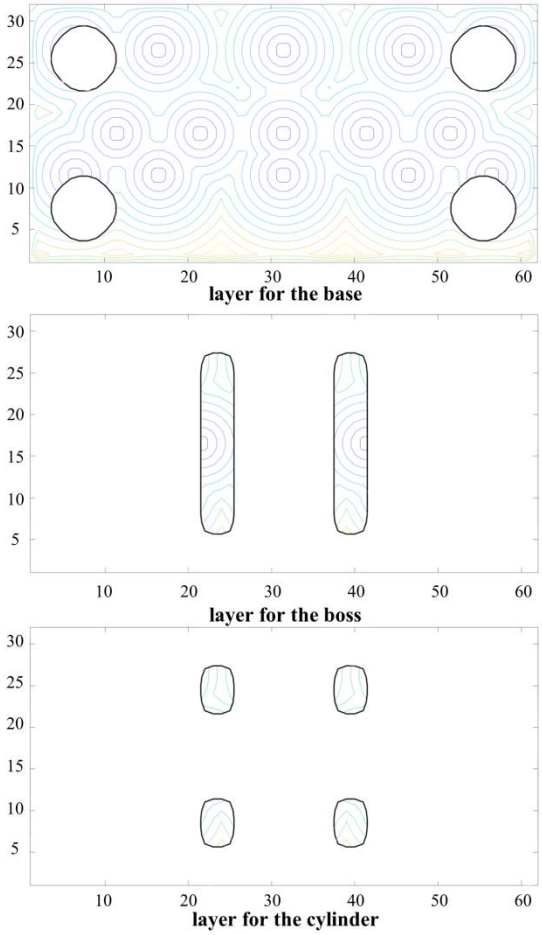

(b) Initial scanning path of each component

Figure 4.5: Initial Setup of the Bearing Bracket Optimization (Compliance 5,267)

The optimization converges with 100 iterations. The compliance has reduced from 5,267 to 4,633. The optimized scanning paths patterns for layer 1, 5, 11, 22, 30 and 34 are presented in Figure. 4.6. Repeated scanning pattern is not found among the layers. The comparison with initial scanning path indicates that the scanning pattern of each layer is optimized to achieve an optimized optimal solution after exploring the design space. The convergence history is summarized in Figure. 4.7.

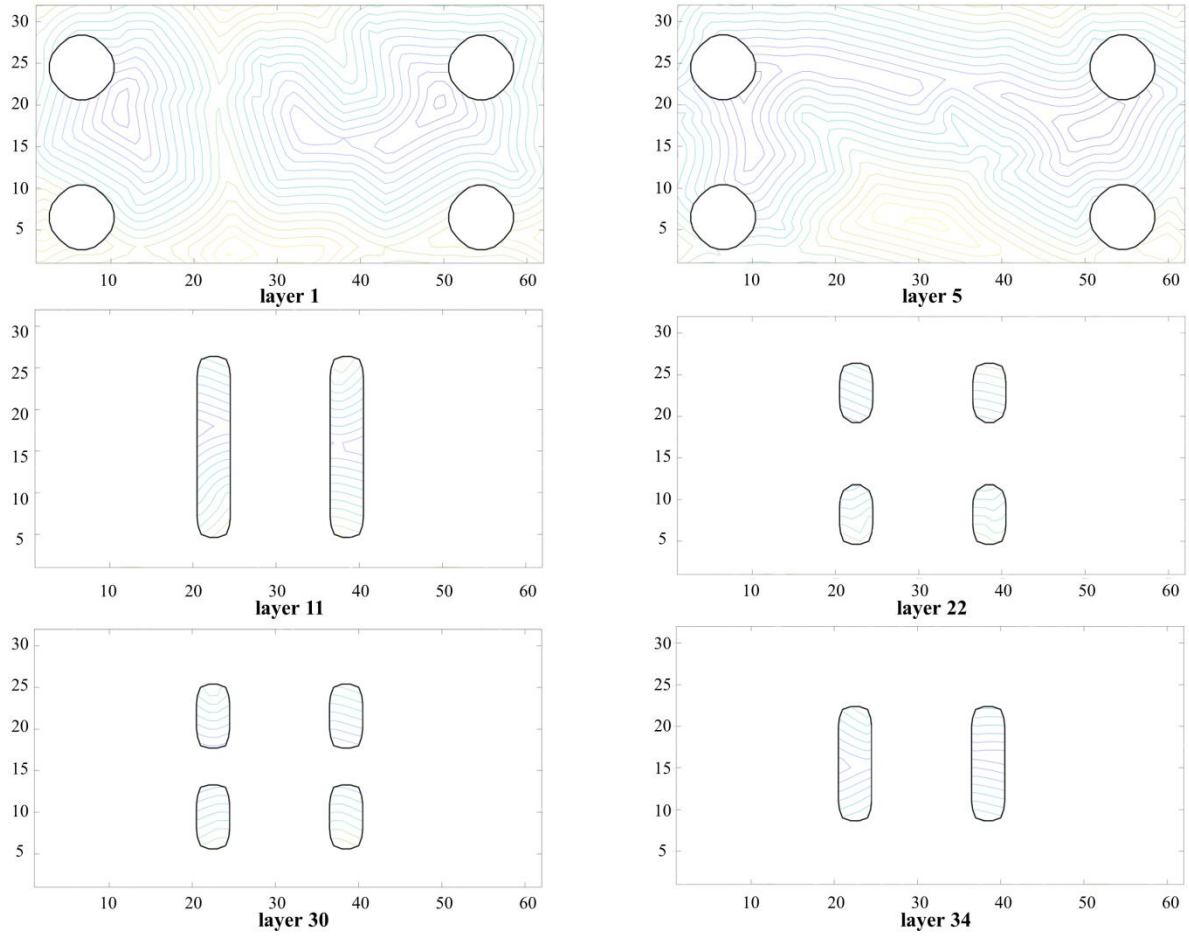

Figure 4.6: Layer-wise Scanning Path after Optimization for the Bearing Bracket

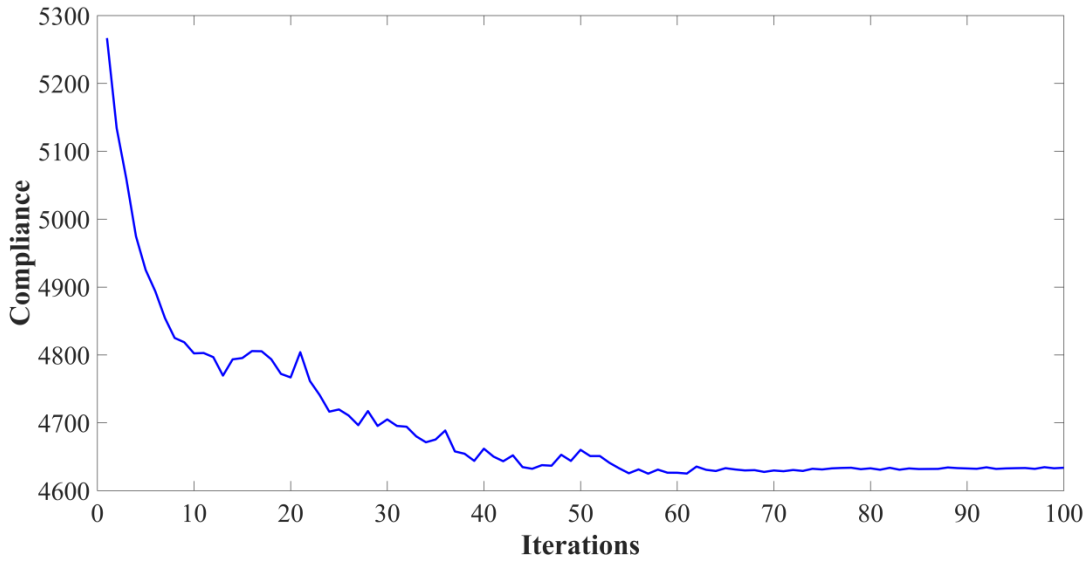

Figure 4.7: Convergence History of the Bearing Bracket Case

4.1.5 Numerical Example: Stress Minimization

Case 3: The case of stress minimization is performed on the 4-layer block with internal holes. The optimized laser scanning path is shown in Figure 4.8. Convergence histories of both the p-norm stress and maximum von Mises stress are summarized in Figure 4.9, wherein the p-norm stress decreases from 78.0 to 71.7 in 100 iterations. Because of the non-linearity and localized behavior, the maximum von Mises stress oscillates and decreases from the initial value 67.6 to 61.2.

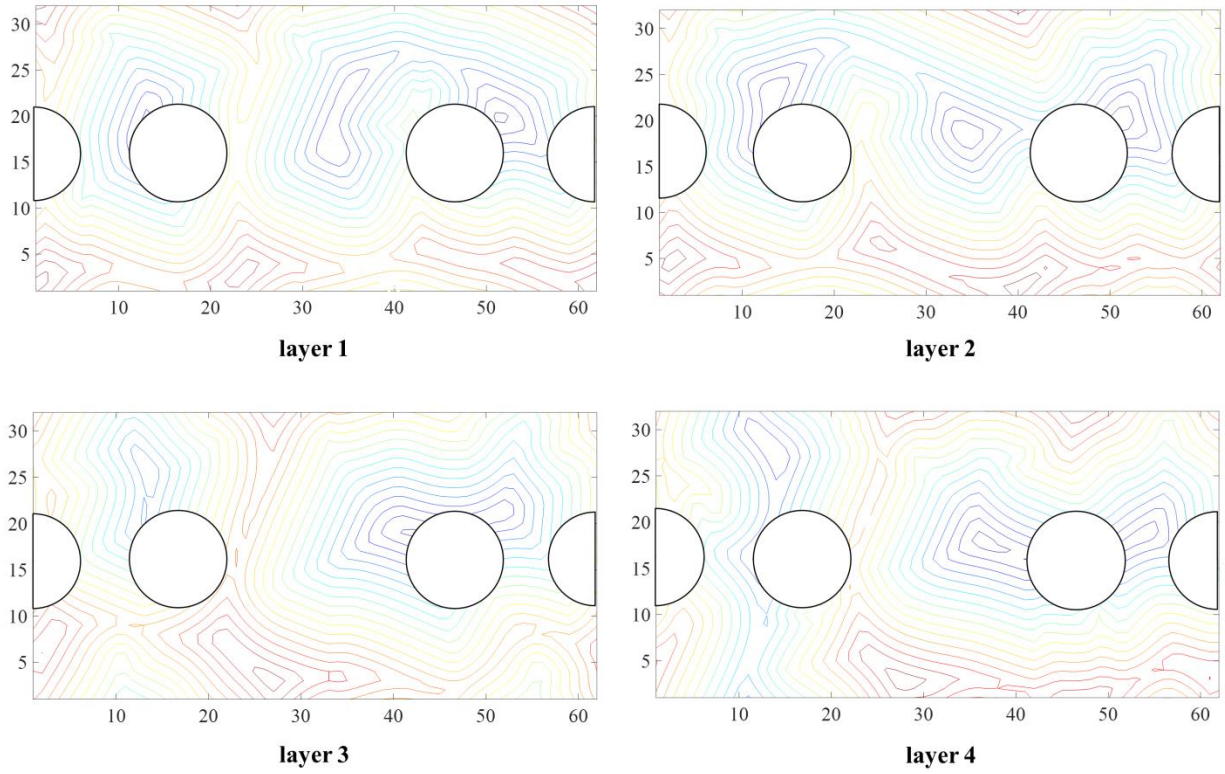

Figure 4.8: Layer-wise Scanning Path after Optimization for the Block Case

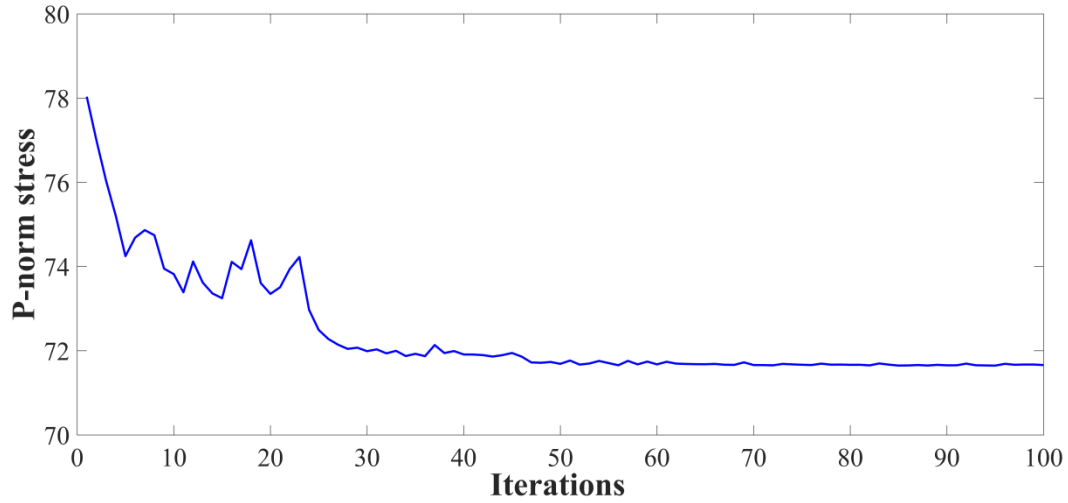

(a) p-norm stress

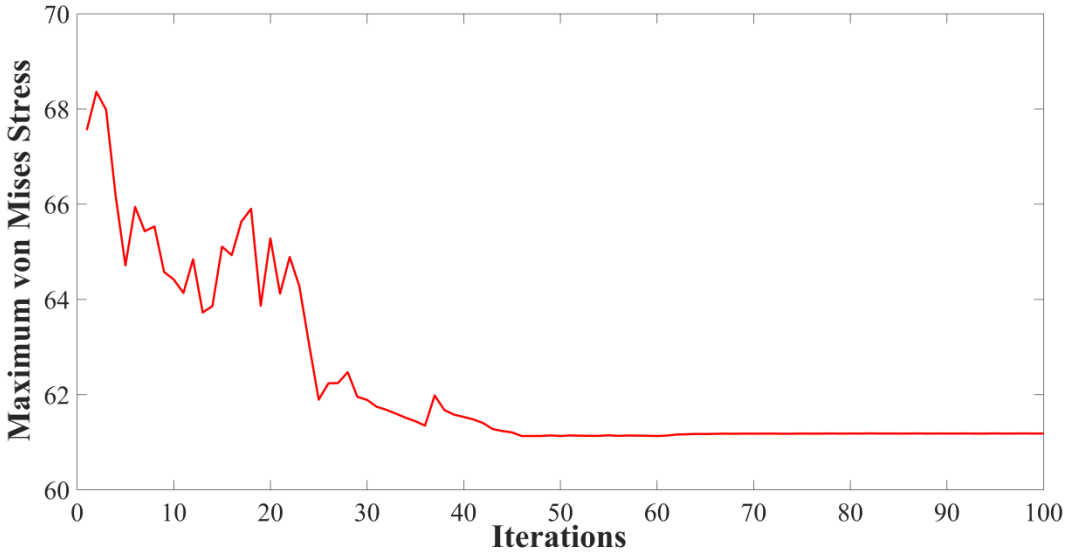

(b) maximum von Mises stress

Figure 4.9: Convergence History of the Block with Internal Holes Stress Minimization Case

Comparison of the stress distribution before and after optimization is shown in Figure 4.10. It can be seen that the stress concentration along the block edges has been evidently mitigated, and we can visibly observe the global stress reduction. Therefore, the effectiveness of scanning path optimization for stress minimization is proved in this case.

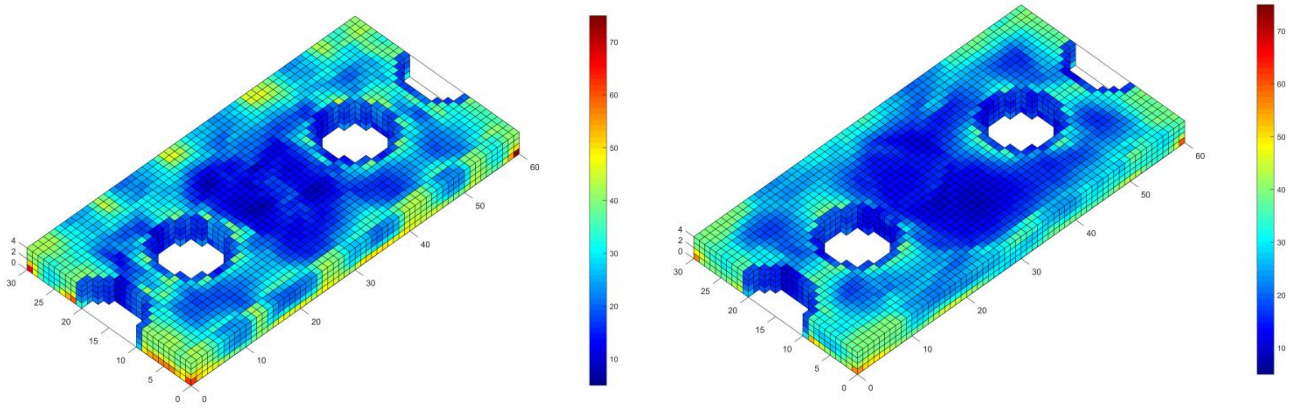

(a) (b)

Figure 4.10: Comparison of Stress Distribution: (a) Before and (b) After Optimization

4.2 Island Scanning Pattern Design

4.2.1 Reformulation of Governing Equations

In this study, elastic finite element analysis with multiple time steps is conducted to compute the part deformation after building and the subsequent cutting off. As shown in Figure 4.11, the part is built on the building platform and sliced into n layers which are activated layer-by-layer from the bottom to top layers. When the building is done, part of the first layer is cut off the large building platform for stress relief and forms a cantilever beam with upward bending shape. Therefore, the finite element analysis for deformation prediction has $n + 1$ time steps totally and the equilibrium equations corresponding to the activation from layer 1 to n are:

$$\mathbf{K}_1\mathbf{U}_1 = \mathbf{f}_1 \tag{4.22.1}$$

$$\mathbf{K}_2\mathbf{U}_2 = \mathbf{K}_1\mathbf{U}_1 + (\mathbf{K}_2 - \mathbf{K}_1)\mathbf{U}_1 + \mathbf{f}_2 \tag{4.22.2}$$

…… ⋮

$$\mathbf{K}_n\mathbf{U}_n = \mathbf{K}_{n-1}\mathbf{U}_{n-1} + (\mathbf{K}_n - \mathbf{K}_{n-1})\mathbf{U}_{n-1} + \mathbf{f}_n \tag{4.22.3}$$

where $\mathbf{K}$, $\mathbf{U}$ and $\mathbf{f}$ are the stiffness matrix, the displacement vector and the force vector associated with scanning orientation dependent inherent strain vector. On the right-hand-side of equations (4.22.2) and (4.22.3), the second term is the load increment through activation which can keep the displacement not changed when activating the new layer; $\mathbf{f}_{\boldsymbol{k}}$ is the force vector when building layer k and can be expressed as a function of inherent strain vector:

$$\mathbf{f}_{\boldsymbol{k}} = \sum_{i \in ele\_act_k} \int_{\Omega_i} \mathbf{B}_\mathbf{e}^\mathbf{T} \mathbf{C} \boldsymbol{\varepsilon}(\theta_i)\, d\Omega \tag{4.23}$$

where $\mathbf{B}_\mathbf{e}^\mathbf{T}$ is the strain-displacement matrix, $\mathbf{C}$ is the element elasticity matrix, $\boldsymbol{\varepsilon}(\theta_i)$ is the inherent strain vector as a function of scanning orientation. In this work, we assume only the strain components within xy plane are dependent on the scanning orientation while the strain vector along the building direction ε_z is constant. According to the classic solid mechanics theory, the plane strain transformation with respect to θ is performed as following:

$$\varepsilon_{xx}(\theta) = \frac{\varepsilon_x + \varepsilon_y}{2} + \frac{\varepsilon_x - \varepsilon_y}{2} cos(2\theta) + \varepsilon_{xy} sin(2\theta) \tag{4.23.1}$$

$$\varepsilon_{yy}(\theta) = \frac{\varepsilon_x + \varepsilon_y}{2} - \frac{\varepsilon_x - \varepsilon_y}{2} cos(2\theta) - \varepsilon_{xy} sin(2\theta) \tag{4.23.2}$$

$$\varepsilon_{xy}(\theta) = -\frac{\varepsilon_x - \varepsilon_y}{2} sin(2\theta) + \varepsilon_{xy} cos(2\theta) \tag{4.23.3}$$

The equilibrium equation at time step $n+1$ corresponding to the cutting off at last time step is:

$$(\mathbf{K}_n - \Delta\mathbf{K}_{cut})\mathbf{U}_{n+1} = \mathbf{K}_n\mathbf{U}_n - \sum_{i \in ele\_cut} \int_{\Omega_i} \mathbf{B}_\mathbf{e}^\mathbf{T} \mathbf{C} \boldsymbol{\varepsilon}(\theta_i)\, d\Omega \tag{4.24}$$

where $\Delta\mathbf{K}_{cut}$ is the assembled stiffness matrix corresponding to elements which are removed in the last time step. It should be noted that on the right-hand-side of Eq. (4.24), the thermal loading vector of these removed elements is subtracted as well.

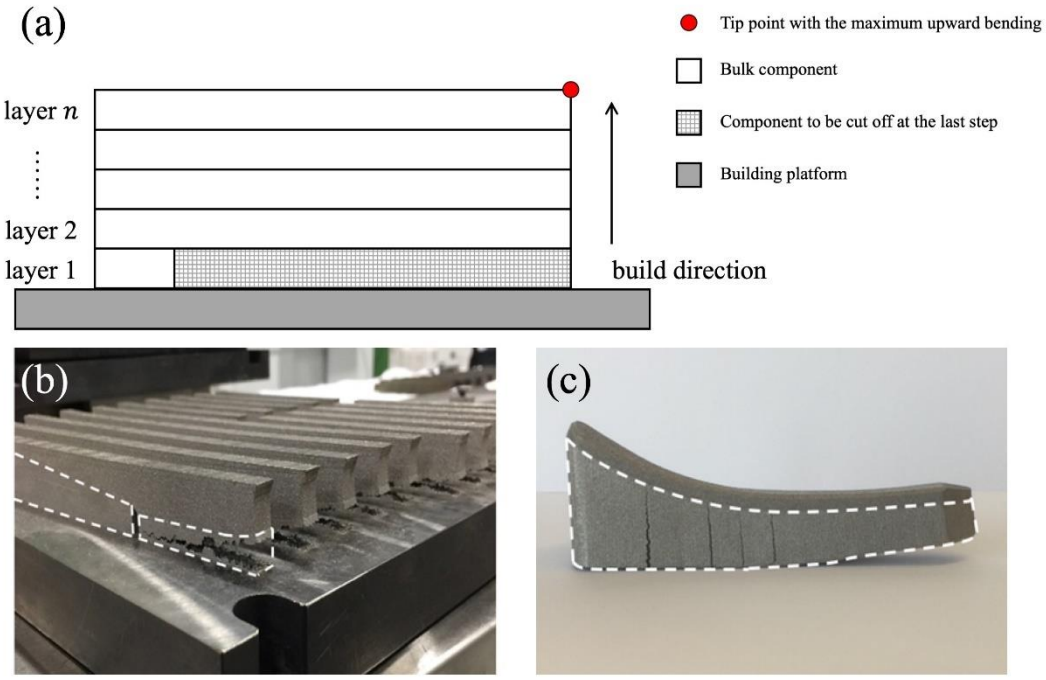

Figure 4.11: (a) Layer-by-layer Building and Subsequent Cutting off Diagram; (b-c) Large Deformation before and after Cutting off the Building Platform[101]

For the ease of sensitivity analysis in Section 4.2.3, the above governing equations in Eqs. (4.22) and (4.24) are reformulated in a more generic format:

$$\mathbf{A}_i\mathbf{U}_i + \mathbf{B}_i\Delta\mathbf{U}_{i-1} = \mathbf{f}_i, i = 1,2,\cdots n+1 \tag{4.25}$$

where $\Delta\mathbf{U}_i = \mathbf{U}_i - \mathbf{U}_{i-1}$ and $\mathbf{U}_0 = \mathbf{0}$, $\mathbf{B}_i = \mathbf{K}_i$ and $\mathbf{B}_{n+1} = \mathbf{K}_n$, $\mathbf{A}_i$ is in the form of:

$$\mathbf{A}_i = \begin{cases} -\Delta\mathbf{K}_{cut}, & i = n+1 \\ \mathbf{0}, & otherwise \end{cases} \tag{4.26}$$

4.2.2 Problem Formulation

After partially cutting the part off the building platform, a cantilever beam forms and the part would bend upward where the tip point as indicated in Figure 4.12 would have the largest deformation. The goal of scanning pattern design is to minimize the upward bending after stress relief and therefore, we pick the displacement along building direction (z) of the tip point as objective function and the optimization is mathematically formulated as:

$$min. U_{n+1}^{m} \tag{4.27}$$

$$w.r.t\ \boldsymbol{\theta}$$

$$s.t. \mathbf{A}_i \mathbf{U}_i + \mathbf{B}_i \Delta \mathbf{U}_{i-1} = \mathbf{f}_i, i = 1,2,\cdots,n+1 \tag{4.28}$$

where U_{n+1}^{m} is the displacement along building direction of the selected tip point at the last time step $n+1$, m is corresponding degree of freedom (DOF) number. The design variables are the orientation of scanning path in each island. It is worth to emphasize that the in the optimization, it is the island scanning orientation to be updated instead of the element. Each island usually has several elements and the thermal loading applied to is identical. The displacement vector has to satisfy the formulated equilibrium equations discussed in Section 4.2.1 where the force vector is a function of the design variables.

4.2.3 Sequential Sensitivity Analysis

Sequential sensitivity analysis is performed in this section to obtain the sensitivities in order to update the design variables of the above formulated optimization. The Lagrangian is obtained from Eqs. (4.27) and (4.28) and defined as follows:

$$L = U_{n+1}^{m} + \sum_{i=1}^{n+1} \boldsymbol{\lambda_i}^{\boldsymbol{T}} (\mathbf{A}_i \mathbf{U}_i + \mathbf{B}_i \Delta \mathbf{U}_{i-1} - \mathbf{f}_i) \tag{4.29}$$

Where the first term is the displacement along building direction (z) of the picked tip point; $\boldsymbol{\lambda_i}$ is the adjoint variable vector for step i; The second term of the Lagrangian is the summation of multiplication of equilibrium equation and corresponding adjoint variable at each time step.

Based on the chain rule, the derivative of the Lagrangian with respect to any design variable θ_k is obtained:

$$\frac{\partial L}{\partial \theta_k} = \frac{\partial U_{n+1}^m}{\partial \theta_k} + \sum_{i=1}^{n+1} \boldsymbol{\lambda_i}^{\boldsymbol{T}} \left(\mathbf{A}_i \frac{\partial \mathbf{U}_i}{\partial \theta_k} + \mathbf{B}_i \frac{\partial \Delta \mathbf{U}_{i-1}}{\partial \theta_k} - \frac{\partial \mathbf{f}_i}{\partial \theta_k} \right) \tag{4.30}$$

The first term on the right-hand-side of the above equation can be rewritten as:

$$\frac{\partial U_{N+1}^m}{\partial \theta_k} = [0 \quad \cdots \quad 0 \quad 1 \quad 0 \quad \cdots \quad 0] \frac{\partial \mathbf{U}_{N+1}}{\partial \theta_k} = \mathbf{H}_{n+1} \frac{\partial \mathbf{U}_{N+1}}{\partial \theta_k} \tag{4.31}$$

where the $\mathbf{H}_{n+1}$ is a sparse vector and only the m^{th} entry corresponding to the picked DOF is one. For the term associated with $\mathbf{B}_i \frac{\partial \Delta \mathbf{U}_{i-1}}{\partial \theta_k}$ in Eq. (4.30), recall that $\Delta \mathbf{U}_i = \mathbf{U}_i - \mathbf{U}_{i-1}$ and $\sum_{i=1}^{n} \Delta u_i v_i = u_{n+1} v_{n+1} - u_1 v_1 - \sum_{i=1}^{n} u_{i+1} \Delta v_i$, so we can expand the all the terms as:

$$\sum_{i=1}^{N+1} \boldsymbol{\lambda_i}^{\boldsymbol{T}} \mathbf{B}_i \frac{\partial \Delta \mathbf{U}_{i-1}}{\partial \theta_k} = \boldsymbol{\lambda_{N+2}}^{\boldsymbol{T}} \mathbf{B}_{N+2} \frac{\partial U_{N+1}}{\partial \theta_k} - \boldsymbol{\lambda_1}^{\boldsymbol{T}} \mathbf{B}_1 \frac{\partial U_0}{\partial \theta_k} - \sum_{i=1}^{N+1} \left(\Delta \boldsymbol{\lambda_i}^{\boldsymbol{T}} \mathbf{B}_{i+1} + \boldsymbol{\lambda_i}^{\boldsymbol{T}} \Delta \mathbf{B}_i \right) \frac{\partial U_i}{\partial \theta_k} \tag{4.32}$$

According to Eqs. (4.30-4.32) and collecting the terms containing $\frac{\partial U_i}{\partial \theta_k}$, the adjoint variable vectors $\boldsymbol{\lambda_i}$ can be obtained by solving the following adjoint equations in a reverse direction from $n+1$ to 1:

$$\mathbf{H}_{n+1} + \boldsymbol{\lambda}_{N+1}{}^{T} (\mathbf{A}_{N+1} + \mathbf{B}_{N+1}) = \mathbf{0} \tag{4.33}$$

$$\boldsymbol{\lambda}_i{}^{T} (\mathbf{A}_i + \mathbf{B}_i) = \boldsymbol{\lambda}_{i+1}{}^{T} \mathbf{B}_{i+1}, i = N, N-1, \cdots 1 \tag{4.34}$$

Finally, the sensitivity, the derivative of the Lagrangian can be obtained:

$$\frac{\partial L}{\partial \theta_k} = -\sum_{i=1}^{N+1} \boldsymbol{\lambda}_i{}^{T} \frac{\partial \mathbf{f}_i}{\partial \theta_k} \tag{4.35}$$

4.2.4 Implementation Steps

The flowchart of the island scanning pattern design method proposed in this study is summarized in Figure 4.12. For any given geometry, the original CAD file is imported and the scanning pattern will then be designed in the following key steps:

- **Voxelization:** In Step 2, voxels are employed in this work to compute part deformation for the sake of mesh generation and computation efficiency. In voxelization, part of the local features of the imported geometry is lost but will be compensated when reconstructing the build path in Step 5.
- **Island discretization:** In Step 3, the voxels generated in the last step is sliced into layers by the building layer thickness; each layer is then discretized into islands of 5mm × 5mm square. The inherent strain vectors for elements in the same island are identical since the scanning track orientations are the same.
- **Scanning path optimization:** In Step 4, the design variable, scanning orientation of each island is updated iteratively until converging. In every iteration, finite element analysis with multiple time steps is conducted to compute part deformation firstly and then sensitivities analysis discussed in Section 4.2.3 is performed. All the element sensitivities in the same island will be grouped together and then update the scanning orientation of each island.
- **Build path reconstruction:** In Step 5, scanning tracks within each island are determined by the optimized scanning orientation, local features and hatching space. Part resolution is partially lost after voxelization in finite element analysis, build path reconstruction can make compensation and reserve all the features in real building process.

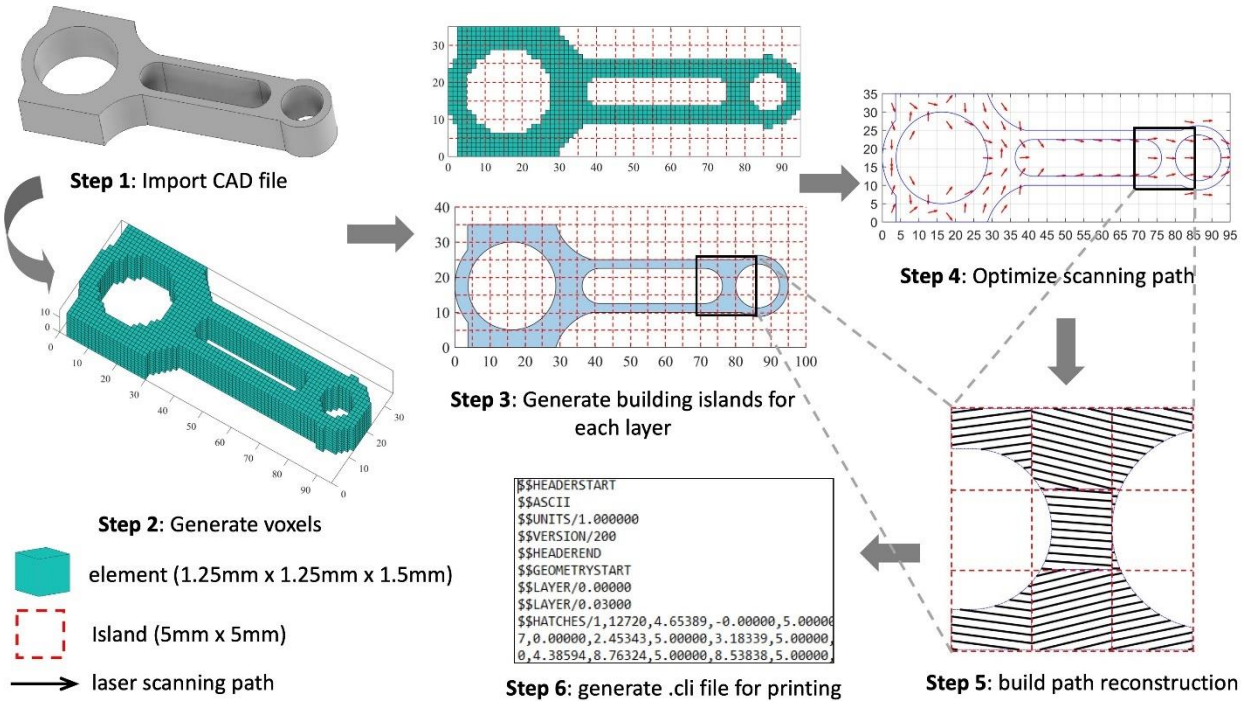

Figure 4.12: Flowchart of Island Scanning Pattern Design

4.2.5 Numerical Examples and Experimental Setup

In this section, the scanning patterns for a block structure and a connecting rod are designed following the proposed method procedure in Figure 4.12. The effectiveness of this method on deformation reduction is experimentally validated. The scanning pattern design including voxelization, finite element and sensitivity analysis, design variable update, build path reconstruction and generating building files is implemented using Matlab R2019a. All the parts with initial and designed scanning pattern are fabricated by Aconity One at University of Texas at El Paso. The material used in the design and building is Ti6Al4V, which has Young's modulus of 104 GPa and Poisson's ratio of 0.34. The layer thickness in the building is 30 μm while in the design 50 physical layers are merged as one layer. The hatch spacing is 100 μm. The power is 250 W and the scan speed is 1200 mm/s.

Experimental Setup: The part manufacturing is performed on an AconityONE L-PBF system (Aconity3D, Aechen, Germany) equipped with a 1kW Yb fiber laser (IPG Photonics, Oxford, MA, USA) and galvanometer scanning via 3D scanning optics (Raylase AxialScan-30, Wessling, Germany). The focused spot size, $d4\sigma$ is 59μm ± 5μm measured with a Beam Watch AM (Ophir-Spricon, LLC, North Logan, UT, USA). The 3D scanning optics allows for programmable beam defocus to alter the spot size at the build plate. The feature is set to 2mm defocus for production of the plates resulting in $d4\sigma \sim 80\mu m$. The Oxygen is continuously monitored during the building and maintained below 500 ppm. Chamber pressure is maintained at 45 mbar, and an inert gas consumption is <2.5 L/min during the build. The layer thickness is 30 μm with a dosing factor of 1.8 which means the supply platform moves upward by 54 μm each layer. Powder spreading is performed with dual carbon fiber bushes attached to a rigid carrier with a 200 mm/s deposition velocity. All builds are performed with a nominal cross flow set pint at 95% of blower motor capacity with parts scanned closed to the exhaust and working towards the gas cross flow to minimize scanning of splatter. The processing parameters for the building of block structure and connecting rod are summarized in Table 4.1.

Table 4.1: Processing Parameters of AconityOne LPBF Systems for Part Fabrication

Processing parameters	Values (units)
Island size	5 mm
Stripe overlap	0 mm
Skywriting	Yes
Power	250 W
Scan speed	1200 mm/s
Defocus	-2 mm
Spot size	0.08 mm
Hatch spacing	0.1 mm

Block Structure: The first case is a rectangle block structure and the dimension of the block is $100 \times 50 \times 15$ mm^3. In the scan pattern optimization, 50 physical layers are merged to

save computation cost and the element size used in this case is $5 \times 5 \times 1.5$ mm^3. In this case, the element size is identical to the island. The finite element of the block is shown in Figure 4.13(a) which has 2,000 elements and 2,541 nodes. For each layer, the initial scan pattern is the same and as shown Figure 4.13(b). Each island is filled with bi-directional hatch lines (0° and 180°) along the block long edge. After optimizing the scan pattern of each island, i.e., the hatch line direction, the maximum bending after partially cutting off at the tip point as indicated Figure 4.13(a) is reduced.

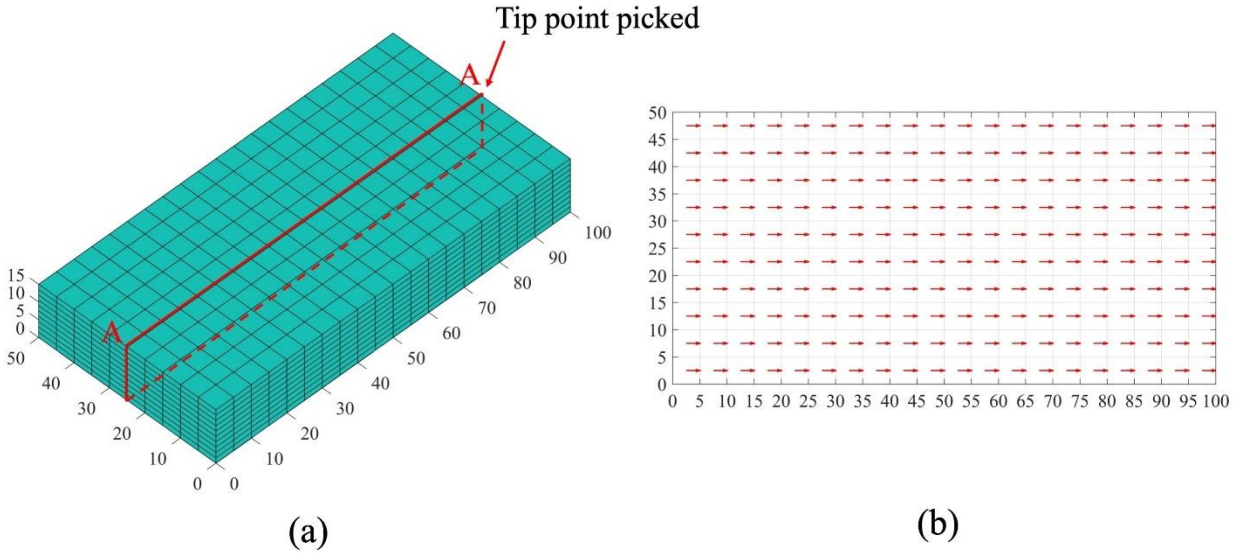

Figure 4.13: (a) Finite element model of the block structure; (b) Initial scan pattern for each layer.

The optimization results are presented in Figure 4.14 including the deformation profile after cutting off before and after scan pattern optimization, optimized layer-wise scan pattern and the convergence history of the object function. As Shown in Figure 4.14(a), the upward bending after partially cut off from the first layer is reduced significantly by optimizing the scan pattern for the block. The upward deformation along the center line after cutting off is plotted in Figure 4.14(b). The deformation of the picked tip point on the top surface along the mid line is 8.354 mm before optimization and is reduced to 5.551 mm after optimization. The layer-wise scan pattern is

presented in Figure 4.14(c). It can be found the global trend of optimized scan pattern direction is vertical, i.e., along the short edge of the block except the first layer. Since the block is partially cut from the substrate and only four islands along the long edge are kept, those islands cut off, as indicated in the blue dashed line box, have two different parts in sensitivity analysis to update the island scan direction. For the sensitivities of these islands, the first contribution is from the first step to build the first layer, and the second part is from the last time step for cutting off. The reason for the optimized scan pattern from layer 2 to layer 10 is that, the deformation is caused by the anisotropic shrinkage of material which shrink more along the beam moving direction and less along the transverse direction. With the initial scan pattern, the inherent strain vector applied is (-0.02, -0.01, 0.015) and the principal shrinkage direction is along the long edge direction which leads to large upward bending. After optimization, the global scan direction is almost vertical and makes the shrinkage along long edge smaller.

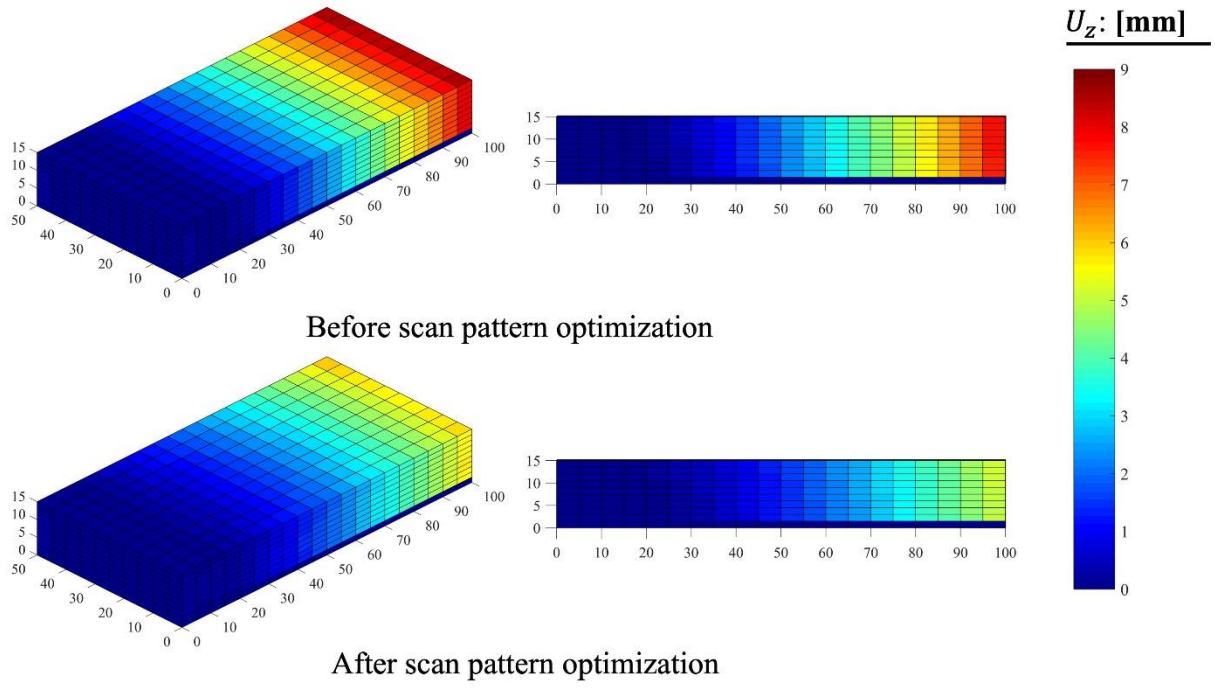

(a)

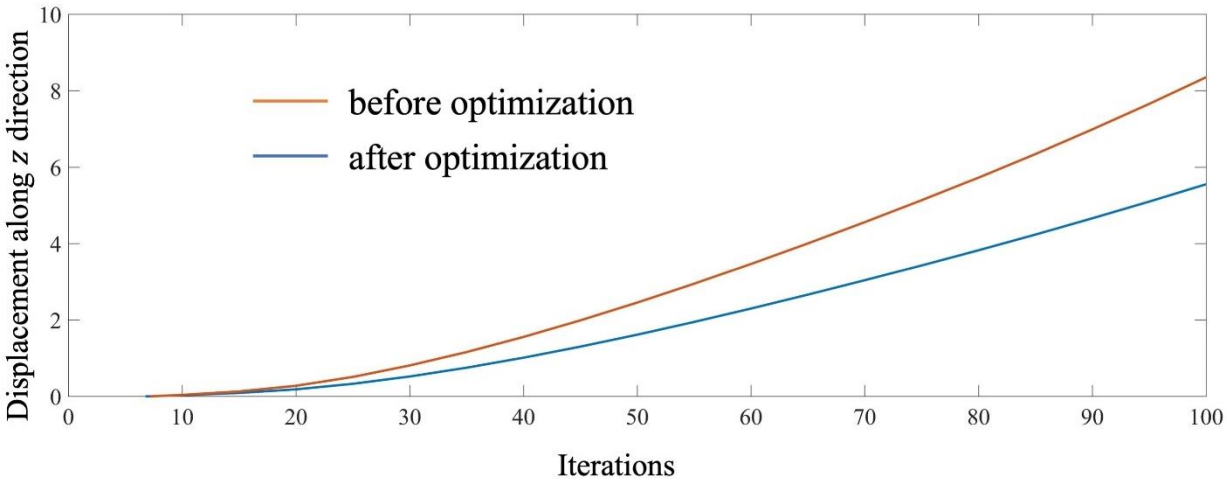
Displacement along z direction
Iterations
before optimization
after optimization
0
2
4
6
8
10
0
10
20
30
40
50
60
70
80
90
100

(b)

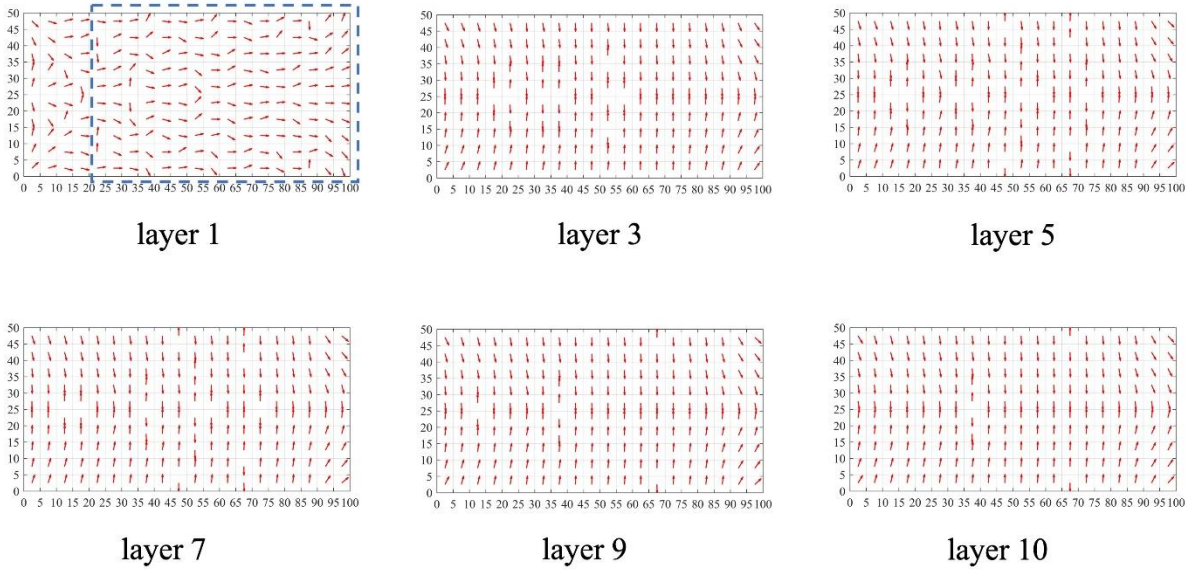
layer 1
layer 3
layer 5
layer 7
layer 9
layer 10

(c)

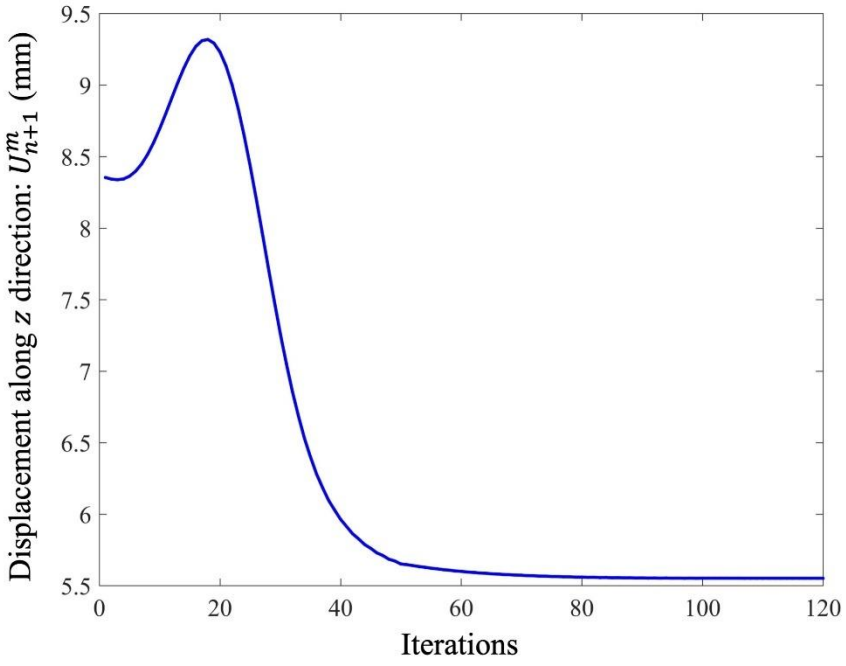

(d)

Figure 4.14: Optimized results for the block structure: (a) Deformation Profile after Cutting off; (b) Displacement along the Center Line on the Top Surface; (c) Layer-wise Optimized Scan Pattern; (d) Convergence History.

To evaluate the performance of optimized scan pattern, the same block structures were built on the same building platform by the initial scan pattern as indicated in Figure 4.13(b) and designed scan pattern in Figure 4.14(c) for deformation measurement and comparison. As shown in Figure 4.15, the as-built parts were partially cut from the platform (20mm along the long edge is kept) by the electron discharge machine (EDM), at the height of 1.5 mm, which equals to the element height. After stress relief, the deformation profile of two parts was measured by Faro Laser ScanArm made by Faro Technologies. Further comparison between the original CAD file and measured deformation after cutting off was made by Geomagic Control X made by 3dSystems.

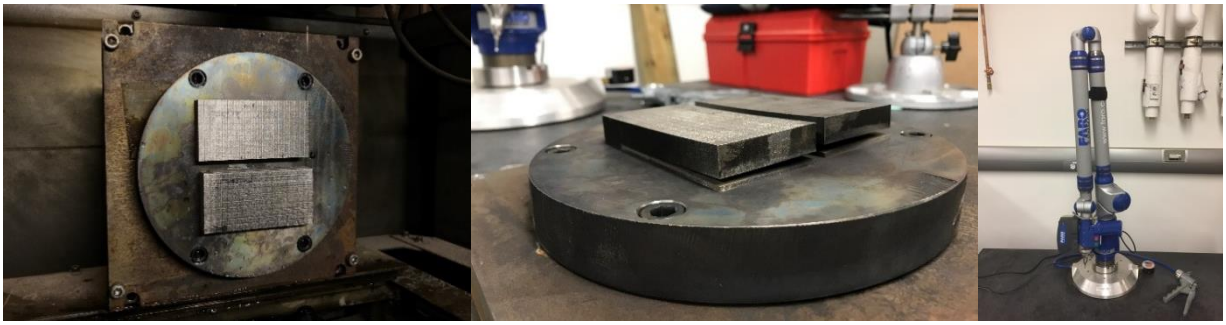

(a) (b) (c)

Figure 4.15: As-built block: (a) before and (b) after Optimization; (c) Faro Laser ScanArm V3 for Distortion Measurement;

Figure 4.16(a) presents the experimental measurement results for the blocks built by the initial and optimized scan pattern after cutting off, respectively. It can be found that both parts exhibit upward bending and have larger deformation near the left short top edge. The block with optimized scan pattern has smaller deformation than the block with initial scan pattern. Figure 4.16(b) presents the comparison of deformation along the center line of the top surface, as indicated by the black dashed line in Figure 4.16(a). The maximum deformation at the tip point is 3.170 mm for the block with initial scan pattern, and is 2.428 mm with the optimized scan pattern. This demonstrates the proposed scan pattern design method can significantly reduce the residual deformation (i.e., 23.41%) for this case. It should be emphasized here that the experimentally measured residual deformation value is smaller than the prediction value in optimization. This deformation overestimation is attributed to the elastic finite element analysis performed in the optimization which neglects the plasticity behavior.

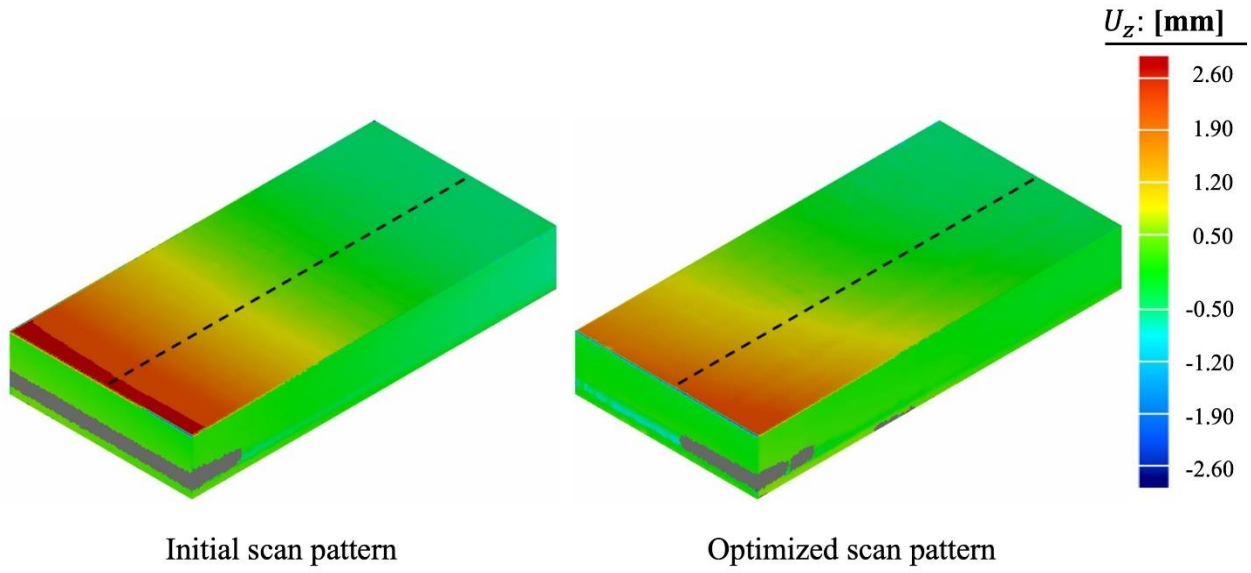

(a)

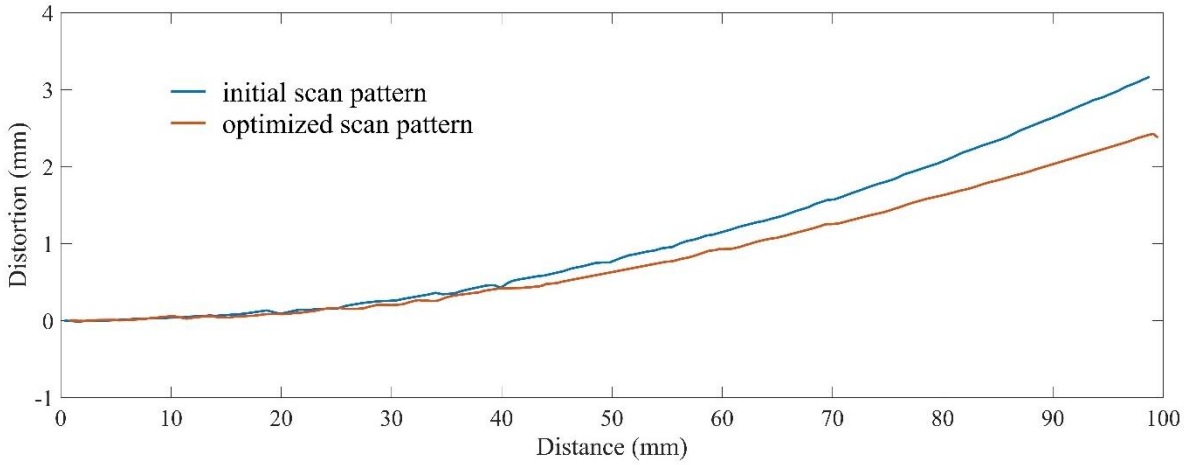

(b)

Figure 4.16: Measured Deformation Comparison: (a) Deformation Profile; (b) Deformation along the Black Dashed Line on the Top Surface

Connecting rod case: The second case is a connecting rod and the dimension is 95 × 35 × 18 mm^3, as shown in Figure 4.17(a). In this case, 60 physical layers are merged as one layer and the part is voxelized with element of 1.25 × 1.25 × 1.8 mm^3. The finite element model of this connecting rod employed in optimization is shown in Figure 4.17(b) which has 21,280 elements

and 24,563 nodes. The island size is 5 ×5 mm^2 in the design and building. Each island is divided into 16 elements as shown in Figure 4.17(c).

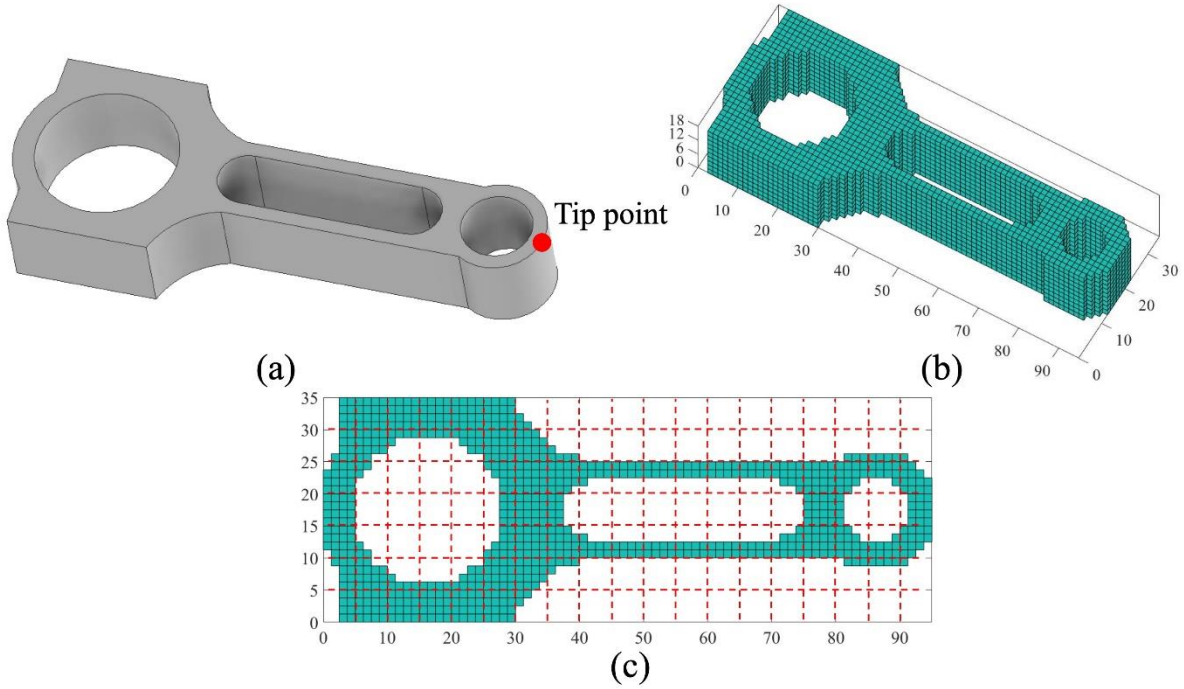

Figure 4.17: (a) Imported Connecting Rod CAD Model; (b) Voxelized Finite Element Model; (c) Generated Islands of Each Layer

The initial scan pattern is the same as the block structure case. Each island is filled with bi-directional horizontal scan lines as shown in Figure 4.18. Build path reconstruction is employed for each island depending on the intersection between island and geometry as shown in Figure 4.18(b). The reconstructed build paths of initial scan pattern are used to build the connecting rod.

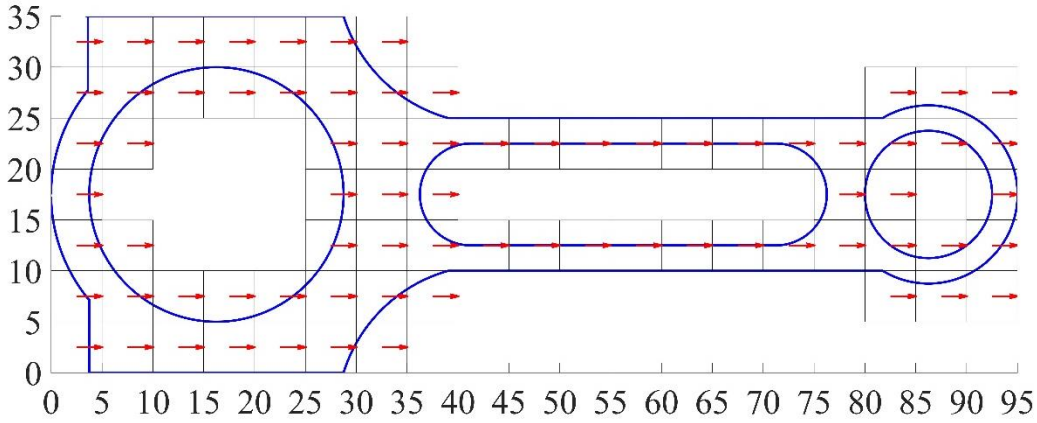

(a)

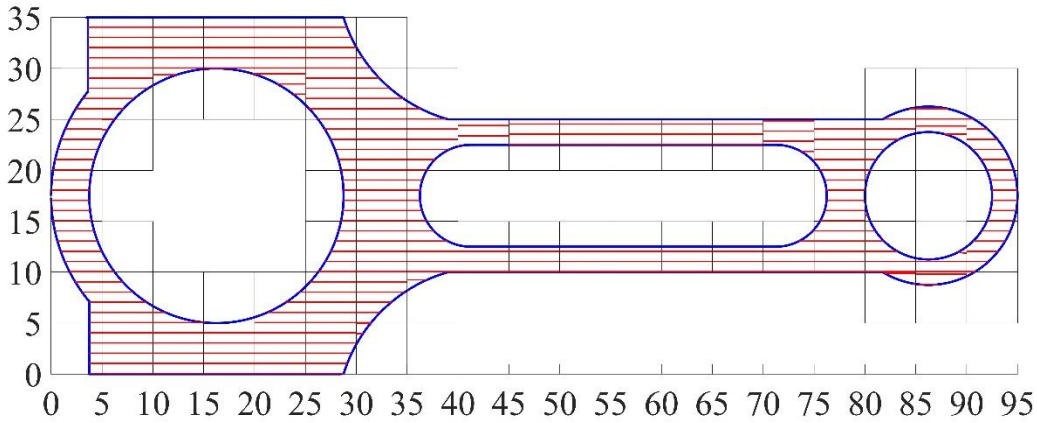

(b)

Figure 4.18: (a) Initial scan pattern (b) Build path reconstruction

The optimized results for the connecting rod case are presented in Figure 4.19 including the deformation profile after cutting off with initial and optimized scan pattern, layer-wised optimized scan pattern and reconstructed building path, and the convergence history. As shown in Figure 4.19(a), the upward bending after partially cutting off the first layer is reduced significantly with optimized scan pattern compared to the deformation with initial scan pattern. The deformation of the picked tip point on the top surface along the mid line, as indicated by the red dot in Figure 4.17(a), is 0.829 mm before optimization and is reduced to 0.450 mm after optimization. The layer-wise scan pattern and reconstructed build path of layer 1, 3, 7 and 9 are presented in Figure 4.19(b).

The convergence history is presented in Figure 4.19(c). The optimization converges with 80 iterations and takes 2.3 hours to with Intel Xeon Gold 6136 3.0 GHz CPU (two processors) and 256GB RAM.

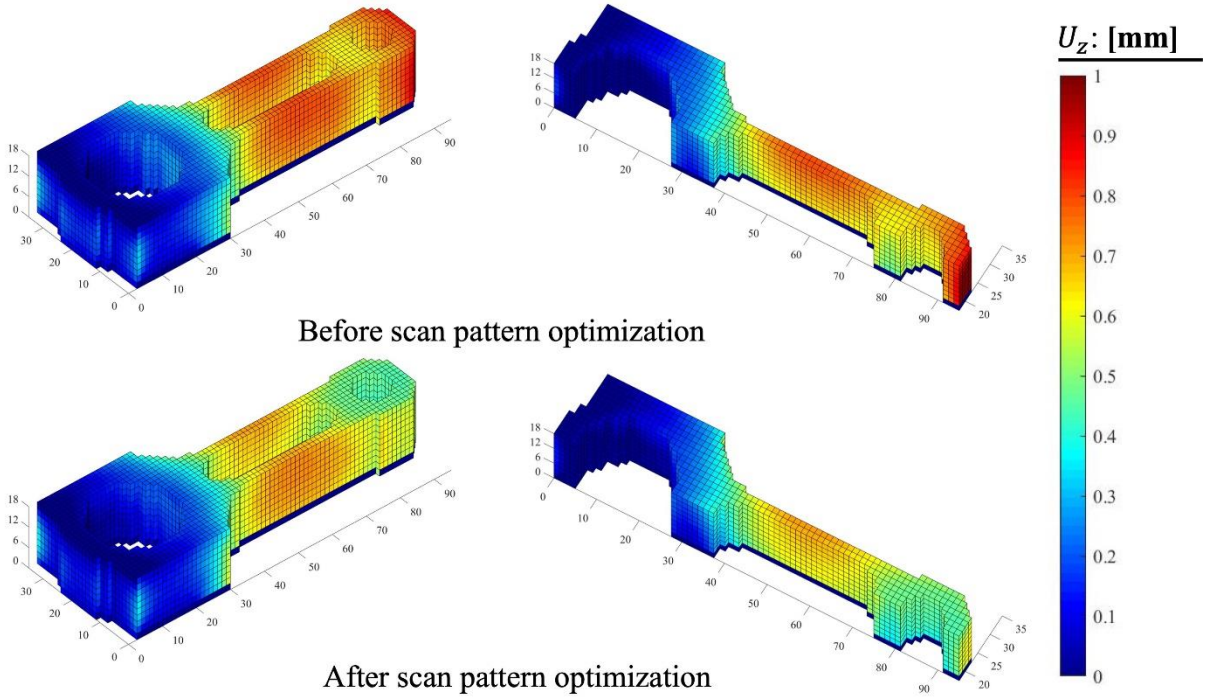

(a)

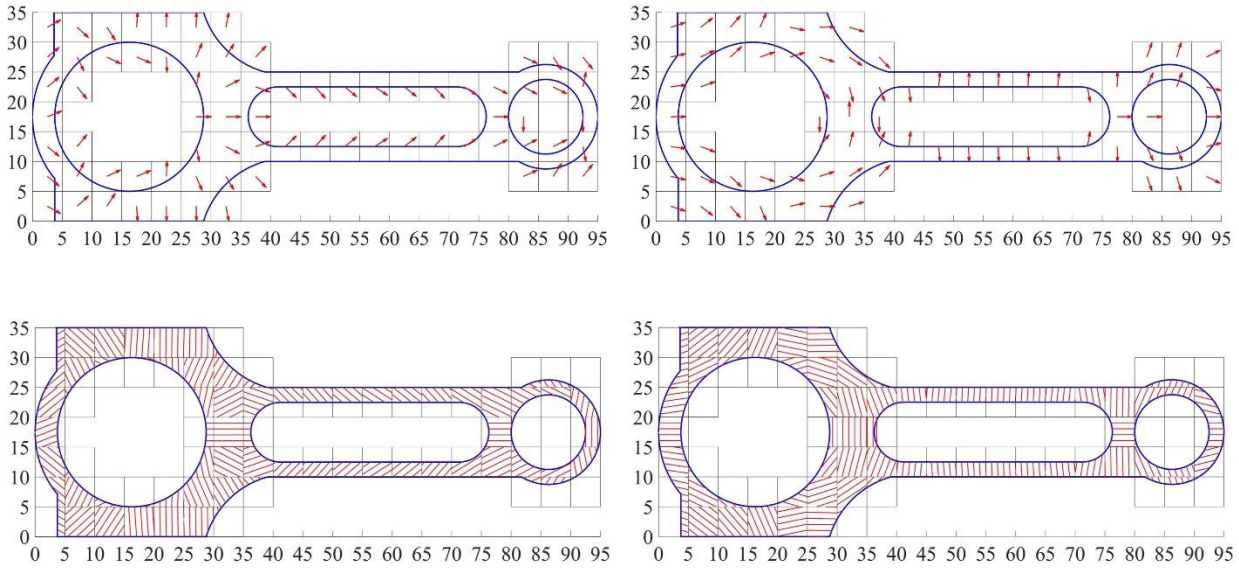

layer 1 layer 3

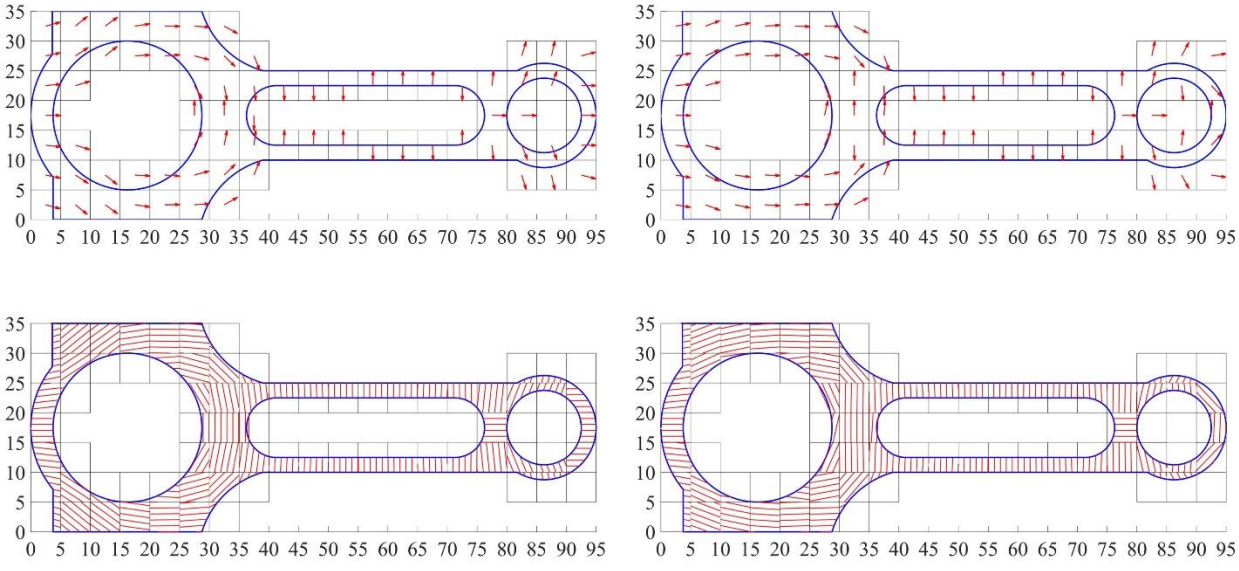

layer 7 layer 10

(b)

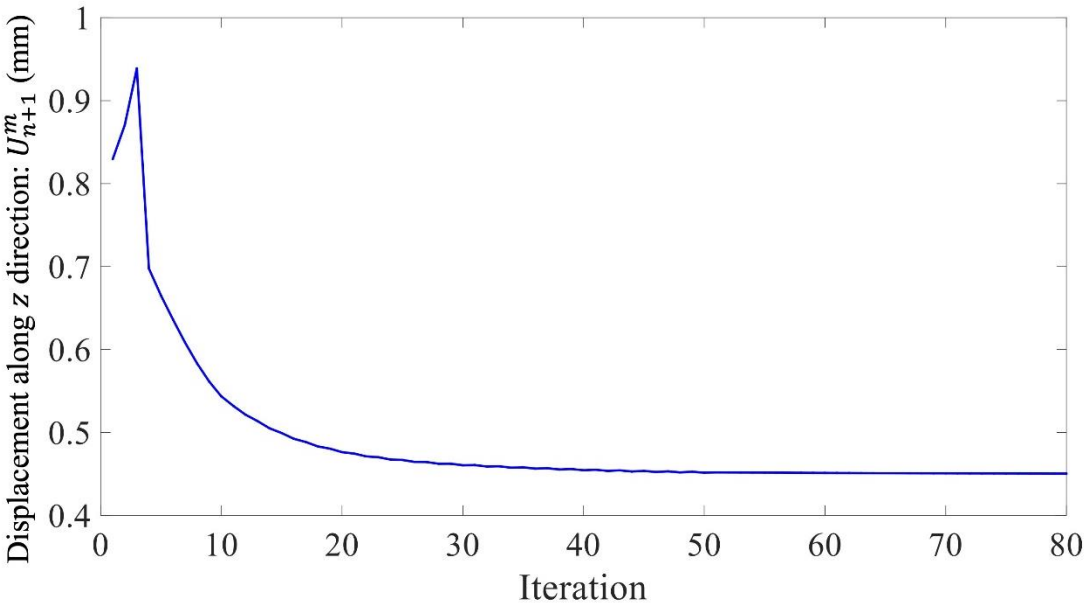

(c)

Figure 4.19: Optimized Results for the Connecting Rod: (a) Deformation Profile after Cutting off; (b) Layer-wise Optimized Scan Pattern; (c) Convergence History

Different from the optimized scanning pattern of the block structure, which mainly consists of vertical scanning tracks, the optimized scanning pattern for connecting rod has islands with horizontal scanning orientation near the small end and crank pin end (i.e. the large end) while the scanning orientation of the thin beams is vertical. Another feature of the optimized scanning pattern is that the island scanning orientation tends to fit the local geometry. For example, the scanning orientations of both large and small end varies along the tangential direction.

In Figure 4.20, connecting rods with the initial parallel scanning pattern as indicated in Figure 4.19 and optimized scanning pattern in Figure 4.20(b) are built by the AconityOne system under the same process conditions as the block structure. The as-built connecting rods were partially cut off from the tip by EDM at the height of 1.8 mm, which equals to one element height, and with 20 mm not cut off, which equals to the length of four islands.

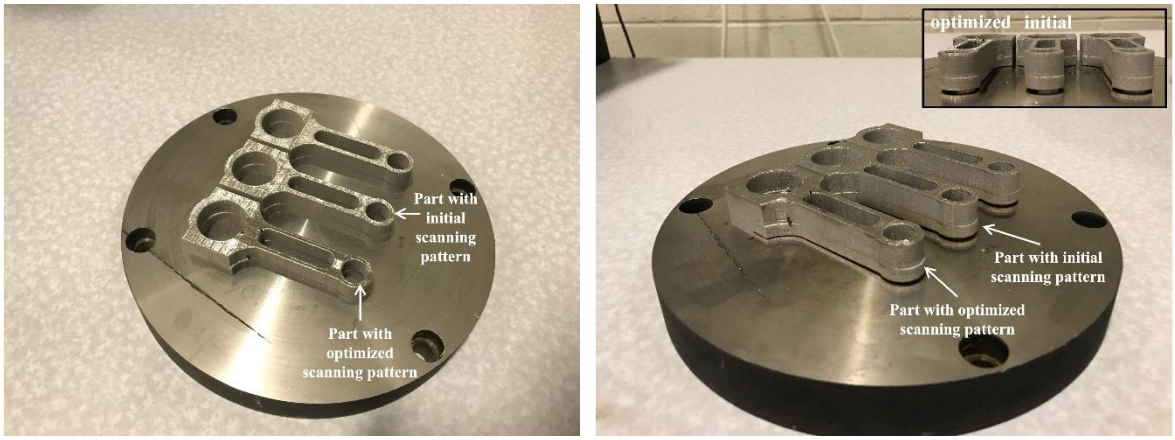

(a) (b)

Figure 4.20: As-built Connecting Rods with Initial and Optimized Scanning Pattern: (a) Before Cutting off; (b) After Cutting off

The measured deformation profiles on the top surface of connecting rod with initial and optimized scanning pattern are presented in Figure 4.21. It can be found that the upward bending deformation after cutting off with initial scanning pattern is around two times larger than the deformation with optimized scanning pattern near the tip point. The deformation values of three picked points as indicated by the black dot near the small end are reduced by 55%, 52% and 53% from left to right after scanning pattern optimization. The effectiveness of the proposed scanning pattern optimization method on connecting rod structure is demonstrated through this comparison.

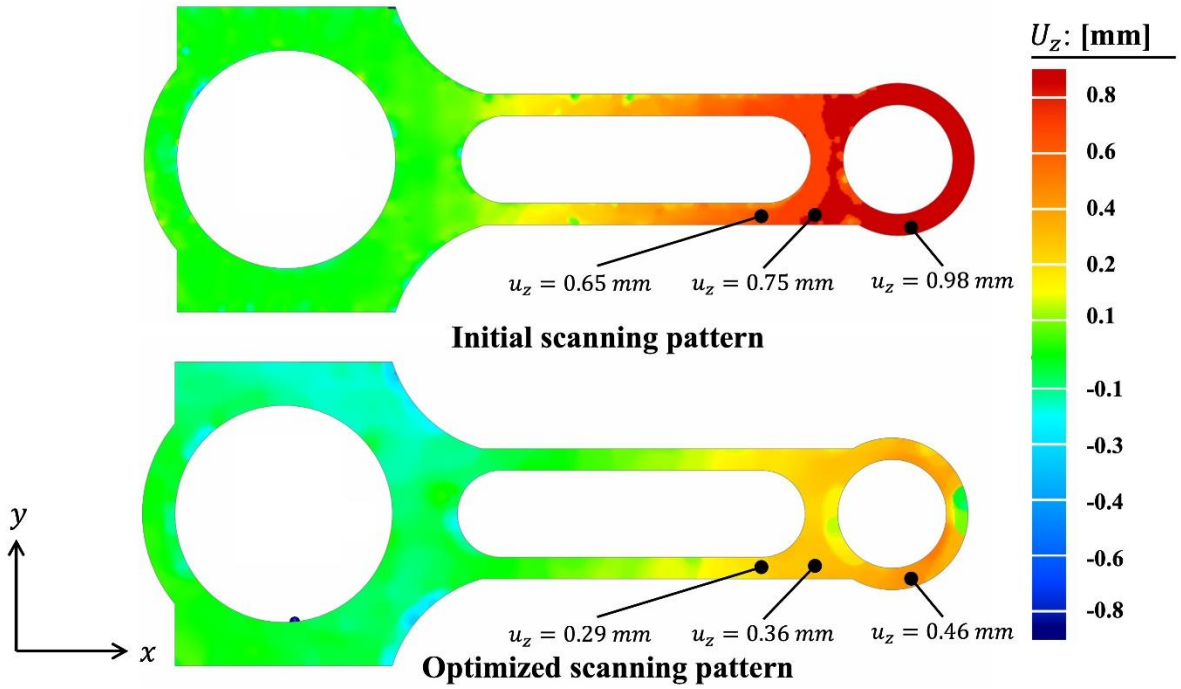

Figure 4.21: Measured Deformation Profile on the Top Surface of Connecting Rods with Initial and Optimized Scanning Pattern

Besides the initial bi-directional horizontal scanning pattern in Figure 4.18, and optimized scanning pattern in Figure 4.19(b), the deformation profiles of the other two commonly used scanning pattern as indicated in Figure 4.22 are computed for comparison. The first one is layer-wise rotation by 90°, and in the second one, the scanning directions in neighboring islands are orthogonal to each other while rotated by 90° layer-wise.

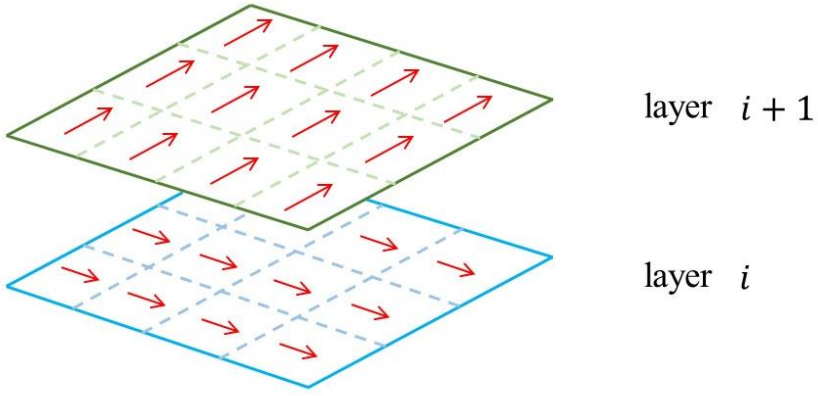

Layer-wise rotate by 90°

(a)

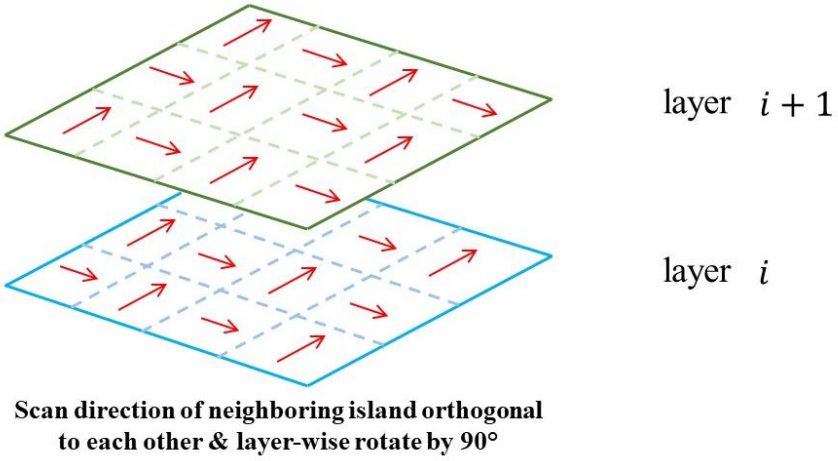

(b)

Figure 4.22: Baseline Scanning Pattern (a) Layer-wise 90° Rotation; (b) Neighboring Island Orthogonal and Layer-wise 90° Rotation

The deformation profiles of the connecting rods with these two scanning patterns after cutting off are presented in Figure 4.23. The deformation at the tip point with the layer-wise 90° rotation is much larger than that with scanning direction orthogonal to neighboring island scanning pattern. The comparison of deformation at the tip point between initial setup, these two commonly used scanning pattern and the optimized scanning pattern are listed in Table 4.2. It could be found that by rotating the scanning direction 90° layer-wise while keeping the scanning directions in neighboring islands could significantly reduce the residual deformation. Among all of these scanning patterns, the optimized one still has the best performance.

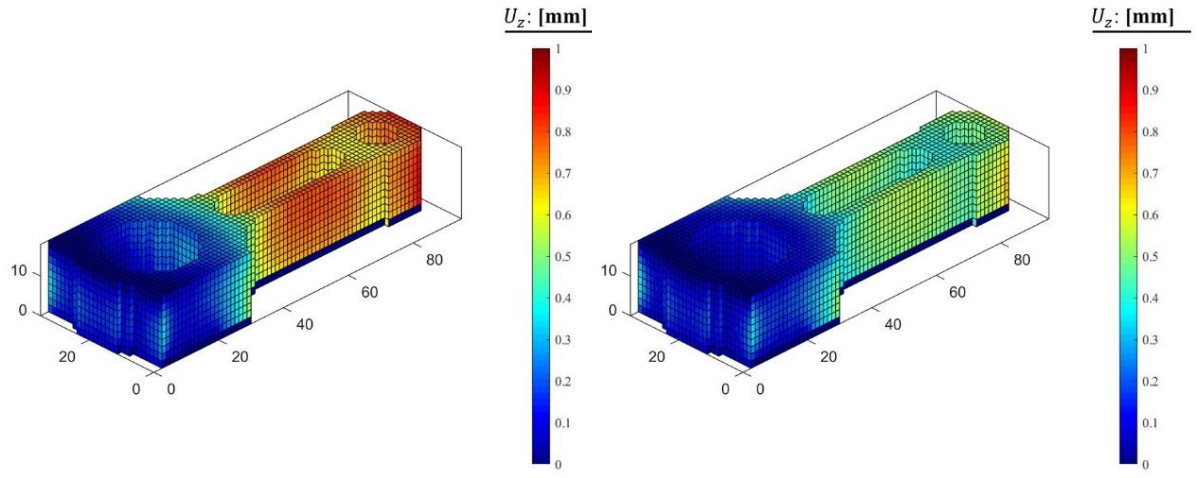

(a) (b)

Figure 4.23: Deformation profile under baseline scanning pattern (a) layer-wise 90° rotation and (b) neighboring island orthogonal and layer-wise 90° rotation

Table 4.2: Deformation of Connecting Rod Tip Point with Different Scanning Pattern

	Initial setup	Layer-wise rotation (90°)	Neighboring island orthogonal & layer-wise rotation (90°)	Optimized
U_z (mm)	0.83	0.83	0.53	0.45

5.0 Data-driven and Real-time Thermal History Prediction at Part-Scale

In this work, a sequential machine learning model including convolutional neural network (CNN) and recurrent neural network (RNN), long short-term memory (LSTM) unit, is proposed for real-time thermal prediction. In this model, the near-field temperature histories caused by the direct interactions with moving laser is predicted by RNN while the far-field temperature due to heat conduction from subsequent building layers is predicted by the CNN-LSTM.

5.1 Network Architecture

This work proposes a multi-scale machine learning framework to predict the complete thermal histories at any locations for a given part. For a point of interest, its thermal history usually has a few cycles of rapid heating and cooling at the beginning corresponding to the laser scanning of the first several layers, and then a long-term heating and cooling caused by heat conduction from the subsequent layers that are far away from this point, and heat dissipation to the substrate and surrounding powder bed. Figure 5.1 depicts this framework schematically. We explore two machine learning models with different network architecture and input data. In the first model, a recurrent neural network (RNN) with three stacked LSTMs is employed to capture the near field temperature history which includes rapid heating and cooling and the peak temperature is above the melting point of material due to laser scanning. In the second model, the LSTMs are integrated with CNN to predict the long-term heating and cooling

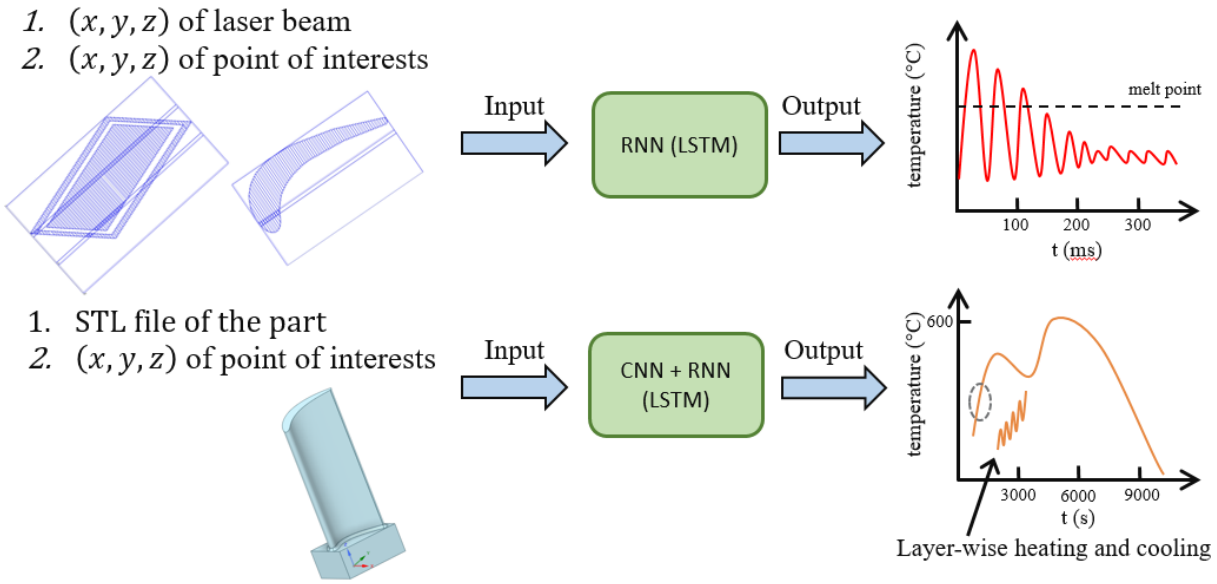

Figure 5.1: Multiscale Machine Learning Framework to Predict Thermal History during Additive Manufacturing Building Process

5.1.1 Recurrent Neural Network (RNN)

Recurrent neural networks (RNNs) are a class of neural networks that allow outputs from previous steps to be used as inputs in current steps and are widely used in natural language processing. In tasks such as speech recognition, text generation and translation, RNNs can model sequential data with complex long-term dynamics, and directly map variable-length input (e.g., sentence in English and video) to variable-length outputs (e.g., sentence in French and image caption). A major limitation of the simple RNN model that restricts its capability to deal with a long-range temporal sequence is the vanishing and exploding gradient problem in backpropagation. Long short-term memory, first proposed in [117], has four gates: input, forget,

cell and output gates and keeps a constant flow of error from cell to cell in backpropagation to avoid vanishing gradient and enable long-range training.

To develop thermal simulation by finite element method, the heat input in each time step corresponding to the moving heat source should be defined as a sequential input. Due to the similarity of data structures, RNN, which is mainly used in natural language processing, has the potential to enhance simulation for additive manufacturing. The architecture of the RNN model employed in this work is presented in Fig. 2. The RNN unit has three layers of LSTMs stacked to process the input vector x_i, the dimension of which is 8×1. The first entry of input vector x_i is the time at step i, the second entry is the laser state: on (1) or off (0), the third to fifth entries are the coordinates of point of interest, and the sixth to eighth entries are the coordinates of moving laser beam at step i. The hidden vectors passed from each LSTM unit to the next step have a dimension of 200×1. There is also a deep neural network (DNN) with 2 fully connected hidden layers to transfer the hidden vector from the LSTM in the third layer to a scalar which is the temperature value in this step.

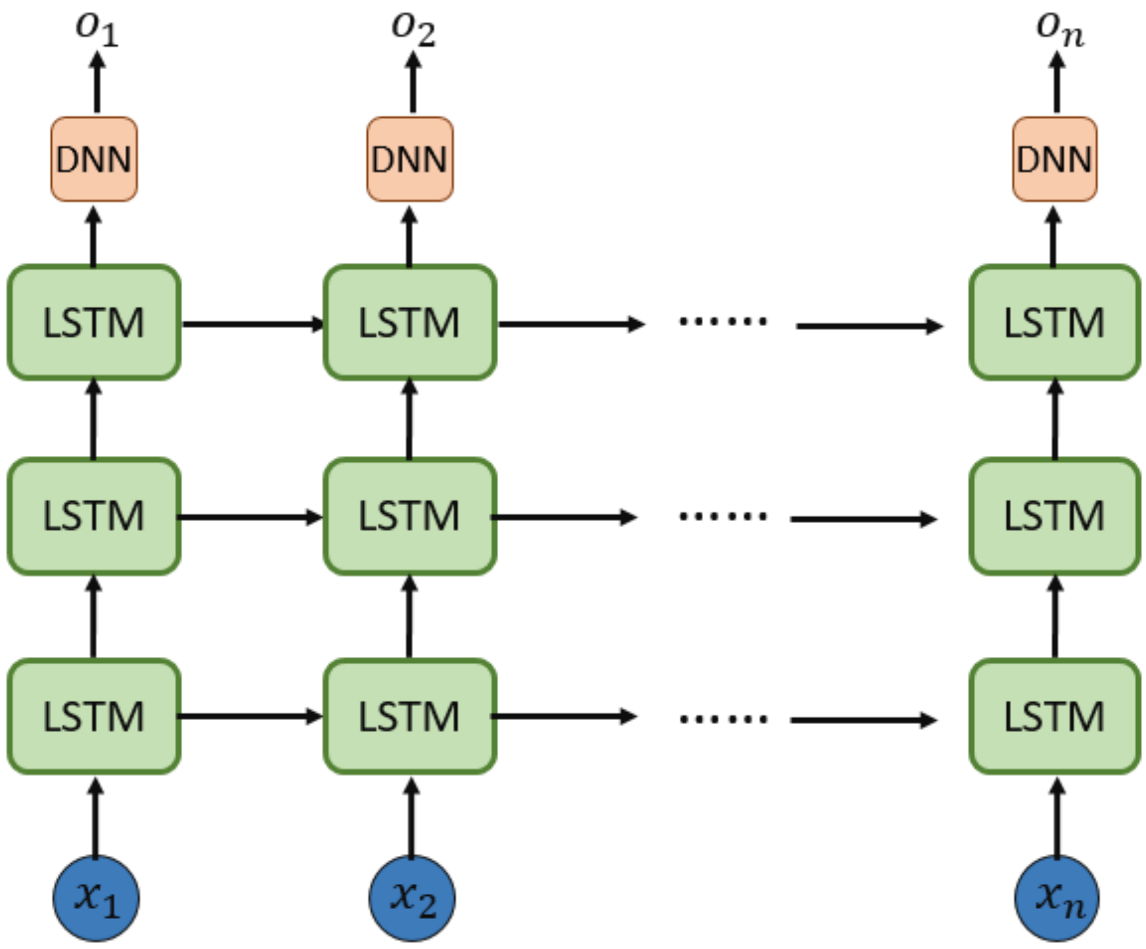

Figure 5.2: Recurrent Neural Network with LSTM for Near-field Temperature Prediction

5.1.2 Convolutional Neural Network and Long Short-Term Memory (CNN-LSTM)

For part-scale thermal modeling, purely tracking the moving laser beam would make the simulation computationally intractable because of the extremely large time step number. Similar issues are encountered using RNN model as discussed in Section 5.1.1 for part-scale thermal prediction. We found that RNN cannot learn the long-term dependencies from sequences longer than 1,000 steps in numerical experiments we have carried out. To predict the long-term heating

and cooling for part-scale model, we propose another machine learning model that integrates recurrent neural network and convolutional neural network together.

Convolutional neural networks (CNNs) [118-120] are another class of neural networks mainly used for computer vision tasks such as image classification [121], segmentation and object detection [122]. CNNs are feedforward networks and have three main types of layers, convolutional layer, pooling layer, and fully-connected (FC) layer. Image features such as colors, edges and spatial dependencies are detected through multiple convolutional and pooling layers as a feature vector. Then, the FC layer in the end performs the classification tasks based on this extracted feature vector. In this work, we use the convolutional and pooling layers to capture the feature of layer-wise geometry in the as-built part, while the FC layer in CNN is replaced by LSTM. In this manner, the spatial relationship of the sliced layer is detected by the convolutional layers while the temporal dependencies are recognized and captured by the LSTM after the CNN part in the model. The architecture of the proposed CNN-LSTM network is schematically illustrated in Fig. 3. The CNN-LSTM network takes in a 512 × 512-pixel grayscale image in each step. There are 5 convolutional layers using a 3 × 3 kernel followed by a rectified linear unit (ReLu). The convolution stride is fixed to 1 pixel so that the spatial resolution is preserved after convolution. After the ReLu unit, there is a 4 × 4 max pooling layer for the first four convolution layers while the last convolutional layer is followed by a 2 × 2 max pooling layer. The output of these convolutional layers is stretched into a 64×1 vector and fed into the 3-layer bidirectional LSTMs, which have a hidden vector size of 128. There is a deep neural network that takes in the 256 ×1 vector from bidirectional LSTMs and outputs a 20 ×1 temperature history vector.

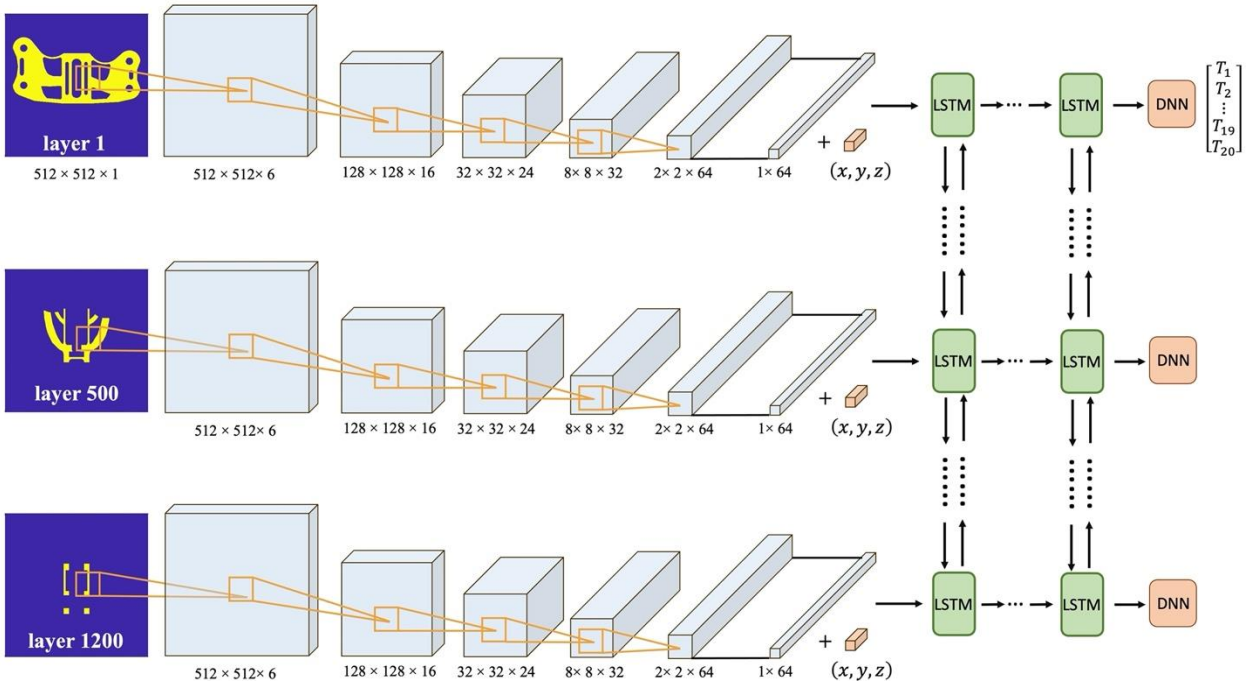

Figure 5.3: CNN-LSTM Network for Far-field Temperature Prediction

5.2 Data Preparation

5.2.1 Near-Field Prediction Based on Analytical Solution

In L-PBF, once the recoater blade spreads a new powder layer, the laser beam then follows the designated path to selectively melt this layer. The near-field temperature rise caused by the interaction between powder particles and laser beam highly depends on the hatch line location, laser scanning strategy and laser parameters including power and scan speed. In this work, the hatch lines in each layer is generated under the default core-skin scanning pattern that the EOS M290 DMLS system employs to process Inconel 718 listed in Table 2.1 [102]. A sliced turbine blade layer is shown in Figure 5.4(a), and the laser scanning orientation in this layer is 135°. To

generate hatch lines for this layer, the turbine blade is divided by two stripes with an overlap of 0.8 mm as indicated in Figure 5.4(b). The intersection of turbine blade and the stripe is filled with scanning lines with a hatch spacing of 110 μm. The stripe width used is 10 mm.

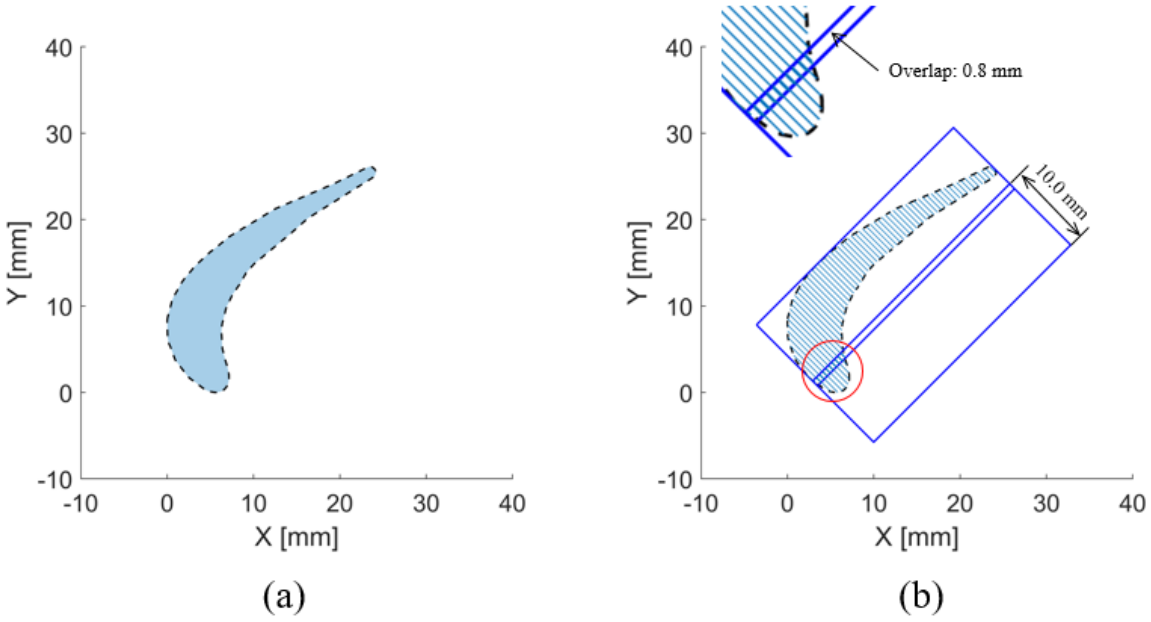

Figure 5.4: Hatch Line Generation

Once the hatch lines for all layers are obtained, we referred to the Discrete Source Model (DSM) in Ref. [123] to represent the continuous and moving heat source as a series of stationary energy source terms as shown in Figure 5. The governing equation for thermal analysis is:

$$\frac{\partial T}{\partial t} = \alpha \nabla^2 T + \sum_{i=1}^{n} q_i(\mathbf{X}_{ci}, \tau_i) \tag{5.1}$$

where T is temperature, t is the time, α thermal diffusivity, and q_i is the discrete heat source according to hatch line, $\mathbf{X}_{ci}$ is the location of the heat source and τ_i is the activation time. According to the general Green's function solution [124], the resulting temperature field caused by the i^{th} heat source term can be written as the multiplication of temporal integral and spatial integral in each dimension:

$$T = T_0 + \frac{1}{\rho C_p}\sum_{i=1}^{n}\int_{t'}\iiint_{x',y',z'} G(\mathbf{X},t,\mathbf{X}',t')q_i(\mathbf{X}',\mathbf{X}_{ci},t')d\Omega dt' \tag{5.2}$$

Where T_0 is the initial temperature, ρ is the material density, C_p is the heat capacity, $\mathbf{X}$ is the location of point of interest, $\mathbf{X}'$ and t' are the variables for spatial and temporal variables for integration, G is the Green's function:

$$G(\mathbf{X},t,\mathbf{X}',t') = \frac{1}{\left(\sqrt{4\pi\alpha(t-t')}\right)^3} exp\left(-\frac{(x-x')^2+(y-y')^2+(z-z')^2}{4\alpha(t-t')}\right) \tag{5.3}$$

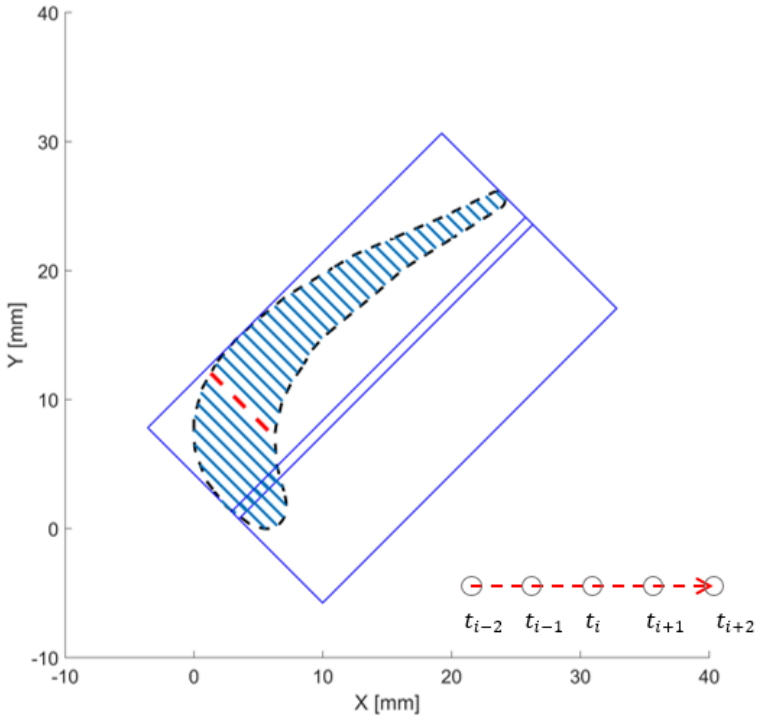

Figure 5.5: Discretize Continuous Hatch Line into Point Heat Sources

In this work, we use Goldak's double ellipsoid energy distribution [73]. The discrete heat source term in Eq. (5.2) is

$$q_i(\mathbf{X}',\mathbf{X}_{ci},t') = \frac{6\sqrt{3}P\eta\Delta t}{abc\pi^{3/2}} exp\left(-3\frac{(x'-x'_{ci})^2}{a^2} - 3\frac{(y'-y'_{ci})^2}{b^2} - 3\frac{(z'-z'_{ci})^2}{c^2}\right)\delta(t'-\tau_i) \tag{5.4}$$

where P is the laser power, η is the energy absorptivity, Δt is the time interval between two heat sources, a and b represent the length and width of the ellipsoid and c is the penetration depth.

Substitute Eq. (5.3) and Eq. (5.4) into Eq. (5.2), we could obtain the closed form analytical solution for the temperature response to a series of discrete heat sources:

$$T = T_0 + \frac{6\sqrt{3}P\eta\Delta t}{\rho C_p \pi^{3/2}} \sum_{i=1}^{n} \frac{exp\left(-3\frac{(x-x_{ci})^2}{12\alpha(t-t')+a^2} - 3\frac{(y-y_{ci})^2}{12\alpha(t-t')+b^2} - 3\frac{(z-z_{ci})^2}{12\alpha(t-t')+c^2}\right)}{\sqrt{12\alpha(t-t')+a^2}\cdot\sqrt{12\alpha(t-t')+b^2}\cdot\sqrt{12\alpha(t-t')+c^2}} \delta(t'-\tau_i)dt' = T_0 +$$

$$\frac{6\sqrt{3}P\eta\Delta t}{\rho C_p \pi^{3/2}} \sum_{i=1}^{n} \frac{exp\left(-3\frac{(x-x_{ci})^2}{12\alpha(t-\tau_i)+a^2} - 3\frac{(y-y_{ci})^2}{12\alpha(t-\tau_i)+b^2} - 3\frac{(z-z_{ci})^2}{12\alpha(t-\tau_i)+c^2}\right)}{\sqrt{12\alpha(t-\tau_i)+a^2}\cdot\sqrt{12\alpha(t-\tau_i)+b^2}\cdot\sqrt{12\alpha(t-\tau_i)+c^2}} \quad (5.5)$$

In this work, we use the derived analytical solution in Eq. (5.5) to generate thermal histories of different locations for the training of the proposed RNN in section 5.1.1. For any given point of interest, it undergoes several cycles of rapid heating and cooling due to the laser scanning. There is a 10 second-cooling between two consecutive layers corresponding to the powder spreading process. For the turbine blade, the thermal history of the point in the middle of the first layer is shown in Figure 5.6. The entire thermal history considers the hatching of four consecutive layers. We set the cutoff layer number to be 5 in the computation which means for any point, only the hatch lines in 4 consecutive layers are considered. The reasons are: 1. When printing the 5^{th} layer, the laser beam is too far away from the point of interest to have a significant temperature rise; 2. The RNN is sensitive to input sequence length (or step number) because of potential gradient vanishing. Therefore, we intentionally control the number of discrete heat source in the computation. In Fig. 4, the temperature rises and subsequent cooling is depicted in blue, while the second layer is in orange, third layer in green and fourth layer in red. In each layer, there are more than one temperature peak which are attributed to the hatch lines close to point of interest. All the data preparation and pre-processing are performed by Matlab R2019. The thermal history of each point of interest is written as one comma-separated values (*csv*) file for the training of RNN.

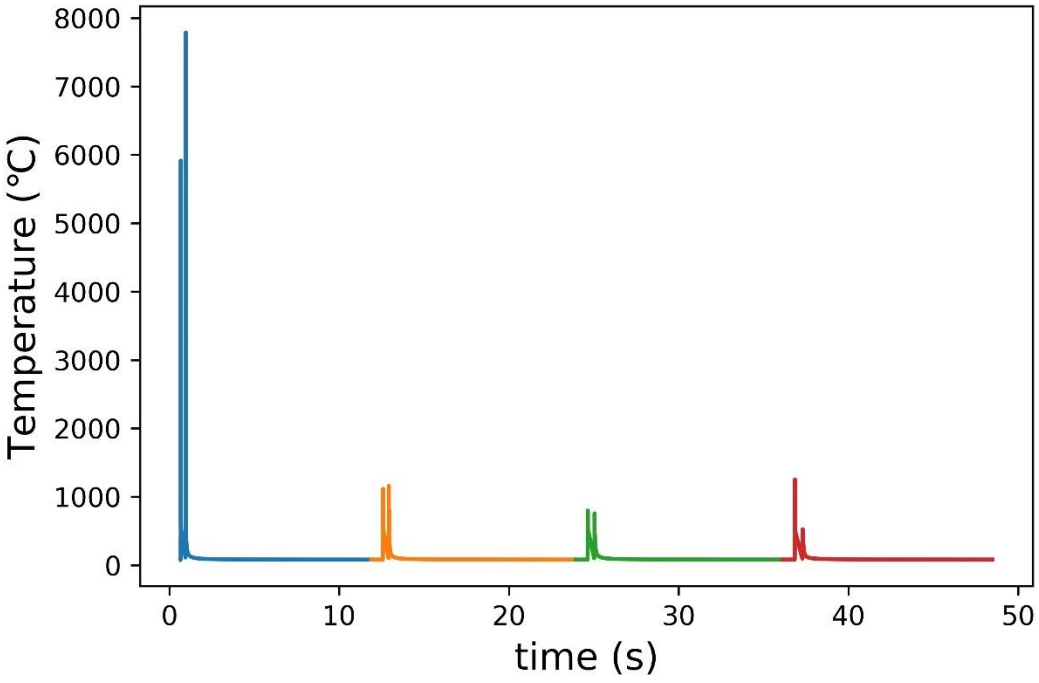
8000
7000
6000
5000
4000
3000
2000
1000
0
Temperature (°C)
0
10
20
30
40
50
time (s)

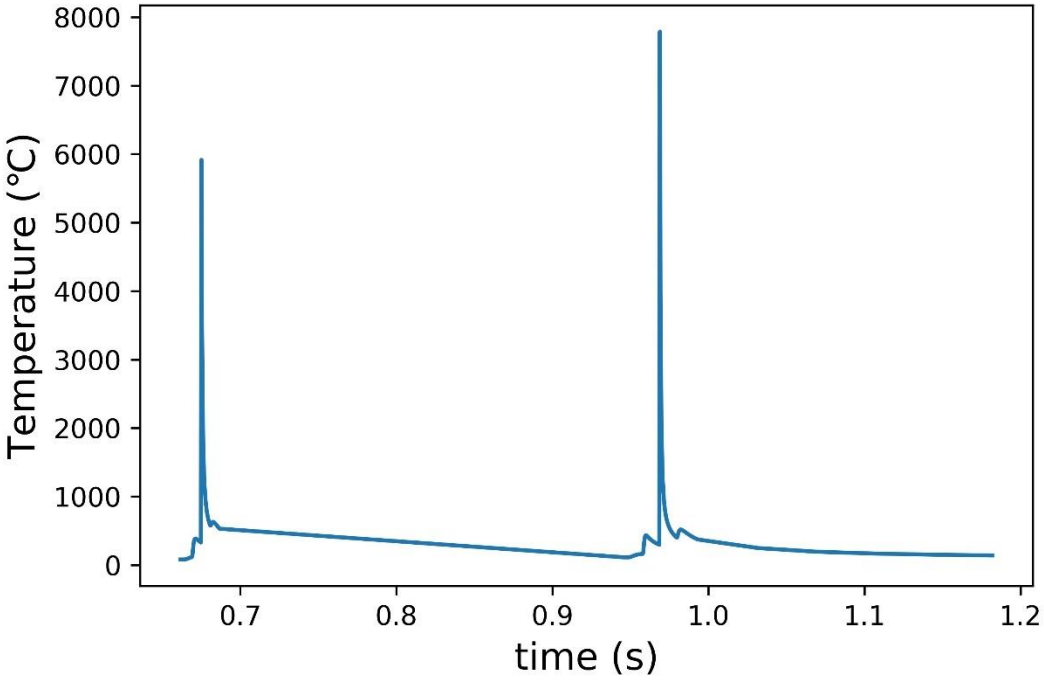
8000
7000
6000
5000
4000
3000
2000
1000
0
Temperature (°C)
0.7
0.8
0.9
1.0
1.1
1.2
time (s)

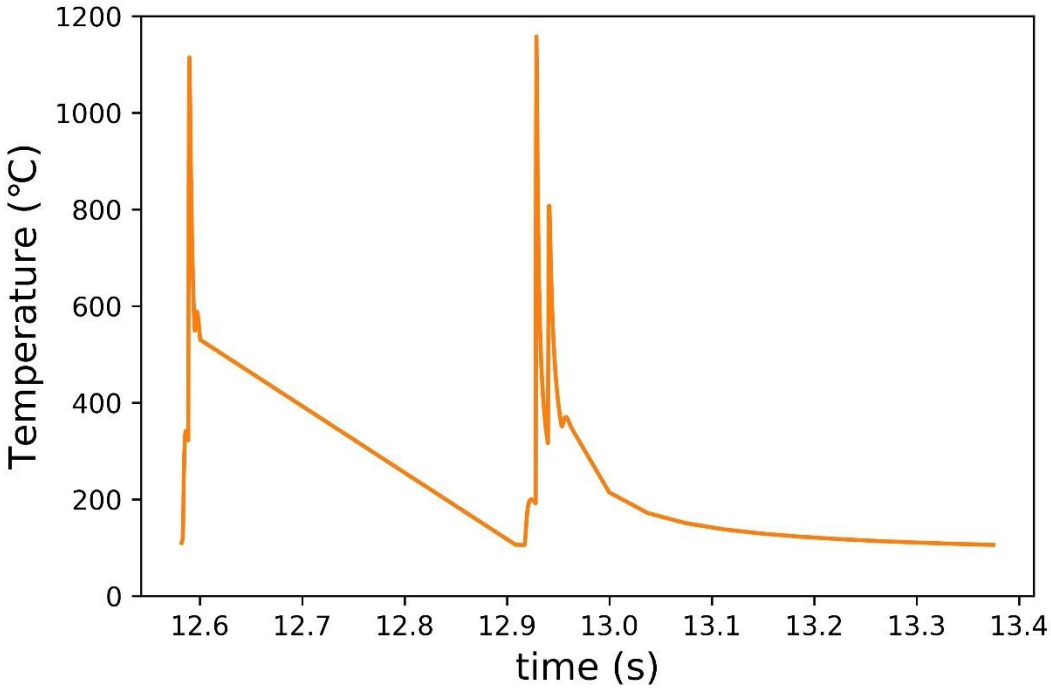

Figure 5.6: Near-field Temperature by Analytical Solution

5.2.2 Mean-field Prediction Based on Finite Element Analysis

The temperature field at part-scale is calculated based on the 3D transient heat conduction equation in Eq. (5.1) as well. Heat convection coefficients are used to prescribe surface boundary conditions. The time discretization is realized with an implicit Euler scheme and the heat generation is applied to the entire layer simultaneously to save computational time and compute larger parts compared to a moving heat source model. The mesh is composed of voxel elements with linear shape functions. In the additive manufacturing process, the mesh needs to be frequently updated so voxel elements are relevant to avoid complex mesh generation. After finite element discretization, the solution is calculated with a preconditioned conjugate gradient (PCG) algorithm,

the Jacobi preconditioner is employed here. The material properties are updated inside the PCG loop so temperature-dependent properties can be used.

The computational domain is composed of two different element sizes as the mesh is coarsened in the build direction when the element is located far away from the newly activated layer (see Figure 5.7). It enables the use of real layer thickness for a small computational cost. Due to the mesh simplicity, a matrix-free algorithm is well suitable to solve this problem, it allows to save memory as the global K matrix in the system $KT = F$ does not need to be stored. Instead the matrix-vector products in the PCG algorithm are computed with the use of the element matrix [125].

The matrix-free PCG algorithm is computed on a Graphics Processing Unit (GPU) to furthermore increase the efficiency of the simulation compared to a single CPU implementation. The GPU card used in this work is a NVIDIA Titan V GPU, with 12 GB of memory and instructions to run calculations are written in CUDA (Compute Unified Device Architecture). The reader is referred to Ref. [126]. Derivation for the volumetric heat generation rate is provided in Appendix B.

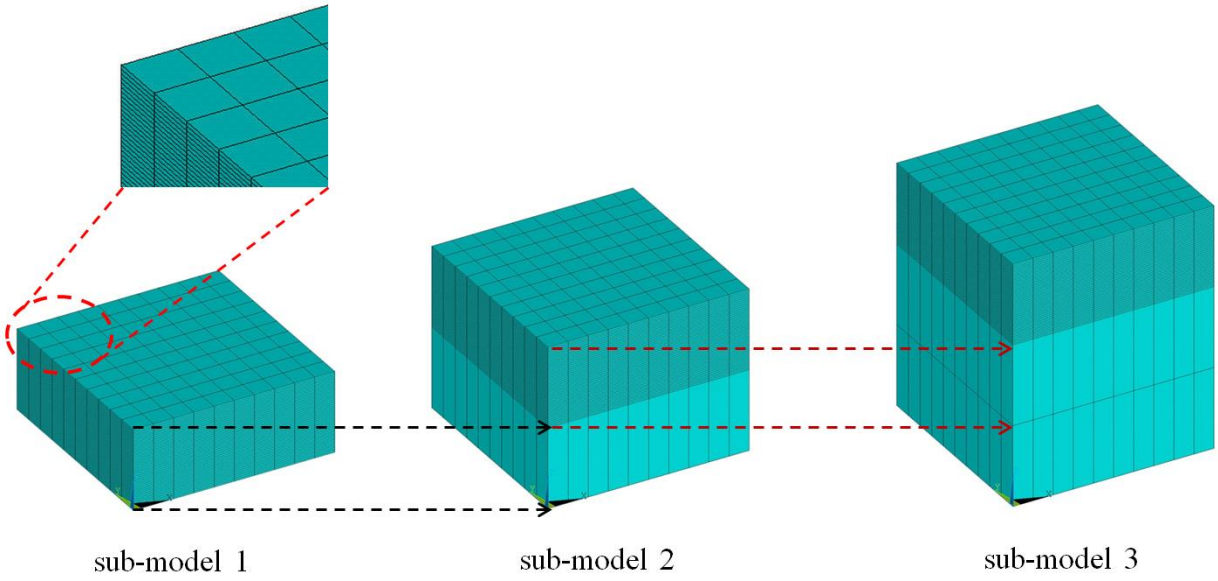

Figure 5.7: Finite Element Model for the Part-scale Thermal Simulation

The geometries used in this work to develop database are turbine blade, jet engine compressor blade and jet engine bracket as shown in Figure 5.8. The height of the turbine blade in Figure 5.8(a) is 102.68 mm and sliced to 2,567 layers, the building time of this part is 8.0 hours. The jet engine compressor blade in Figure 5.8(b) has a height of 30.12 mm and is divided to 753 layers in the building. The part takes 5.06 hours to be built. The third geometry is the bracket for aircraft engines in Figure 5.8(c) which is also a benchmark model commonly used by lightweight design and topology optimization challenge. The part has a height of 62.44 and is sliced to 1,561 layers in the building that takes 16.38 hours.

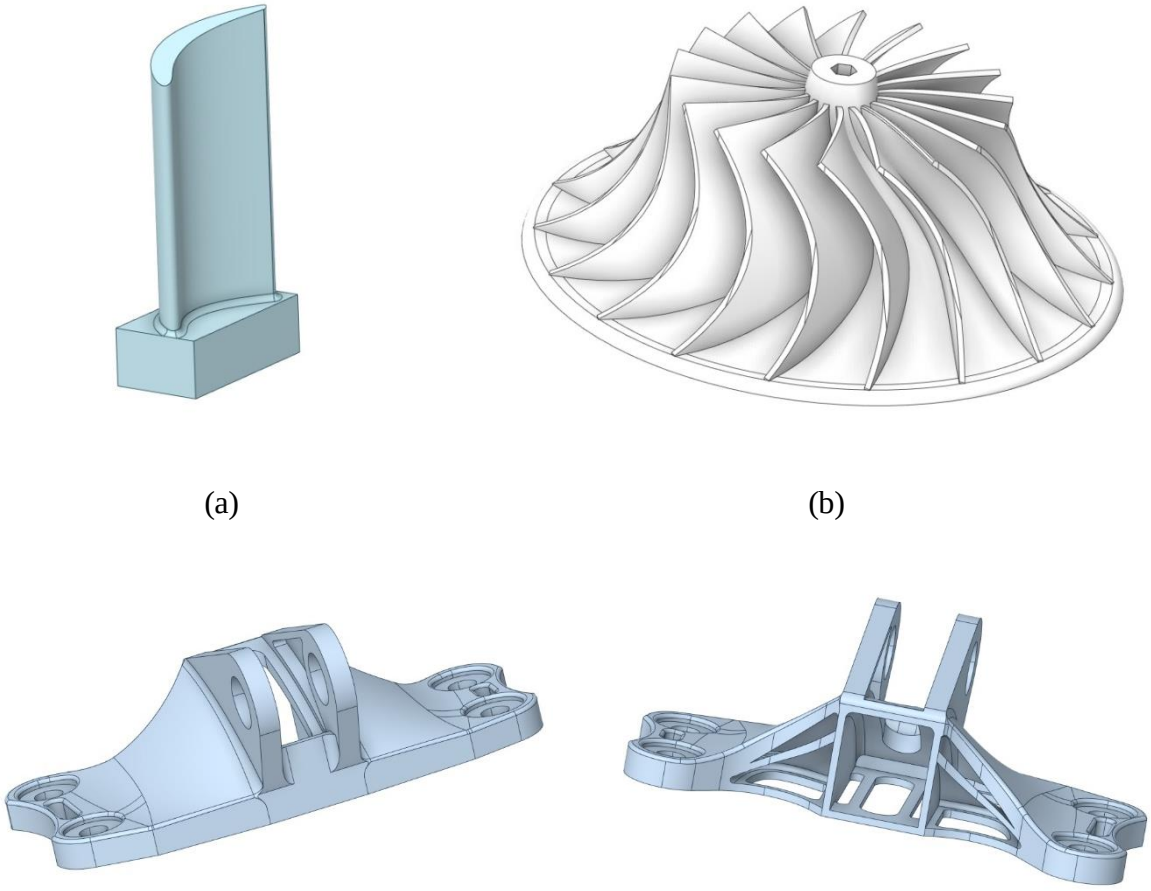

(a) (b)

(c)

Figure 5.8: The Structures Used for Part-scale Thermal Modeling: (a) Turbine Blade; (b) Jet Engine Compressor Blade; (4) Jet Engine Bracket

Temperature profile snapshots of these three geometries are presented in Fig. 9. For the thermal profile of the turbine blade shown in Figure 5.9(a), it can be found that the temperature of the newly deposited layers keeps increasing along the building direction. However, the cross sectional area of the turbine decreases significantly from the 2270 layer to the last layer which also reduces the laser dwell time and heat generation rate applied. Therefore, the entire part cools down very rapidly to the ambient temperature in the end of the building. The jet engine compressor has a temperature profile similar to the turbine blade in Figure 5.9(b) since the area of the sliced layer

decreases along the building direction. For the jet engine bracket, higher temperature is observed near the end of the building which is attributed to the overhangs of the cylinders.

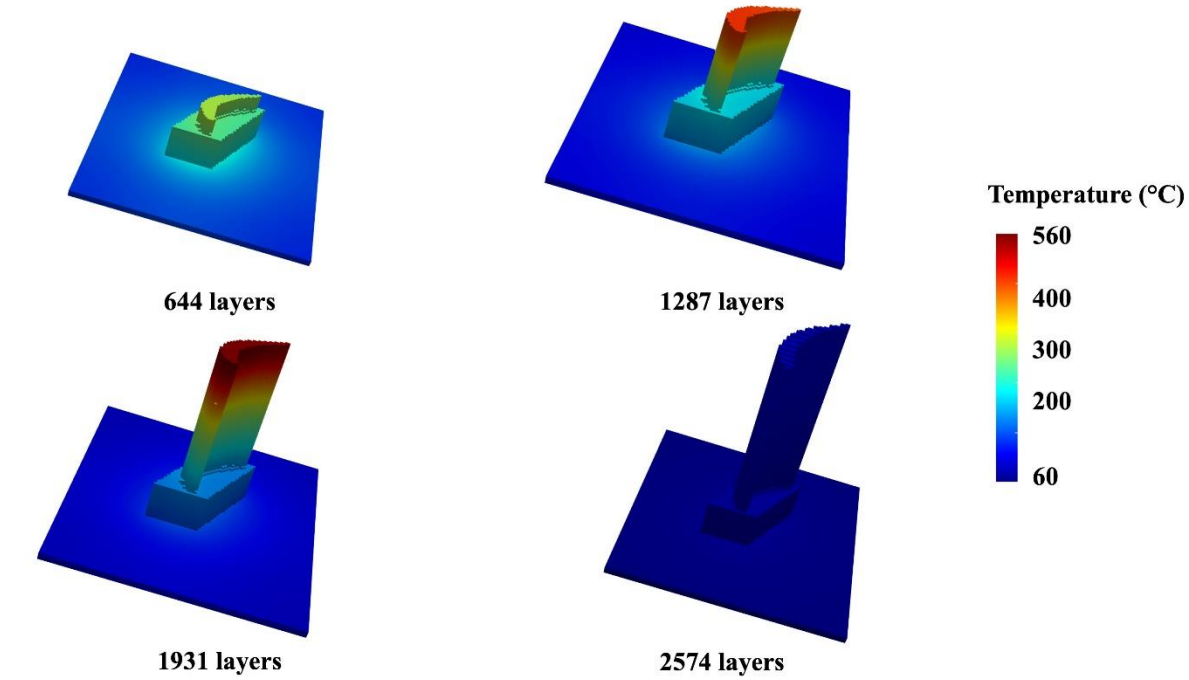

(a)

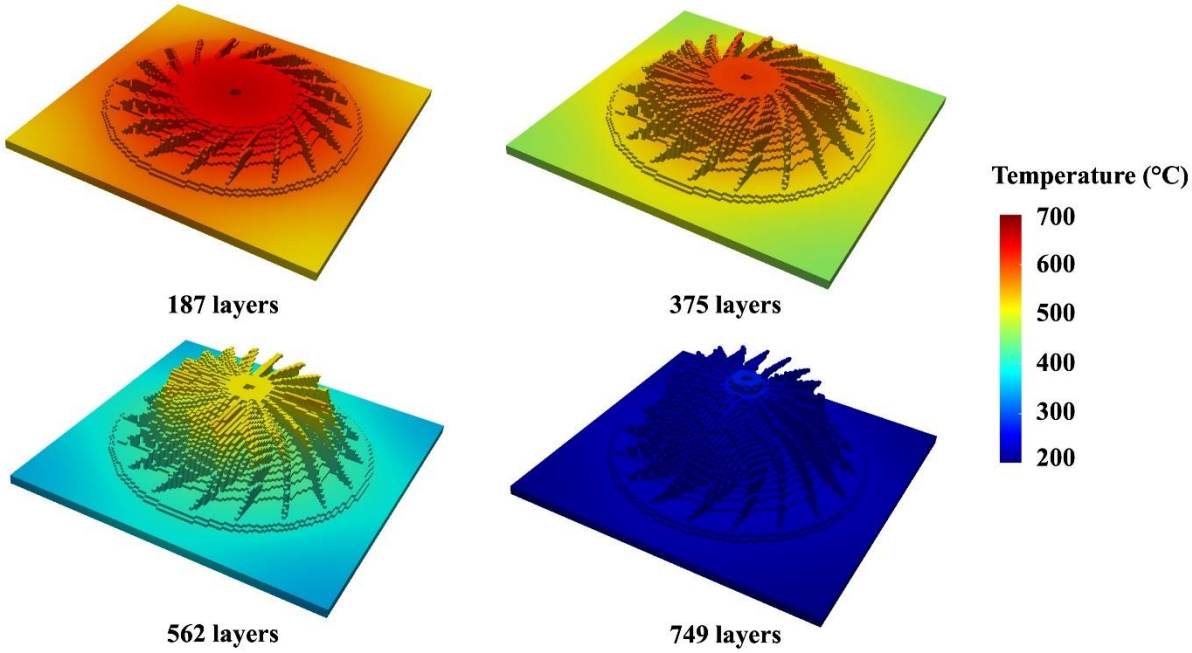

(b)

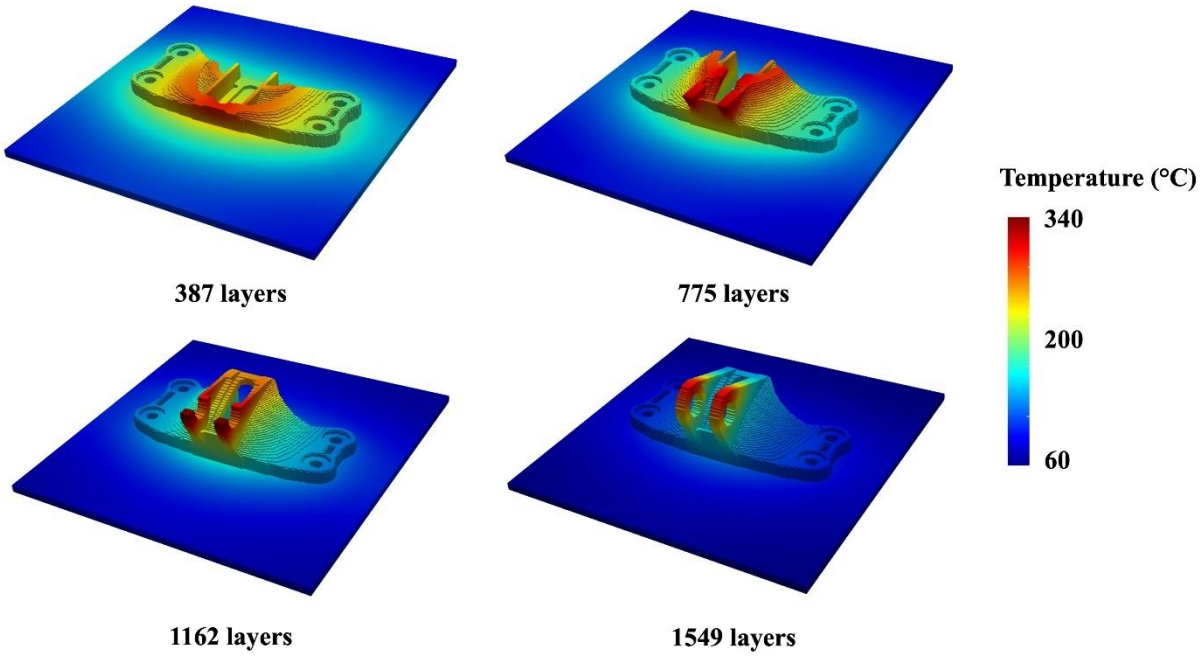

(c)

Figure 5.9: Layer-wise Temperature Profile of the Geometries from Part-scale Thermal Simulation: (a) Turbine Blade; (b) Jet Engine Compressor Blade; (c) Jet Engine Bracket

5.3 Results and Discussion

5.3.1 Model Training

To train the RNN model for near-field temperature prediction, we used analytical solution presented in Section 3.1 to generate thermal histories for different locations of the turbine blade. The layer-wise rotation angle is set to 0°, 45°, 67° and 90°, respectively. We generated thermal histories for 1,250 points for each rotation angle, and had 5,000 data points in total for the training.

The training dataset has 4,000 data points while there are 1,000 data points in the test dataset to evaluate the performance of the trained RNN.

We used one NVIDIA Quadro RTX 5000 graphic card with a GPU memory of 16 GB to train the RNNs, and three NVIDIA A-100 graphic cards with a GPU memory of 40 GB to train the CNN-LSTM model. The machine learning library used to develop and train the models is PyTorch. The Python version is 3.8, PyTorch version is 1.8.1, and the CUDA version is 11.1. The loss function used to train the model is mean squared error (MSE) and the optimization algorithm used is Adam. The batch size is 4 and we used padding to guarantee the sequence lengths of these 4 data points in the same batch identical. It is also worth to talk about the impact of initialization on the performance of the model. Initialization is a process to create weight before the training. It has been pointed out in literature that the initialization has a significant impact on the performance of RNN. PyTorch usually initializes parameters with a Gaussian distribution, but we noticed that this initialization cannot lead to an acceptable loss even though increasing the epoch number. We recommend to use orthogonal initialization to alleviate the vanishing and exploding gradient in the training. For LSTM, the biases of forget gates is recommended to be 1, while the biases of the other gates are 0.

5.3.2 Model Prediction

5.3.2.1 Near-field Prediction by RNN

The loss curve during the training is presented in Figure 5.10. We used *lr_scheduler* in PyTorch to decay the learning rate by 0.9 every 100 epochs. The training takes 2,000 epochs to converge and has a MSE loss around 0.01.

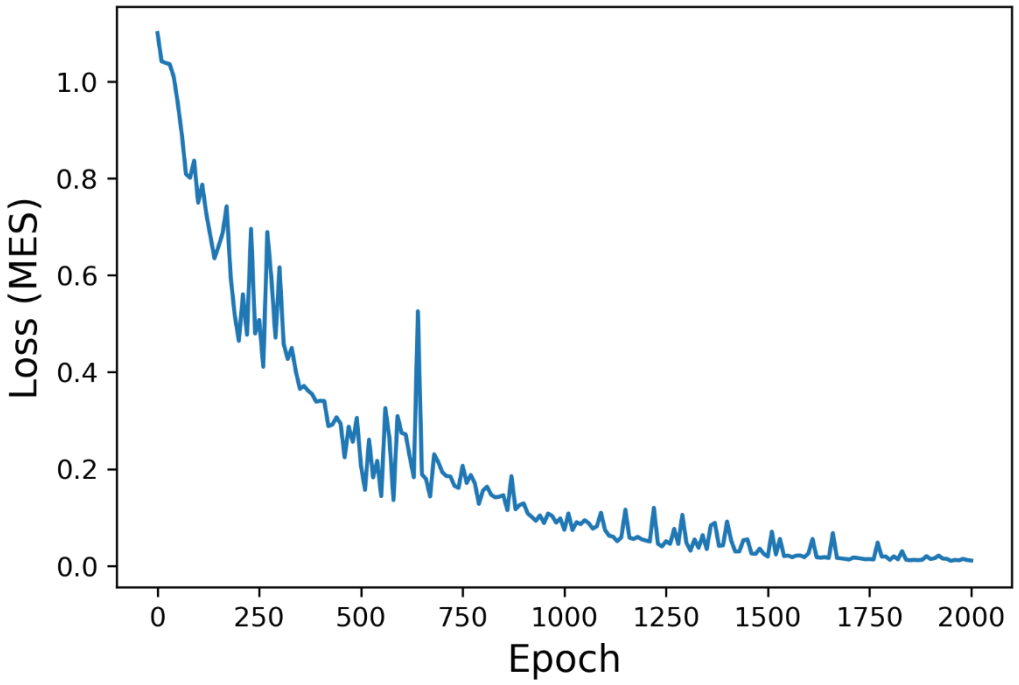

Figure 5.10: Convergence History of the RNN Model

The performance of the trained RNN is evaluated on the test dataset which has 1,000 data points. For data unseen before, the trained RNN could also capture the trend and magnitude of the thermal histories induced by moving laser as shown below in Figure 5.11. For a data point, the thermal history obtained from RNN model perfectly matches the curve by analytical solution except the last peak induced by the laser scanning in the fourth layer above this point. The temperature curves between RNN and analytical solution in the first two peaks are compared as shown in Figure 5.11(b)-(c). The trained RNN could predict the rapid heating caused by the interactions between material and laser and subsequent cooling very accurately. We noticed there is a gap between RNN and analytical solution during the rapid cooling period. However, the magnitude of this difference is still acceptable.

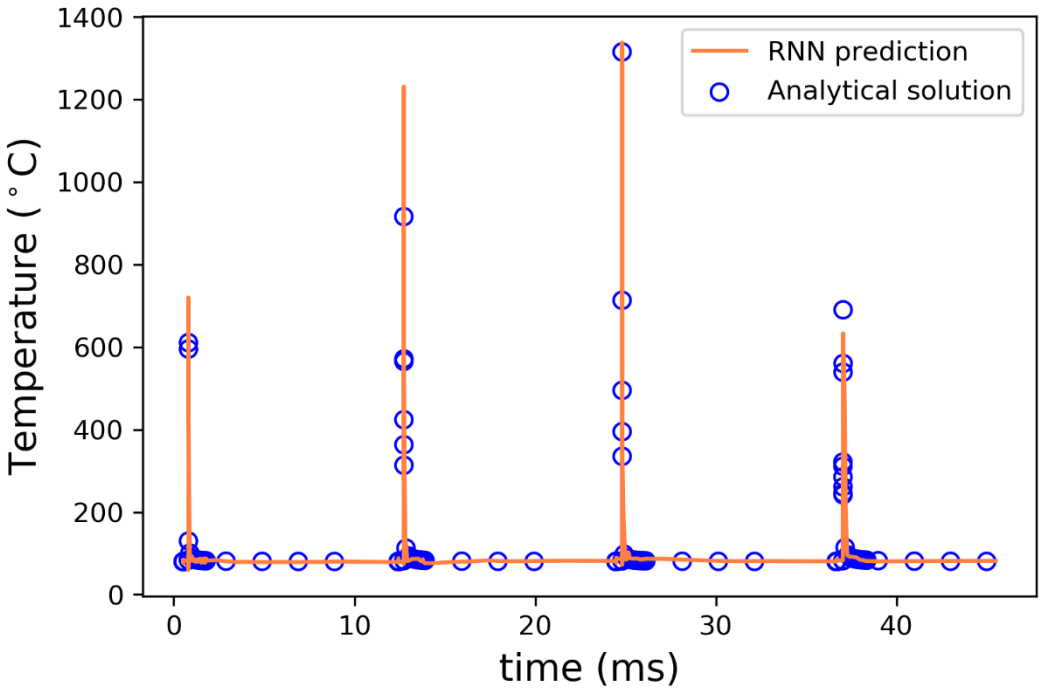
RNN prediction
Analytical solution
Temperature (°C)
time (ms)
0
200
400
600
800
1000
1200
1400
0
10
20
30
40

(a)

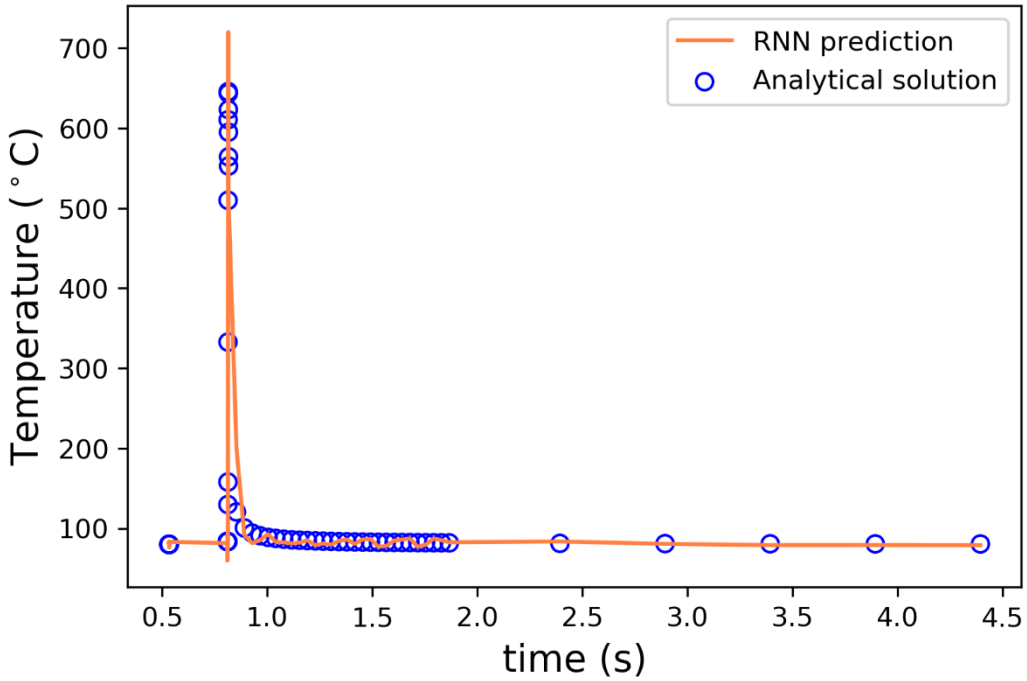
RNN prediction
Analytical solution
Temperature (°C)
time (s)
100
200
300
400
500
600
700
0.5
1.0
1.5
2.0
2.5
3.0
3.5
4.0
4.5

(b)

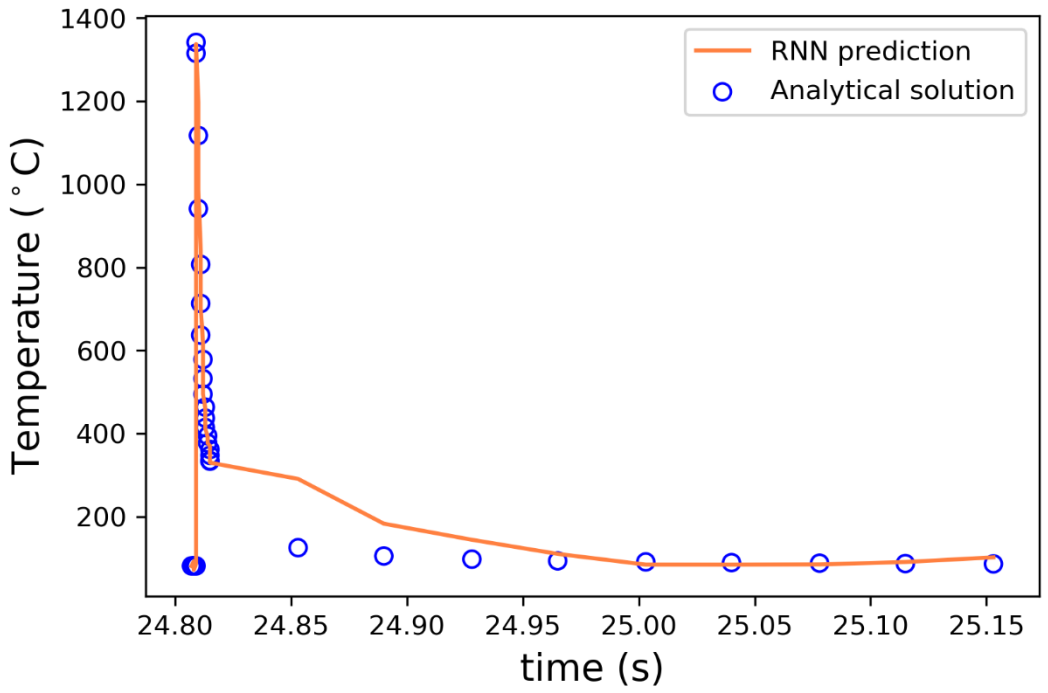

(c)

Figure 5.11: Predictions of the Trained RNN on Test Dataset: (a) Thermal History of 4 Layers; (b) Peak of the First Layer; (c) Peak of the Second Layer

The performance of RNN models with GRU and LSTM unit are compared and the summarized in Table 5.1. GRU has one reset gate and one update gate while LSTM has three gates, the input, output and forget gate. The parameter number of GRU is smaller than the LSTM unit with the same layer number. In the experiments, we also noticed that training time per epoch of GRU is also 5 to 6 times smaller than LSTM. However, LSTM has better prediction accuracy than GRU on the test dataset.

Table 5.1: Comparison of the Performance of Models with Different RNN Units (GRU vs LSTM)

Model	Layer number	R2 score	MSE	Number of parameters	Training time per epoch (seconds)
GRU	2	0.54	0.087	391,381	5.25
GRU	3	0.62	0.044	632,581	6.52
LSTM	2	0.76	0.028	513,781	24.91
LSTM	3	0.93	0.010	835,381	35.50

5.3.2.2 Mean-field Prediction by CNN-LSTM

Besides the coordinate (x, y, z) of point of interest, another input of the CNN-LSTM network is the layer-wise geometry. The building of layers above the point of interest leads to temperature fluctuations while geometry of layers below the point of interest has a significantly impact on the heat conduction. We used a 512 × 512-pixel grayscale image to represent the geometry of each layer and the domain size is 200 mm^2. The layer-wise input images for the turbine blade, jet engine compressor and jet engine bracket are shown in Figure 5.12.

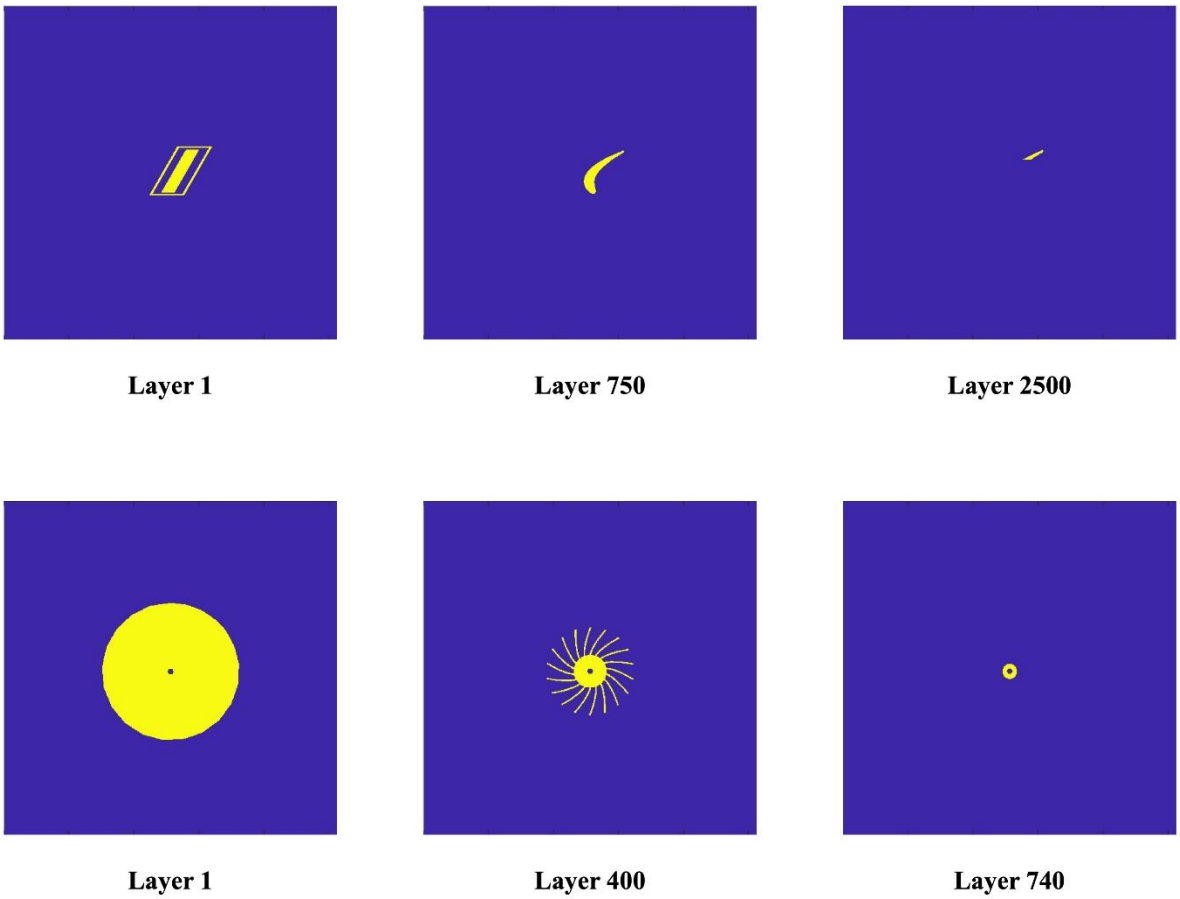

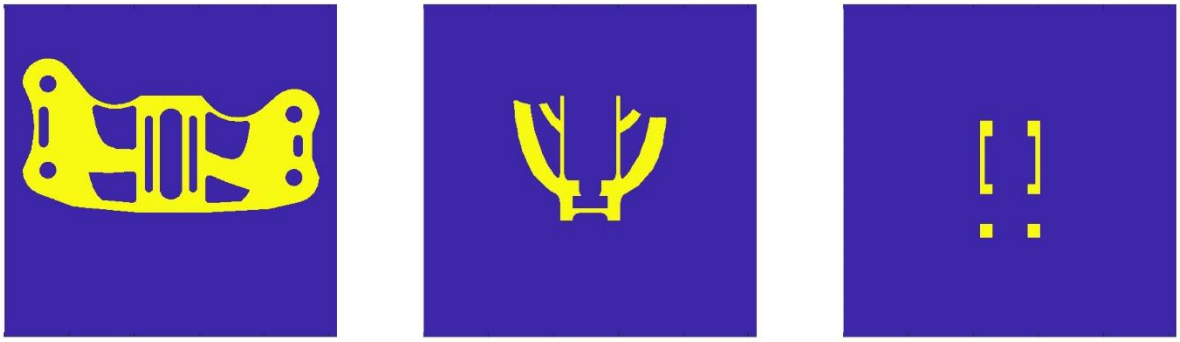

Figure 5.12: Input Layer-wise Geometry for (a). Turbine Blade; (b) Jet Engine Compressor Blade; (c) Jet Engine Bracket

The CNN-LSTM is trained with the part-scale simulation data discussed in Section 5.2.2. The performance of the trained CNN-LSTM is evaluated on test dataset and some of the prediction results for turbine blade and jet engine compressor blade are shown in Figure 5.13. It can be found in Figure 5.13 that the long-term temperature history predicted by CNN-LSTM as indicated by the orange curve has a very good agreement with the simulation data represented by the blue curve. For both the turbine blade and compressor blade, the CNN-LSTM could predict the temperature histories over 3 hours very accurately. The predicted temperatures are close to simulation data in both heating and cooling period.

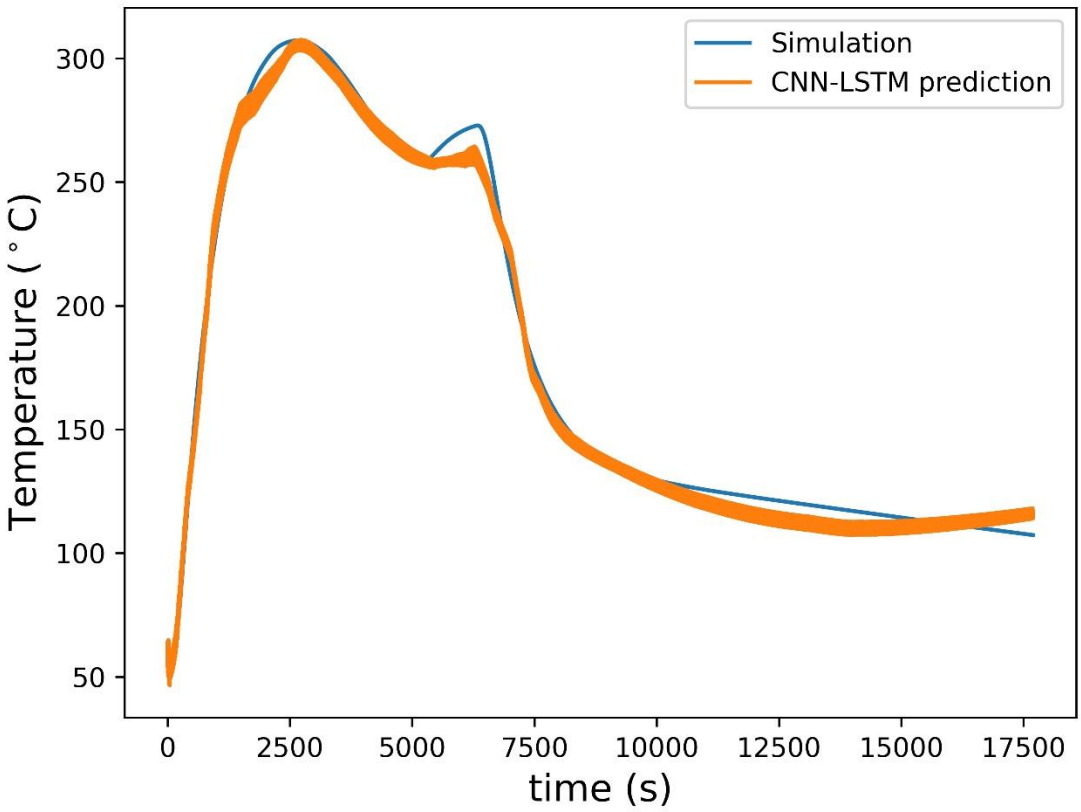
Simulation
CNN-LSTM prediction
Temperature (°C)
300
250
200
150
100
50
0
2500
5000
7500
10000
12500
15000
17500
time (s)

(a)

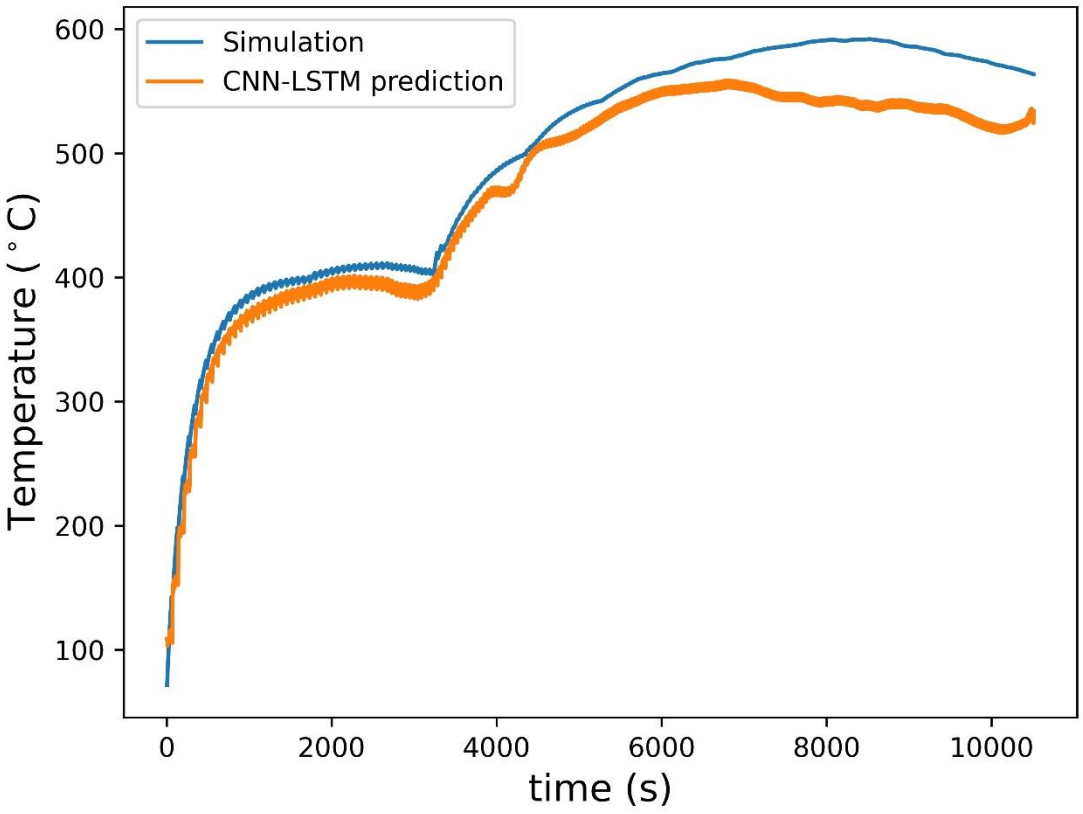

(b)

Figure 5.13: Temperature Prediction from the CNN-LSTM on Test Dataset for (a) Turbine Blade; (b) Compressor Blade

5.4 Conclusion

In this work, we developed two machine learning models, the RNN and CNN-LSTM model, to predict the thermal histories at different spatial and temporal scales for laser powder bed fusion. The RNN model uses multiple stacked layers of LSTM unit and could fit the thermal

history with rapid heating and cooling within a few milliseconds very well on test dataset. The CNN-LSTM network gives thermal histories at part-scale for the long-term heating and cooling. This model takes in the sliced geometry which is a grayscale image as input. This 512×512 image is processed by the convolutional layers to extract feature vector. This extracted feature vector is then fed into 3 layers of bidirectional LSTMs to consider the long-term dependency between building layers and output the temperature histories from a deep neural network.

To train the RNN model, we used the analytical solution to obtain the near-field temperature caused by direct interactions between material and laser beam. Part-scale simulation data by GPU-based matrix-free algorithm is used to train the CNN-LSTM model. When training both the RNN and CNN-LSTM networks, we noticed that there are some tricks that could significantly improve the model performance:

Initialization of the weights before training could reduce the epoch number for convergence and also avoid vanishing or exploding gradient issue when back propagation. We used orthogonal initialization for all the LSTM units and Kaiming uniform for the convolutional kernels before training.

Batch size also has an important impact on the model training. Increasing the batch size could make the gradient less stochastic and the variance between batches smaller. We recommended to use batch size larger than 4 even though larger batch size requires larger memory and longer training time in the iteration.

For the optimizer, we found Adam is the best option for RNN model and SGD for the CNN-LSTM.

The proposed CNN-LSTM has a complicated model architecture and consists of three parts: convolutional layers, multiple layers of LSTMS and a deep neural network. In the training,

we used three GPUS and distributed each part to one GPU which could improve the training efficiency and avoid potential out of memory issues.

Although the results from the proposed machine learning framework is encouraging, our method is subjected to a few limitations. Firstly, near-field temperature history is generated by analytical solution as a proof of concept. High resolution simulation data or in-situ monitoring temperatures can be employed for the training in the future. Additionally, the dataset to train the CNN-LSTM is small and only consists the simulation data of three geometries. This dataset can be extended in order to generalize. Lastly, more advanced NLP model, transformer that adopts attention mechanism [127] enables pretrained systems such as BERT (Bidirectional Encoder Representations from Transformers) by Google [128] and GPT-3 (Generative Pre-trained Transformers 3) by OpenAI. These networks are more powerful than the classical RNN used in this work to deal with time series sequences and can be applied to the thermal modeling for laser powder bed fusion as well.

6.0 Conclusions

6.1 Main Contributions

The research in this dissertation mainly focuses on the multiscale modeling on laser powder bed fusion process to predict the residual stress at part-scale and melt pool dynamics including melt pool dimension variation and porosity formation mechanisms at meso-scale. Machine learning technique is employed to fully exploit the existing simulation and experiment data and develop a data-driven framework for thermal history prediction. Path planning and optimization methodology is proposed based on the part-scale residual deformation model to tailor laser scanning orientation in order to reduce the residual deformation and build failures. The major contributions are summarized as follows:

(1) **An inherent strain-based simulation framework is developed to predict the residual stress and deformation at part-scale.** A meso-scale detailed process simulation model with three layers using Goldak's point heat source model is employed to extract the inherent strains via the modified inherent strain theory. The extracted inherent strains are applied as thermal expansion coefficients (CTEs) in a series of quasi-static equilibrium analysis to predict part-scale residual distortion and stress. Specifically, several physical layers are merged as one element layer and activated layer-by-layer with a unit temperature rise in a quasi-static analysis. The accuracy of the multiscale model has been determined via experimental measurement.

(2) **Multiphysics models including powder particles, solid substrate, moving laser and multiphase flow are developed to study the underlying mechanism for melt pool dimension variations and porosity formation due to laser process parameters and spattering particles.**

Discrete element method is employed to simulate the powder particle spreading and spattering process while laser welding simulation is performed for melt pool in conduction, transition and keyhole regimes and calibrated by *ex-situ* cross-sectional measurements. The specific contributions are as follows:

a) For melt pool in conduction regime, it is revealed by analytical solution that both melt pool width and depth only depend on heat conduction at low preheating temperature when the vapor depression does not penetrate the heat conduction zone. At higher preheating temperature, vapor depression becomes stronger and the semi-circular heat conduction zone is penetrated which leads to a deeper melt pool.

b) In transition regime, melt pool width increases with preheating temperature which is also attributed to enhanced heat conduction due to thermal conductivity being temperature dependent. Recoil pressure is the dominating factor for melt pool depth in transition regime. High preheating temperature increases the evaporation mass and leads to strong vapor depression.

c) In keyhole regime, melt pool with deeper penetration and narrower width is formed at higher preheating temperature. The keyhole front wall angle is found to increase with preheating temperature in simulation, indicating a stronger laser drilling rate at higher preheating temperature. Higher preheating temperature leads to deeper penetration depth, and therefore, increases the incidents of keyhole collapse and porosity defects. A possible explanation for the narrow melt pool width in keyhole regime at high preheating is the plume caused by vapor reflection pressure.

d) Preheating temperature also significantly elongate the melt track length. At higher preheating temperature, the backward melt flow originating from the laser hot spot driven by Marangoni force has larger velocity because higher preheating temperature leads to larger recoil

pressure and stronger vapor depression. The flow rate also increases at higher preheating temperature.

e) Two porosity formation mechanisms associated with spattering particles are revealed by the coupling simulation between laser welding and mass particles. The first one is the spattering particles falling into melt pool directly and leaving an un-melted or partially melted pores to the final product. The second mechanism is the particles near the melt track are dragged to the melt pool bead and partially melted due to heat conduction. This partially melted particles can be reserved as well in the as-built part.

3) **Path planning and optimization methodology is proposed for continuous scanning strategy and island scanning pattern to reduce residual deformation for as-built part.** Inherent strain depending on laser or electron beam scan orientation is employed to efficiently predict the deformation caused by powder particle melting and solidification. Part deformation is obtained from a multi-step static equilibrium analysis including layer-by-layer activation and cutting off at last step. Since post removal after building is considered in both finite element and sensitivity analysis, deformation of the as-built part after cutting off the build platform is minimized directly in the optimization. Experimental validations for the designed patterns are conducted on an open-architecture machine. The fabrication experiments demonstrated that the residual deformation of parts fabricated by optimized scanning pattern can be reduced by over 50% compared to the initial scanning patterns, which demonstrate the effectiveness of the proposed method.

4) **Data-driven and real-time thermal history prediction at part-scale.** Machine learning technique is employed to fully exploit the existing simulation and experiment data to predict complete thermal history during L-PBF process. The RNN model uses multiple stacked

layers of LSTM unit and could fit the thermal history with rapid heating and cooling within a few milliseconds very well on test dataset. The CNN-LSTM network gives thermal histories at part-scale for the long-term heating and cooling. This model takes in the sliced geometry which is a grayscale image as input. This 512×512 image is processed by the convolutional layers to extract feature vector. This extracted feature vector is then fed into 3 layers of bidirectional LSTMs to consider the long-term dependency between building layers and output the temperature histories from a deep neural network

6.2 Future Work

Although the meso-scale and part-scale simulation models, path planning and optimization method and data-driven framework based on machine learning techniques have been extensively studied in the dissertation and calibrated by various experiments including part distortion measurement and *ex-situ* melt pool cross-sections, there is still a lot of room to further establish the proposed models and frameworks. The potential future works in this dissertation are summarized below:

1) **Residual deformation and stress prediction at part-scale.** For future work, in order to improve part-scale distortion prediction accuracy, the varying thermal effects of part geometry on inherent strain values should be considered Since the layers at different height for a large AM part may experience varying thermal history due to difference in layer geometry and heat accumulation by previous layers. Besides, the micro-scale detailed process simulation model only simulates the core-skin scanning in each layer but neglects the contour scanning which has higher laser scanning velocity and lower power. The effect of neglecting contour scanning in the inherent

strain model on the surface stress prediction has not been quantified. Additionally, for part-scale simulation, investigations on issues, such as effects of layer lumping and numerical stability on highly complex parts, will be the focus of future investigation to improve the prediction accuracy and efficiency.

2) **Multiphysics modeling at meso-scale.** cold powder particles from reservoir which are usually not heated and the variation of powder layer thickness should be considered. More detailed multi-physics model will be developed comprehensively in order to simulate the powder particle spreading on preheated surface, multiple laser reflections inside the powder bed, nonuniform powder bed and particle motion such as spattering. A more advanced in-situ monitoring system will be beneficial to obtaining more accurate temperature profiles within the melt region. The more detailed multi-physics simulation and real time data by the in-situ monitoring system is expected to provide much more detailed physical insights into melt pool formation and morphology variation. This can aid in process parameter selection which aims to prevent defects and increase the overall quality of parts fabricated via L-PBF processes.

3) **Path planning design.** high performance computing techniques such as GPU-based finite element analysis could be employed to optimize the scan pattern of physical layers, instead of merged layers, for further residual deformation minimization. Layer-wise rotation or shift is usually employed in the real building process with island scanning strategy and has been reported to be effective in residual stress reduction. Layer-wise rotation angle and shifting distance can be another design variable to optimize as part of the future work. Although deformation comparison shows the effectiveness of this method, the accuracy of finite element analysis can still be improved by taking plasticity into consideration, which will make the sensitivity analysis much

more challenging as well. In addition to residual deformation, the influence of optimized scanning patterns on microstructures, defects and build efficiency is also worth to investigate.

4) **Data-driven and real-time thermal histories prediction at part-scale.** Although the results from the proposed machine learning framework is encouraging, our method is subjected to a few limitations. Firstly, near-field temperature history is generated by analytical solution as a proof of concept. High resolution simulation data or in-situ monitoring temperatures can be employed for the training in the future. Additionally, the dataset to train the CNN-LSTM is small and only consists the simulation data of three geometries. This dataset can be extended in order to generalize. Lastly, more advanced NLP model, transformer that adopts attention mechanism [127] enables pretrained systems such as BERT (Bidirectional Encoder Representations from Transformers) by Google [128] and GPT-3 (Generative Pre-trained Transformers 3) by OpenAI. These networks are more powerful than the classical RNN used in this work to deal with time series sequences and can be applied to the thermal modeling for laser powder bed fusion as well.

Appendix A Melt Pool Dimensions

The *ex-situ* cross-sectional measurement data for single tracks under the power of 200 W, 250 W, 285 W and 300 W, and scan speed of 0.5 m/s, 0.75 m/s, 1 m/s and 1.5 m/s at the preheating temperature of 100 °C, 200 °C, 300 °C, 400 °C and 500 °C are summarized in Appendix Table 1.

Appendix Table 1 Melt Pool Dimensions at Different Preheating Temperature

Sample	Power (W)	Velocity (m/s)	100 °C		200 °C		300 °C		400 °C		500 °C	
			Width (μm)	Depth (μm)	Width (μm)	Depth (μm)	Width (μm)	Depth (μm)	Width (μm)	Depth (μm)	Width (μm)	Depth (μm)
1	200	1.50	110.13	50.22	111.89	54.19	128.63	58.59	128.67	69.60	117.62	65.64
2		1.00	107.72	66.67	111.58	75.44	115.09	78.95	129.47	86.67	130.87	94.74
3		0.75	137.89	106.67	138.47	100.70	144.21	107.02	167.02	132.98	153.68	135.44
4		0.50	165.96	179.65	171.93	172.98	188.77	193.33	189.82	209.81	177.19	234.74
5	250	1.50	113.66	59.74	122.91	61.24	130.40	74.01	129.96	86.78	131.28	88.99
6		1.00	114.16	96.46	132.30	101.76	136.28	102.65	151.33	125.66	150.44	128.32
7		0.75	162.83	131.42	156.63	127.43	169.47	150.00	165.93	162.83	161.50	176.11
8		0.50	186.73	243.36	186.77	236.28	201.77	258.41	172.57	295.58	176.99	300.89
9	285	1.50	122.47	73.57	126.43	74.89	127.31	84.14	125.55	102.64	139.65	95.59
10		1.00	129.20	118.14	132.74	111.50	140.26	120.35	140.71	136.28	153.98	154.87
11		0.75	158.41	163.27	165.93	165.49	189.38	182.74	180.53	204.87	169.47	200.00
12		0.50	161.94	271.68	184.07	259.29	202.65	292.92	192.04	340.71	191.92	353.98
13	350	1.50	128.63	98.24	134.80	96.92	139.65	113.66	131.28	121.15	135.68	130.40
14		1.00	150.89	147.35	138.50	134.51	153.10	156.64	157.52	180.53	166.37	182.30
15		0.75	176.99	200.89	180.53	187.61	177.88	209.73	172.57	243.36	171.68	252.21
16		0.50	161.95	343.36	206.19	340.71	199.12	377.88	181.42	407.96	184.96	457.52

Based on the melt pool *ex-situ* measurement data in Appendix Table 1, processing map of met pool depth in P-V and preheating temperature space is constructed as shown in Appendix Figure 1. The constructed processing map clearly captures the melt pool depth behavior as a function of preheating temperature.

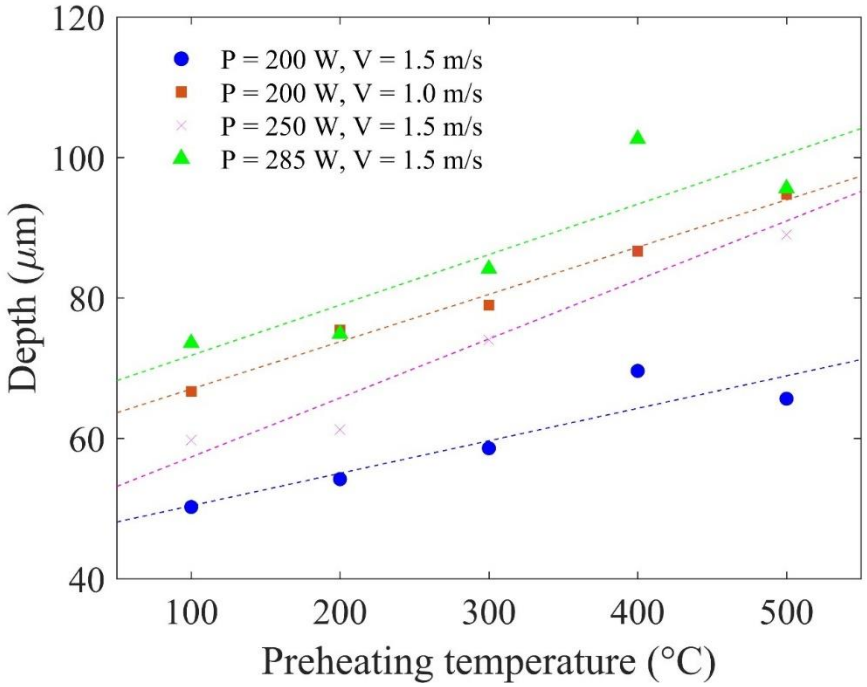

(a) conduction regime

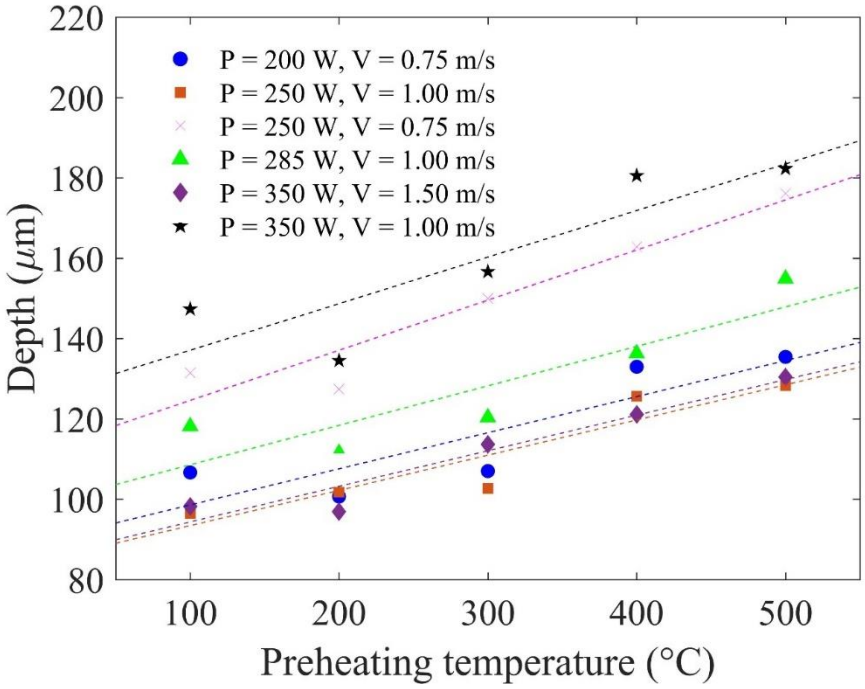

(b) transition regime

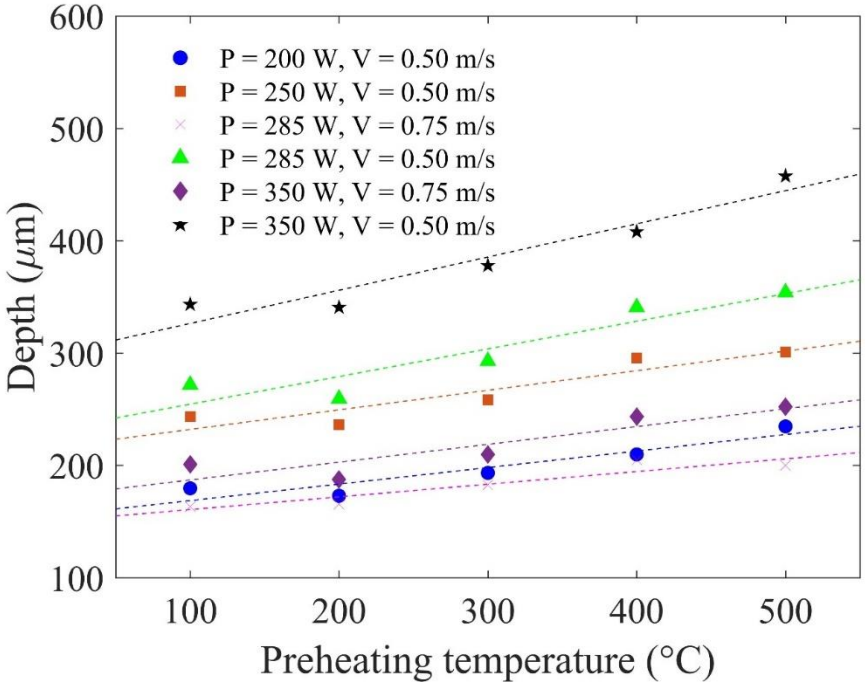

(c) keyhole regime

Appendix Figure 1 Melt Pool Depth across the P-V and Preheating Temperature Space

Appendix B Derivation for the Volumetric Heat Generation Rate

The Goldak's double ellipsoid heat source model is widely used to model the moving heat source in welding and additive manufacturing process:

$$Q = \frac{6\sqrt{3}P\eta}{abc\pi\sqrt{\pi}} exp\left(-3\frac{(x_0+v_s t-x)^2}{a^2} - 3\frac{(y_0-y)^2}{b^2} - 3\frac{(z_0-z)^2}{c^2}\right) \quad (1)$$

where P is the power; V is the scan speed; η is the absorptivity; a and b represent the beam spot size and c is the penetration depth. In this study, all the columns with different height is built under EOS M290 default parameters where is 285W, V is 1m/s, the beam spot size a and b is 50μm and the penetration depth c is 120μm which equals to the thickness of three layers. The absorptivity is set to be 0.72 after experiment calibration.

By averaging the energy input over the scan line, we can get the time average line input (W/m^3):

$$\bar{Q} = \frac{1}{\Delta t}\int_0^{t_{end}} Q\, dt = \frac{3P\eta}{\pi bc\, v_s \Delta t} exp\left(-3\frac{y^2}{b^2} - 3\frac{z^2}{c^2}\right)\left\{erf\left[\frac{\sqrt{3}(x_{end}-x)}{a}\right] - erf\left[\frac{\sqrt{3}(x_{start}-x)}{a}\right]\right\} \quad (2)$$

By taking spatial integration, we can get the equivalent heat input of one scan line (W):

$$\tilde{Q} = \int_{-\infty}^{+\infty}\int_{-\infty}^{+\infty}\int_{-\infty}^{-\infty} \bar{Q}\, dxdydz \approx \int_0^c \int_{-b/2}^{b/2}\int_{-a/2}^{a/2} \bar{Q}\, dxdydz \quad (3)$$

The integration along y and z direction can be obtained easily from Eq. (4) and Eq. (5):

$$\int_{-b/2}^{b/2} e^{\left(-3\frac{y^2}{b^2}\right)} dy = \frac{b}{\sqrt{3}}\int_{-\sqrt{3}/2}^{\sqrt{3}/2} e^{(-t^2)}\, dt = \frac{b\sqrt{\pi}}{2\sqrt{3}} \cdot \left[\mathrm{erf}\left(\frac{\sqrt{3}}{2}\right) - \mathrm{erf}\left(-\frac{\sqrt{3}}{2}\right)\right] \quad (4)$$

$$\int_0^c e^{\left(-3\frac{z^2}{c^2}\right)} dz = \frac{c}{\sqrt{3}}\int_0^{\sqrt{3}} e^{(-t^2)}\, dt = \frac{c\sqrt{\pi}}{2\sqrt{3}} \cdot \mathrm{erf}(\sqrt{3}) \quad (5)$$

Therefore, the equivalent heat input $\tilde{Q}$ for a scan line in Eq. (3) can be rewritten as:

$$\tilde{Q} = \frac{4P\eta}{v_s \Delta t} \cdot \mathrm{erf}(\sqrt{3}) \cdot \left[\mathrm{erf}\left(\frac{\sqrt{3}}{2}\right) - \mathrm{erf}\left(-\frac{\sqrt{3}}{2}\right)\right] \int_{-a/2}^{a/2} \left\{\mathrm{erf}\left[\frac{\sqrt{3}(x_{end} - x)}{a}\right] - \mathrm{erf}\left[\frac{\sqrt{3}(x_{start} - x)}{a}\right]\right\} dx \quad (6)$$

The integration part in Eq. (6) is solved numerically and the total equivalent heat input within one layer can be obtained by summing up all the scan lines. The volumetric heat generation rate is the ratio of sum of equivalent heat input of each line over the three times of layer volume because of the penetration depth:

$$Q_V = \frac{\sum_{i=1}^{n} \tilde{Q}_i}{3 * V_{layer}} \quad (7)$$

Bibliography

[1] I. Astm, ASTM52900-15 Standard Terminology for Additive Manufacturing—General Principles—Terminology, ASTM International, West Conshohocken, PA 3(4) (2015) 5.

[2] W.E. King, A.T. Anderson, R.M. Ferencz, N.E. Hodge, C. Kamath, S.A. Khairallah, A.M. Rubenchik, Laser powder bed fusion additive manufacturing of metals; physics, computational, and materials challenges, Applied Physics Reviews 2(4) (2015) 041304.

[3] W. Yan, Y. Lu, K. Jones, Z. Yang, J. Fox, P. Witherell, G. Wagner, W.K. Liu, Data-driven characterization of thermal models for powder-bed-fusion additive manufacturing, Additive Manufacturing (2020) 101503.

[4] K. Dai, L. Shaw, Thermal and stress modeling of multi-material laser processing, Acta Materialia 49(20) (2001) 4171-4181.

[5] K. Dai, L. Shaw, Distortion minimization of laser-processed components through control of laser scanning patterns, Rapid Prototyping Journal 8(5) (2002) 270-276.

[6] S.S. Bo Cheng, Kevin Chou, Stress and deformation evaluations of scanning strategy effect in selective laser melting, Additive Manufacturing (2017).

[7] C. Fu, Y. Guo, Three-dimensional temperature gradient mechanism in selective laser melting of Ti-6Al-4V, Journal of Manufacturing Science and Engineering 136(6) (2014) 061004.

[8] P. Prabhakar, W.J. Sames, R. Dehoff, S.S. Babu, Computational modeling of residual stress formation during the electron beam melting process for Inconel 718, Additive Manufacturing 7 (2015) 83-91.

[9] A. Hussein, L. Hao, C. Yan, R. Everson, Finite element simulation of the temperature and stress fields in single layers built without-support in selective laser melting, Materials & Design (1980-2015) 52 (2013) 638-647.

[10] P.Z. Qingcheng Yang, Lin Cheng, Zheng Min, Minking Chyu, Albert C. To, articleFinite element modeling and validation of thermomechanicalbehavior of Ti-6Al-4V in directed energy deposition additivemanufacturing, Additive Manufacturing (2016).

[11] E.R. Denlinger, J. Irwin, P. Michaleris, Thermomechanical Modeling of Additive Manufacturing Large Parts, Journal of Manufacturing Science and Engineering 136(6) (2014) 061007.

[12] E.R. Denlinger, M. Gouge, J. Irwin, P. Michaleris, Thermomechanical model development and in situ experimental validation of the Laser Powder-Bed Fusion process, Additive Manufacturing 16 (2017) 73-80.

[13] V.J. Erik R Denlinger, G.V. Srinivasan, Tahany EI-Wardany, Pan Michaleris, Thermal modeling of Inconel 718 processed with powder bed fusionand experimental validation using in situ measurements, Additive Manufacturing 11 (2016) 7-15.

[14] N. Patil, D. Pal, H.K. Rafi, K. Zeng, A. Moreland, A. Hicks, D. Beeler, B. Stucker, A Generalized Feed Forward Dynamic Adaptive Mesh Refinement and Derefinement Finite Element Framework for Metal Laser Sintering—Part I: Formulation and Algorithm Development, Journal of Manufacturing Science and Engineering 137(4) (2015) 041001.

[15] D. Pal, N. Patil, K.H. Kutty, K. Zeng, A. Moreland, A. Hicks, D. Beeler, B. Stucker, A Generalized Feed-Forward Dynamic Adaptive Mesh Refinement and Derefinement Finite-Element Framework for Metal Laser Sintering—Part II: Nonlinear Thermal Simulations and Validations, Journal of Manufacturing Science and Engineering 138(6) (2016) 061003.

[16] N. Keller, V. Ploshikhin, New method for fast predictions of residual stress and distortion of AM parts, Solid Freeform Fabrication Symposium, Austin, Texas, 2014, pp. 1229-1237.

[17] S.A. Khairallah, A.T. Anderson, A. Rubenchik, W.E. King, Laser powder-bed fusion additive manufacturing: Physics of complex melt flow and formation mechanisms of pores, spatter, and denudation zones, Acta Materialia 108 (2016) 36-45.

[18] M.J. Matthews, G. Guss, S.A. Khairallah, A.M. Rubenchik, P.J. Depond, W.E. King, Denudation of metal powder layers in laser powder bed fusion processes, Acta Materialia 114 (2016) 33-42.

[19] A.A. Martin, N.P. Calta, S.A. Khairallah, J. Wang, P.J. Depond, A.Y. Fong, V. Thampy, G.M. Guss, A.M. Kiss, K.H. Stone, Dynamics of pore formation during laser powder bed fusion additive manufacturing, Nature communications 10(1) (2019) 1987.

[20] R. Shi, S.A. Khairallah, T.T. Roehling, T.W. Heo, J.T. McKeown, M.J. Matthews, Microstructural control in metal laser powder bed fusion additive manufacturing using laser beam shaping strategy, Acta Materialia (2019).

[21] S.A. Khairallah, A.A. Martin, J.R. Lee, G. Guss, N.P. Calta, J.A. Hammons, M.H. Nielsen, K. Chaput, E. Schwalbach, M.N. Shah, Controlling interdependent meso-nanosecond dynamics and defect generation in metal 3D printing, Science 368(6491) (2020) 660-665.

[22] W. Yan, W. Ge, Y. Qian, S. Lin, B. Zhou, W.K. Liu, F. Lin, G.J. Wagner, Multi-physics modeling of single/multiple-track defect mechanisms in electron beam selective melting, Acta Materialia 134 (2017) 324-333.

[23] S. Shrestha, Y. Kevin Chou, A Numerical Study on the Keyhole Formation During Laser Powder Bed Fusion Process, Journal of Manufacturing Science and Engineering 141(10) (2019).

[24] S. Shrestha, B. Cheng, K. Chou, An Investigation into Melt Pool Effective Thermal Conductivity for Thermal Modeling of Powder-Bed Electron Beam Additive Manufacturing.

[25] D. Rosenthal, Mathematical theory of heat distribution during welding and cutting, Welding journal 20 (1941) 220-234.

[26] P. Promoppatum, S.-C. Yao, P.C. Pistorius, A.D. Rollett, A comprehensive comparison of the analytical and numerical prediction of the thermal history and solidification microstructure of Inconel 718 products made by laser powder-bed fusion, Engineering 3(5) (2017) 685-694.

[27] M. Tang, P.C. Pistorius, J.L. Beuth, Prediction of lack-of-fusion porosity for powder bed fusion, Additive Manufacturing 14 (2017) 39-48.

[28] T. Moran, P. Li, D. Warner, N. Phan, Utility of superposition-based finite element approach for part-scale thermal simulation in additive manufacturing, Additive Manufacturing 21 (2018) 215-219.

[29] Y. Yang, M. Knol, F. van Keulen, C. Ayas, A semi-analytical thermal modelling approach for selective laser melting, Additive Manufacturing 21 (2018) 284-297.

[30] B. Cheng, S. Shrestha, K. Chou, Stress and deformation evaluations of scanning strategy effect in selective laser melting, Additive Manufacturing 12 (2016) 240-251.

[31] L.H. Ahmed Hussein, Chunze Yan, Richard Everson, Finite element simulation of the temperature and stress fields in single layers built without-support in selective laser melting, Materials and Design 52 (2013) 638-647.

[32] H. Peng, D.B. Go, R. Billo, S. Gong, M.R. Shankar, B.A. Gatrell, J. Budzinski, P. Ostiguy, R. Attardo, C. Tomonto, Part-scale model for fast prediction of thermal distortion in DMLS additive manufacturing; Part 2: a quasi-static thermo-mechanical model, Austin, Texas (2016).

[33] M.F. Zaeh, G. Branner, Investigations on residual stresses and deformations in selective laser melting, Production Engineering 4(1) (2010) 35-45.

[34] C. Li, C. Fu, Y. Guo, F. Fang, A multiscale modeling approach for fast prediction of part distortion in selective laser melting, Journal of Materials Processing Technology 229 (2016) 703-712.

[35] C. Li, Z. Liu, X. Fang, Y. Guo, On the Simulation Scalability of Predicting Residual Stress and Distortion in Selective Laser Melting, Journal of Manufacturing Science and Engineering 140(4) (2018) 041013.

[36] S. Afazov, W.A. Denmark, B.L. Toralles, A. Holloway, A. Yaghi, Distortion Prediction and Compensation in Selective Laser Melting, Additive Manufacturing 17 (2017) 15-22.

[37] Y. Lee, W. Zhang, Modeling of heat transfer, fluid flow and solidification microstructure of nickel-base superalloy fabricated by laser powder bed fusion, Additive Manufacturing 12 (2016) 178-188.

[38] L. Scime, J. Beuth, A multi-scale convolutional neural network for autonomous anomaly detection and classification in a laser powder bed fusion additive manufacturing process, Additive Manufacturing 24 (2018) 273-286.

[39] L. Scime, J. Beuth, Using machine learning to identify in-situ melt pool signatures indicative of flaw formation in a laser powder bed fusion additive manufacturing process, Additive Manufacturing 25 (2019) 151-165.

[40] X. Xie, J. Bennett, S. Saha, Y. Lu, J. Cao, W.K. Liu, Z. Gan, Mechanistic data-driven prediction of as-built mechanical properties in metal additive manufacturing, npj Computational Materials 7(1) (2021) 1-12.

[41] C. Wang, X. Tan, S. Tor, C. Lim, Machine learning in additive manufacturing: State-of-the-art and perspectives, Additive Manufacturing (2020) 101538.

[42] J. Li, R. Jin, Z.Y. Hang, Integration of physically-based and data-driven approaches for thermal field prediction in additive manufacturing, Materials & Design 139 (2018) 473-485.

[43] M. Mozaffar, A. Paul, R. Al-Bahrani, S. Wolff, A. Choudhary, A. Agrawal, K. Ehmann, J. Cao, Data-driven prediction of the high-dimensional thermal history in directed energy deposition processes via recurrent neural networks, Manufacturing letters 18 (2018) 35-39.

[44] A. Paul, M. Mozaffar, Z. Yang, W.-k. Liao, A. Choudhary, J. Cao, A. Agrawal, A real-time iterative machine learning approach for temperature profile prediction in additive manufacturing processes, 2019 IEEE International Conference on Data Science and Advanced Analytics (DSAA), IEEE, 2019, pp. 541-550.

[45] S. Clijsters, T. Craeghs, J.-P. Kruth, A priori process parameter adjustment for SLM process optimization, Innovative developments on virtual and physical prototyping, Taylor & Francis Group., 2012, pp. 553-560.

[46] R. Mertens, S. Clijsters, K. Kempen, J.-P. Kruth, Optimization of scan strategies in selective laser melting of aluminum parts with downfacing areas, Journal of Manufacturing Science and Engineering 136(6) (2014) 061012.

[47] J.-P. Kruth, J. Deckers, E. Yasa, R. Wauthlé, Assessing and comparing influencing factors of residual stresses in selective laser melting using a novel analysis method, Proceedings of the institution of mechanical engineers, Part B: Journal of Engineering Manufacture 226(6) (2012) 980-991.

[48] Y. Lu, S. Wu, Y. Gan, T. Huang, C. Yang, L. Junjie, J. Lin, Study on the microstructure, mechanical property and residual stress of SLM Inconel-718 alloy manufactured by differing island scanning strategy, Optics & Laser Technology 75 (2015) 197-206.

[49] E. Foroozmehr, R. Kovacevic, Effect of path planning on the laser powder deposition process: thermal and structural evaluation, The International Journal of Advanced Manufacturing Technology 51(5-8) (2010) 659-669.

[50] L.H. Ahmed Hussein, Chunze Yan, Richard Everson, Finite element simulation of the temperature and stress fields in single layers built without-support in selective laser melting, Materials and Design (2013).

[51] J.-P. Kruth, M. Badrossamay, E. Yasa, J. Deckers, L. Thijs, J. Van Humbeeck, Part and material properties in selective laser melting of metals, Proceedings of the 16th international symposium on electromachining, 2010, pp. 1-12.

[52] L. Thijs, K. Kempen, J.-P. Kruth, J. Van Humbeeck, Fine-structured aluminium products with controllable texture by selective laser melting of pre-alloyed AlSi10Mg powder, Acta Materialia 61(5) (2013) 1809-1819.

[53] D. Ding, Z.S. Pan, D. Cuiuri, H. Li, A tool-path generation strategy for wire and arc additive manufacturing, The international journal of advanced manufacturing technology 73(1-4) (2014) 173-183.

[54] B.E. Carroll, T.A. Palmer, A.M. Beese, Anisotropic tensile behavior of Ti–6Al–4V components fabricated with directed energy deposition additive manufacturing, Acta Materialia 87 (2015) 309-320.

[55] D. Ding, Z. Pan, D. Cuiuri, H. Li, A practical path planning methodology for wire and arc additive manufacturing of thin-walled structures, Robotics and Computer-Integrated Manufacturing 34 (2015) 8-19.

[56] D. Ding, Z. Pan, D. Cuiuri, H. Li, S. van Duin, N. Larkin, Bead modelling and implementation of adaptive MAT path in wire and arc additive manufacturing, Robotics and Computer-Integrated Manufacturing 39 (2016) 32-42.

[57] R. Ponche, O. Kerbrat, P. Mognol, J.-Y. Hascoet, A novel methodology of design for Additive Manufacturing applied to Additive Laser Manufacturing process, Robotics and Computer-Integrated Manufacturing 30(4) (2014) 389-398.

[58] D.E. Smith, R. Hoglund, Continuous fiber angle topology optimization for polymer fused fillament fabrication, Annu. Int. Solid Free. Fabr. Symp. Austin, TX, 2016.

[59] J. Liu, J. Liu, H. Yu, H. Yu, Concurrent deposition path planning and structural topology optimization for additive manufacturing, Rapid Prototyping Journal 23(5) (2017) 930-942.

[60] Q. Xia, T. Shi, Optimization of composite structures with continuous spatial variation of fiber angle through Shepard interpolation, Composite Structures 182 (2017) 273-282.

[61] C. Kiyono, E. Silva, J. Reddy, A novel fiber optimization method based on normal distribution function with continuously varying fiber path, Composite Structures 160 (2017) 503-515.

[62] C.J. Brampton, K.C. Wu, H.A. Kim, New optimization method for steered fiber composites using the level set method, Structural and Multidisciplinary Optimization 52(3) (2015) 493-505.

[63] J. Liu, A.C. To, Deposition path planning-integrated structural topology optimization for 3D additive manufacturing subject to self-support constraint, Computer-Aided Design 91 (2017) 27-45.

[64] H. Shen, J. Fu, Z. Chen, Y. Fan, Generation of offset surface for tool path in NC machining through level set methods, The International Journal of Advanced Manufacturing Technology 46(9-12) (2010) 1043-1047.

[65] C. Zhuang, Z. Xiong, H. Ding, High speed machining tool path generation for pockets using level sets, International Journal of Production Research 48(19) (2010) 5749-5766.

[66] K.C. Mills, Recommended values of thermophysical properties for selected commercial alloys, Woodhead Publishing2002.

[67] S.S. Sih, J.W. Barlow, The prediction of the emissivity and thermal conductivity of powder beds, Particulate Science and Technology 22(4) (2004) 427-440.

[68] L. Dong, A. Makradi, S. Ahzi, Y. Remond, Three-dimensional transient finite element analysis of the selective laser sintering process, Journal of materials processing technology 209(2) (2009) 700-706.

[69] J.J. Beaman, J.W. Barlow, D.L. Bourell, R.H. Crawford, H.L. Marcus, K.P. McAlea, Solid freeform fabrication: a new direction in manufacturing, Kluwer Academic Publishers, Norwell, MA 2061 (1997) 25-49.

[70] G. Bugeda Miguel Cervera, G. Lombera, Numerical prediction of temperature and density distributions in selective laser sintering processes, Rapid Prototyping Journal 5(1) (1999) 21-26.

[71] T. Mukherjee, W. Zhang, T. DebRoy, An improved prediction of residual stresses and distortion in additive manufacturing, Computational Materials Science 126 (2017) 360-372.

[72] A.J. Dunbar, E.R. Denlinger, M.F. Gouge, P. Michaleris, Experimental validation of finite element modeling for laser powderbed fusion deformation, Additive Manufacturing 12 (2016) 108-120.

[73] J. Goldak, A. Chakravarti, M. Bibby, A new finite element model for welding heat sources, Metallurgical and Materials Transactions B 15(2) (1984) 299-305.

[74] J. Liu, Q. Chen, Y. Zhao, W. Xiong, A. To, Quantitative Texture Prediction of Epitaxial Columnar Grains in Alloy 718 Processed by Additive Manufacturing, Proceedings of the 9th International Symposium on Superalloy 718 & Derivatives: Energy, Aerospace, and Industrial Applications, Springer, 2018, pp. 749-755.

[75] J. Irwin, P. Michaleris, A line heat input model for additive manufacturing, Journal of Manufacturing Science and Engineering 138(11) (2016) 111004.

[76] M. Gouge, J. Heigel, P. Michaleris, T. Palmer, Modeling forced convection in the thermal simulation of laser cladding processes, International Journal of Advanced Manufacturing Technology 79 (2015).

[77] J. Heigel, P. Michaleris, E. Reutzel, Thermo-mechanical model development and validation of directed energy deposition additive manufacturing of Ti–6Al–4V, Additive manufacturing 5 (2015) 9-19.

[78] E.R. Denlinger, J.C. Heigel, P. Michaleris, Residual stress and distortion modeling of electron beam direct manufacturing Ti-6Al-4V, Proceedings of the Institution of Mechanical Engineers, Part B: Journal of Engineering Manufacture 229(10) (2015) 1803-1813.

[79] X. Liang, Q. Chen, L. Cheng, Q. Yang, A. To, A modified inherent strain method for fast prediction of residual deformation in additive manufacturing of metal parts, 2017 Solid Freeform Fabrication Symposium Proceedings, Austin, Texas, 2017.

[80] X. Liang, L. Cheng, Q. Chen, Q. Yang, A. To, A Modified Method for Estimating Inherent Strains from Detailed Process Simulation for Fast Residual Distortion Prediction of Single-Walled Structures Fabricated by Directed Energy Deposition, Additive Manufacturing 23 (2018) 471-486.

[81] L. Sochalski-Kolbus, E.A. Payzant, P.A. Cornwell, T.R. Watkins, S.S. Babu, R.R. Dehoff, M. Lorenz, O. Ovchinnikova, C. Duty, Comparison of residual stresses in Inconel 718 simple parts made by electron beam melting and direct laser metal sintering, Metallurgical and Materials Transactions A 46(3) (2015) 1419-1432.

[82] P. Mercelis, J.-P. Kruth, Residual stresses in selective laser sintering and selective laser melting, Rapid Prototyping Journal 12(5) (2006) 254-265.

[83] N. Hodge, R. Ferencz, J. Solberg, Implementation of a thermomechanical model for the simulation of selective laser melting, Computational Mechanics 54(1) (2014) 33-51.

[84] A.S. Wu, D.W. Brown, M. Kumar, G.F. Gallegos, W.E. King, An experimental investigation into additive manufacturing-induced residual stresses in 316L stainless steel, Metallurgical and Materials Transactions A 45(13) (2014) 6260-6270.

[85] C. Li, J. liu, Y. Guo, Efficient predictive model of part distortion and residual stress in selective laser melting, Solid Freeform Fabrication 2016, 2017.

[86] Y. Zhao, Y. Koizumi, K. Aoyagi, D. Wei, K. Yamanaka, A. Chiba, Molten pool behavior and effect of fluid flow on solidification conditions in selective electron beam melting (SEBM) of a biomedical Co-Cr-Mo alloy, Additive Manufacturing 26 (2019) 202-214.

[87] J.-H. Cho, S.-J. Na, Implementation of real-time multiple reflection and Fresnel absorption of laser beam in keyhole, Journal of Physics D: Applied Physics 39(24) (2006) 5372.

[88] Q. Guo, C. Zhao, M. Qu, L. Xiong, L.I. Escano, S.M.H. Hojjatzadeh, N.D. Parab, K. Fezzaa, W. Everhart, T. Sun, In-situ characterization and quantification of melt pool variation under constant input energy density in laser powder-bed fusion additive manufacturing process, Additive Manufacturing (2019).

[89] E. Assuncao, S. Williams, D. Yapp, Interaction time and beam diameter effects on the conduction mode limit, Optics and Lasers in Engineering 50(6) (2012) 823-828.

[90] R. Cunningham, C. Zhao, N. Parab, C. Kantzos, J. Pauza, K. Fezzaa, T. Sun, A.D. Rollett, Keyhole threshold and morphology in laser melting revealed by ultrahigh-speed x-ray imaging, Science 363(6429) (2019) 849-852.

[91] W. Tan, N.S. Bailey, Y.C. Shin, Investigation of keyhole plume and molten pool based on a three-dimensional dynamic model with sharp interface formulation, Journal of Physics D: Applied Physics 46(5) (2013) 055501.

[92] W. Tan, Y.C. Shin, Analysis of multi-phase interaction and its effects on keyhole dynamics with a multi-physics numerical model, Journal of Physics D: Applied Physics 47(34) (2014) 345501.

[93] R. Fabbro, K. Chouf, Keyhole modeling during laser welding, Journal of applied Physics 87(9) (2000) 4075-4083.

[94] Q. Guo, C. Zhao, M. Qu, L. Xiong, S.M.H. Hojjatzadeh, L.I. Escano, N.D. Parab, K. Fezzaa, T. Sun, L. Chen, In-situ full-field mapping of melt flow dynamics in laser metal additive manufacturing, Additive Manufacturing 31 (2020) 100939.

[95] Y. Ueda, K. Fukuda, K. Nakacho, S. Endo, A new measuring method of residual stresses with the aid of finite element method and reliability of estimated values, Journal of the Society of Naval Architects of Japan 1975(138) (1975) 499-507.

[96] M.R. Hill, D.V. Nelson, The inherent strain method for residual stress determination and its application to a long welded joint, ASME-PUBLICATIONS-PVP 318 (1995) 343-352.

[97] H. Murakawa, Y. Luo, Y. Ueda, Prediction of welding deformation and residual stress by elastic FEM based on inherent strain, Journal of the society of Naval Architects of Japan 1996(180) (1996) 739-751.

[98] M. Yuan, Y. Ueda, Prediction of residual stresses in welded T-and I-joints using inherent strains, Journal of Engineering Materials and Technology, Transactions of the ASME 118(2) (1996) 229-234.

[99] L. Zhang, P. Michaleris, P. Marugabandhu, Evaluation of applied plastic strain methods for welding distortion prediction, Journal of Manufacturing Science and Engineering 129(6) (2007) 1000-1010.

[100] M. Bugatti, Q. Semeraro, Limitations of the Inherent Strain Method in Simulating Powder Bed Fusion Processes, Additive Manufacturing 23 (2018) 329-346.

[101] L. Cheng, X. Liang, J. Bai, Q. Chen, J. Lemon, A. To, On Utilizing Topology Optimization to Design Support Structure to Prevent Residual Stress Induced Build Failure in Laser Powder Bed Metal Additive Manufacturing, Additive Manufacturing (2019).

[102] Q. Chen, X. Liang, D. Hayduke, J. Liu, L. Cheng, J. Oskin, R. Whitmore, A.C. To, An inherent strain based multiscale modeling framework for simulating part-scale residual deformation for direct metal laser sintering, Additive Manufacturing 28 (2019) 406-418.

[103] S. Osher, J.A. Sethian, Fronts propagating with curvature-dependent speed: algorithms based on Hamilton-Jacobi formulations, Journal of computational physics 79(1) (1988) 12-49.

[104] M.Y. Wang, X. Wang, D. Guo, A level set method for structural topology optimization, Computer methods in applied mechanics and engineering 192(1) (2003) 227-246.

[105] G. Allaire, F. Jouve, A.-M. Toader, Structural optimization using sensitivity analysis and a level-set method, Journal of computational physics 194(1) (2004) 363-393.

[106] Y. Wang, Z. Luo, Z. Kang, N. Zhang, A multi-material level set-based topology and shape optimization method, Computer Methods in Applied Mechanics and Engineering 283 (2015) 1570-1586.

[107] P. Dunning, C. Brampton, H. Kim, Simultaneous optimisation of structural topology and material grading using level set method, Materials Science and Technology 31(8) (2015) 884-894.

[108] P. Liu, Y. Luo, Z. Kang, Multi-material topology optimization considering interface behavior via XFEM and level set method, Computer methods in applied mechanics and engineering 308 (2016) 113-133.

[109] J. Liu, Q. Chen, Y. Zheng, R. Ahmad, J. Tang, Y. Ma, Level set-based heterogeneous object modeling and optimization, Computer-Aided Design (2019).

[110] J. Liu, Q. Chen, X. Liang, A.C. To, Manufacturing cost constrained topology optimization for additive manufacturing, Frontiers of Mechanical Engineering 14(2) (2019) 213-221.

[111] Z. Kang, Y. Wang, Integrated topology optimization with embedded movable holes based on combined description by material density and level sets, Computer methods in applied mechanics and engineering 255 (2013) 1-13.

[112] P.D. Dunning, H. Alicia Kim, A new hole insertion method for level set based structural topology optimization, International Journal for Numerical Methods in Engineering 93(1) (2013) 118-134.

[113] J.A. Sethian, A fast marching level set method for monotonically advancing fronts, Proceedings of the National Academy of Sciences 93(4) (1996) 1591-1595.

[114] J.A. Sethian, Level set methods and fast marching methods: evolving interfaces in computational geometry, fluid mechanics, computer vision, and materials science, Cambridge university press1999.

[115] C. Le, J. Norato, T. Bruns, C. Ha, D. Tortorelli, Stress-based topology optimization for continua, Structural and Multidisciplinary Optimization 41(4) (2010) 605-620.

[116] A. Takezawa, G.H. Yoon, S.H. Jeong, M. Kobashi, M. Kitamura, Structural topology optimization with strength and heat conduction constraints, Computer Methods in Applied Mechanics and Engineering 276 (2014) 341-361.

[117] S. Hochreiter, J. Schmidhuber, Long short-term memory, Neural computation 9(8) (1997) 1735-1780.

[118] A. Krizhevsky, I. Sutskever, G.E. Hinton, Imagenet classification with deep convolutional neural networks, Advances in neural information processing systems 25 (2012) 1097-1105.

[119] K. Simonyan, A. Zisserman, Very deep convolutional networks for large-scale image recognition, arXiv preprint arXiv:1409.1556 (2014).

[120] K. He, X. Zhang, S. Ren, J. Sun, Deep residual learning for image recognition, Proceedings of the IEEE conference on computer vision and pattern recognition, 2016, pp. 770-778.

[121] O. Russakovsky, J. Deng, H. Su, J. Krause, S. Satheesh, S. Ma, Z. Huang, A. Karpathy, A. Khosla, M. Bernstein, Imagenet large scale visual recognition challenge, International journal of computer vision 115(3) (2015) 211-252.

[122] S. Ren, K. He, R. Girshick, J. Sun, Faster r-cnn: Towards real-time object detection with region proposal networks, Advances in neural information processing systems 28 (2015) 91-99.

[123] E.J. Schwalbach, S.P. Donegan, M.G. Chapman, K.J. Chaput, M.A. Groeber, A discrete source model of powder bed fusion additive manufacturing thermal history, Additive Manufacturing 25 (2019) 485-498.

[124] D.G. Duffy, Green's functions with applications, Chapman and Hall/CRC2015.

[125] J. Martínez-Frutos, D. Herrero-Pérez, Efficient matrix-free GPU implementation of fixed grid finite element analysis, Finite Elements in Analysis and Design 104 (2015) 61-71.

[126] F. Dugast, P. Apostolou, A. Fernandez, W. Dong, Q. Chen, S. Strayer, R. Wicker, A.C. To, Part-scale thermal process modeling for laser powder bed fusion with matrix-free method and GPU computing, Additive Manufacturing 37 (2021) 101732.

[127] A. Vaswani, N. Shazeer, N. Parmar, J. Uszkoreit, L. Jones, A.N. Gomez, Ł. Kaiser, I. Polosukhin, Attention is all you need, Advances in neural information processing systems, 2017, pp. 5998-6008.

[128] J. Devlin, M.-W. Chang, K. Lee, K. Toutanova, Bert: Pre-training of deep bidirectional transformers for language understanding, arXiv preprint arXiv:1810.04805 (2018).